

**Genesis and evolution of bedforms on cohesive mud beds
and simulated bedrock channels**

Daowei Yin

Submitted in accordance with the requirements for the degree of
Ph.D.

The University of Leeds
School of Earth and Environment

September, 2013

The candidate confirms that the work submitted is his/her own and that appropriate credit has been given where reference has been made to the work of others.

This copy has been supplied on the understanding that it is copyright material and that no quotation from the thesis may be published without proper acknowledgement.

The right of Daowei Yin to be identified as Author of this work has been asserted by him in accordance with the Copyright, Designs and Patents Act 1988.

© 2013 The University of Leeds and Daowei Yin

Acknowledgements

First and the most important is that I would like to express my gratitude to my supervisors, Prof. Jeff Peakall and Prof. Dan Parsons for encouraging me to apply for PhD in the University of Leeds five years ago, and providing the endless guidance and support during my work in the last 4 years. Without their patience, constant encouragement and valuable advice, it is impossible for me to complete my work so smoothly.

I am particularly grateful to the Chinese Government, China scholarship council and the University of Leeds for offering the scholarship for supporting my PhD study and my life in UK.

I really appreciate Dr. Gareth Keevil and Mr. Russell Dixon for all their strong support during the course of my experimental work in the Sorby lab and their sound advice for improving my experimental methodology. I would like to thank Dr. Rob Thomas, Lesley Neve, Kat Hunter and Brendan Murphy for their great help on my laboratory work. I also would like to thank Prof. Paul Wignall and his wife Karen Wignall, for their hospitality and help.

I would especially like to thank Prof. Zhongyuan Chen and his team members (Prof. Zhanghua Wang, Jing Chen, Maotian Li, Qianli Sun, Bin Chen, Yan Liu, and Hao Xu) and Prof. Heqin Cheng in East China Normal University, who provided me their endless supports and advice on both my life and my work before and after I came to UK.

I also would like to thank Yiwen Zhao, Taoyuan Wei and his wife, Qun Guo for their endless help and care since my first arrived in Leeds. Thanks to all my friends in Leeds, Yangwen Pei, Ke san Yam, Yadong Sun, Jinling Peng, Jihui Gao, Xiaolin Wang, Xin Li, Dr. Yanqing Sheng, Faith Chen, Bin Hou, Liang Wang, Yanan Jiang and Wang Hao for bringing me so colourful life in Leeds.

Last but not the least, I would like to thank my family for their endless support and love throughout my life. Thank you, Mum, Dad, and Grandma.

This thesis is dedicated in loving memory of my deeply loved grandfather.

Abstract

Most previous studies on the genesis and evolution of bedforms have focused on aggradational bedforms within cohesionless sediments, with very few investigations that concern either erosive bedform genesis and evolution or bedrock channel abrasion processes. The study presented here details experiments that involve the genesis and formation of erosional bedform features within natural (soft clay) cohesive sediment beds and analogue bedrock substrates by modelling clay under the effect of both open-channel plain water flows, and sediment-laden flows. A new approach without using plaster-of-Paris or real bedrock developed provides a feasible method to simulate the genesis and evolution of the erosional bedforms in cohesive sediment beds and sculpted forms in bedrock channels on relatively short time-scales in the laboratory by using a realistic substrate substitute.

A series of flume experiments are presented herein where the undrained shear strength of two different kinds of substrate material is systematically varied under constant flow conditions. Experiments using plain water flow indicated that erosive bedforms in cohesive sediment substrate cannot be produced only under the effect of sediment-free flow. Particulate-laden flows do form erosional bedforms in both kinds of clay beds and the shear strength of the bed material plays a key role in determining the diversity of erosional features forming on such substrates. Optimisation of modelling clay beds has enabled us to successfully replicate a suite of bedrock bedforms, including potholes, flutes, longitudinal furrows, etc., that have clear equivalents to those observed in bedrock rivers and contributed to investigate the genesis and evolution process of them and explore the flow structures within and above them in experimental analogue bedrock substrate for the first time.

Table of Contents

| | |
|---|------------|
| Acknowledgements..... | iii |
| Abstract..... | v |
| Chapter 1 Thesis rationale | 1 |
| 1.1 Introduction | 1 |
| 1.2 Thesis objectives..... | 3 |
| 1.3 Thesis structure..... | 4 |
| Chapter 2 Morphology and processes controlling erosional features on cohesive and bedrock substrates | 7 |
| 2.1 Introduction | 7 |
| 2.2 The morphology of erosional features on cohesive substrates | 7 |
| 2.3 Sculpted forms in bedrock channels | 17 |
| 2.3.1 Introduction | 17 |
| 2.3.2 Bedforms in open bedrock channels | 19 |
| 2.4 Undrained shear strength measurement of continental marine sediments and experimental mud beds..... | 30 |
| 2.4.1 The composition and texture of marine sediments..... | 31 |
| 2.4.2 Shear strength measurement of continental marine sediments..... | 31 |
| 2.5 Summary..... | 36 |
| Chapter 3 Erosion experiments on mud substrates: Methodology | 39 |
| 3.1 Introduction | 39 |
| 3.2 Experimental setup..... | 42 |
| 3.2.1 Flume tank | 42 |
| 3.2.2 Clay preparation and undrained shear strength measurement | 44 |
| 3.2.3 Sediment addition and water sampling..... | 51 |
| 3.2.4 Flow velocity measurements by ultrasonic Doppler velocity profiling (UDVP) | 54 |
| 3.2.5 Topographic measurement using Seatek Ultrasonic Ranging System..... | 56 |
| 3.2.6 Production of a fixed bed morphology | 58 |
| 3.2.7 3-D Flow velocity measurement by Acoustic Doppler velocimetry (ADV) | 59 |
| 3.3 Summary..... | 62 |

| | |
|---|------------|
| Chapter 4 Cohesive mud bed channel erosion: bedform dynamics and formative processes | 63 |
| 4.1 Introduction..... | 63 |
| 4.2 Erosion and bedform development on experimental cohesive mud beds | 63 |
| 4.2.1 Experimental setup..... | 63 |
| 4.2.2 Mud erosion in sediment-free flows..... | 66 |
| 4.3 Overall development of clay beds in each of the runs with suspended sediment | 71 |
| 4.3.1 Evolution of bedforms of Exp. 1 and Exp. 2 | 71 |
| 4.3.2 Comparison of bedform development over time..... | 78 |
| 4.4 Bedforms in experimental cohesive clay beds..... | 86 |
| 4.5 Experiments with medium hard clay bed | 90 |
| 4.6 Discussion | 96 |
| Chapter 5 Physical modelling of erosional bedrock bedforms | 99 |
| 5.1 Motivation and research objective | 99 |
| 5.2 Experimental setup and background | 99 |
| 5.3 Erosional bedforms observed in the experiments..... | 105 |
| 5.3.1 The evolution of the experimental modelling clay beds | 105 |
| 5.3.2 Potholes | 107 |
| 5.3.3 Longitudinal features | 119 |
| 5.3.4 Non-longitudinal furrows..... | 142 |
| 5.3.5 Convex and undulating surfaces | 144 |
| 5.3.6 Composite forms | 145 |
| 5.4 Discussion | 148 |
| 5.5 Summary | 150 |
| Chapter 6 The evolution of erosional bedforms on bedrock..... | 151 |
| 6.1 Introduction..... | 151 |
| 6.2 Evolution of erosional features on experimental analogue bedrock | 152 |
| 6.2.1 Potholes | 152 |
| 6.2.2 Flutes | 179 |
| 6.2.3 Longitudinal furrows | 195 |
| 6.2.4 Non-longitudinal furrows..... | 213 |
| 6.2.5 Convex and undulating surfaces | 215 |
| 6.2.6 Composite forms | 218 |

| | |
|---|------------|
| 6.3 Discussion..... | 220 |
| 6.4 Summary..... | 223 |
| Chapter 7 Flow structure within and above analogue bedrock bedforms..... | 225 |
| 7.1 Introduction | 225 |
| 7.2 Experimental setup and background..... | 225 |
| 7.3 Flow structure above and within erosional marks in an experimental analogue bedrock channel..... | 230 |
| 7.3.1 Potholes | 230 |
| 7.3.2 Flutes | 246 |
| 7.3.3 Longitudinal furrows | 259 |
| 7.3.4 Other erosional features..... | 267 |
| 7.4 Discussion..... | 275 |
| 7.4.1 General flow pattern above potholes in experiments | 276 |
| 7.4.2 General flow pattern above flutes in experiments | 277 |
| 7.4.3 General flow pattern above longitudinal furrows in experiments..... | 279 |
| 7.4.4 General flow pattern above other erosional features in experiments..... | 279 |
| 7.4.5 The classification of the flow structures above different erosion features in experimental beds | 280 |
| 7.5 Summary..... | 285 |
| Chapter 8 Summary and conclusion: generation of erosional features on cohesive materials with different characteristics | 287 |
| 8.1 Introduction | 287 |
| 8.2 Summary of physical modelling experiments with terracotta pottery clay..... | 287 |
| 8.3 Summary of physical modelling experiments with modelling clay..... | 288 |
| 8.4 Summary of flow velocity measurement over bedrock bedforms using ADV | 289 |
| 8.5 Conclusion | 290 |
| 8.6 Perspectives on future work..... | 290 |
| List of References | 293 |
| List of Abbreviations..... | 307 |

List of Tables

| | |
|---|-----|
| Table 3.1 Experimental setting and results of main previous experimental work on both of the cohesive and bedrock bedforms..... | 41 |
| Table 3.2 The experimental time intervals for experiments 1 and 2 | 43 |
| Table 3.3 The experimental time intervals for experiments 3 to 5 | 44 |
| Table 3.4 The experimental time intervals for the sediment-laden experiments 6-8 | 44 |
| Table 3.5 XRD analysis of Terracotta potters clay used as experimental beds in experiments 0, 1, 2, 3, 4 and 5 (Macdonald, 2010) | 45 |
| Table 3.6 XRD analysis of modelling clay used as experimental beds in experiments 5, 6, 7 and 8..... | 45 |
| Table 3.7 The calibration certification of the vane shear strength meter provided by the manufacturer..... | 46 |
| Table 3.8 Difference among each experiment: sand addition amount, water sampling time, and velocity monitoring time. | 52 |
| Table 3.9 Parameters for the UDVP used in the presented experiments | 55 |
| Table 3.10 Vectrino-II ADV operating configuration | 60 |
| Table 4.1 Shear velocity u^* (ms^{-1}) and basal shear stress τ (Nm^{-2}) measured at 6 mm above the experimental bed in Exps. 1, 2, 3 and 5. For details of the position of the UDVP probes, please refer to Section 3.2.5 in Chapter 3. | 65 |
| Table 4.2 Strength of the experimental substrate for all experiments. Exp. 0: hard pottery clay bed; Exp. 1: hard pottery clay bed; Exp. 2: hard pottery clay bed; Exp. 3: soft pottery clay bed; Exp. 4: medium pottery clay bed; Exp. 5: medium pottery clay bed. | 66 |
| Table 4.3 Flow velocity u (ms^{-1}), shear velocity u^* (ms^{-1}) and basal shear stress τ (Nm^{-2}) measured at 6 mm above the experimental bed in Exp. 4. For details of the position of the UDVP probes, see Section 3.2.5 in Chapter 3..... | 94 |
| Table 5.1 The experimental time intervals for the sediment-laden experiments..... | 101 |
| Table 7.1 The features of the flow structures within and above the different erosional features in simulated bedrock beds. | 284 |

List of Figures

| | |
|---|----|
| Figure 1.1 Flow chart diagram of the thesis structure. | 5 |
| Figure 2.1 High-resolution bed topography of the studied cases of Vachtman and Laronne (2011) and schematic illustration of the corresponding flow patterns. Case I and II demonstrate the 3-D model of single trough and single ridge and the related flow patterns, respectively; Case II illustrates a case of combination of troughs and ridges and related flow pattern. From Vachtman and Laronne (2011)..... | 9 |
| Figure 2.2 Schematic of the classic flute mark model showing the chief morphological features and linear dimensions. A: the general geometric morphology of a classic flute mark; B: the longitudinal-section of a classic flute marks; C: the cross-section of a classic flute mark. From Allen (1971a)..... | 12 |
| Figure 2.3 Schematic types of transverse erosional mark in profile and plan on cohesive beds (Allen, 1971a). The symmetrical bedforms: (a) wave-like, (b) broad parabolic, (c) narrow parabolic, (d) spindle-shaped, (e) comet-shaped, and (f) polygonal erosional marks; The asymmetrical bedforms: (g) simple, (h) corkscrew, (i) twisted, and (j) polygonal erosional marks. From Allen (1982)..... | 14 |
| Figure 2.4 Types of assemblage of erosional marks. Each of the classes shown has been observed under natural conditions. Heterogeneous assemblages: (a) clustered, (b) longitudinal, and (c) diagonal; Homogeneous assemblages: (a) broad parabolic flutes, (b) narrow parabolic flutes, (c) spindle-shaped flutes, (d) comet-shaped flutes, (e) asymmetrical simple flutes, (f) wave-like marks, also known as mud ripples, (g) dense broad parabolic flutes, (h) dense narrow parabolic flutes, and (i) asymmetrical polygonal erosional marks. From Allen (1982)..... | 15 |
| Figure 2.5 Erosional features produced by experiments conducted by Johnson and Whipple (2007) and their natural equivalents. (a) Runnel with alternating scour produced by experiments. (b) A natural similar form of runnel in (a) in the south fork of Maidenwater Creek. (c) a broad projection on experimental bed. Flume width 40 cm. (d) Similar geometry of a trough in the field. (e) and (f) Two potholes with both entry and exit furrows formed in the experiments; Pothole diameter 5–6 cm; (g) natural pothole with diameter of about 60 cm and partially filled with sediment clasts. (h) Natural pothole with diameter of about 2 m. From Johnson and Whipple (2007). | 22 |
| Figure 2.6 Schematic morphology of potholes. Arrows indicate flow directions. Dashed lines (where present) indicate lines of cross sections. From Richardson and Carling, 2005. | 24 |
| Figure 2.7 Schematic morphology of flutes, short furrows and parallel-sided furrows in bedrock channels. Note that all flute marks are shown as flaring, yet the definition includes forms that close at the downstream end. From Richardson and Carling (2005)..... | 27 |

| | |
|--|----|
| Figure 2.8 Compound longitudinal furrows. A: regular compound furrows and irregular compound furrows; B: two kinds of expanding furrows: funnel-shaped and bulbous furrows. Arrows indicate flow directions (where appropriate). From Richardson and Carling (2005). | 29 |
| Figure 2.9 Vane shear apparatus used by Richards (1961). Each vane is 1.3 cm in diameter and 1.9 cm long. It is rotated by a constant-speed motor at a rate of 6 degrees per minute (0.1° per second). The vane needs to be buried into sediment by a distance not less than its length (Richards, 1961). | 32 |
| Figure 2.10 Undrained shear strength as function of relative water content (W/PI) for mud sampled from IJmuiden Harbour, Netherland. From Winterwerp and Van Kesteren (2004). | 34 |
| Figure 2.11 Shear strength versus penetration for ocean sediments (on the basis of Bryant et al. (1981) and Davie et al. (1978)). The red dashed square shows the shear strength values of the material near the sea floor, the depth of which is less than 25 m below the sea floor. The curve of Bouma and Moore (1975) SITE 294 shows that the shear strength of pelagic clays increases exponentially with increasing depth of burial and is less than 10 kPa when the increase of depth of burial is less than 25 m; Dashed line of DSDP (1969-1986) demonstrates that the shear strength of hemipelagic and terrigenous clays increases linearly with increase of depth of burial. The value of the uppermost layer of hemipelagic and terrigenous clays is about 10 kPa. | 35 |
| Figure 3.1 The recirculating Hydraulic Slurry Flume in the Sorby Environment Fluid Dynamics Laboratory; looking downstream. The false floor composed of Perspex can be clearly seen. | 42 |
| Figure 3.2 Schematic drawing of the experimental setup of the Hydraulic Slurry Flume. The brown area represents the clay bed with a tray system which was lowered into position, so that the top surface of the clay bed was at the same level of the surrounding false floor..... | 43 |
| Figure 3.3 Images of the H-60 field inspection vane tester 26-3335, with a range of different size vanes (http://www.aisys.com.sg/items/Item_Details.aspx?itemid=157&cateid=74). | 46 |
| Figure 3.4 Relationship between the vane meter reading and torque, based on the manufacturer's calibration data (see Table 3.6)..... | 47 |
| Figure 3.5 A schematic figure of the undrained shear strength measurement positions (+) on the mud bed in the hydraulic flume. Flow direction is from right to left. Except for the first 6 hours soaking in a side box, all the remaining measurements were done directly in the flume. The rationale for dividing the clay bed into compressed and uncompressed areas was to identify the influence of uncertain pressure inadvertently applied to the mud bed on shear strength when flattening the surface of the mud bed. | 48 |

| | |
|--|----|
| Figure 3.6 The relation between undrained shear strength and soaking time of the downstream part of the mud bed, for uncompressed clay bed..... | 49 |
| Figure 3.7 The relation between undrained shear strength and soaking time of the downstream part of the mud bed, for compressed clay bed..... | 50 |
| Figure 3.8 Undrained shear strength change with soaking time. Exp. 0, 1 & 2: 19 kPa; Exp. 3: 6.5-7 kPa; Exp. 4: 9 kPa; Exp. 5: 9 kPa; Exp. 6: 10.5 kPa; Exp. 7: 7-7.5 kPa; Exp. 8: 5.5 kPa. | 51 |
| Figure 3.9 Grain size distribution curve of the suspended sediment in the flow as calculated using a Malvern Mastersizer 2000 laser diffractometer. | 52 |
| Figure 3.10 Suspended sediment concentration for experiments 1-4. | 53 |
| Figure 3.11 Suspended sediment concentration for experiments 6-8. | 53 |
| Figure 3.12 Schematic figure showing (A) the downstream, and (B) the vertical positioning of the ultrasonic Doppler velocity profiler's (UDVP) probe arrays..... | 54 |
| Figure 3.13 Downstream velocity profiles of Exp. 1 over time, taken at the channel centreline above the mud bed. | 55 |
| Figure 3.14 Seatek Ultrasonic Ranging System (5 MHz) with transducers. From Seatek Instrumentation. | 56 |
| Figure 3.15 Plan view of arrangement for bathymetric profiling of experimental beds. A: All the data were collected within the red box by the Seatek system. The clay bed showed in A is the original flat bed before the start of the experiments. B: Schematic figure of the array of the Seatek sampling point on the clay bed. The resolution of a single scan is 2 mm x 15 mm. C: The probe holder moved in Y direction by 3 mm after each single scan to increase the sampling resolution. Such scans were repeated 6 times for each time interval. | 57 |
| Figure 3.16 The cast made by the plaster-of-Paris and the replica of the final bed formation of Exp. 8 made using latex. A: cast made by the plaster-of-Paris; B: Latex replica of the final bed of Exp. 8..... | 59 |
| Figure 3.17 The Nortek Vectrino-II Acoustic Doppler velocimetry (ADV). From Nortek AS, Norway (http://www.nortekusa.com/usa/products/acoustic-doppler-velocimeters/vectrino-ii) | 60 |
| Figure 3.18 A schematic figure of the working principle of the Vectrino-II ADV. Only 2 of 4 receiver beams are shown in this figure. The included angle between 2 adjacent receiver transducers is 90 degrees. The red area shown in this figure is the effective measurement coverage, 3 cm. From Nortek AS, Norway (http://www.nortekusa.com/usa/products/acoustic-doppler-velocimeters/vectrino-ii) | 61 |

| | |
|--|----|
| Figure 3.19 One series of the velocity profiles over and within an erosional feature measured by Vectrino-II ADV. | 62 |
| Figure 4.1 A & B: Planform images of pottery clay beds of Exp. 0 under the effect of recirculating clear water after 15 minutes and 60 minutes, respectively. C, D, E & F: Planform images of pottery clay beds under the effect of recirculating sediment-laden flow after 15 minutes and 60 minutes, respectively. C & D are clay beds of Exp. 1; E & F are clay beds of Exp. 2. All the beds are 30 cm wide. Flow is from right to left. | 69 |
| Figure 4.2 Experiment 5 conducted using sediment-free flow and terracotta pottery clay with undrained shear strength of 9 kPa. Flow from right to left. All the clay beds are 30 cm wide..... | 70 |
| Figure 4.3 Experimental beds of Exp. 1 and Exp. 2: T0 to T60. Each label on beds of Exp. 1 contains 13 black squares with white crosses, each of which is 1.0 cm long and 1.0 cm wide. Flow from right to left. All the beds are 30 cm wide..... | 74 |
| Figure 4.4 Experimental beds of Exp. 1 and Exp. 2: T120 to T300. Each label on beds of Exp. 1 contains 13 black squares with white crosses, each of which is 1.0 cm long and 1.0 cm wide. Flow from right to left. All the beds are 30 cm wide. The white squares tag the wavy features. The white arrows point the heads of wavy features. Yellow curves represent the short sinuous furrows on the beds. Yellow rectangles tag the gullies. | 75 |
| Figure 4.5 Experimental beds of Exp. 1 and Exp. 2: T360 to T540. Each label on beds of Exp. 1 contains 13 black squares with white crosses, each of which is 1.0 cm long and 1.0 cm wide. Flow from right to left. All the beds are 30 cm wide. The white squares tag the wavy features. Yellow rectangles tag the gullies. | 76 |
| Figure 4.6 Experimental beds of Exp. 1 and Exp. 2: T600 to T780. Each label on beds of Exp. 1 contains 13 black squares with white crosses, each of which is 1.0 cm long and 1.0 cm wide. Flow from right to left. All the beds are 30 cm wide..... | 77 |
| Figure 4.7 Comparison of the clay beds of Exp.1, Exp, 2 and Exp. 3: From the beginning of the experiments to 180 minutes experimental time (T0 to T180). Flow from right to left. Red boxes point the wavy features on the beds of Exp. 2. All the clay beds are 30 cm wide. The dimension of each black box in the scale bar is 1 cm x 1 cm..... | 82 |
| Figure 4.8 3D elevation plots of the experimental beds of Experiment Exp. 1, 2 and 3 (T0 to T240) showing bedform development with time (in minutes). Flow from right to left. Each bed is 90 cm long and 30 cm wide. The colour scale bar is in centimetre..... | 83 |
| Figure 4.9 Comparison of the clay beds of Exp.1, 2 and 3: From 240 minutes to 480 minutes experimental time (T240 to T480). Red boxes point the wavy features on the beds of Exp. 2. All the clay beds are 30 cm wide. | 84 |

| | |
|--|-----|
| Figure 4.10 3D elevation plots of the experimental bed of Experiment Exps. 1, 2 and 3 (T300 to T780) showing bedform development with time (in minutes). Each bed is 90 cm long and 30 cm wide. Flow from right to left. The colour scale bar is in centimetre. | 85 |
| Figure 4.11 Example of tiny erosional marks and potholes formed in the experiments. a. several solo tiny erosional marks observed in Exp. 1 bed; b. compound erosional pits observed in Exp. 2 bed; c. a pothole observed in Exp. 1 bed. Flow from right to left. | 86 |
| Figure 4.12 Typical forms of different type flutes observed in the experiments. a. Solo flute marks from Exp. 1; b. Flute marks with median-ridge from Exp. 2; c. Spindle-shaped flute marks from Exp. 2; d. Comet-shaped flute marks from Exp. 2; e. Compound flute marks from Exp. 1; f. Flute marks with internal structures from Exp. 1; g. Flute marks with external structures from Exp. 2; h. curved flutes with secondary external furrows from Exp. 2. Flow direction is from right to left. | 88 |
| Figure 4.13 Furrows formed in the experiments. a. slight curved short furrows from Exp. 1; b. long curved furrows; c. compound convergent furrows; d. bifurcating furrows; e. long sinuous furrows. b-e from Exp. 2. Flow direction is from right to left. | 89 |
| Figure 4.14 A long broad gully formed in Exp. 2. Flow direction is from right to left. | 90 |
| Figure 4.15 Plan view photographs and 3D elevation plots of the experimental bed of Exp. 4 (T0 to T420) showing bedform development with time (in minutes). Flow from right to left. The colour scale bar is in centimetre. The vertical scale bar is in centimetre. | 91 |
| Figure 4.16 Plan view photographs and 3D elevation plots of the experimental bed of Exp. 4 (T480 to T960) showing bedform development with time (in minutes). Flow from right to left. The colour scale bar is in centimetre. The vertical scale bar is in centimetre. | 92 |
| Figure 4.17 The velocity profiles of Exp. 4. | 93 |
| Figure 4.18 Shear velocity u^* (ms^{-1}) and basal shear stress τ (Nm^{-2}) measured at 6 mm above the experimental bed in Exp. 4. | 95 |
| Figure 5.1 Undrained shear strength change with soaking time. Exp. 6: 10.5 kPa; Exp. 7: 7.5 kPa; Exp. 8: 5.5 kPa. | 100 |
| Figure 5.2 Experimental beds of Exp. 6, 7 and 8: T0 to T1080. The initial clay bed of Exp. 6. The big hollows are 2.4 cm in diameter and 0.3 cm in depth. The small hollows are 0.9 cm in diameter and 0.2 cm in depth. Flow from right to left. All the beds are 30 cm wide. | 102 |
| Figure 5.3 Experimental beds of Exp. 6 and 7: T1200 to T1680. Flow from right to left. All the beds are 30 cm wide. | 103 |
| Figure 5.4 Grain size distribution of the sediment added into the flow | 104 |

| | |
|---|-----|
| Figure 5.5 Suspended sediment concentration for Exp. 6, Exp. 7 and Exp. 8..... | 104 |
| Figure 5.6 3D elevation plots of the experimental beds of Experiment Exp. 6, 7 and 8 showing bedform development with time (in minutes). Flow from right to left. The colour scale bar is in centimetre. The vertical scale bar is in centimetre. | 106 |
| Figure 5.7 Standard round pothole (SRP). A and B demonstrate simple potholes in Exp. 7. C is a simple pothole from the River Lune (Halton), UK (from Richardson and Carling (2005)) with a length : width ratio of 1.35. The bedrock is fine-grained sandstone. The scale bar in C is 60 cm long. Flow from right to left in all images. | 108 |
| Figure 5.8 Spiral furrowed potholes (SFP). A and B illustrate SFP in Exp. 6 and 7, respectively. Flow from right to left. C shows a spiral furrowed pothole with a central boss in Nam Mae Chaem (Ob Luang), Thailand (from Richardson and Carling (2005)). D is a schematic diagram to show how the wall and the bottom of a spiral furrowed pothole erode by sediment-laden flow (from Alexander (1932)). | 109 |
| Figure 5.9 Potholes with exit furrows (PwEF) A and B are PwEF from Exp. 7 and Exp. 8, respectively. C are PwEF in the River Lune (Halton), UK (from Richardson and Carling (2005)). The scale in C is 60 cm long. Flow is from right to left in all cases. | 110 |
| Figure 5.10 Potholes with extended exit furrows (PwEEF). The exit furrows of this kind of pothole are much longer than in PwEF. A and C are two PwEEF obtained by Exp. 7. B and D are two observed in the field (from Richardson and Carling (2005)). C and D are compound potholes with extended exit furrows. The pothole in A is 3.69 cm long and 1.59 cm wide. The exit furrow of C is 2.20 cm long. Pen is for scale. Flow direction is from right to left in all images. | 111 |
| Figure 5.11 Potholes with both entry and exit furrows (PwEnEF) in Exp. 7. | 111 |
| Figure 5.12 Open potholes (OP). A was observed in Exp. 7 and was 2.85 cm long and 1.54 cm wide. B is an OP from the River Lune (Halton), UK. It is 120 cm long with a diameter of 60 cm (from Richardson and Carling (2005)). Flow from right to left in both images..... | 112 |
| Figure 5.13 Spiral-furrowed pothole with a spiral rib (SFPwSR). The spiral rib (red arrowed) is a little entry furrow which is much smaller than the scale of the primary pothole. A and B are from the central part of the bed in Exp. 7; A is about 1.29 cm wide and B is 1.31 cm wide. C is observed in Woolshed Creek, Australia. The pothole is ~1.5 m (from Richardson and Carling (2005)). Flow is from right to left in all cases..... | 113 |

| | |
|---|-----|
| Figure 5.14 Potholes with horizontal furrows (PwHF). These tend to form in deeper potholes. A observed in Exp. 8, represents experimentally derived features. B shows a complex pothole with horizontal furrows in the River Lune (Tebay), UK. The arrows show the rims of a PwHF; Flow from right to left. The scale is 60 cm long (from Richardson and Carling (2005)). | 114 |
| Figure 5.15 Potholes with external secondary furrow (PwESF). The primary pothole in A is 2.4 cm long and 1.3 cm wide from Exp. 6; B and C are from Exp. 7. Flow direction is from right to left. | 115 |
| Figure 5.16 Complex potholes (CoP). A & B are CoP observed in Exp. 6 and 8, respectively. C is a compound lateral pothole in Nam Mae Chaem (Ob Luang), Thailand (from Richardson and Carling (2005). Flow from right to left. Notebook is for scale. | 116 |
| Figure 5.17 Hierarchical potholes (HP). HPs contain at least two classes of pothole. The most obvious part is that there is a great variety in internal scour depth within them. A and B are two HP in Exp. 6. Flow from right to left. C is the HP observed in the real bedrock surface, Nam Mae, Chaem (Ob Luang), Thailand. Flow from top to bottom. The notebook (15 cm long) is for scale. (from Richardson and Carling (2005)). | 116 |
| Figure 5.18 Horseshoe-shaped paired potholes (HSPP). A and B are observed in Exp. 6; C and D are observed in Exp. 8. Their dimensions range from 4 – 6 cm in width, and from 5 – 8 cm in length. The depth ranges from 0.4 cm to 2.9 cm. Figure 5. 15A is 4.10 cm wide 5.50 cm long and 2.3 cm deep. Flow direction from right to left. E: paired lateral potholes in Wadi Hazazon, Israel. Upstream to the right. Dolomite. Coin for scale. (from Richardson and Carling (2005)) | 117 |
| Figure 5.19 Approximate-symmetrical paired pothole with both entry and exit furrows (ASPPwEEF). This system contains two asymmetrical potholes with both entry and external furrows which connect with each other and form on a central axis of the whole system. A and B are observed in Ex. 7. Flow from right to left. | 118 |
| Figure 5.20 Broad and narrow flutes. A shows broad flutes formed on an experimental substrate of Exp. 7. They are 2.75 cm wide and 1.09 cm long. B is a natural broad flute in Wadi Hazazon, Israel. Limestone. Coin is for scale (from Richardson and Carling (2005)). C and D are the narrow flutes in experiments and natural bedrock, respectively. The small one in C is observed in Exp. 7, which is 1.77 cm long and 0.79 cm wide. Flow from right to left. (from Richardson and Carling (2005)) | 121 |
| Figure 5.21 Deep and shallow flutes. A. deep flute in Exp. 6; B. deep flute in the natural environment (from Richardson and Carling (2005)); C. shallow flute in Exp. 7; D. extremely shallow flute in Exp. 8. Flow from right to left in all cases. | 122 |

| | |
|---|-----|
| Figure 5.22 Flutes with median ridges (FwMR). A, B, C and D are flutes with median ridges selected from the experimental bed. A, , and C are observed in Exp. 7. D is in Exp.8. E is the one with two internal secondary structures observed in the River Lune (Tebay), UK. Knife is for scale. (from Richardson and Carling (2005)). | 123 |
| Figure 5.23 Overhanging flutes (OF). A: 1.53 cm in width; B: 4.26 cm in length. Both A and B are observed in Exp. 7. Flow from right to left. | 124 |
| Figure 5.24 Spindle-shaped flutes (SF). A is a typical spindle-shaped flute in Exp. 7. B is a group of SF observed in volcanic rock in Huai Nang Rong, Thailand. Flow from left to right. Pen is for scale (from Richardson and Carling (2005)). | 125 |
| Figure 5.25 Comet-shaped flutes (CSF). CF is kind of sinuous narrow flute with cuspsate proximal ends. A is in Exp. 7 and B is in Exp. 8. Flow from right to left. | 125 |
| Figure 5.26 Flutes with internal secondary structure (FwISS). The internal secondary structures are usually small furrows within the outline of the flutes. A and B are FwISS Exp. 7 with internal secondary furrows on one side of their flanks (yellow arrowed). C contains a flute close to its upper rim (pointed by the pen) in Borrow Beck, UK. Flow from right to left. Pen is for scale (from Richardson and Carling (2005)). | 126 |
| Figure 5.27 Flutes with external secondary structures (FwESS). A, B, C and D are several rows of flutes developing in Exp. 7. Normally the first flute in a row is regarded as the primary flute. The remaining flutes are the secondary ones. E is a row of small flutes (tagged by yellow ellipse) from the River Dee, UK. Flow from right to left. Ruler in centimetres for scale. (from Richardson and Carling (2005)). | 127 |
| Figure 5.28 Paired flutes (PF). A and B are PF from Exp. 7 and 6, respectively. Two solo flutes which share a flank rim comprise paired flutes. These two flutes are symmetrical or approximately symmetrical. C is a paired flute developed in Nam Mae Chaem (Ob Luang), Thailand. Flow from right to left. Pen is for scale. (from Richardson and Carling (2005)). | 128 |
| Figure 5.29 Paired convergent flutes (PCF). Two symmetrical slightly curved flutes with lateral secondary furrows and a big median ridge form a PCF. The whole system is observed in Exp. 7, which is about 2.38 cm wide. Flow from right to left. (from Richardson and Carling (2005)). | 129 |
| Figure 5.30 A. Lineations as seen on the bed of Exp. 7. These short flutes and furrows are about 1.0 - 1.5 cm long and 0.2-0.4 cm wide. B shows lineations in the field, from the River Dee, UK. Flow from right to left. Hammer is for scale. (from Richardson and Carling (2005)). | 130 |

| | |
|--|-----|
| Figure 5.31 A shows a set of En echelon flutes formed in Exp. 7. Each of the flutes is about ~1.0-2.5 cm long, ~1.0-1.5 cm wide and ~0.8 cm deep. Flow is from right to left. B shows en echelon flutes in Nam Mae Chaem (Ob Luang), Thailand. Flow from bottom right to top left. The rock projection is about 4 m across (from Richardson and Carling (2005)). | 131 |
| Figure 5.32 Straight short furrows (SSFrw). A and C are straight short furrows in Exp. 7. Furrows in A are 2.5-2.95 cm long and 1-1.15 cm wide. B and D are those in the field, River Dee, UK. Flow from right to left. Knife is for scale. (from Richardson and Carling (2005)). | 132 |
| Figure 5.33 Curved short furrows (CSFrw). A and B are curved short furrows in Exp. 7 and in the natural bedrock channel respectively. A is about 2.33 cm long and 0.85 cm wide. Flow from right to left. B. Knife is for scale. (from Richardson and Carling (2005)). | 133 |
| Figure 5.34 Straight parallel-sided furrows (SPFrw). Straight furrows have parallel flank rims which are round or cusped. A is from Exp. 8 and B is from Exp. 7. Flow from right to left. (from Richardson and Carling (2005)). | 134 |
| Figure 5.35 Cusped and non-cusped parallel-sided furrows (CPSFrw or NCPSFrw). A: non-cusped straight parallel sided furrow; B: cusped curved parallel sided furrow. They are from Exp. 7. Flow from right to left. | 134 |
| Figure 5.36 Sinuous parallel-sided furrows (SPSFrw). A, C & D: examples of features observed in Exp. 8, 7 and 6, respectively. Flow from right to left. B was observed in River Lune (Halton), UK. Flow from bottom right corner to top left corner. The scale is 60 cm long. (from Richardson and Carling (2005)). | 135 |
| Figure 5.37 Shear zone furrows (SZFrw). Flow from right to left. A & B are shear zone furrows in Exp. 7; the red circles mark the position of an elevated region that may have acted as an obstacle to the flow. C is one found in a real bedrock channel, from Birk Beck, UK. Flow from top to bottom. The scale is about 30 cm long. (from Richardson and Carling (2005)). | 136 |
| Figure 5.38 Bifurcating furrows (BFrw). A, B & C: bifurcating furrows in the experiments; A is observed in Exp. 7; B and C are in the bed of Exp. 8. Flow from right to left; D: Bifurcating furrow in the field, Woolshed Creek, Australia. Flow from top right to bottom left (from Richardson and Carling (2005)). | 137 |
| Figure 5.39 Convergent furrows (CFrw) in the bed of Exp. 7. Flow from right to left. | 138 |
| Figure 5.40 Groups of parallel-sided furrows (GPSF). A: GPSF obtained in Exp. 7. Flow from right to left. B: GPSF in the field, Wadi Hazazon, Israel. 20 cm wide camera bag is for scale. Flow from right to left (from Richardson and Carling (2005)). | 139 |

| | |
|--|-----|
| Figure 5.41 Regular compound furrows (RCFrw). A RCF in Exp. 7; B: RCF in the field, from Than Rattana, Thailand. Flow from right to left. The notebook (15 cm long) is for scale (from Richardson and Carling (2005)). | 140 |
| Figure 5.42 Irregular compound furrows (IRCF). A & B: IRCF in Exp. 7; Flow from right to left. C: IRCF in the field, Nahal Zin, Israel. Camera bag (20 cm wide) is for scale. Flow from top right to bottom left (from Richardson and Carling (2005)). | 141 |
| Figure 5.43 Expanding furrows (EF). A, B & C: EF in the experiments. A and B are in Exp. 7; C is in Exp. 8. Flow from right to left. D: Funnel-shaped furrow in the field, Stakeley Beck, UK. Flow top right to bottom left. The scale is 60 cm long. D: Bulbous furrow in the River Lune (Halton), UK. Flow from right to left. Scale is 60 cm long (from Richardson and Carling (2005)). | 142 |
| Figure 5.44 Reversed furrows (RF). A, B & C: reversed furrows in experimental bed. A is in Exp. 8; B and C are in Exp. 6. Flow from right to left. D to G: RF in the field from Nam Mae Chaem (Ob Luang), Thailand; flow from top to bottom (from Richardson and Carling (2005)). | 143 |
| Figure 5.45 Hummocky forms (HF). A-B: Regular trains of sharp-crested hummocky forms (SCHF) obtained in Exp. 7 and 8, respectively. Flow from right to left. C to F: HF found in natural bedrock surfaces (from Richardson and Carling (2005)). | 144 |
| Figure 5.46 Bladed forms (BFm). A & B: Bladed forms observed in Exp. 7 and 8, respectively. Flow from right to left; C: Bladed forms in a real bedrock surface from River Lune (Tebay), UK. Flow from top right to bottom left (from Richardson and Carling (2005)). | 145 |
| Figure 5.47 Obstacle marks (OM): Current Crescent (CC). A & F: Obstacle marks with secondary sculpting; B, C, D & E: Obstacle marks with internal secondary structures; A, C, D, and E are observed in Exp. 6; B and F are in Exp. 8 and 7, respectively; G & H: Obstacle marks in the field. G was observed from Sichiri-gawa, Japan. H was observed from Nam Mae Chaem (Ob Luang), Thailand. Flow from right to left (from Richardson and Carling (2005)). | 147 |
| Figure 6.1 Evolution of standard round potholes. Both potholes were observed in the clay bed of Exp. 7. Flow from right to left. Yellow curved arrows refer to the possible path of secondary flow. a, b, c and d refer to flow separation points. | 154 |
| Figure 6.2 Evolution of spiral furrowed potholes. The pothole in Plot A was observed in the clay bed of Exp. 6 and the pothole in Plot B was observed in the clay bed of Exp. 7. Flow from right to left. Yellow curved arrows refer to the possible path of secondary flow. | 157 |

| | |
|--|-----|
| Figure 6.3 Evolution of a pothole with exit furrows. The pothole was observed in the clay bed of Exp. 7. Flow from right to left. Red ellipses refer to the bigger pothole; the yellow ellipses refer to a secondary small pothole that eventually changed the overall form to be a secondary furrow..... | 159 |
| Figure 6.4 Evolution of potholes with extended exit furrow. Both of the potholes were observed in the clay bed of Exp. 7. Flow from right to left. Yellow curves refers to the possible paths of secondary flow within and around the potholes. | 162 |
| Figure 6.5 Evolution of a pothole with both entry and exit extended furrows. It was observed in the clay bed of Exp. 7. Flow from right to left. Yellow curves refer to possible paths of secondary flow within and around the potholes. Blue ellipse refers to the change of a smaller flute..... | 164 |
| Figure 6.6 Evolution of an open pothole. The whole system was observed in the clay bed of Exp. 7. Flow from right to left. Yellow curves refer to the possible paths of secondary flow within and around the potholes. Red and blue ellipses refer to the change of the three small potholes. | 167 |
| Figure 6.7 Evolution of a spiral-furrowed pothole with a spiral rib. It was observed in the clay bed of Exp. 8. Flow from right to left. Yellow curves refer to the possible paths of secondary flow within and around the potholes. | 170 |
| Figure 6.8 Evolution of a pothole with horizontal furrows. It was observed in the clay bed of Exp. 8. Flow from right to left. Green rectangle refers to an entry furrow. Yellow ellipses refer to the rims of marks. Red ellipse refers to a lateral furrow. Blue ellipses refer to the overhanging rim. Yellow arrows tagged to the inlet of flow..... | 170 |
| Figure 6.9 Evolution of a pothole with external secondary furrow. It was observed in the clay bed of Exp. 7. Flow from right to left. Yellow curves refer to the possible paths of secondary flow within and around the potholes. | 173 |
| Figure 6.10 Evolution of a complex pothole. It was observed in the clay bed of Exp. 8. Flow from right to left. Yellow curves refer to the possible paths of secondary flow within and around the potholes..... | 173 |
| Figure 6.11 Evolution of a hierarchical pothole. It was observed in the clay bed of Exp. 6. Flow from right to left. Yellow curves refer to the possible paths of secondary flow within and around the potholes. 1 to 4 refer to the different secondary structures. | 173 |
| Figure 6.12 Evolution of circle-shaped paired potholes. Potholes in Plot A were observed in the clay bed of Exp. 6 and those in Plot B were in Exp. 8. Flow from right to left. Yellow curve refers to the possible paths of secondary flow within and around the potholes. Red circle refers to the preset defect. The red rhombus refers to the projection. | 176 |

| | |
|--|-----|
| Figure 6.13 Evolution of approximate-symmetrical paired potholes with both entry and exit furrows. Both systems were observed in the clay bed of Exp. 7. Flow from right to left. Yellow curves refer to the possible paths of secondary flow within and around the potholes. Red ellipses refer to the entry furrows. | 178 |
| Figure 6.14 Evolution of broad and narrow flutes. Both of them were observed in the clay bed of Exp. 7. Flow from right to left. 1 to 4 refer to the number of narrow flutes. | 180 |
| Figure 6.15 Evolution of deep and shallow flutes. Flute in Plot A is observed in the clay bed of Exp. 6 and that in Plot B is in Exp. 7. Flow from right to left..... | 182 |
| Figure 6.16 Evolution of a flute with median ridge. It was observed in the clay bed of Exp. 7. Flow from right to left. | 182 |
| Figure 6.17 Evolution of an overhanging flute. It was observed in the clay bed of Exp. 7. Flow from right to left. | 185 |
| Figure 6.18 Evolution of a spindle-shaped flute. It was observed in the clay bed of Exp. 7. Flow from right to left. | 185 |
| Figure 6.19 Evolution of a comet-shaped flute. It was observed in the clay bed of Exp. 7. Flow from right to left. Yellow curves refer to the shape of the flute..... | 185 |
| Figure 6.20 Evolution of flutes with external secondary structures. They were observed in the clay bed of Exp. 7. Flow from right to left. Yellow curves refer to the right rims of flutes. 1 to 5 refer to flutes. Curve 2 disappeared over time. | 187 |
| Figure 6.21 Evolution of flute with internal secondary structure. It was observed in the clay bed of Exp. 7. Flow from right to left. | 189 |
| Figure 6.22 Evolution of paired flutes. They were observed in the clay bed of Exp. 6. Flow from right to left. Yellow closed curves refer to the left flute. Red curve refers to the right flute. Yellow rectangle refers to the final form of paired flutes. | 192 |
| Figure 6.23 Evolution of paired convergent flutes. They were observed in the clay bed of Exp. 7. Flow from right to left. Yellow curves refer to the possible path of flow within the right flute. Yellow closed curves refer to a plan area. Red closed curve refers to the early form of the left flute. Yellow ellipse refers to the extended lee-side slope of the projection..... | 192 |
| Figure 6.24 Evolution of lineations. They were observed in the clay bed of Exp. 7. Flow from right to left..... | 194 |
| Figure 6.25 Evolution of En echelon flutes. They were observed in the clay bed of Exp. 7. Flow from right to left. | 194 |
| Figure 6.26 Evolution of straight short furrows. They were observed in the clay bed of Exp. 6. Flow from right to left. | 197 |
| Figure 6.27 Evolution of curved short furrow. It was observed in the clay bed of Exp. 7. Flow from right to left. | 197 |

| | |
|--|-----|
| Figure 6.28 Evolution of a straight paralleled-sided furrow. It was observed in the clay bed of Exp. 7. Flow from right to left..... | 199 |
| Figure 6.29 Evolution of sinuous parallel-sided furrows. They were observed in the clay bed of Exp. 7. Flow from right to left..... | 199 |
| Figure 6.30 Evolution of cusped and non-cusped parallel-sided furrows. They were observed in the clay bed of Exp. 7. Flow from right to left. a and b refer to the upstream and downstream parts of the furrow, respectively. | 201 |
| Figure 6.31 Evolution of shear zone furrows. They were observed in the clay bed of Exp. 7. Flow from right to left. Yellow curves refer to the possible paths of flow in the shear zone furrows. Red dashed curves refer to a shared crest of two shear zone furrows. Red ellipses refer to a projection on the bed..... | 204 |
| Figure 6.32 Evolution of a group of parallel-sided furrows. They were observed in the clay bed of Exp. 7. Flow from right to left. a and b refer to the individual marks on the experimental bed..... | 204 |
| Figure 6.33 Evolution of bifurcating furrows. They were observed in the clay bed of Exp. 7. Flow from right to left. Yellow curves refer to the possible paths of flow within the primary furrow. Yellow arrowed dashed curves refer to branches. Red ellipse refers to a projection on the bed..... | 205 |
| Figure 6.34 Evolution of convergent furrows: They were observed in the clay bed of Exp. 7. Flow from right to left. Yellow curves refer to the possible path of flow within the bigger sinuous furrow. Yellow arrowed dashed curves refer to branches. Red curves refer to a lateral furrow. Blue circles tag a projection and short red lines in Plot 1440 refer to inlets of flow entering into the primary furrow. | 207 |
| Figure 6.35 Evolution of regular compound furrows. They were observed in the clay bed of Exp. 7. Flow from right to left. Yellow rectangles refer to the formative process of these furrows. 1, 2 and 3 refer to the specific furrows. | 209 |
| Figure 6.36 Evolution of irregular compound furrows. It was observed in the clay bed of Exp. 7. Flow from right to left. Yellow rectangles refer to the change of a pair of regular furrows and red rectangles refer to the change of a long sinuous parallel-sided furrow..... | 210 |
| Figure 6.37 Evolution of expanding furrow. It was observed in the clay bed of Exp. 7. Flow from right to left. Yellow curves refer to the possible path of flow within the furrow. Yellow ellipse tagged the secondary pothole in the junction of the narrow furrow and expanding area. | 212 |
| Figure 6.38 Evolution of reversed furrows. Furrows in Plot A and B were observed in the clay bed of Exp. 6, and C in Exp. 8 . Flow from right to left. Yellow arrowed curves refer to the possible paths of flow within the furrows. | 214 |

| | |
|---|-----|
| Figure 6.39 Evolution of hummocky forms. They were observed on the clay bed of Exp. 7. Flow from right to left. | 216 |
| Figure 6.40 Evolution of bladed forms. They were observed in the clay bed of Exp. 7. Flow from right to left. Yellow rectangles refer to the main bladed forms in the later experimental bed..... | 217 |
| Figure 6.41 Evolution of obstacle marks. Both of them were observed in the clay bed of Exp. 6. Flow from right to left. Yellow curves refer to the possible paths of flow within the furrows..... | 219 |
| Figure 6.42 The distribution of all types of erosional features on the experimental modelling clay bed under different basal shear stress. The undrained shear stress of the clay bed is around 7.5 kPa. | 222 |
| Figure 6.43 A phase space diagram of the relation between the bed substrate and flow conditions where conditions are optimal for current bedform reproduction. The blue diamonds refer to the experiments using the terracotta pottery clay. The red dots refer to the experiments using the modelling clay. The small downwards arrows refer to the undrained shear strength of the beds dropped with time. The big upwards arrow refers to that the diversity of the erosional features in the terracotta clay bed increased with undrained shear strength. 'All types' refers to that all types of erosional features could be produced by the modelling clay beds with any undrained shear stress..... | 223 |
| Figure 7.1 The locations of erosional marks in the experimental clay bed of Exp. 8 for flow velocity measurements by ADV. The flow structures above and within the areas indicated by the yellow rectangles and lines are discussed in this chapter. The yellow lines are parts of different transects, e.g. Line 6.9-3 located in the bottom left corner means the third sub-transect selected from the Transect-6.9. Flow is from right to left. | 228 |
| Figure 7.2 Elevation map of a central transect (Transect-14) and vertical flow profiles above selected erosional marks. The blue curves (X-velocity: receivers 1 & 3) in the plots of vertical flow profiles; represent the longitudinal flow velocities; the green curves (Y-velocity: receivers 2 & 4) represent transvers flow velocities; and, the red and light blue cures (Z1 and Z2 velocities) are the vertical velocity (Z1) estimates associated with receivers 1&3 (X) and (Z2) 2&4 (Y). In all the figures in this chapter, X-axis in elevation map illustrates the distance from the downstream edge. Y-axis shows the distance below the basal level of the original surface of the flat bed. The Y-axis of the velocity profile is the depth below the central transducer of the ADV. X-axis shows the time averaged velocity. Numbers above the profiles refer to the x position. Flow is from right to left. The clay bed is defined as left bank and right bank as looking downstream. | 229 |

- Figure 7.3 Flow structure above a simple pothole with entry furrow. The dashed line divided the water into several layers, which will be discussed in detail in the text. The gray boxes with arrows refer to the overhead view (x-y) and the side view (x-z) of the changes of flow direction with increasing height from the bottom. Flow is from right to left. This sampling area is numbered as Y20.7-2, which can be found in Figure 7.2. 232
- Figure 7.4 Pothole with exit furrow-1. Black line refers to the bottom level of the erosional feature; Areas between black line and red dashed line are the near bed bottom layers; areas above the purple dashed line are outer layers; areas between red and purple dashed lines are shear layers; yellow and green dashed lines sub-divided the shear layers into several sub-layers. The gray boxes with arrows refer to the overhead view (x-y) and the side view (x-z) of the changes of flow direction with increasing height from the bottom. Flow is from right to left. This sampling area is numbered as 17.4-1, which can be found in Figure 7.2. 237
- Figure 7.5 Pothole with exit furrow-2. The dashed line divided the water into several layers and the coloured ellipses tag different features of the flow profiles, which will be discussed in detail in the text. The gray boxes with arrows refer to the overhead view (x-y) and the side view (x-z) of the changes of flow direction with increasing height from the bottom. Flow is from right to left. This sampling area is numbered as 6.4-1, which can be found in Figure 7.2..... 238
- Figure 7.6 Pothole with extended exit furrows. The dashed line divided the water into several layers and the coloured ellipses tag different features of the flow profiles, which are discussed in detail in the text. The gray boxes with arrows refer to the overhead view (x-y) and the side view (x-z) of the changes of flow direction with increasing height from the bottom. Flow is from right to left. The sampling area is numbered as 12.5-2, which can be found in Figure 7.2..... 241
- Figure 7.7 Hierarchical pothole. a: the shallow secondary pothole; b: the deep secondary pothole; The yellow circle tagged the sub-pothole in the proximal end of the shallow secondary pothole. The dashed line divided the water into several layers and the coloured ellipses tag different features of the flow profiles, which are discussed in detail in the text. The gray boxes with arrows refer to the overhead view (x-y) and the side view (x-z) of the changes of flow direction with increasing height from the bottom. Flow is from right to left. The sampling area is numbered as 13.1-1, which can be found in Figure 7.2. 245

- Figure 7.8 Simple flute. The dashed line divided the water into several layers and the coloured ellipses tag different features of the flow profiles, which will be discussed in detail in the text. The gray boxes with arrows refer to the overhead view (x-y) and the side view (x-z) of the changes of flow direction with increasing height from the bottom. Flow is from right to left. This sampling area is numbered as 8.65-3, which can be found in Figure 7.2. 248
- Figure 7.9 Flute without proximal end rim. The dashed line divided the water into several layers and the coloured ellipses tag different features of the flow profiles, which will be discussed in detail in the text. The gray boxes with arrows refer to the overhead view (x-y) and the side view (x-z) of the changes of flow direction with increasing height from the bottom. Flow is from right to left. This sampling area is numbered as 20.7-4, which can be found in Figure 7.2. 251
- Figure 7.10 Flute with median ridge. The dashed line divided the water into several layers and the coloured ellipses tag different features of the flow profiles, which will be discussed in detail in the text. The gray boxes with arrows refer to the overhead view (x-y) and the side view (x-z) of the changes of flow direction with increasing height from the bottom. Flow is from right to left. This sampling area is numbered as 6.9-3, which can be found in Figure 7.2. 253
- Figure 7.11 Comet-shaped flutes. The dashed line divided the water into several layers and the coloured ellipses tag different features of the flow profiles, which will be discussed in detail in the text. The gray boxes with arrows refer to the overhead view (x-y) and the side view (x-z) of the changes of flow direction with increasing height from the bottom. Flow is from right to left. This sampling area is numbered as 4-3, which can be found in Figure 7.2. 256
- Figure 7.12 Narrow flute with entry furrow. The dashed line divided the water into several layers and the coloured ellipses tag different features of the flow profiles, which will be discussed in detail in the text. The gray boxes with arrows refer to the overhead view (x-y) and the side view (x-z) of the changes of flow direction with increasing height from the bottom. Flow is from right to left. This sampling area is numbered as 4-2, which can be found in Figure 7.2. 258
- Figure 7.13 Sinuous parallel-sided furrow. The dashed line divided the water into several layers, which will be discussed in detail in the text. The gray boxes with arrows refer to the overhead view (x-y) and the side view (x-z) of the changes of flow direction with increasing height from the bottom. The gray boxes with arrows refer to the overhead view (x-y) and the side view (x-z) of the changes of flow direction with increasing height from the bottom. Flow is from right to left. This sampling area is numbered as 8.1-1, which can be found in Figure 7.2. 260

| | |
|---|-----|
| Figure 7.14 Regular compound furrows. The dashed line divided the water into several layers and the coloured ellipses tag different features of the flow profiles, which will be discussed in detail in the text. The gray boxes with arrows refer to the overhead view (x-y) and the side view (x-z) of the changes of flow direction with increasing height from the bottom. Flow is from right to left. This sampling area is numbered as 6.9-2, which can be found in Figure 7.2..... | 263 |
| Figure 7.15 Expanding furrow. The dashed line divided the water into several layers and the coloured ellipses tag different features of the flow profiles, which will be discussed in detail in the text. The gray boxes with arrows refer to the overhead view (x-y) and the side view (x-z) of the changes of flow direction with increasing height from the bottom. Flow is from right to left. This sampling area is numbered as 10.1-1, which can be found in Figure 7.2..... | 266 |
| Figure 7.16 Reversed furrow-1 (Flow is from right to left). The dashed line divided the water into several layers and the coloured ellipses tag different features of the flow profiles, which will be discussed in detail in the text. The gray boxes with arrows refer to the overhead view (x-y) and the side view (x-z) of the changes of flow direction with increasing height from the bottom. This sampling area is numbered as 4-1, which can be found in Figure 7.2..... | 269 |
| Figure 7.17 Reversed furrow-2. The dashed line divided the water into several layers and the coloured ellipses tag different features of the flow profiles, which will be discussed in detail in the text. The gray boxes with arrows refer to the overhead view (x-y) and the side view (x-z) of the changes of flow direction with increasing height from the bottom. Flow is from right to left. This sampling area is numbered as 3.35-1, which can be found in Figure 7.2..... | 270 |
| Figure 7.18 Hummocky forms. The dashed line divided the water into several layers and the coloured ellipses tag different features of the flow profiles, which will be discussed in detail in the text. The gray boxes with arrows refer to the overhead view (x-y) and the side view (x-z) of the changes of flow direction with increasing height from the bottom. Flow is from right to left. This sampling area is numbered as 18.3-1, which can be found in Figure 7.2..... | 272 |
| Figure 7.19 Obstacle marks. The dashed line divided the water into several layers and the coloured ellipses tag different features of the flow profiles, which will be discussed in detail in the text. Flow is from right to left. This sampling area is numbered as 8.65-1, which can be found in Figure 7. 2. The gray boxes with arrows refer to the overhead view (x-y) and the side view (x-z) of the changes of flow direction with increasing height from the bottom. | 274 |
| Figure 7.20 Subsection along longitudinal section of erosion features..... | 275 |
| Figure 7.21 Vertical layering of flow field..... | 276 |

Figure 7.22 The classification of the typical flow velocity structures over the different parts of the erosional features on the experimental beds. A-1: the flow structure above the upstream part of the potholes and flutes; A-2: the flow structure above the plane part of reversed furrow and hummocky forms; B: the flow structure above the lee-side slope and the deepest part of some potholes; C-1 and C-2: the flow structure in the deepest part of the depressions of the erosional features. C-1: longitudinal velocity increases logarithmically, and C-2: longitudinal velocity increases with fluctuation; D-1 and D-2: the flow structures above the stoss-side slope of different erosional features. The ellipses refer to the obvious changes of the velocity profiles. The gray boxes with arrows refer to the overhead view (x-y) and the side view (x-z) of the changes of flow direction with increasing height from the bottom. Flow is from right to left. 283

Chapter 1

Thesis rationale

1.1 Introduction

Bedforms in cohesive river channels and bedrock channels are two most common but understudied types of bedforms compared to alluvial river bedforms. The genesis and geometry of them, including potholes, flute marks, and furrows, etc., are also very different from that of their alluvial channel counterparts, such as ripples, dunes, and anti-dunes, etc. (Alexander, 1932; Allen, 1971a; Carling et al., 2009; Johnson and Whipple, 2007; Richardson and Carling, 2005, 2006; Whipple et al., 2000b; Wilson et al., 2012). Previous studies on cohesive bedforms have primarily been based upon flume-scale experiments using plaster-of-Paris as a base material and there have been no systematic investigations of the influence of bed material properties, notably shear strength, on erosive bedform generation and evolution (Allen, 1971a, 1982; Bridge, 2008, 2009; Chien and Wan, 1999; Flood, 1983). For bedrock bedforms, our understanding of sedimentary processes within these has been restricted by the slow rate of bedform development limiting field studies, and the difficulty of replicating such features in the laboratory (Ashley et al., 1988; Richardson and Carling, 2005; Selby, 1985; Tinkler and Wohl, 1998; Wende, 1999; Whipple et al., 2000a; Wohl, 1993). As a consequence fieldwork on bedrock channel erosion features has mainly concentrated on the geometric forms, and associated classifications (Carling and Tinkler, 1998; Hancock et al., 1998; Johnson et al., 2010; Lorenc et al., 1994; Richardson and Carling, 2005, 2006; Springer and Wohl, 2002; Whipple, 2004; Wilson et al., 2012; Wohl, 2000). Few flume-scale experiments have been conducted to investigate the evolution process of sculpted bedforms in bedrock channels, because short-period erosion on bedrock produces very limited geomorphic change, and long-period experiments are typically unfeasible (Alexander, 1932; Goodchild and Ford, 1971; Hsu et al., 2008; Johnson and Whipple, 2007, 2010; Shepherd and Schumm, 1974; Sklar and Dietrich, 2001; Wilson et al., 2012). In particular, there have been no studies on simulating the whole process of erosional bedform genesis, evolution and development in bedrock channels.

Although the characteristics of cohesive substrates and bedrock beds are different, and the factors influencing the genesis of bedforms vary as well, there are none-the-less lots of types of erosional bedforms which are shared by cohesive rivers and bedrock channels (Alexander, 1932; Allen, 1971a, 1982; Richardson and Carling, 2005; Wohl, 1998a). The main kinds of erosional marks, including, potholes, flutes, and longitudinal furrows can be observed in both cohesive beds and bedrock channels in the field, although some features are present in slightly different forms in the two different kinds of substrate (Allen, 1971a; Richardson and Carling, 2005; Wohl, 1998a). This similarity of bedforms on two kinds of substrate suggests that the underlying formative processes also share some similarities. This study investigates whether bedrock erosion is an extreme case of cohesive sediment bed erosion, and whether it is possible to reproduce the whole evolution process of bedrock erosion by utilising a cohesive substitute as the analogue bedrock in flume-scale experiments in the laboratory, since using real bedrock as experimental beds appears impractical at realistic timescales.

The first part of this thesis examines the genesis and evolution of cohesive bedforms under different flow conditions using terracotta pottery clay, at a range of different undrained shear strengths, as the experimental substrate. Many kinds of erosional marks were produced in the experiments, including potholes, flutes and longitudinal furrows. The results of these experiments were, firstly, applied to assess the role of sediment-laden flow in the genesis of erosional features on cohesive beds. Secondly the role of substrate strength is examined in controlling the erosion rate and the types of cohesive bedforms that develop. The second part of this thesis documents the method of bedrock bedforms simulation by using modelling clay as the analogue bedrock substrate. A large array of erosional features was produced in the experiments and the profiles of them were compared with natural bedrock bedforms. The third part of this thesis concentrates on the genesis and evolution processes of a variety of erosional features in beds formed of modelling clay. It shows the continuity of different bedforms and the inter-transformation processes of different forms of erosional marks with time. The last section of this thesis examines the flow pattern within and over some typical kinds of erosional features. A large database of flow fields over each key erosional feature was established and the details of flow structures within a variety of erosional features are assessed.

1.2 Thesis objectives

This thesis aims to: 1. investigate the relationship between the strength of the bed the formation and development of erosional features on a natural clay substrate; 2. discover a new and feasible approach to exploring the genesis of bedrock bedforms by using flume-scale experiments in the laboratory; and 3. verify the hypothesis that bedrock erosion can be considered as an extreme case of cohesive bed erosion. In order to achieve these three objectives, nine series of physical modelling experiments, using two kinds of materials with different undrained shear strengths, were conducted under controlled flow conditions. Ultrasonic techniques were utilized throughout the experiments in order to quantify the bathymetry of bedforms and their associated flow structures. The key stages of this work are:

1. Producing erosional features on terracotta pottery clay:
 - a. to assess whether erosional features can be produced under the effect of pure plain water flow without suspended sediments in the flow;
 - b. to confirm the repeatability of the experimental results;
 - c. to reveal the relationship between the erosion rate and the strength of the beds;
 - d. to examine the typical erosional features that develop in pottery clay beds.
2. Creating bedforms on modelling clay bed:
 - a. in order to try to simulate bedrock bedforms without using real bedrock in the laboratory;
 - b. to investigate the similarity between bedforms produced by experiments and the real bedrock bedforms observed in natural bedrock channels and typical cohesive bedforms;
 - c. to try to discover the evolution process of natural bedrock bedforms on the basis of the development of bedforms in modelling clay.
3. Monitoring flow conditions by using Acoustics Doppler Velocimetry (ADV) over a stable rubber replica of the final experimental bed in order to reveal, for the first time, the flow structures in detail within and around many of the key erosional structures produced in the modelling clay beds.

1.3 Thesis structure

Chapter 2. 'Morphology and processes controlling erosional features on cohesive and bedrock substrates' documents the literature associated with: 1) previous experimental work and field observation on both cohesive sediment beds and bedrock channels, and 2) the field investigation of undrained shear strength of sea floor surfaces and estuarine muds, and the measurement methodology of undrained shear strength in the laboratory.

Chapter 3. 'Erosion experiments on mud substrates: Methodology' introduces the experimental background, setup and methodology.

Chapter 4. 'Cohesive mud bed channel erosion: bedform dynamics and formative processes' shows the results of experiment 0 to 5 on the evolution of cohesive bedforms over time under the effect of three flow conditions and various undrained shear strengths.

Chapter 5. 'Physical modelling of erosional bedrock bedforms' compares the variety of bedrock bedforms produced by experiments 6 to 8 using modelling clay under steady flow, and their equivalents in natural bedrock channels.

Chapter 6. 'Genesis and evolution of bedrock bedforms' illustrates the evolution process over time of each kind of erosional feature observed on the experimental analogue bedrock substrate, most of which were selected from experiment 7, with additional examples from experiments 6 and 8.

Chapter 7. 'Flow structure within and above analogue bedrock bedforms' details the flow patterns within and around specific erosional features in the final bed of Experiment 8.

Chapter 8. 'Summary and conclusion: generation of erosional features on cohesive materials with different characteristics' summarizes the experimental findings, discusses how feasible and reasonable the new approach is to producing erosional features similar to those observed in natural bedrock channels, and examines the opportunities for future work in this field (Figure 1.1).

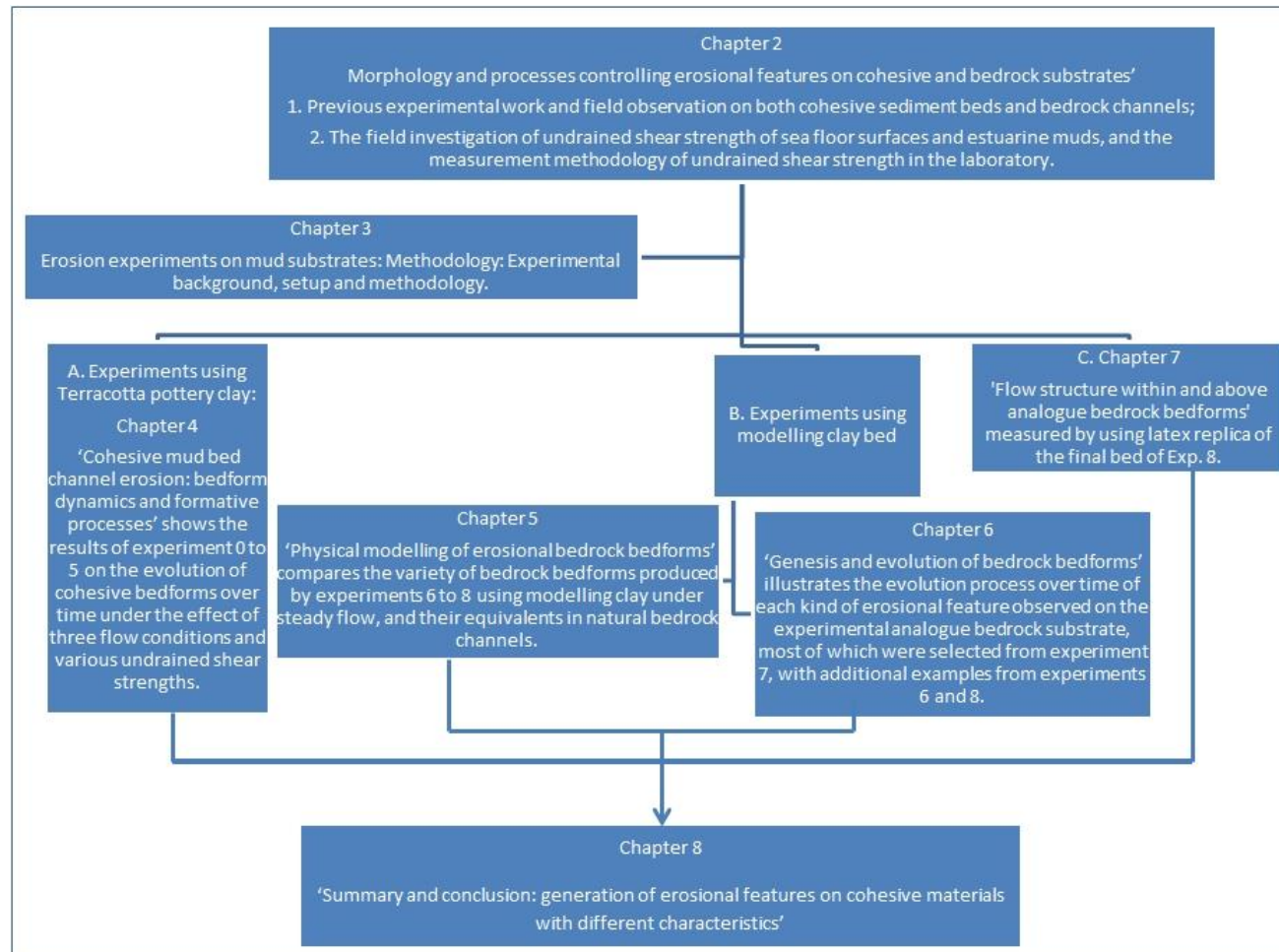


Figure 1.1 Flow chart diagram of the thesis structure.

Chapter 2

Morphology and processes controlling erosional features on cohesive and bedrock substrates

2.1 Introduction

Natural rivers can be normally classified into 3 types: cohesionless, cohesive and bedrock rivers according to the characteristics of the material of the river beds. The bedforms in the different types of the river beds present totally different geometric morphology under the influence of the sediment-laden flow. In view of that the bedforms on the cohesionless beds have been well studied (Allen, 1968, 1973b; Baas and Best, 2002; Baas et al., 1993; Bridge and Best, 1988; Cao and Carling, 2005; Cao et al., 2003; Carling and Breakspear, 2006; Carling et al., 2006a; Carling et al., 2005; Carling and Shvidchenko, 2002; Costello and Southard, 1981; Julien and Klaassen, 1995; Southard, 1991; Southard and Boguchwal, 1973), this chapter principally focuses on introducing the typical bedforms on the cohesive beds and the bedrock channels on the basis of previous studies. Furthermore, since the undrained shear strength is a crucial parameter on determining the bedforms in the cohesive beds (Bryant et al., 1981; Burland, 1990; Francisca et al., 2005; Richards, 1961; Winterwerp et al., 2012b), the methodology on the undrained shear strength measurement will be documented as well.

2.2 The morphology of erosional features on cohesive substrates

Our knowledge on the genesis, evolution and mechanics of erosive bedforms is still quite limited owing to the difficulty of observing and measuring these processes in the field (Allen, 1971a, 1987; Flood, 1981, 1983; Packman and MacKay, 2003). Most previous work is based on field observations and mainly focuses on the final bedforms of cohesive substrates (Allen, 1987; Baker, 1973, 1978; Carling et al., 2009; Dzulynski and Sanders, 1962; Embley et al., 1980; Flood, 1981; Vachtman and Laronne, 2011; Williams et al., 2008). Sonar techniques has been widely used throughout the last 30 years ((Alexander et al., 2008; Barbhuiya and Talukdar, 2010; Biron et al., 1998; Cossu and Wells, 2013; Craig et al., 2011; Debnath et al., 2012; Embley et al., 1980; Flood, 1981; Lane et al., 1998; Lohrmann et al., 1994; McManus and Woodson, 2012; Nikora and

Goring, 1998; Rolland and Lemmin, 1997; Zedel and Hay, 2011)). In the early 1980s, Embley et al. (1980) conducted field work on the western Bermuda Rise in order to survey mud waves, the distribution of both large furrows and small furrows, and the related flow strength and sediment erodibility using sonar, coring and near bottom flow measurement data. This study demonstrated that the distribution of the furrows on different sides of the mud waves could be attributed to the flow strength and the sediment erodibility. Flood (1981) used sonar to detect furrows in Southampton Water. The study shows that the accumulation rates of narrow furrows and wide furrows varies with the grain-size of the sediments and the duration of large furrows is much longer than narrow ones. The Severn Estuary, UK is a very popular and ideal location for study of cohesive bedforms and sedimentation (Allen, 1987, 1990; Carling et al., 2009; French and Spencer, 1993; Kirby and Parker, 1983; Williams et al., 2008). Allen (1987) examined scoured surfaces in the form of streamwise erosional ridges and furrows in the cohesive intertidal zone of the Seven Estuary, UK and suggested that large erosional streamwise furrows did not originate due to the effect of obstacle marks. The secondary currents in the tidal streams owing to the instability of the shear flow was regarded as the main mechanism for of existence of the furrows in the Severn Estuary (Allen, 1982; Flood, 1981, 1983). Williams et al. (2008) and Carling et al. (2009) investigated the ridge-runnel bedforms on the intertidal mudflat in the Severn Estuary. They pointed out that ridges are distinct accretion units instead of residual masses of uneroded mud and runnels are erosional bedforms which are largely affected by the persistent spanwise second vortices in runnels that have a big impact on mud erosion. Vachtman and Laronne (2011) illustrated a beautiful picture of high-resolution *in situ* 3D bed topography of natural cohesive straight channel reaches with bed irregularities, and the related 3D flow pattern over these bedforms based on *in situ* measurements in the Dead Sea (Figure 2.1). Both bed topography data and the flow velocity profiles were measured and collected by Acoustic Doppler Velocimetry (ADV). The very detailed topography data and flow velocity data help to understand the relationship between the general flow field, secondary circulation and the related bed topography.

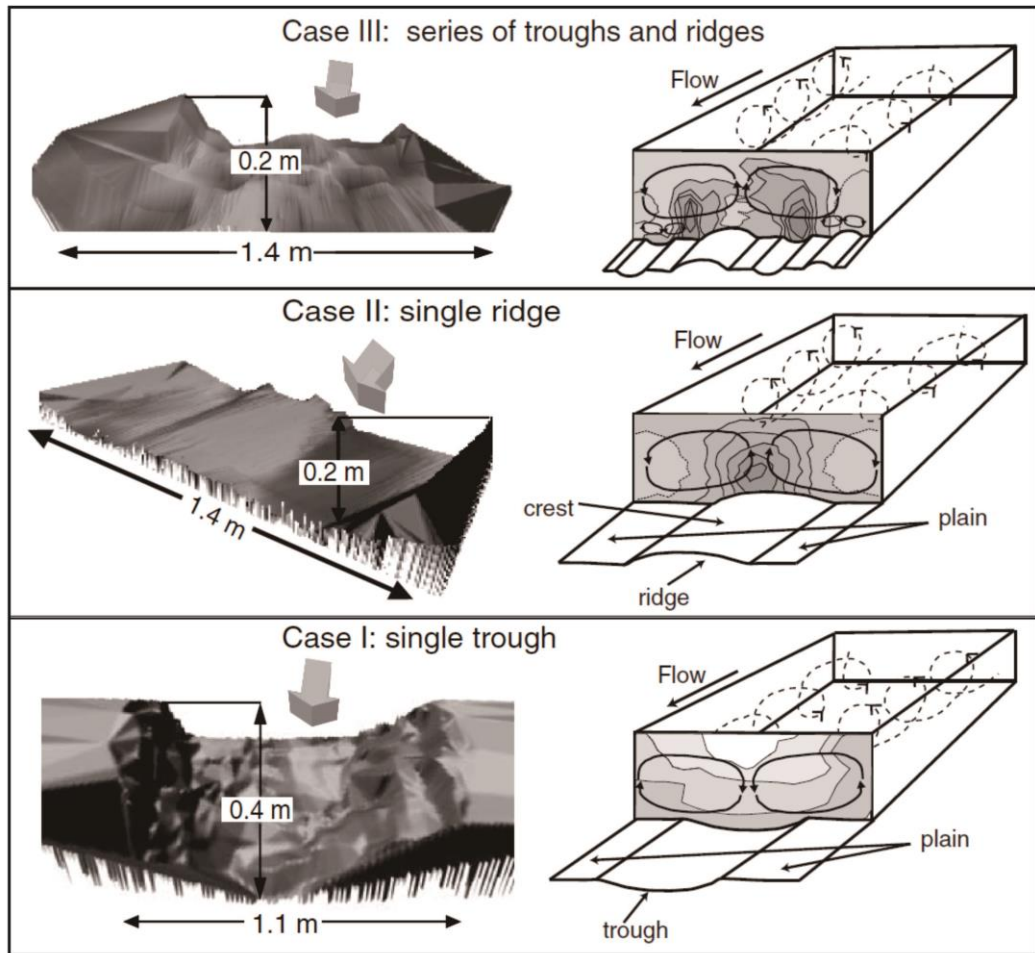


Figure 2.1 High-resolution bed topography of the studied cases of Vachtman and Laronne (2011) and schematic illustration of the corresponding flow patterns. Case I and II demonstrate the 3-D model of single trough and single ridge and the related flow patterns, respectively; Case II illustrates a case of combination of troughs and ridges and related flow pattern. From Vachtman and Laronne (2011).

Physical modelling provides an alternative approach for studying bedform development and has been widely utilized in the study of cohesionless bedforms (Alexander et al., 2001; Allen, 1968, 1971a, 1982; Baas, 1994; Baas and Best, 2008; Baas et al., 2009; Baas et al., 1993; Bennett and Best, 1995b, 1995c; Best, 1992, 1993; Bridge, 2008, 2009; Bridge and Best, 1988; Chien and Wan, 1999; Costello and Southard, 1981; Flood, 1983; Müller and Gyr, 1986; Packman et al., 2000; Saunderson and Lockett, 1983; Southard, 1991; Southard and Boguchwal, 1973; Thibodeaux and Boyle, 1987). However, in contrast, little work has been conducted on the genesis and evolution of the specific erosional features on cohesive beds (Allen, 1969, 1971a, 1971b, 1973a, 1975, 1982; Debnath et al., 2012; Dzulynski, 1965; Dzulynski and Sanders, 1962; Einsele et al., 1974; Fedele and Garcia, 2009;

Flood, 1983; Gardner, 1983; Schieber et al., 2010). Furthermore, most of the work focused on yielding single bedforms instead of the whole range of erosional bedforms in one experimental cohesive substrate (Allen, 1969, 1971b, 1973a, 1975; Fedele and Garcia, 2009; Flood, 1983; Gardner, 1983).

Early experiments on generating erosional features on cohesive sediments by physical modelling were conducted by Allen (1969, 1971a, 1971b). Experiments using non-recirculating clay suspension flows and weak cohesive mud beds were conducted in order to generate erosional features (Allen, 1969). The clay used as the experimental bed in these experiments was very soft and weakly cohesive; but the undrained shear strength was not measured. The thickness of the bed varied from (3.5 to 6 cm) and the suspended clay ($D_{50} = 4 \mu\text{m}$) in the flow was no coarser than the clay bed. Longitudinal grooves, flutes and transverse erosional features were produced. The experiments used a mechanism to initiate the flow. Before the experiments, the flume with original plane weak cohesive mud bed and clay suspension flow above it was prepared and the elevation of the original bed was measured. Once the cross wall and the tailgate in one end of the flume were removed, the flow went out of the flume and meanwhile altered the topography of the mud bed. Casts were made after each experiment by plaster of Paris in order to study the form of the erosional features. The flow was non-recirculating and varied in all 8 experiments. The results of these 8 experiments demonstrated that grooves yielded under the effect of low flow velocities ($< 50 \text{ cms}^{-1}$) and flute marks and transverse erosional marks were produced by relative high flow rates (from 50 to 138 cms^{-1}). One problem with these experiments was that the flow depth and the thickness of the mud bed were not constant during all 8 experiments, the flow depth ranging from 3.1 to 7.2 cm and the thickness of mud bed ranging from 3.5 to 6.0 cm. Therefore the results could not tell clearly that under what rate of flow velocity, certain kinds of erosional features can form. These experiments showed that the bedforms were sensitive to the flow rate and water depth but didn't examine the role of either bedload or suspended sediment in the flow and how these affect the bedforms.

Allen (1971b) conducted experiments with cohesive plaster-of-Paris experimental beds under the effect of a controlled recirculating turbulent flow in order to simulate the development of the flutes and scallops by the effect of solution. In this series of experiments, the water discharge, water depth, bed thickness and flume slope were kept constant in order to maintain the equilibrium experimental conditions. This study illustrated that flow

separation contributed to the formation and development of flutes and scallops on cohesive beds. All the erosional features, including flutes, scallops, ridges and furrows and grooves, produced by the experiments were mainly influenced by two kinds of kinematic structures, rollers and vortices. There was no sediment in the flow and shear strength is irrelevant for a plaster-of-Paris bed. Plaster-of-Paris is an excellent material for the simulation of substrates such as limestone that undergo erosion by dissolution, however, it is questionable if it is a good analogue for cohesive mud beds where erosion occurs by other processes.

A systematic review on bedforms in cohesive mud and rock was given by Allen (1971a, 1982). In these works, the definition and typical forms of a huge array of erosional features were given for the first time. A key aspect of this work is that the classic idealized model of flute marks was defined (Figure 2.2). This model shows the major morphological elements flute marks should contain. On cohesive sediment substrates, flute marks can form on smooth surfaces but preferentially develop around prior inhomogeneities on the erosional surface, for example, a burrow or obstacles, which can help the flow above to form a flow separation zone (Allen, 1971a). Ideal flute marks in cohesive substrates as defined by Allen (1971a), are parabolic with rims flaring in the downstream direction in plan view (Figure 2.2). They have a depression at the upstream end with a steeply sloping lee side and gentler upstream-facing tail, which eventually become indistinguishable from the following general bed surface. Idealized flute marks are symmetric with a lower rounded median ridge, cusped rims, principal furrow, lateral ridges and lateral furrows.

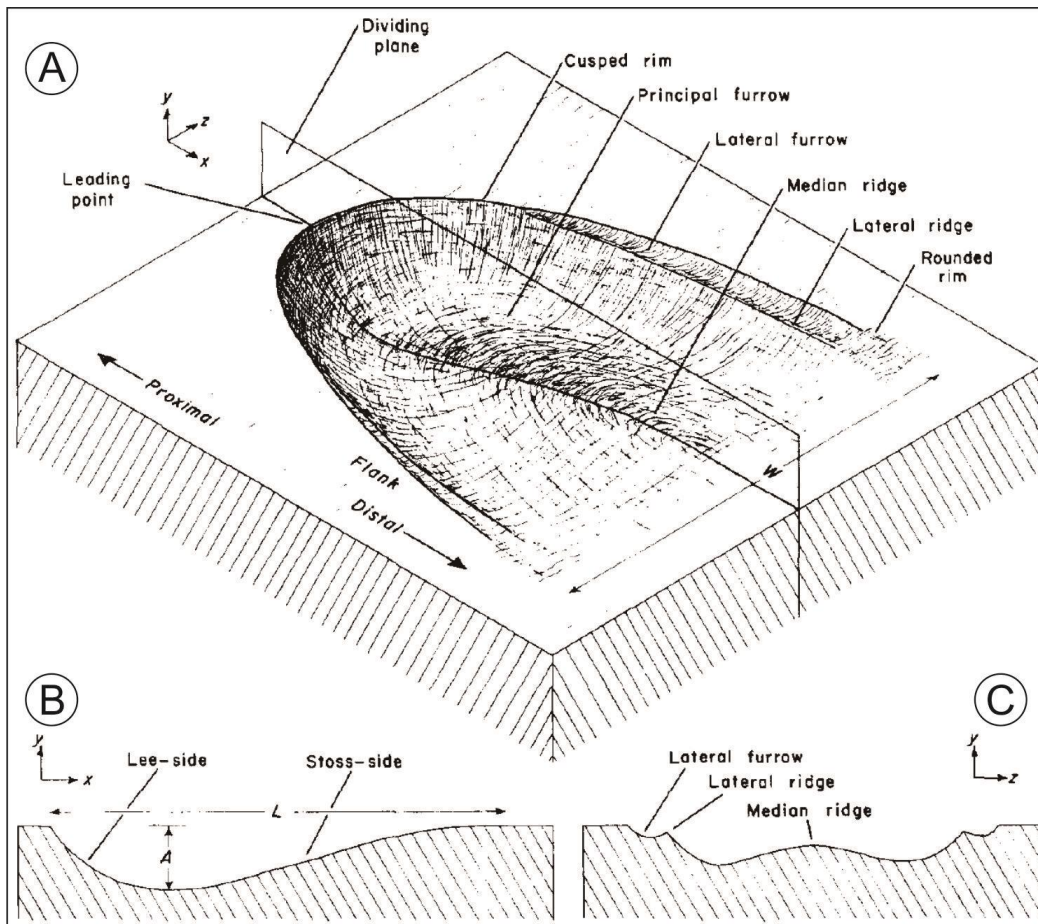


Figure 2.2 Schematic of the classic flute mark model showing the chief morphological features and linear dimensions. A: the general geometric morphology of a classic flute mark; B: the longitudinal-section of a classic flute marks; C: the cross-section of a classic flute mark. From Allen (1971a).

Although Allen (1971a) defined classic flute marks, flute marks on cohesive bed exist in many different forms. They can be classified according to the shape and their spatial patterns and divided into symmetrical and asymmetrical forms according to the plan view shape (Allen, 1973a). Based on the plan shape of isolated simple flute marks, they can be classified into the following types: symmetrical wave-like, parabolic, spindle-shaped, comet-shaped, and polygonal erosional marks. The wave-like marks are marks whose width is several times bigger than their length with cusped straight or sinuous rims and no lateral furrows and ridges (Figure 2.3 (a)). A simple symmetrical parabolic flute mark is a standard flute mark with most of the ideal characteristics mentioned above. Both the broad and narrow parabolic erosional marks have symmetrical outlines, a deeper proximal depression, median ridge, lateral furrows and ridges and cusped proximal

rim and rounded distal rim. The difference between them is that the width of the broad marks is bigger than its length, and the narrow ones vice versa (Figure 2.3 (b) & (c)). Spindle-shaped flute marks are generally shallow with length (between 0.05 and 0.15 m) several times longer than their width. They have a relatively sharp point at the proximal upstream end and straight and cusped lateral rims, but no median ridge, lateral furrows or ridges (Allen, 1971a) (Figure 2.3 (d)). Comet-shaped flute marks are flutes with a sharp point at the proximal end and sinuous lateral rims like a comet. They are shallow, barely more than 0.1 m long and comparatively rare (McBride, 1962) (Figure 2.3 (e)). The polygonal erosional marks are different from the other symmetrical erosional forms. They have closed outlines instead of an open distal end that flutes have and are always in contact with adjacent polygonal marks. The lee-side slope of the principal hollow is slightly steeper than the stoss-side slope. Their width is approximately as long as their length, and the median ridge of them is indistinct (Figure 2.3 (f)).

The asymmetrical erosional marks include simple marks, corkscrew marks, twisted marks, and polygonal marks (Figure 2.2 (g) to (j)). Simple asymmetrical erosional marks can be regarded as a normal parabolic flutes having more than one lateral furrow, and ridges on one flank, but without a lateral furrow and ridges on the other flank. The median ridge is no longer the central axis of the marks (Figure 2.3 (g)). The corkscrew erosional marks have a distinct spiral proximal end which twists either clockwise or anti-clockwise to an extent from 130° to 250° (Figure 2.3 (h)). The rest of the asymmetrical forms look like simple asymmetrical erosional marks. The twisted erosional marks contain more than two cusped inner ridges which are parallel with one side flank. The plan view of this kind of erosional mark looks like a spirally threaded rod with the length much bigger than the width (Figure 2.3 (i)). The last kind of asymmetrical erosional mark are polygonal marks. Except for having a curved low median ridge, all the other features are as same as for polygonal erosional marks (Figure 2.3 (j)). These different isolated flute marks can assemble to be conjugate and can in many cases cover the whole surface of a cohesive mud bed. In this stage, the rims of adjacent flutes will connect with some features of isolated flutes. The assemblage of the erosional marks can be divided in to heterogeneous and homogeneous assemblages (Figure 2.4). The heterogeneous assemblages can be sub-divided into clustered, longitudinal and diagonal (Figure 2.4). Since the assemblage is not the key point of this study, details won't be stated here.

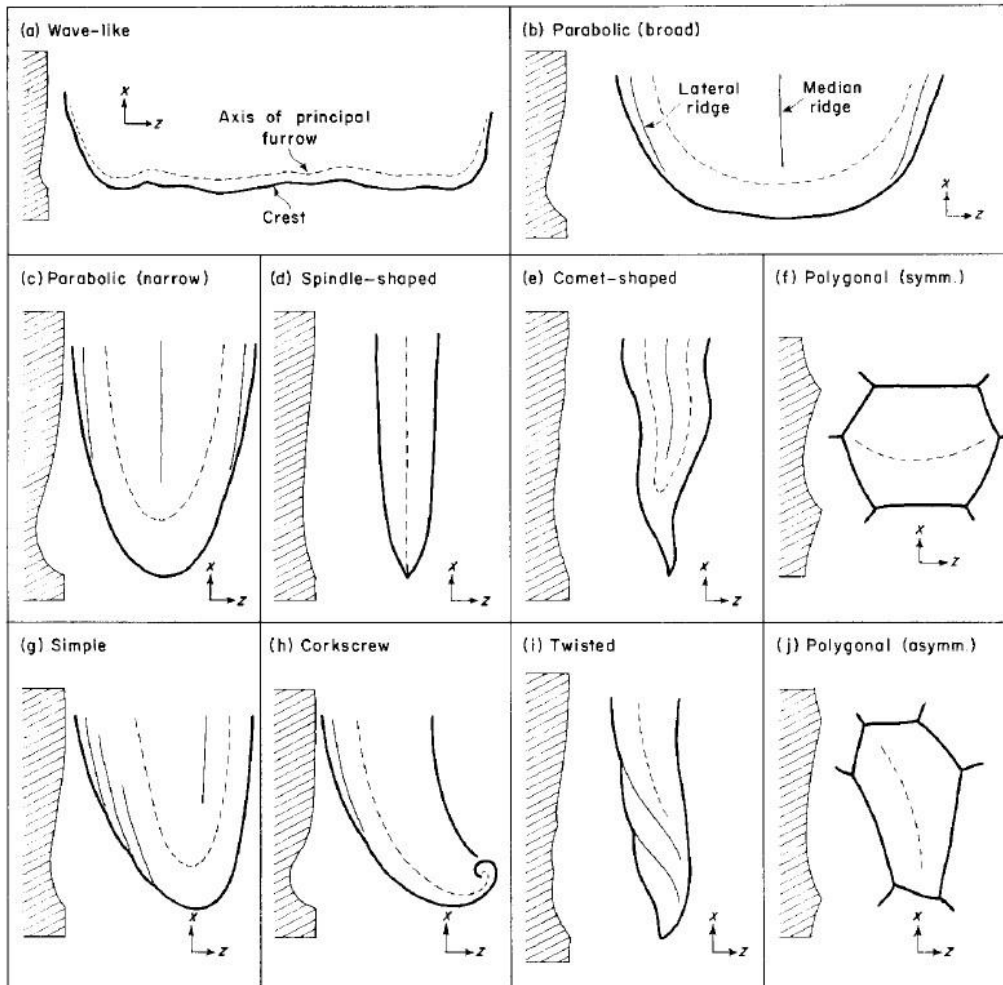


Figure 2.3 Schematic types of transverse erosional mark in profile and plan on cohesive beds (Allen, 1971a). The symmetrical bedforms: (a) wave-like, (b) broad parabolic, (c) narrow parabolic, (d) spindle-shaped, (e) comet-shaped, and (f) polygonal erosional marks; The asymmetrical bedforms: (g) simple, (h) corkscrew, (i) twisted, and (j) polygonal erosional marks. From Allen (1982).

| Flute marks | | | | | |
|---------------------------|------------------------|------------------------|-----------------------|------------------|----------------------|
| HETEROGENEOUS ASSEMBLAGES | | | | | |
| (a) Clustered | (b) Longitudinal | | (c) Diagonal | | Patterned ISOLATE |
| | | | | | |
| HOMOGENEOUS ASSEMBLAGES | | | | | Random ISOLATE |
| (a) Parabolic (broad) | (b) Parabolic (narrow) | (c) Spindle-shaped | (d) Comet-shaped | (e) Asymmetrical | |
| | | | | | |
| (f) Wave-like | (g) Parabolic (broad) | (h) Parabolic (narrow) | (i) Polygonal (asymm) | | CONJUGATE |
| | | | | | |
| Mud ripples | | | | | |

Figure 2.4 Types of assemblage of erosional marks. Each of the classes shown has been observed under natural conditions. Heterogeneous assemblages: (a) clustered, (b) longitudinal, and (c) diagonal; Homogeneous assemblages: (a) broad parabolic flutes, (b) narrow parabolic flutes, (c) spindle-shaped flutes, (d) comet-shaped flutes, (e) asymmetrical simple flutes, (f) wave-like marks, also known as mud ripples, (g) dense broad parabolic flutes, (h) dense narrow parabolic flutes, and (i) asymmetrical polygonal erosional marks. From Allen (1982).

Allen's work systematically summarises the features of erosional marks on cohesive beds and established an idealized flute mark model (Allen, 1971a, 1982). However, there are a number of limitations of Allen's work: a. no details of the shear strength of the experimental mud beds are given; b. in some of the experiments, the thickness of the bed varied. c. information on the suspended sediment concentration and related grain size information are not available; d. the flow velocity was calculated from discharge instead of

measured directly (Allen, 1971a, 1971b, 1982); and, e. features formed by dissolution on plaster-of-Paris may not be a good analogue for erosive bedforms on non-limestone substrates, because the dissolution process does not mimic the processes of abrasion, plucking and cavitation that are thought to occur in substrates that do not undergo dissolution (Richardson and Carling, 2005).

Following Allen's early work on bedforms in cohesive beds, from the 2000s, a number of studies exploring the development of bedforms on mud beds have been conducted (Debnath et al., 2012; Fedele and Garcia, 2009). For example, Fedele and Garcia (2009) conducted experiments to yield longitudinal subaqueous depositional gullies on a slope change under the influence of successive supercritical, depositional turbidity currents in order to simulate the genesis of gullies in areas of relatively steep seabed gradients. The results of their experiments showed that the slope change induced the formation of the longitudinal gullies and the gully spacing is controlled by the centrifugal force. Both of these two results support their centrifugal force drive hypothesis of that gullies could be the result of a centrifugal instability that sets in interfaces of gravity currents as they flow through a bedslope transition.

Besides the work on the formation of bedforms, the other work principally focused on sediment transport processes and the related flow patterns above the stream bed. But most of this work was focused on flow structure over cohesionless beds or stable artificial stream beds (Allen, 1987; Baas and Best, 2008; Baas et al., 2009; Bennett and Best, 1995a, 1995b, 1995c; Best, 1992, 1993, 1996; Best et al., 1997; Best and Leeder, 1993; Carling et al., 2002; Carling et al., 2006b; Kostaschuk and Villard, 1999; Kuhnle and Southard, 1988; McLelland et al., 1999; Rijn, 1984; Wan, 1985; Yalin and Selim, 1992). Little work on flow patterns and related sediment transport processes over cohesive beds has been undertaken (Allen, 1971a; Debnath et al., 2012; Fedele and Garcia, 2009; Flood, 1981; Hollister et al., 1974; Lonsdale et al., 1973; Vachtman and Laronne, 2011; Winterwerp et al., 2012b). Allen (1971a) undertook a detailed study on the flow structure within each kind of erosional mark. Later, Flood (1981) conducted field work to detail the formation and morphology of longitudinal furrows and drew a conclusion that large-scale secondary circulation within the bottom boundary layer played an important role in furrow initiation and the coarse suspended sediment induced the formation of the mini-furrows by abrasion. Recently, Vachtman and Laronne (2011) carried out field work in order to establish a

high-resolution *in situ* 3D bed topography and flow field over bed irregularities which has been mentioned before. For details, please see Figure 2.1 and the relevant content. Debnath et al. (2012) investigated suspended sediment-laden flow turbulence over a scoured cohesive kaolinite-sand mixed bed, the bed shear strength of which was 12.77 kPa, around a circular cylinder/pier by conducting flume experiments with ADV. The results illustrated that the flow structures around the pier on a cohesive bed is different from that on cohesionless sediment. Sweeping events are the major contributor to the Reynolds shear stress within the inner region and scour hole and ejection events control the outer flow region. The geometry of the scour hole varies a lot as a function of different clay proportion under influence of turbulence.

2.3 Sculpted forms in bedrock channels

2.3.1 Introduction

The study of morphology and the formation of bedrock sculpted forms is relatively limited (Ashley et al., 1988; Richardson and Carling, 2005; Selby, 1985; Wende, 1999; Whipple et al., 2000a). The major obstacle in the study of bedrock channel bedforms is that the development of bedforms in bedrock channels is a very slow process compared with that in alluvial channels. Therefore, direct measurement of erosion rates of bedrock channels and their associated bedforms formation is nearly impossible, since it may take place over many years to decades (Tinkler and Wohl, 1998; Wohl, 1993). Simulating the bedrock channel erosion in flumes has also proved problematic, due to the difficulty of producing an appropriate substrate (Richardson and Carling, 2005). Although few work has successfully created some sculpted forms in the laboratory by using certain substitutes of real bedrock, the types of sculpted forms produced were still limited (Johnson and Whipple, 2007; Wilson et al., 2012). As a consequence, relatively little is known about the genesis and evolution of bedforms in bedrock substrates (Wohl, 1998a).

There are a number of fundamental differences between bedrock channel bedforms and alluvial bedforms: 1. The development of bedrock channels is a one way process with only erosion instead of erosion and deposition in alluvial bedforms (Allen, 1971a; Tinkler and Wohl, 1998); 2. The variety of bedforms: concave sculpted forms can only be observed in bedrock channels (Allen, 1971a, 1982; Richardson and Carling, 2005, 2006); 3. Relative stability of bedforms: the erosional features on bedrock channels

are the products of many different individual erosional events in a relatively long period, but those on alluvial reaches rapidly adjust to flow parameters (Baker and Kale, 1998; Tinkler and Wohl, 1998); 4. Bedrock bedforms in contrast to alluvial bedforms can occur on surfaces of any orientation (Richardson and Carling, 2005); 5. The time-scale for the formation of bedrock bedforms is different from alluvial bedforms (Baker and Kale, 1998; Tinkler and Wohl, 1998); 6. Bedrock channels have relatively irregular and rough channel boundaries (Richardson and Carling, 2005); 7. The flow patterns in bedrock channels have greater variability and are more complex than those in alluvial channels owing to their topographical complexity (Richardson and Carling, 2005). 8. The genesis and development of erosional features are highly variable owing to the importance and variability of local substrate characteristics/strength and local stream stress (Richardson and Carling, 2005).

Previous studies of bedrock channels can be divided into two: Large scale and small scale (Richardson and Carling, 2005). Large scale studies paid attention to the whole river system like river channel reaches, or drainage basins. On the contrary, small scale studies mainly focused on the specific erosional features and bedforms on the surface of the bedrock. Large scale studies mainly focus on: (a) anabranching bedrock channel (Baker, 1978; Bretz, 1924; Kale et al., 1996; Tooth and McCarthy, 2004); (b) meandering bedrock channels (Ashley et al., 1988; Itakura and Ikeda, 1997); (c) the relationship between the channel width and slope (Kobor and Roering, 2004; Montgomery and Gran, 2001); (d) the role of substrate strength and related stream power on the formation of the long profile (Seidl et al., 1996; Weissel and Seidl, 1997; Wohl, 2000; Wohl and Achyuthan, 2002; Wohl and Ikeda, 1998; Wohl and Merritt, 2001a); and (e) the erosion rates of the bedrock channels (Foley, 1980; Kale and Joshi, 2004; Smith et al., 1995; Whipple et al., 2000a; Wohl and Achyuthan, 2002).

The small scale studies mainly examined different kinds of erosional features, including potholes (Alexander, 1932; Allen, 1982; Blank, 1958; Lorenc et al., 1994; Tinkler, 1997a; Whipple et al., 2000a; Wohl, 1993; Wohl and Achyuthan, 2002), flutes, longitudinal furrows (Hancock et al., 1998; Sato et al., 1987; Selby, 1985; Whipple et al., 2000a; Wohl, 1993; Wohl and Achyuthan, 2002), non-longitudinal features, such as transverse furrows and reversed furrows (Ängeby, 1951; Jennings, 1983; Shepherd and Schumm, 1974; Tinkler, 1993; Tinkler and Wohl, 1998b), and convex and undulating forms (King, 1927; Kor et al., 1991; Tinkler, 1993). These kinds of small

scale erosional features on bedrock channels are the key area of the focus of the current study.

Previous studies on bedforms in bedrock channels were mainly based on the field observation and numerical modelling (Cao et al., 2006; Carling and Tinkler, 1998; Hancock et al., 1998; Richardson and Carling, 2005, 2006; Springer and Wohl, 2002; Tinkler, 1993; Whipple et al., 2000a; Wilson et al., 2012; Wohl and Achyuthan, 2002). However relatively little physical modelling has been undertaken on bedrock bedforms (Alexander, 1932; Allen, 1971a; Gjessing, 1967; Johnson and Whipple, 2007, 2010; Macdonald, 2010; Schieber et al., 2010; Sklar and Dietrich, 2001, 2004; Wilson et al., 2012). Most of the previous work on simulating bedforms on bedrock channels has been highly restricted to the final formation of erosional features, or to the limited range of erosional features (Alexander, 1932; Allen, 1971a; Goodchild and Ford, 1971; Springer et al., 2005; Wilson et al., 2012). They are also restricted by the nature of substrate substitutes for real bedrock that can be used in flume-scale experiments. For example, bedrock dissolution features in limestones have been modelled through the dissolution of plaster-of-Paris (Blumberg and Curl, 1974; Goodchild and Ford, 1971). Cohesive sand-clay mixtures were utilized to be the experimental substrate to investigate the development of different kinds of bedrock features, such as the development of the inner channel (Shepherd and Schumm, 1974), the evolution of the knick point and longitudinal profile (Gardner, 1983), and the role of gradient in the changes of channel morphology (Koyama and Ikeda, 1998; Wohl and Ikeda, 1998). However, for bedrock rivers that evolve through physical erosion, these dissolution based experiments and the sand-clay mixed substrate are not applicable. Compared to the study of the final form of bedforms, there have only been a few studies that have examined the evolution process of different types of erosional features (Hsu et al., 2008; Johnson and Whipple, 2007, 2010; Koyama and Ikeda, 1998; Macdonald, 2010; Shepherd and Schumm, 1974; Wilson et al., 2012). This is mainly attributed to the difficulty of producing erosional features on real bedrock in flume-based experiments in a short time scale.

2.3.2 Bedforms in open bedrock channels

The major factors controlling the morphology and genesis of bedrock channels include: plucking (Whipple et al., 2000b; Whipple et al., 2000a), abrasion or corrasion (Allen, 1971a; Egholm et al., 2013; Hancock et al., 1998; Johnson and Whipple, 2007; Sklar and Dietrich, 2001, 2004; Wilson et

al., 2012; Wohl, 1998a), cavitation (Baker, 1973; Baker and Kale, 1998; Gupta et al., 1999; Hancock et al., 1998; Sato et al., 1987; Tinkler and Wohl, 1998; Whipple et al., 2000a; Wohl, 1992, 1998a), and dissolution (Wohl, 1998a). The recent studies illustrate that among these factors, abrasion induced by bedload in the flow plays an important role in producing and developing erosional bedforms on bedrock channels (Egholm et al., 2013; Johnson and Whipple, 2007, 2010; Sklar and Dietrich, 2004; Wilson et al., 2012). Sklar and Dietrich (2004) developed a numerical model of bedrock abrasion under the effect of saltating bedload and conducted experiments to validate the model. The experimental results proved that (1) abrasion by bedload sometimes dominates the formation of bedforms on bedrock; (2) bedrock erosion rate partially depends on the grain size of the bedload, quantity of the sediment supply, the bedload transport capacity, and the exposed extent of the bedrock surface. The flume experiments conducted by Johnson and Whipple (2007) might be one of the most successful experiments to simulate bedrock incision in the lab (Figure 2.5). A uniform sand-cement mixed brittle substrate was utilized to simulate natural bedrock in their experiments. The grain size of the sediment as bedload was controlled. The abrasion was regarded as the only mechanism to affect the experimental substrate. Sinuous parallel-sided long furrows, runnels, circular furrows, and potholes with entry and exit furrows were produced. The results of their work show that non-uniform abrasion occurs when the bedload transport capacity of the flow is greater than the sediment supply. Johnson and Whipple (2010) conducted experiments changing sediment flux and water discharge in order to understand the change in bedrock erosion rate under different flow conditions. Their results showed the bedrock erosion rate depends on the sediment flux and alluvial cover effects. The other important result is that once the sediment flux and the alluvial cover effect are controlled to be constant, the erosion rate shows little dependence with flow shear stress, no matter how big the discharge was which is different from the results of the work conducted by Sklar and Dietrich (2004). They concluded that bed roughness is a very important parameter in terms of bedrock incision, because it affects almost every other parameter influencing the bedrock erosion, including local shear stress, flow structure, sediment transport and deposition. The work of Wilson et al. (2012) focused on the form of upstream-facing convex surfaces (UFSCs) in bedrock channels. Their work illustrated that UFSCs are produced by bedload abrasion based on both natural observations and laboratory experiments. However the only weakness of this work is the real rock were not actually abraded by the extra

huge bedload in the experiments, which was only used for demonstrating the transport pattern of the bedload in front of and behind the rock. Egholm et al. (2013) is use a numerical model to scale the lifespan and evolution of mountains by using the relationship between landsliding and bedrock river incision. Although it does not focus on the process of bedrock river evolution, it shows that overwhelming landsliding may induce a cover effect that stops bedrock river incision. On the other hand, if abrasion sediment from landsliding does not exceed the capacity of bedload transportation, it will accelerate bedrock river incision. This supports the results of previous work that abrasion is the key control on bedrock erosion (Johnson and Whipple, 2007, 2010; Wilson et al., 2012).

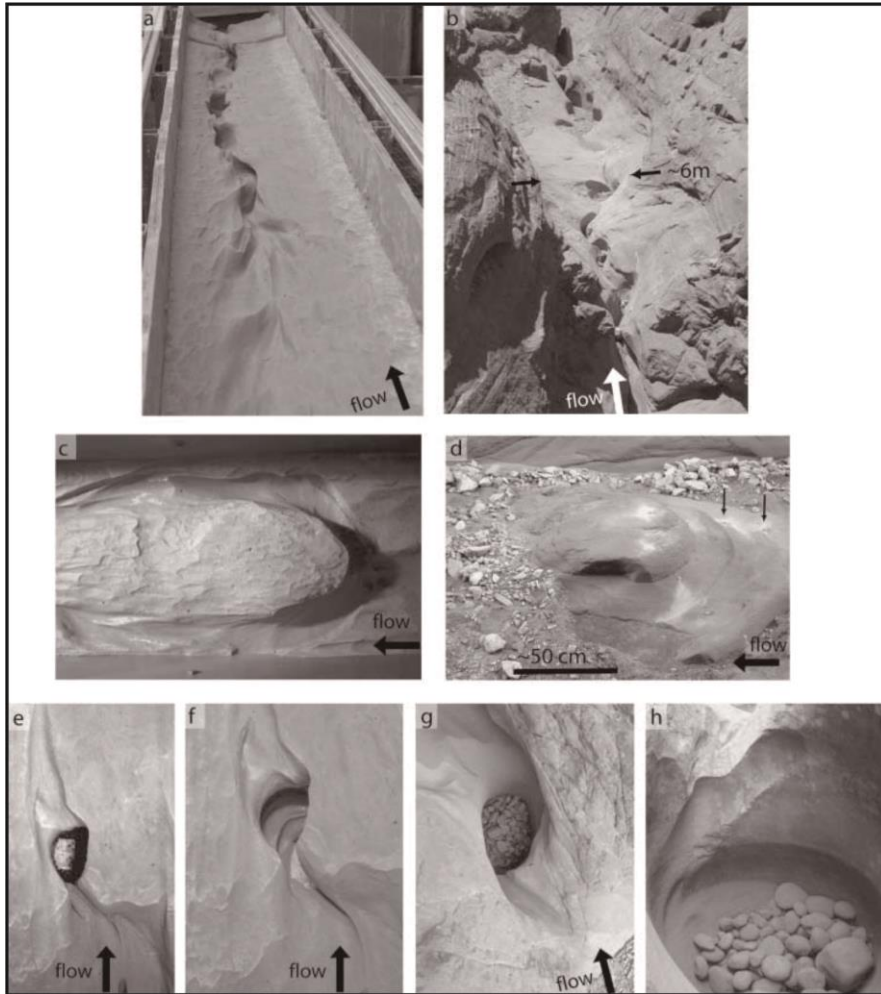


Figure 2.5 Erosional features produced by experiments conducted by Johnson and Whipple (2007) and their natural equivalents. (a) Runnel with alternating scour produced by experiments. (b) A natural similar form of runnel in (a) in the south fork of Maidenwater Creek. (c) a broad projection on experimental bed. Flume width 40 cm. (d) Similar geometry of a trough in the field. (e) and (f) Two potholes with both entry and exit furrows formed in the experiments; Pothole diameter 5–6 cm; (g) natural pothole with diameter of about 60 cm and partially filled with sediment clasts. (h) Natural pothole with diameter of about 2 m. From Johnson and Whipple (2007).

The sculpture forms produced by plucking, abrasion, cavitation and dissolution on bedrock channels includes potholes (Alexander, 1932; Allen, 1982; Ängeby, 1951; Gjessing, 1967; Lorenc et al., 1994; Spaggiari et al., 1999; Whipple et al., 2000a; Wohl, 1993; Wohl and Achyuthan, 2002), flutes (Allen, 1965, 1968, 1969, 1971a, 1971b; Baker and Pickup, 1987; Collinson and Thompson, 1982; Dzulynski and Sanders, 1962; Hancock et al., 1998; Leeder, 1982), longitudinal furrows (Allen, 1965, 1971a; Collinson and Thompson, 1982; Kor and Cowell, 1998; Kor et al., 1991; Maxson and

Campbell, 1935; Tinkler, 1993), grooves (Allen, 1969, 1971b; Bryant, 2008; Maxson and Campbell, 1935; Shepherd and Schumm, 1974; Wohl, 1993; Wohl and Ikeda, 1998), and runnels (Ford and Williams, 1989; Hutchinson, 1996; Richardson and Carling, 2005).

Potholes

Potholes are one of the most common erosional features on both cohesive mud beds and bedrock channels. They are generally defined as round to elliptical closed depressions in plan view whose depth is no less than a quarter of their width, and the length of them is no more than twice their width, and their walls are near vertical (Alexander, 1932; Allen, 1982; Maxson and Campbell, 1935; Whipple et al., 2000a; Wohl, 1992, 1993; Wohl and Ikeda, 1998; Zen and Prestegard, 1994). Simple potholes are present in many kinds of forms, including circular potholes (Figure 2.6 A i) (Allen, 1982), ovoid potholes (Figure 2.6 A ii) (Kunert and Coniglio, 2002; Nemeč et al., 1982; Sato et al., 1987), spiral-furrowed potholes (Figure 2.6 A iii) (Alexander, 1932; Allen, 1982; Ängeby, 1951; Baker and Pickup, 1987; Diffendal, 1982; Gjessing, 1967; Glasser and Nicholson, 1998; Jennings, 1983; Kor and Cowell, 1998; Kor et al., 1991; Maxson and Campbell, 1935; Morgan, 1970; Shaw, 1996; Wohl, 1992), incipient potholes (Figure 2.6 A vi) (Elston, 1918; Lorenc et al., 1994; Nemeč et al., 1982), undercut potholes (Figure 2.6 A iv) (Alexander, 1932; Ives, 1948; Kunert and Coniglio, 2002; Lorenc et al., 1994; Nemeč et al., 1982), and potholes with a central boss (Figure 2.6 A v) (Allen, 1982; Ives, 1948; Jennings, 1983; Lorenc et al., 1994; Morgan, 1970; Nemeč et al., 1982; Wohl and Ikeda, 1998). Some other more complex potholes can be observed, such as potholes with external furrows (Figure 2.6 B) (Alexander, 1932; Allen, 1982; Gjessing, 1967; Kor and Cowell, 1998; Lugt, 1983; Morgan, 1970; Sato et al., 1987), compound potholes (Figure 2.6 C) (Gjessing, 1967; Lorenc et al., 1994; Morgan, 1970; Nemeč et al., 1982; Sato et al., 1987; Whipple et al., 2000a), breached potholes (Figure 2.6 D) (Ives, 1948; Jennings, 1983; Lorenc et al., 1994; Nemeč et al., 1982; Sato et al., 1987; Whipple et al., 2000a; Wohl and Ikeda, 1998; Zen and Prestegard, 1994), and lateral potholes (Figure 2.6 E) (Ängeby, 1951; Gjessing, 1967; Kor and Cowell, 1998; Lorenc et al., 1994; Maxson and Campbell, 1935; Sato et al., 1987; Shepherd and Schumm, 1974; Springer and Wohl, 2002; Whipple et al., 2000a; Wohl and Achyuthan, 2002; Wohl and Ikeda, 1998; Zen and Prestegard, 1994).

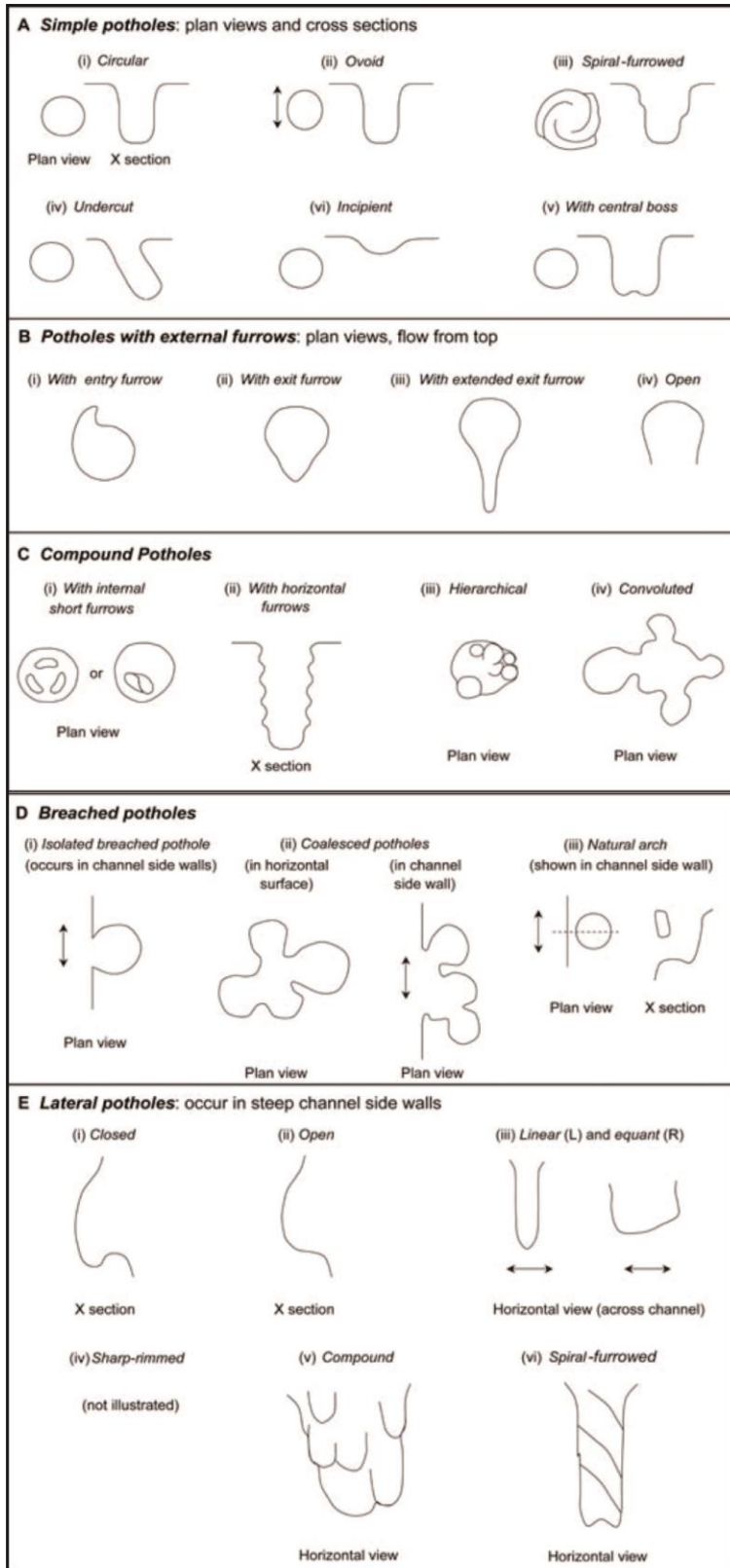


Figure 2.6 Schematic morphology of potholes. Arrows indicate flow directions. Dashed lines (where present) indicate lines of cross sections. From Richardson and Carling, 2005.

Flutes

The erosional origin of flute marks on bedrock substrates is normally related to the heterogeneous nature of the rock and a topographical irregularity to promote flow separation or expansion (Hancock et al., 1998; Tritton, 1988; Whipple et al., 2000a). The flutes in bedrock channels are defined in a similar way to those on cohesive mud beds, but have greater depth relative to width, exhibit only rare median ridges, have no lateral ridge and furrow, and sometimes have rims overhanging at the upstream end (Richardson and Carling, 2005). In sharp contrast to flutes in cohesive mud beds, the definition of flutes in bedrock channels includes examples that close at their downstream end rather than flaring (Richardson and Carling, 2005). This feature makes them similar in planform shape to short furrows (see Figure 2.7C). With these exceptions, flutes on bedrock exhibit relatively similar parabolic forms to those on cohesive beds as described by Allen (1971a). However, bedrock flutes typically lack the complex forms described from cohesive mud beds (Allen, 1971a; Richardson and Carling, 2005).

According to the shapes of the isolated flutes, they can be mainly sorted into broad and narrow flutes, deep and shallow ones, flutes with median ridges, flutes with overhanging depression on proximal end, and spindle-shaped flute marks (Allen, 1971a; Richardson and Carling, 2005). Flute marks are defined as broad when the width is greater than or equal to its length, and narrow ones are defined vice versa (Figure 2.7 A-I) (Allen, 1971a; Richardson and Carling, 2005). In terms of the longitudinal sectional profile, simple flute marks can be divided into deep flute marks, the depth of which is more than a quarter of its length, and shallow flutes (Figure 2.7 A-II) (Richardson and Carling, 2005). Whilst rare, flutes with median-ridges are like the classic model flutes on cohesive sediments in a symmetric parabolic form (Allen, 1971a). Overhanging flutes have an overhanging depression on the upstream proximal end which provides evidence of the upstream migration of these features (Figure 2.7 A-IV) (Hancock et al., 1998; Maxson and Campbell, 1935). Finally spindle marks are the smallest type of flute; the length of these flutes is much greater than their widths and they have a sharp upstream pointed end and no median ridge (Figure 2.7 A-V). The form of spindle-shaped flutes on bedrock is the same as that on cohesive beds.

Over time isolated simple flutes grow and connect, and consequently more complex forms appear with time. The combination of flute marks on the bed, can be divided into the following types: (1) flute marks with internal secondary structures (Figure 2.7 A-VI) (Allen, 1971a; Hancock et al., 1998);

(2) Flute marks with external secondary structures (Figure 2.7 A-VII) (Allen, 1971a; Hancock et al., 1998; Kor et al., 1991; Maxson, 1940; Shaw, 1996); and (3) Paired flute marks (Figure 2.7 A-VII) (Richardson and Carling, 2005). Flutes with internal secondary features exhibit smaller scale sub-erosional features, such as smaller potholes, flutes, or furrows within the lateral boundary of the primary flutes (Allen, 1971a; Hancock et al., 1998). In contrast, flutes with external secondary features have flutes developing outside or adjacent to the primary flutes. The sizes of these flutes are very similar to the primary ones. The same situation can also be found in cohesive beds, on which these sorts of flutes were defined as multiple flutes (Allen, 1971a). Sometimes, the external secondary flutes combine with the primary one to form a linear erosional series (Hancock et al., 1998). On cohesive beds, this linear erosional series is defined as a diagonal assemblage (Figure 2.4). Paired flutes are two approximately symmetrical flutes with one shared lateral rim as a symmetry axis.

Striations

Striations are ridges and furrows parallel to the flow with widths no larger than 2 cm and lengths less than a few centimetres. They are rare and do not have a clear head or end. Although they do not have features of typical flutes, they are still considered as a type of isolated flute by Richardson and Carling (2005). However, it is debatable whether they should be classified in this way.

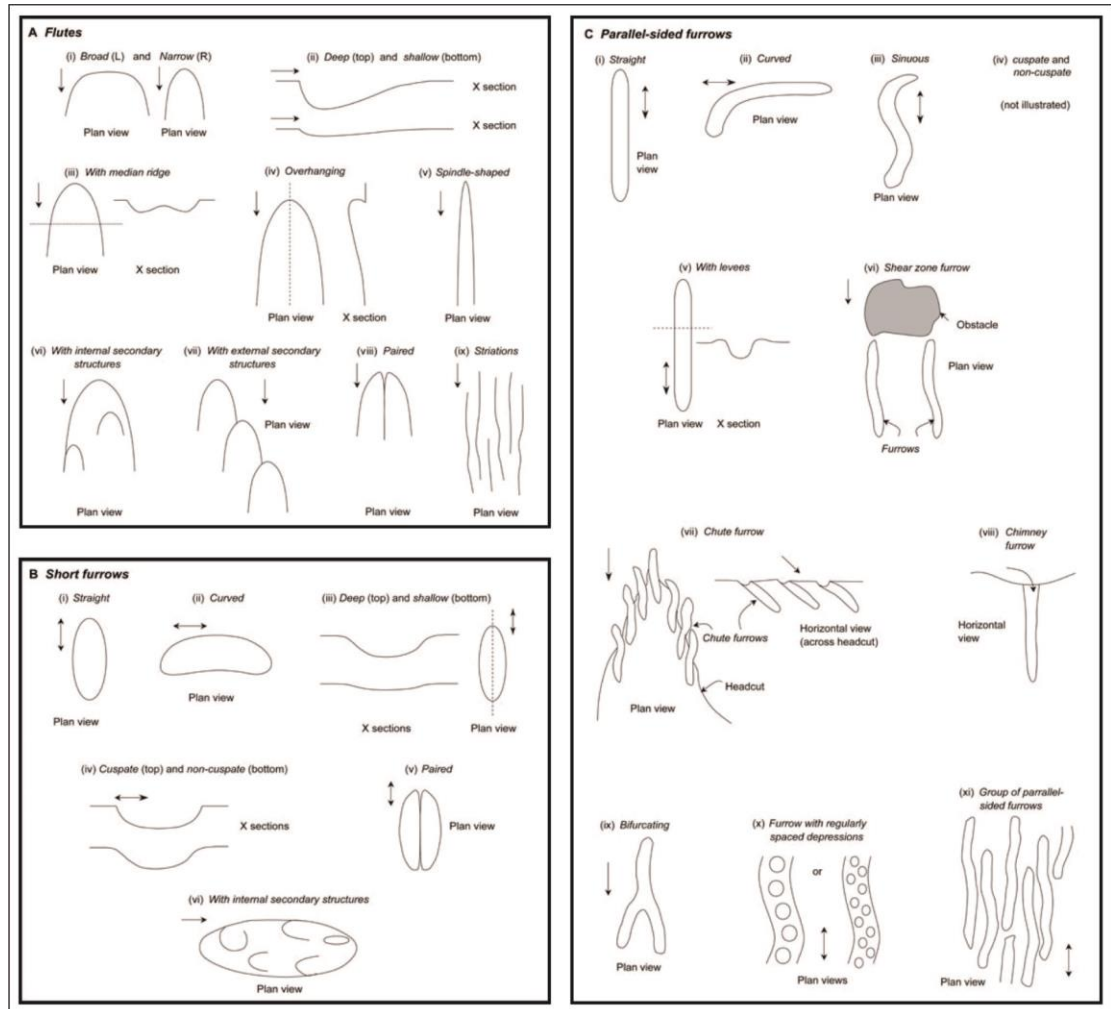


Figure 2.7 Schematic morphology of flutes, short furrows and parallel-sided furrows in bedrock channels. Note that all flute marks are shown as flaring, yet the definition includes forms that close at the downstream end. From Richardson and Carling (2005).

Furrows

In addition to the flute marks, furrows are the other common erosional feature in bedrock channels (Allen, 1971a; Richardson and Carling, 2005). Furrows can be divided into short furrows and parallel-sided long furrows (Figure 2.7 B & C) (Richardson and Carling, 2005).

Short furrows are defined as depressions with near-elliptical outline in plan view, a symmetric longitudinal section profile along their length (typically up to ~0.4 m), and length to width ratios greater than two (Allen, 1971a; Richardson and Carling, 2005). They sometimes look like potholes or flute marks. Shallow potholes have length to width ratios of less than one. Whilst the end members are defined using these specific criteria there is in fact a

continuum between short furrows and saucer-shaped shallow potholes. The main difference between flute marks and furrows is that flute marks have asymmetric longitudinal profiles with the deepest depression at their proximal end and an indistinguishable tail at their downstream end, whilst short furrows have a symmetric bowl-shaped longitudinal profile. Furrows are classified by their planform shape into straight, curved, deep, shallow, paired, cusped and non-cusped forms, some of which exhibit secondary structures (Figure 2.7B) (Richardson and Carling, 2005). For example, a straight furrow has a depression with an elliptical closed rim and straight longitudinal central axis as an elliptical bowl. Curved furrows often develop as secondary structures of other scour marks, like potholes (Richardson and Carling, 2005). This classification scheme for short furrows is very similar to that of flute marks.

Parallel-sided long furrows are not elliptical in plan view, but have long parallel sides in plan view orientated in the downstream direction and the cross-section of their main body is approximately uniform (Figure 2.7C). The boundary of this kind of furrow is rounded in cross section. An isolated long furrow may have open ends at both ends or at only one of them. If many furrows emerge on a bed, rims may be unapparent because they may be cut through by the flow leading to linkage of adjacent long furrows to form conjugate forms.

The most common types of parallel-sided long furrows in bedrock channels consist of straight furrows (Pollard et al., 1996; Tinkler and Stenson, 1992), curved furrows which curve towards one side (Pollard et al., 1996; Tinkler and Stenson, 1992), sinuous furrows (Bryant, 2008; Richardson and Carling, 2005; Wohl and Achyuthan, 2002), cusped and non-cusped furrows, bifurcating furrows that divide into two sub-furrows in the downstream direction (King, 1927; Kor et al., 1991; Shaw et al., 2000), and groups of parallel-sided furrows (Baker, 1973; Blank, 1958; King, 1927; Shepherd and Schumm, 1974; Wohl, 1993) (Figure 2.7C). A basic classification of long furrows on bedrock approximates to that described for the short furrows. A number of other rare forms have also been described, including 1) parallel-sided furrows with levees: a furrow with rounded raised margins (Richardson and Carling, 2005), 2) shear zone furrows: an obstacle is needed to form a shear zone to initialize shear zone furrows (Tinkler, 1997a), 3) chute furrows: this kind of furrow normally forms above waterfalls where the flow is rapid but still interacts with the bedrock boundary of the top of the waterfall (Maxson and Campbell, 1935), 4) chimney furrows: vertical or near vertical

furrows, which can be regarded as an extension of chute furrows (Richardson and Carling, 2005), and 5) furrows with regularly spaced depressions: a line of linear furrows which link end to end with regularly spaced short elliptical depressions (Wohl, 1993).

In natural environments, parallel-sided furrows are usually in a compound structure. Adjacent long furrows combine with time (Figure 2.8A). Once the height of the relatively higher space between adjacent furrows is cut or polished to become lower than the outer rim of furrows, these groups of parallel-sided long furrows develop into bigger compound furrows. Similarly sized isolated furrows form regular compound furrows. In contrast, a series of randomly spaced depressions with random size form an irregular compound furrow (Richardson and Carling, 2005).

Expanding furrows (Figure 2.8B) are not parallel-sided and have lateral rims that flare towards the downstream end (Richardson and Carling, 2005). This kind of furrow can be sub-divided into two types: funnel-shaped furrows with uniform downstream end and bulbous furrows with parallel-sided rims at the upstream end and a quickly developing deep and wide hollow in the downstream end (Richardson and Carling, 2005).

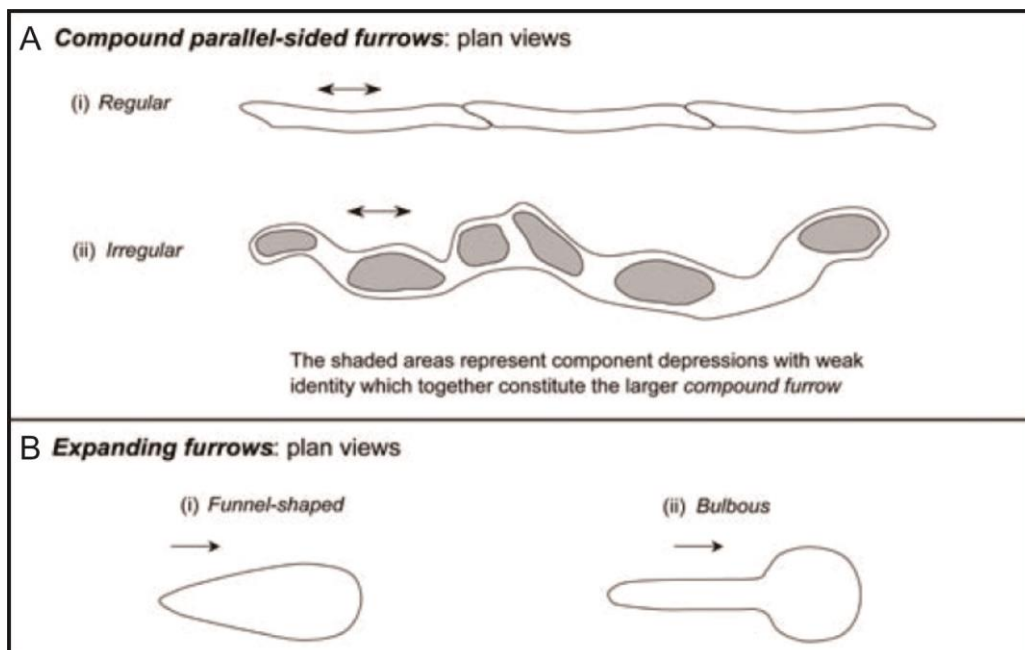


Figure 2.8 Compound longitudinal furrows. A: regular compound furrows and irregular compound furrows; B: two kinds of expanding furrows: funnel-shaped and bulbous furrows. Arrows indicate flow directions (where appropriate). From Richardson and Carling (2005).

Other erosive features in bedrock channels

There are many other bedforms that develop in bedrock channels, including concave or convex features, such as 1) runnels which mainly affect low velocity, low discharge flow when the main channel is dry (Koyama and Ikeda, 1998; Wohl, 1993; Wohl and Ikeda, 1998); 2) non-longitudinal furrows that principally form due to the formative discharges containing reversed flow (Bryant, 2008; Richardson and Carling, 2005; Shrock, 1948; Tinkler, 1993; Tinkler and Wohl, 1998a); 3) hummocky forms on smooth undulating bedrock (Bryant, 2008; Glasser and Nicholson, 1998; King, 1927; Kor et al., 1991; Tinkler, 1993), 4) obstacle marks (Baker, 1973; Lorenc et al., 1994) and, 5) solution pits (Richardson and Carling, 2005).

2.4 Undrained shear strength measurement of continental marine sediments and experimental mud beds

Continental marine sediments have been an area of very active research by scientists, industrial groups and military government organizations in the past several decades (Chassefiere and Monaco, 1987; Emiliani, 1981; Forster et al., 2010; Johnson et al., 2012; Sawyer et al., 1997). The geological characteristics of the continental margin, including continental shelf, continental slope and continental rise, play an important role in marine geological research and engineering studies (Chassefiere and Monaco, 1987; Davie et al., 1978; Forster et al., 2010; Johnson et al., 2012; Sawyer et al., 1997). The majority of studies on the geological properties of marine sediments have been on the basis of hydrocarbon-related drill cores from continental margins (Chassefiere and Monaco, 1987; Forster et al., 2010; Sawyer et al., 1997). In addition, a series of worldwide scale geological surveys on the geotechnical/engineering properties of the continental marine sediments were achieved by the Deep Sea Drilling Project (DSDP) (Davie et al., 1978; DSDP, 1969-1986; Emiliani, 1981). The main achievement of DSDP is coring and sampling of the continental margin to hundreds of metres below the sediment-water interface in water depths ranging from 2000-3000 metres throughout almost all of the major ocean basins around the world (Davie et al., 1978; DSDP, 1969-1986; Emiliani, 1981). The main properties of the continental marine sediments obtained by DSDP are undrained shear strength, consolidation, water content, porosity, grain size, and permeability. Among these, the primary property for cohesive sediments is the undrained shear strength (Forster et al., 2010), which is one of the most important factors influencing the development of seabed geometry on

the continental margin. The field undrained shear strength data of marine sediments can be considered as a standard to verify the applicability of experimental mud beds enabling analysis of the accuracy and dependability of the experimental results.

2.4.1 The composition and texture of marine sediments

The major types of marine sediments are terrigenous-derived deposits and pelagic deposits. The terrigenous-derived deposits consist of clay, silt, fine sand, and coarser gravel sediments, and are predominantly found on continental margins. Pelagic deposits form predominantly in the open ocean and consist mainly of ooze and brown/red clay (Davie et al., 1978; Nicholson, 1989). At least one-third of pelagic deposits are ooze, which are composed of pelagic foraminifera, radiolarians, diatoms, pteropods, or nanofossil shells (Chassefiere and Monaco, 1987; Davie et al., 1978; Forster et al., 2010; Nicholson, 1989; Sawyer et al., 1997). Brown/red clay is a deep-ocean clay and is usually composed of inorganic clay, and carbonate particles (Bennett et al., 1980; Emiliani and Milliman, 1966; Hèuneke and Mulder, 2011; Keller and Bennett, 1970; Neuendorf et al., 2005; Rothwell, 2004) that originate from continental-derived atmospheric dust brought by ocean currents, or material produced by solution in the ocean (Bennett et al., 1980; Davie et al., 1978; DSDP, 1969-1986; Hèuneke and Mulder, 2011; Neuendorf et al., 2005; Rothwell, 2004). The quantities and distribution of these materials depends on a lot of factors, including availability of source material and their physical and chemical properties, the temporal and spatial variations in environments (local and global), hydrological characteristics, weather patterns, and biologic activity, etc. (Bennett et al., 1980; Bouma and Moore, 1975; Davie et al., 1978; Emiliani and Milliman, 1966; Hèuneke and Mulder, 2011; Neuendorf et al., 2005; Rothwell, 2004).

2.4.2 Shear strength measurement of continental marine sediments

Shear strength, in engineering, is a term used to describe the strength of a material or component against the type of yield or structural failure where the material or component fails in shear (Barton and Choubey, 1977; Ollgaard et al., 1971; Vallejo and Mawby, 2000). In geological studies, it is the ability of a rock or soil to withstand shearing, which can be measured in river banks with a shear vane tester (Bennett et al., 1980; Chassefiere and Monaco, 1987; Davie et al., 1978; Emiliani, 1981; Forster et al., 2010; Richards, 1988; Sawyer et al., 1997), and is also the main influencing factor to the genesis of erosional features on continental marine sediments (Bouma and Moore,

1975; Burland, 1990; Chassefiere and Monaco, 1987; Forster et al., 2010; Fredlund et al., 1996; Sawyer et al., 1997). According to the finding of the composition and texture of the marine sediments mentioned before, the marine sediments can be regarded as fine-grained cohesive materials (Bennett et al., 1980; Davie et al., 1978; Emiliani, 1981; Forster et al., 2010; Richards, 1988; Sawyer et al., 1997), because the major components of the sediments on much of the seafloor are clay and silt.

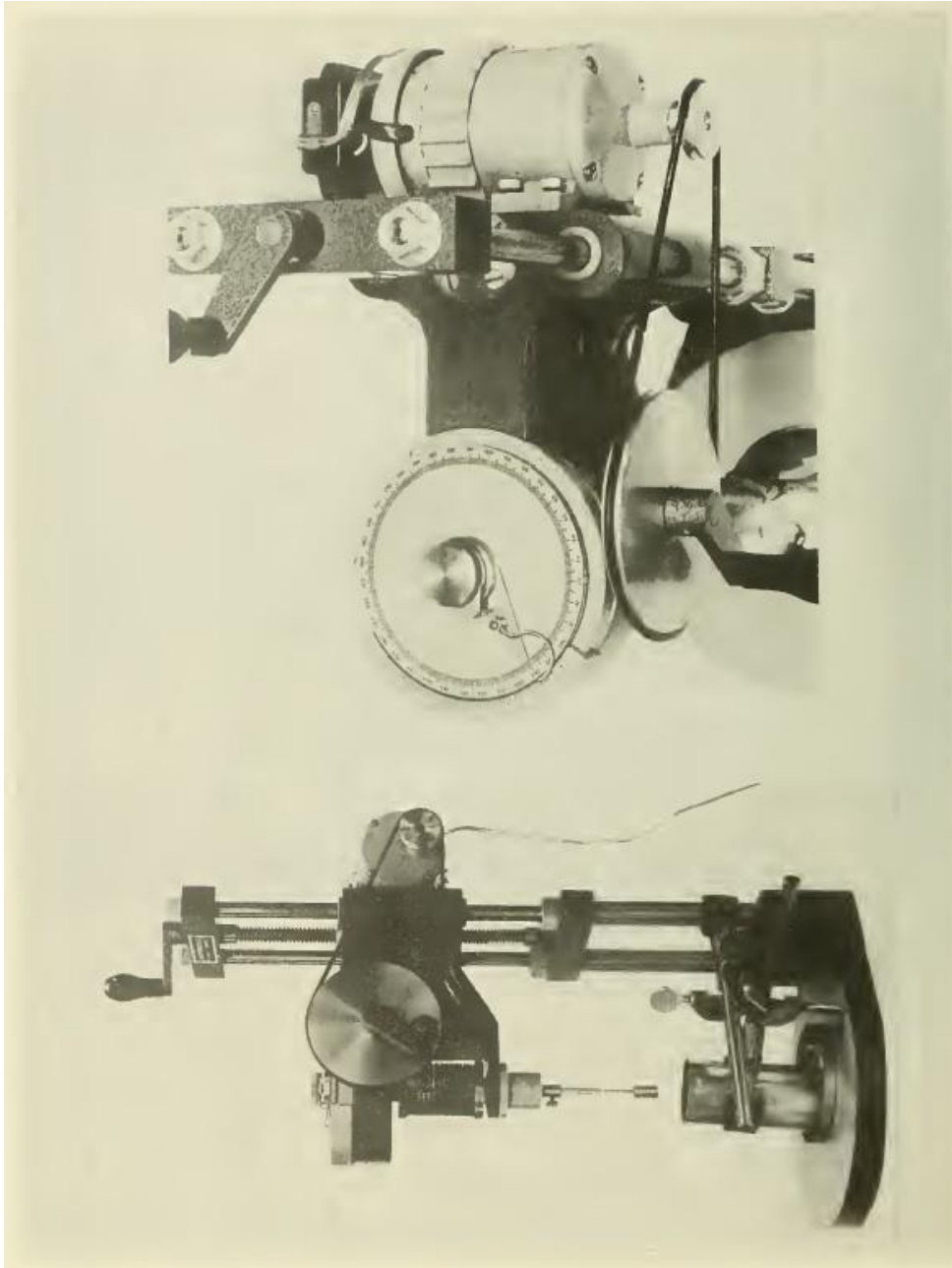


Figure 2.9 Vane shear apparatus used by Richards (1961). Each vane is 1.3 cm in diameter and 1.9 cm long. It is rotated by a constant-speed motor at a rate of 6 degrees per minute (0.1° per second). The vane needs to be buried into sediment by a distance not less than its length (Richards, 1961).

From the 1940s, the shear strength of marine sediments was initiated (Hvorslev, 1948; Richards, 1961). A commercial laboratory vane shear meter began to use vane shear apparatus to measure the strength of samples by Richards (1961) (Figure 2.9). A large number of laboratory study results on deep continental margin sediments are available from the 1970s (Bennett et al., 1980; Bennett and Keller, 1973; Bouma and Moore, 1975; Boyce, 1977; Burland, 1990; Chassefiere and Monaco, 1987; Davie et al., 1978; Demars and Nacci, 1978; Emiliani, 1981; Emrich, 1971; Forster et al., 2010; Fredlund et al., 1996; Hvorslev, 1948; Keller and Bennett, 1970, 1973; Richards, 1961, 1988; Richards et al., 1972; Richards et al., 1975; Richards and Parker, 1968; Sawyer et al., 1997). However, almost all these results, as a result of the technology restriction, are on the basis of lab measurement results instead of *in situ* measurement results (Richards et al., 1972). Richards et al. (1972) introduced the vane shear meter into field work to collect the undrained shear strength data, which is designed to operate at a water depth of up to 4.6 km and to penetrate nearly 3 m below the seabed surface in steps of 0.3 m. Before the DSDP programme, shear strength data from marine sediments was hard to obtain owing to the lack of an efficient approach to onboard measurement in the deep sea. Two major methods were utilized initially to quantify the shear strength of marine sediments. One technique was using an asphalt (AP-210) penetrometer to measure the shear strength of sediments, which could not give quantitative strength data but a rough approximations of relative (Bennett and Keller, 1973; Boyce, 1977; Keller and Bennett, 1973). The other was the vane shear apparatus used by DSDP (Bennett and Keller, 1973; Bouma and Moore, 1975; Boyce, 1977; Demars and Nacci, 1978; Keller and Bennett, 1973; Rucker, 1974). Figure 2.11 shows a summary of most of the previous achievements on shear strength measurements of different seafloors, including DSDP's onboard measurement results on the basis of these methods. Curves in Figure 2.11 illustrate very clearly that the shear strength of all seafloor sediments increases with the depth of burial, though different sediments exhibit different rates with burial depth. With the exception of the curves of Bouma and Moore (1975) SITE 294, and SITE 296, all the other lines demonstrate that the profile of shear strength is linear with penetration depth below the seafloor. The curves of the Bouma and Moore (1975) SITE 294 and Deep Sea Drilling Project (1976) indicate that the shear strength of pelagic clays and hemipelagic and terrigenous-derived clays rise with increasing burial depth. In the uppermost layers of the sea floor (depth of

burial < 10 m), the shear strength of the hemipelagic and terrigenous-derived clays is no more than 20 kPa (Figure 2.11). The average value is 7-8 kPa on the continental slope. On the upper and middle part of the slope, the shear strength is less than 7 kPa. In contrast, on the lower slope to rise, the shear strength is higher ranging from 7-14 kPa. Lower values, 2-4 kPa, were measured in the submarine canyons (Davie et al., 1978; DSDP, 1969-1986; Emiliani, 1981; GH et al., 1979). The observed variability mentioned above is a function of the presence or absence of cementation and other diagenetic processes, depth of burial and associated over burden stress, rates of sedimentation, and relative age (Bennett et al., 1980; Bennett and Keller, 1973; Burland, 1990; Chassefiere and Monaco, 1987; Demars and Nacci, 1978; Emiliani, 1981; Emrich, 1971; Forster et al., 2010; Hvorslev, 1948; Richards, 1988; Richards et al., 1972; Richards and Parker, 1968; Sawyer et al., 1997). In addition the results may in part be influenced by the lack of a standard on measurement techniques and methods, and various degrees of coring disturbance. The undrained shear strength of estuarine ranges between 1.0 kPa and 10.0 kPa with the relative water content of about 1.5 (Figure 2.10) (Winterwerp and Van Kesteren, 2004). For rivers and near river mouth areas, the undrained shear strength of upper layer of soft soil river beds ranges from 1 kPa to 7 kPa (Soltanpour et al., 2009; Winterwerp et al., 2012a). In summary, however, a general point can be made that a wide range of surficial continental margin sediments are less than 12 kPa near the surface.

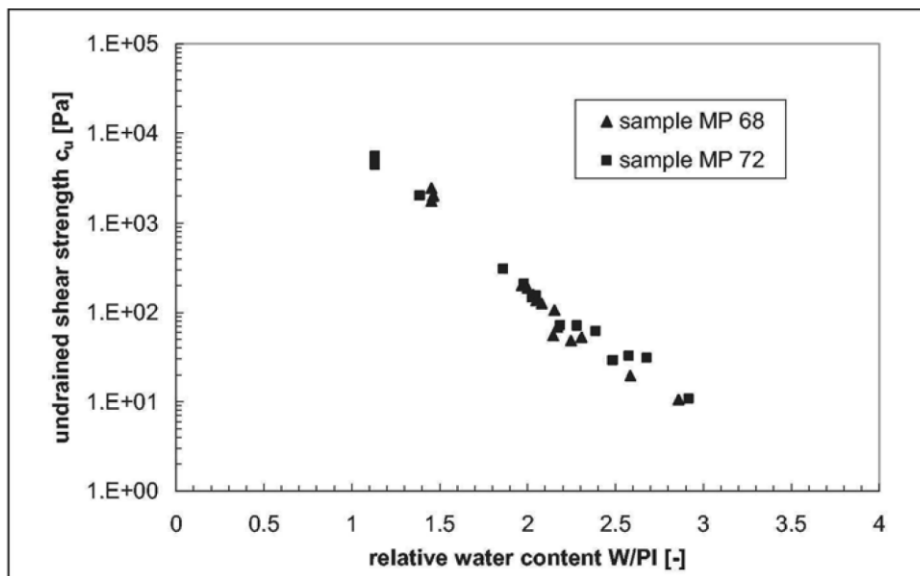


Figure 2.10 Undrained shear strength as function of relative water content (W/PI) for mud sampled from IJmuiden Harbour, Netherland. From Winterwerp and Van Kesteren (2004).

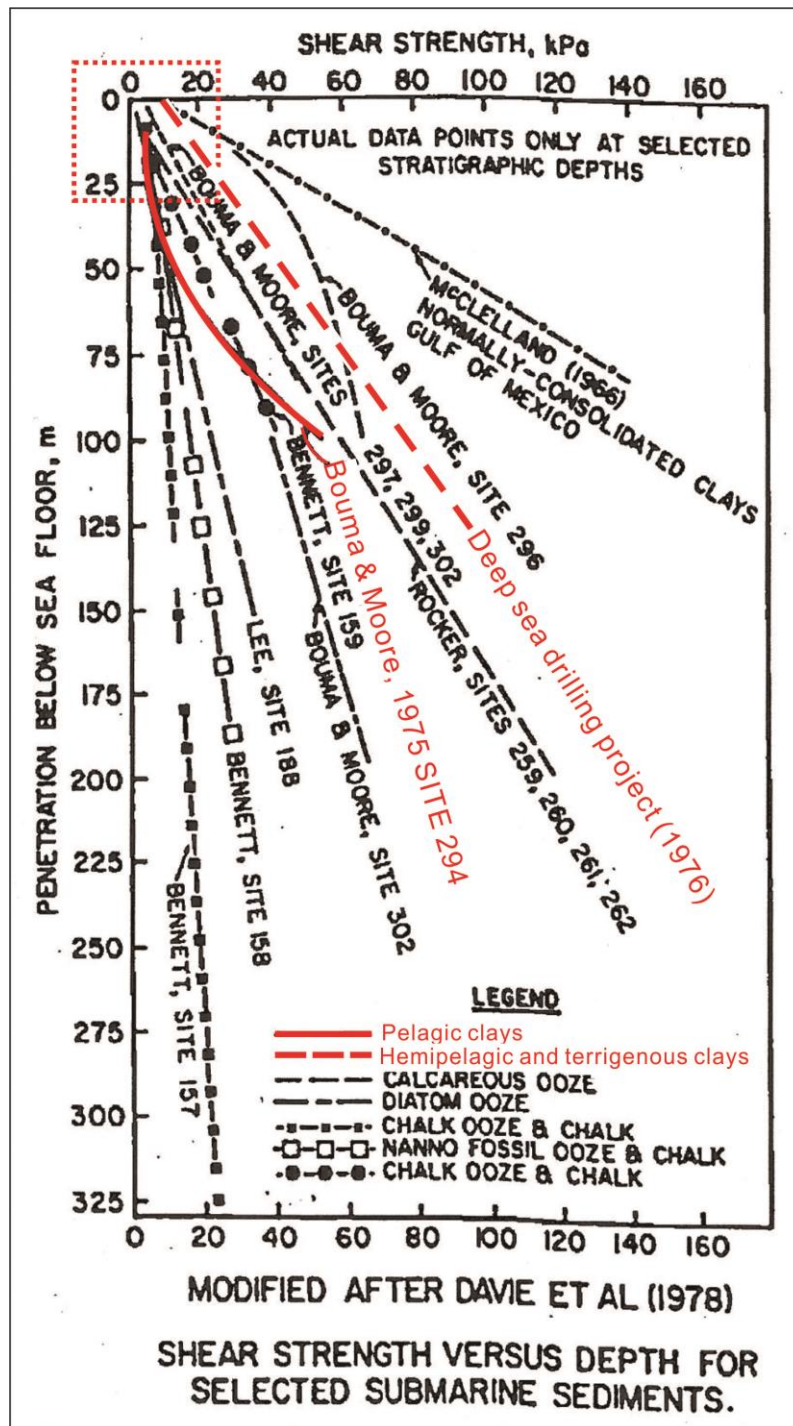


Figure 2.11 Shear strength versus penetration for ocean sediments (on the basis of Bryant et al. (1981) and Davie et al. (1978)). The red dashed square shows the shear strength values of the material near the sea floor, the depth of which is less than 25 m below the sea floor. The curve of Bouma and Moore (1975) SITE 294 shows that the shear strength of pelagic clays increases exponentially with increasing depth of burial and is less than 10 kPa when the increase of depth of burial is less than 25 m; Dashed line of DSDP (1969-1986) demonstrates that the shear strength of hemipelagic and terrigenous clays increases linearly with increase of depth of burial. The value of the uppermost layer of hemipelagic and terrigenous clays is about 10 kPa.

2.5 Summary

Although the typology and geometric morphology of a very wide array of the bedrock features and the cohesive mud bedforms, including potholes, flutes, longitudinal furrows, etc., have been well described from the previous field observation, the previous experimental work has still been restricted. In the case of the cohesive mud/clay beds, the key parameters such as the substrate strength have not been measured and the relationship between undrained shear strength and the genesis of cohesive bedforms is still unclear. For the bedrock channels, although the major factors controlling the morphology and genesis of the bedrock channels have been studied, including plucking (Whipple et al., 2000b; Whipple et al., 2000a), abrasion or corrosion (Allen, 1971a; Hancock et al., 1998; Johnson and Whipple, 2007; Wilson et al., 2012), cavitation (Hancock et al., 1998; Sato et al., 1987; Tinkler and Wohl, 1998; Whipple et al., 2000a; Wohl, 1998a), and dissolution (Wohl, 1998a), the recent studies illustrate that abrasion induced by the bedload and the roughness of the bed surface play an important role in the genesis and evolution of the erosional bedforms on the bedrock substrate (Egholm et al., 2013; Johnson and Whipple, 2007, 2010; Sklar and Dietrich, 2004; Wilson et al., 2012). However, the kinds of sculpted forms produced by the recent experiments were still limited (Johnson and Whipple, 2007; Wilson et al., 2012).

All the previous work described herein above shows that we still lack an efficient approach for flume modelling and simulation of erosion of bedrock channels. As a consequence, it has not been possible to produce many different kinds of erosional bedforms that are observed in natural bedrock channels. The genesis and development of most of the erosional features in cohesive mud beds are also not particularly clear. Therefore, a better approach to investigating the morphology of erosional forms on bedrock channels and cohesive sediments is necessary. Such an approach would help to understand how a relatively hard cohesive substrate is eroded under a given stream power, and controlled sediment supply, and whether bedrock channel erosion can be considered as an extreme condition of cohesive bed erosion. Additionally, in view of that undrained shear strength of cohesive sediments are typically $< 12\text{kPa}$ in natural seafloor sediments, it is not hard to adjust the strength of experimental clay to fit this range for investigating the relationship between bed strength and bedform formation, which will contribute to understand what kind of role the undrained shear strength plays in controlling the topography of the cohesive mud bed. In Chapter 5 to

7, a new methodology is demonstrated, that enables the detailed morphodynamics of bedrock bedforms to be assessed for the first time.

Chapter 3

Erosion experiments on mud substrates: Methodology

3.1 Introduction

The genesis, evolution and mechanics of erosive bedforms remain difficult to constrain. This in part is due to the difficulty of measuring these processes in the field. Direct field observations of bedform development in cohesive muds have not been obtained, and bedrock river channel bedform studies are restricted by the extremely low rates of bedform growth (Alexander, 1932; Allen, 1971a; Goodchild and Ford, 1971; Johnson and Whipple, 2007). Physical modelling provides an alternative approach for studying bedform development and has been widely utilised in the study of cohesionless bedforms (Alexander et al., 2001; Allen, 1968, 1982; Baas, 1994; Baas and Best, 2008; Baas et al., 2009; Baas et al., 1993; Bennett and Best, 1995b, 1995c; Best, 1992, 1993; Bridge, 2008, 2009; Bridge and Best, 1988; Chien and Wan, 1999; Costello and Southard, 1981; Müller and Gyr, 1986; Packman et al., 2000; Saunderson and Lockett, 1983; Southard, 1991; Southard and Boguchwal, 1973; Thibodeaux and Boyle, 1987).

In contrast, most of the previous work on cohesive bedforms has focused on field observations and in particular on the flow structure above the bedforms (Allen, 1971a, 1987; Baker, 1973, 1978; Carling et al., 2009; Debnath et al., 2012; Dzulynski and Sanders, 1962; Embley et al., 1980; Fedele and Garcia, 2009; Flood, 1981; Hollister et al., 1974; Lonsdale et al., 1973; Vachtman and Laronne, 2011; Williams et al., 2008; Winterwerp et al., 2012b). There has been little focus on the genesis and evolution of specific erosional features on cohesive beds, although early work utilised physical modelling to generate erosional features on cohesive mud beds (Allen, 1969, 1971a, 1971b). Experiments using non-recirculating clay suspension flows and very weak cohesive mud beds were conducted and produced longitudinal grooves, flutes and transverse erosional features (Allen, 1969). Simulation of the genesis of scallops and flutes on limestone by solution was achieved by using hardened plaster-of-Paris substrates that dissolved beneath a controlled equilibrium turbulent flow (Allen, 1971a, 1971b). Some of these experiments initialized from a plane bed with random defects (Allen, 1971b).

On the other hand, previous studies on bedforms in bedrock channels were mainly based on the field observation and numerical modelling (Cao et al.,

2006; Carling and Tinkler, 1998; Egholm et al., 2013; Hancock et al., 1998; Jennings, 1983; Nelson and Seminara, 2012; Richardson and Carling, 2005, 2006; Springer and Wohl, 2002; Tinkler, 1993; Tinkler and Wohl, 1998a; Whipple et al., 2000b; Wilson et al., 2012; Wohl, 1993, 2000). However relatively little physical modelling has been undertaken for bedrock bedforms in the last decades (Hsu et al., 2008; Johnson and Whipple, 2007; Koyama and Ikeda, 1998; Schieber et al., 2010; Schieber et al., 2007; Sklar and Dietrich, 2001; Wilson et al., 2012). Most of the previous work on simulating bedforms on bedrock channels has been highly restricted to the final formation of erosional features, or formation of specific erosional features, and there has been a lack of studies examining the evolution process of different types of erosional features (Hsu et al., 2008; Johnson and Whipple, 2007; Macdonald, 2010; Wilson et al., 2012). This is mainly attributed to the difficulty of producing erosional features on real bedrock in flume-based experiments in a short time scale. Artificial substrates have been developed but are largely restricted to the production of individual bed features with dimensions (Johnson and Whipple, 2007) (Table 3.1). For details, see Chapter 2.

The present physical experiments use clay beds as a substrate for erosive bedform development following in part the pioneering work of Allen (1971a). Nine separate experiments, experiments 0-8, were conducted to achieve the objective of physically modelling erosional features in cohesive mud beds. Here a range of substrates are examined, and the substrate shear strength of these both controlled and measured. Flow velocity profiles are measured using an ultrasonic technique enabling bed shear stress to be calculated, and therefore for the first time both the key properties of the flow and the substrate are recorded. Casting of one of the eroded mud beds has also been utilized to provide a fixed surface that can be used to examine the fluid dynamics of some of the erosive bedforms formed in the experiments. This latter work uses another ultrasonic measurement technique in order to examine the three-dimensional flow over and within the bedforms. The overall modelling approach, the details of the experimental runs, and the suite of measurement techniques are examined in more detail below.

Table 3.1 Experimental setting and results of main previous experimental work on both of the cohesive and bedrock bedforms.

| | Experiments setting | Results |
|----------------------------|---|---|
| Cohesive bedforms | | |
| 1. Allen, 1969 | a. Non-recirculating clay suspension flow b. Very weak cohesive mud bed with no specific undrained stress strength information | i. Longitudinal grooves ii. Flutes iii. Transverse erosional features |
| 2. Allen, 1971 a & b | a. Using hardened plaster-of-Paris substrates that dissolved beneath a controlled equilibrium turbulent flow to simulate the cohesive bedforms on limestone b. Random defects were pre-set on the experimental beds (Allen 1971b). | i. Scallops ii. Flutes |
| Bedrock bedforms | | |
| 1. Hsu et al. 2008 | a. Experiments using vertical rotating drum b. granular flows with single grain sizes, bimodal grain mixtures, and coarse mixtures with clay-rich fluid matrix c. Flows with more natural grain size distributions | i. Bedrock erosion is related to grain collisional stress which scale with shear rate and particle size. ii. Granular flow erosion varies as the inverse of bedrock |
| 2. Johnson & Whipple, 2007 | a. Substrate: homogenous brittle substrate (sand and cement) b. Flume: an adjustable slope, non-recirculating flume c. Sediment: a single sediment size primarily transported as bedload: fine gravel $D_{50}=2.50$ mm as bedload d. Water discharge is 45 L/s e. A single erosion mechanism (abrasion) f. Sediment-starved transport conditions | i. Abrasion only occurs where sediment impacts the bed. ii. The sediment preferentially drawn to topographic lows by gravity to further erode these lows. iii. Tortuous flow paths and erosional forms, including inner channels, scoops and potholes. iv. Patterns of erosion both create and are sensitive functions of the evolving bed topography. |
| 3. Wilson, et al., 2012 | a. Flume: a transparent one-fifth scale Attal flume b. Bedload grains are 1 cm cubes c. Rock specimen is 2 cm tall | i. UFCs are produced by bedload abrasion ii. Micropitting on downstream facing surfaces are dominantly formed by suspended load abrasion. iii. Abrasion by bedload is the controlling process in the formation of this variety of bedrock bedform and possibly the channel. |

3.2 Experimental setup

3.2.1 Flume tank

The experiments were conducted in the Sorby Environmental Fluid Dynamics Laboratory (SEFDL) in the School of Earth and Environment (SEE), University of Leeds. An 8.75-metre long, tilting, recirculating Hydraulic Slurry Flume with dimensions, 30 cm wide by 30 cm deep, was used for the present experimental programme (Figure 3.1).



Figure 3.1 The recirculating Hydraulic Slurry Flume in the Sorby Environment Fluid Dynamics Laboratory; looking downstream. The false floor composed of Perspex can be clearly seen.

The hydraulic flume possesses an inverter controlled centrifugal pump for accurate maintenance of the flow discharge during experiments. Any remaining air in the pump was expelled thoroughly by filling the flume with water before starting to recirculate the water. A turbulence-damping grid and a horizontal stack of steel pipes, each of which is 20 cm long and 3.8 cm in diameter were mounted parallel to the flow direction in front of the inlet in order to straighten flow and suppress turbulence within the flow at the inlet. A wooden board at the upstream end of the flume was set flush with the water surface to suppress turbulence within the flow. After flow exited the

pipe stack, it moved onto a 7.4 cm high, flat, smooth, false floor made of Perspex (Figure 3.2). The section in which most data were collected was located about 4-5 m from the flume inlet. An 89.6 cm long, 28 cm wide Perspex removable tray was placed into the flume facilitating the accurate positioning of a clay bed that could be located into a fixed location within the Perspex floor inserts (Figure 3.2). The flume was filled up to the final water depth of 14 cm above the Perspex floor in all of the present experiments. Uniform flow was obtained by adjusting the flume slope to 1/200. Prior to the start of each experiment the flume was fully cleaned in order to make sure that no sediment was left in the pipework, enabling the sediment concentration to be controlled in each experiment.

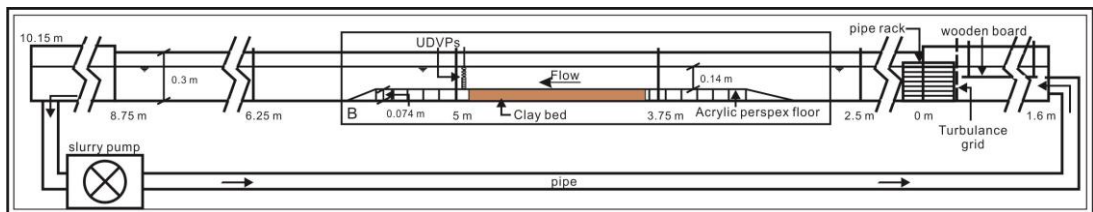


Figure 3.2 Schematic drawing of the experimental setup of the Hydraulic Slurry Flume. The brown area represents the clay bed with a tray system which was lowered into position, so that the top surface of the clay bed was at the same level of the surrounding false floor.

In all nine experiments, Exp. 0 was conducted by filling the clay directly into the slot between the false floors, without using the clay tray. No water samples were collected during Exp. 0. The rest eight experiments were conducted using a 90 cm long clay tray and were paused to collect water samples (Table 3.2-3.3). For detail, please see Chapter 4.

Table 3.2 The experimental time intervals for experiments 1 and 2

| Time | T0 | T15 | T30 | T45 | T60 | T75 | T90 | T105 | T120 | T135 |
|--------|------|------|------|------|------|------|------|------|------|------|
| Exp. 1 | √ | √ | √ | √ | √ | √ | √ | √ | √ | √ |
| Exp. 2 | √ | √ | √ | X | √ | X | X | X | √ | X |
| Time | T150 | T165 | T180 | T195 | T210 | T225 | T240 | T255 | T270 | T285 |
| Exp. 1 | √ | √ | √ | √ | √ | √ | √ | √ | √ | √ |
| Exp. 2 | X | X | √ | X | X | X | √ | X | X | X |
| Time | T300 | T330 | T360 | T390 | T420 | T450 | T480 | T540 | T600 | T660 |
| Exp. 1 | √ | √ | √ | √ | √ | X | √ | √ | √ | √ |
| Exp. 2 | √ | X | √ | X | √ | X | √ | √ | √ | √ |
| Time | T720 | T780 | | | | | | | | |
| Exp. 1 | √ | √ | | | | | | | | |
| Exp. 2 | √ | √ | | | | | | | | |

Table 3.3 The experimental time intervals for experiments 3 to 5

| Time | T0 | T30 | T60 | T90 | T120 | T180 | T210 | T240 |
|--------|------|------|------|------|------|------|------|------|
| Exp. 3 | √ | √ | √ | √ | √ | √ | √ | √ |
| Exp. 4 | √ | √ | X | √ | √ | √ | X | √ |
| Exp. 5 | √ | √ | √ | X | √ | X | X | √ |
| Time | T270 | T300 | T330 | T360 | T390 | T420 | T450 | T480 |
| Exp. 3 | √ | √ | √ | √ | √ | √ | √ | √ |
| Exp. 4 | X | √ | X | √ | X | √ | X | √ |
| Exp. 5 | X | X | X | √ | X | X | X | √ |
| Time | T540 | T600 | T660 | T720 | T780 | T840 | T900 | T960 |
| Exp. 3 | X | X | X | X | X | X | X | X |
| Exp. 4 | √ | √ | √ | √ | √ | √ | √ | √ |
| Exp. 5 | X | √ | X | √ | X | X | X | X |

Table 3.4 The experimental time intervals for the sediment-laden experiments 6-8

| Time | T0 | T30 | T60 | T120 | T240 | T360 | T480 | T600 | T720 |
|--------|------|------|-------|-------|-------|-------|-------|-------|-------|
| Exp. 6 | √ | √ | √ | √ | √ | √ | √ | √ | √ |
| Exp. 7 | √ | X | √ | √ | √ | √ | √ | √ | √ |
| Exp. 8 | √ | X | √ | √ | √ | √ | √ | √ | √ |
| Time | T840 | T960 | T1080 | T1200 | T1320 | T1440 | T1560 | T1680 | T1800 |
| Exp. 6 | √ | √ | √ | √ | √ | √ | √ | √ | X |
| Exp. 7 | √ | √ | √ | √ | √ | √ | √ | √ | √ |
| Exp. 8 | √ | √ | √ | X | X | X | X | X | X |

3.2.2 Clay preparation and undrained shear strength measurement

Two different types of clay substrate were used in the experiments. Experiments 0 to 5 utilised a clay that is typically used in pottery manufacture (Terracotta Red – from Valentines Clays Ltd, www.valentineclays.co.uk). This clay has previously been shown to be a suitable substrate for the simulation of erosive features in flume scale experiments (Macdonald, 2010). Modelling clay was subsequently used in experiments 6 to 8 (SCOLA air-drying modelling clay:

<http://www.craftmill.co.uk/scola-air-drying-modelling-clay>). The composition of the two clay substrates were measured by X-ray diffraction (XRD) (Philips PW1050 XRD). The result of which are shown in Table 3.5 and Table 3.6.

Table 3.5 XRD analysis of Terracotta potters clay used as experimental beds in experiments 0, 1, 2, 3, 4 and 5 (Macdonald, 2010)

| Mineral | Quartz | Albite | Microcline | Mica | Total |
|---------------------|------------------------|------------------|-------------------|-----------------|--------------|
| Percent content (%) | 33.70 | 1.00 | 1.00 | 1.50 | 99.40 |
| Mineral | Illite-smectite | Kaolinite | Chlorite | Hematite | |
| Percent content (%) | 30.80 | 18.00 | 7.70 | 5.70 | |

Table 3.6 XRD analysis of modelling clay used as experimental beds in experiments 5, 6, 7 and 8

| Mineral | Quartz | Illite-smectite | Kaolinite | Hematite | Total |
|---------------------|---------------|------------------------|------------------|-----------------|--------------|
| Percent content (%) | 36.4 | 40.1 | 21.1 | 4.5 | 102.2 |

The shear strength of the clay substrates was controlled by soaking the beds in water for pre-determined lengths of time in order to reach a specific strength for each experiment (see Section 3.2.3) in order to investigate whether different substrates with different strength can produce different types of bedforms. At the required strength the clay was moulded into a moveable tray and inserted into the flume. In order to ensure the original bed surface was flat, a clay trowel and a piece of thick metal sheet with straight edge were used to smooth the clay surface to the same level of the Perspex floor. The clay was exposed to the air for about one hour during this procedure.

The undrained shear strength measurements of the different substrates were measured using a hand shear vane meter (H-60 field inspection vane tester 26-3335) with a four-blade vane (H-612 vane, 25.4 mm x 50.8 mm. Weight: 50g) (Figure 3.3).



Figure 3.3 Images of the H-60 field inspection vane tester 26-3335, with a range of different size vanes (http://www.aisys.com.sg/items/Item_Details.aspx?itemid=157&cateid=74).

Table 3.7 The calibration certification of the vane shear strength meter provided by the manufacturer.

| Vane meter reading | Torque, T (N/m) | Direct Kpa Conversion |
|--------------------|-----------------|------------------------|
| | | 25.4(d) x 50.8(h) (mm) |
| 0 | 0 | 0 |
| 1 | 0.3 | 5.094 |
| 2 | 0.5 | 8.49 |
| 3 | 0.7 | 11.886 |
| 4 | 1.1 | 18.678 |
| 5 | 1.2 | 20.376 |
| 6 | 1.4 | 23.772 |
| 7 | 1.7 | 28.867 |
| 8 | 2 | 33.961 |
| 9 | 2.5 | 42.451 |
| 10 | 3.2 | 54.337 |
| 11 | 3.9 | 66.223 |
| 12 | 4.2 | 71.317 |

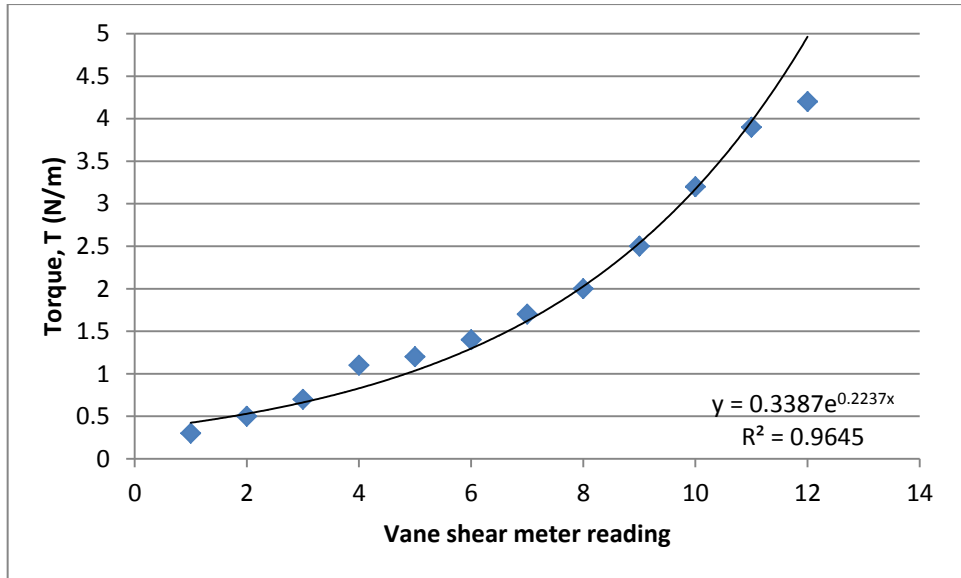


Figure 3.4 Relationship between the vane meter reading and torque, based on the manufacturer’s calibration data (see Table 3.6).

The calibration equation for calculating the undrained shear strength given by the manufacturer is:

$$C_u = \frac{6T}{(\pi d^2 (d + 3h))} \quad \text{Eq. 1.1}$$

where d is diameter (m) of the vane, h is height (m), T is torque (N/m), and C_u is undrained shear strength (kPa). In order to calculate the torque from the meter reading, for anything other than an integer value, the relationship between the two variables must be known. This relationship between the meter reading and T is shown in Figure 3.4 and in equation 1.2.

$$T = 0.3387e^{0.2237X} \quad (R^2 = 0.9645) \quad \text{Eq. 1.2}$$

where T is Torque (N/m), and X is the vane meter reading.

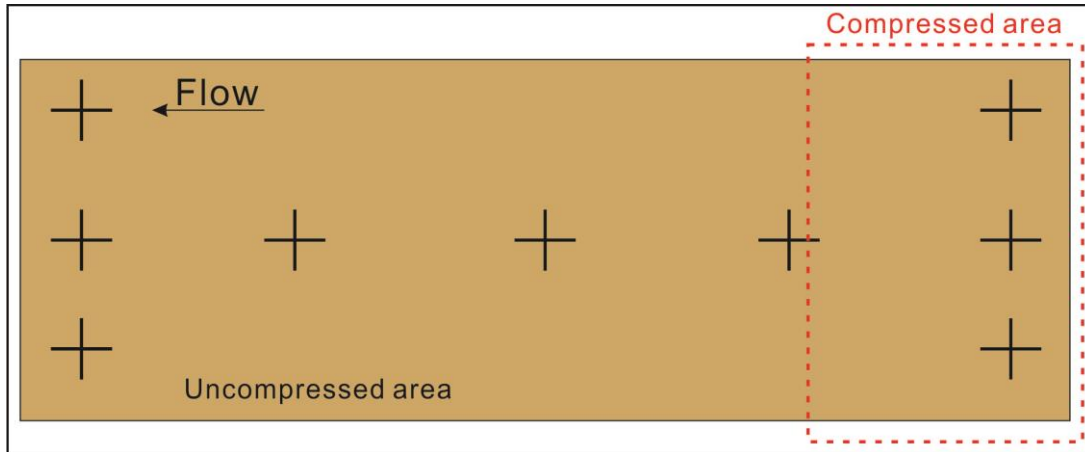


Figure 3.5 A schematic figure of the undrained shear strength measurement positions (+) on the mud bed in the hydraulic flume. Flow direction is from right to left. Except for the first 6 hours soaking in a side box, all the remaining measurements were done directly in the flume. The rationale for dividing the clay bed into compressed and uncompressed areas was to identify the influence of uncertain pressure inadvertently applied to the mud bed on shear strength when flattening the surface of the mud bed.

The first two measurements of undrained shear strength using the vane shear meter were undertaken in a side box, where clay was soaking, with the top of the vane positioned at a depth of 4 vane widths as recommended by the British standard BS1377-7. The rest of the measurements were undertaken in the flume after the clay had been flattened and moved into the flume. However, the thickness of the clay in the flume was only 7.4 cm and therefore far too thin for shear vane testing using the recommended 4 vane widths. Therefore the rest of the measurements of undrained shear strength were undertaken with the top of the vane positioned at a depth of 1.5 vane widths in the flume (Figure 3.5).

Nine positions from upstream to downstream on the mud bed were selected to measure the undrained shear strength, as a function of soaking time. Although all attempts are made to keep the clay in its original condition during flattening and moving, there is potential for additional pressure to be applied. This unexpected pressure cannot be qualified. In order to identify the effect of this unexpected pressure on the clay bed, the clay bed was divided into two parts, uncompressed and compressed parts. The area in the red dash square in Figure 3.5 was compressed with 1.25 kPa pressure applied to the surface of the mud bed for 2 minutes. Unexpected pressure was controlled to a minimum on the rest of the clay bed.

Figure 3.6 and Figure 3.7 indicate the testing results on both the compressed and uncompressed areas. Before being moved into the tray/flume, the original clay was soaking in a corner box (W x D x H: 71 cm x 46 cm x 38 cm) for 6 hours. The uppermost 2 points in the top left corner of both Figure 3.6 and Figure 3.7 are the values obtained during clay soaking in the corner box. The rest of the data were obtained during clay soaking in the tray/flume. Undrained shear strength decreased exponentially in both the compressed and uncompressed areas in the first 45 to 50 hours. After 50 hours, the shear strength can be regarded as a quasi-constant value (Figure 3.6 & Figure 3.7).

The results on both the compressed and uncompressed clay bed demonstrate that the external pressure has some effect on the undrained shear strength of the clay bed. The value of the undrained shear strength of the compressed bed is higher than that of the uncompressed bed by ~0.5 kPa at the same measurement time. The uncertain pressure applied on the clay bed is far less than 1.25 kPa for 2 minutes and therefore spatial variations in bed shear strength within the clay bed are likely to be minimal. All the data for undrained shear strength mentioned in the following text, such as the data in Figure 3.8, are regarded as being measured from the uncompressed clay bed.

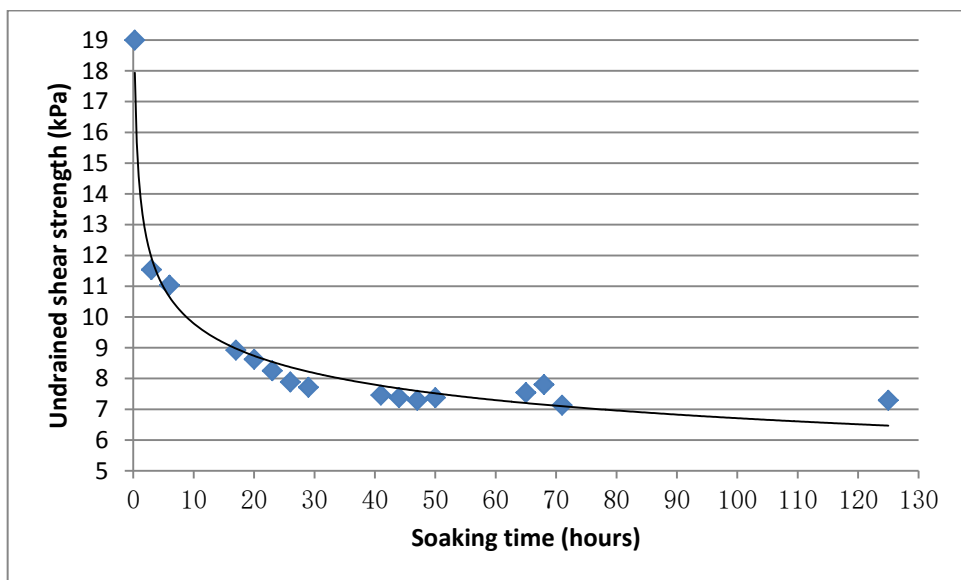


Figure 3.6 The relation between undrained shear strength and soaking time of the downstream part of the mud bed, for uncompressed clay bed.

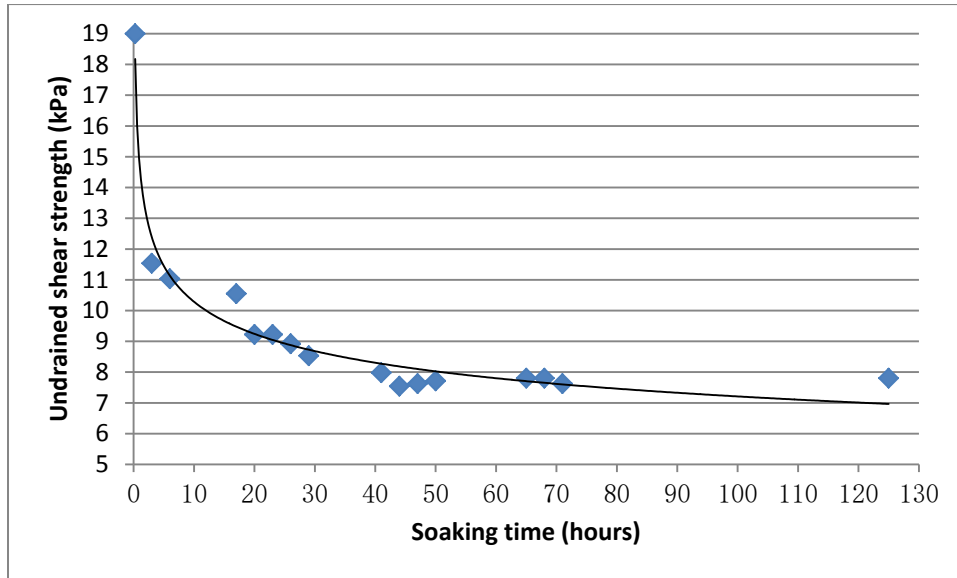


Figure 3.7 The relation between undrained shear strength and soaking time of the downstream part of the mud bed, for compressed clay bed.

Variability in shear strength with time enables experiments to be initiated with undrained shear strength in the range of 7 kPa to 11.5 kPa (Terracotta clay), and 5.5 kPa to 12.7 kPa (modelling clay), respectively (Figure 3.8). The undrained shear strength of each experiment is as follows: Exp. 0, 1 & 2: 19 kPa; Exp. 3 : 6.5-7 kPa; Exp. 4: 9 kPa; Exp. 5: 9 kPa; Exp. 6: 10.5 kPa; Exp. 7: 7-7.5 kPa; Exp. 8: 5.5 kPa (Figure 3.8). According to the data from Deep sea drilling project (DSDP), the undrained shear strength of the sea surface composed by pelagic, hemipelagic and terrigenous clay ranges from 7 kPa to 14 kPa which shows the shear strength used in the current experiments are within the range of natural samples (Bouma and Moore, 1975 Site 294; DSDP 1976).

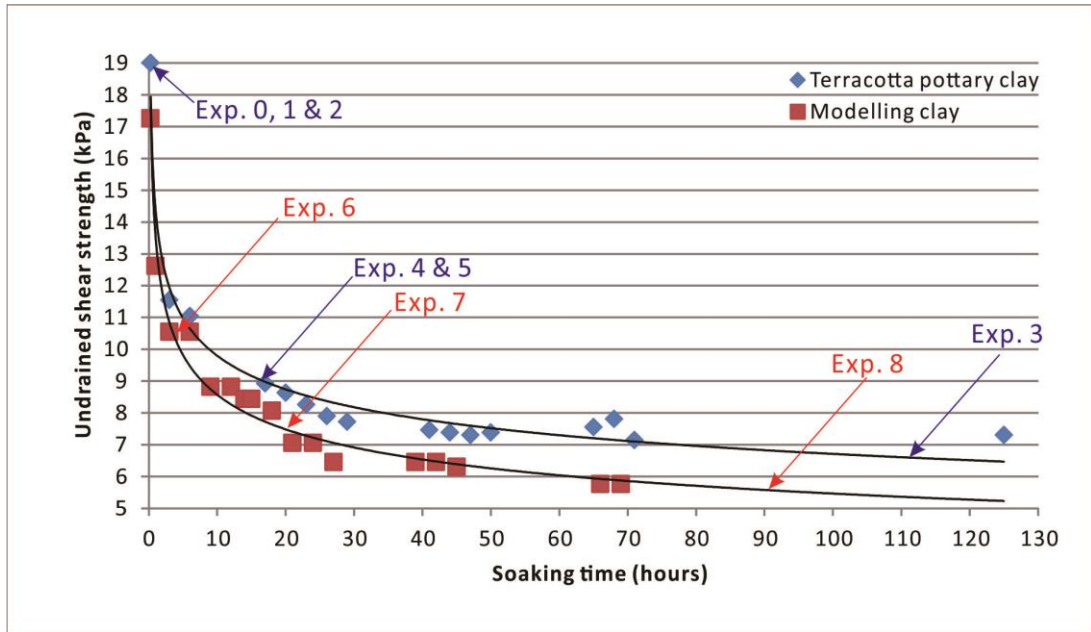


Figure 3.8 Undrained shear strength change with soaking time. Exp. 0, 1 & 2: 19 kPa; Exp. 3: 6.5-7 kPa; Exp. 4: 9 kPa; Exp. 5: 9 kPa; Exp. 6: 10.5 kPa; Exp. 7: 7-7.5 kPa; Exp. 8: 5.5 kPa.

3.2.3 Sediment addition and water sampling

The silica sand, Redhill 110, used in the experiments was mined in Surrey and is of Lower Cretaceous age. The grain-size distribution was determined by a Malvern Mastersizer 2000 laser grain-sizer. Redhill 110 is a very fine to fine well-sorted angular sand with a mean diameter, D_{mean} , of 129 μm ; a diameter for which 10% of the sediment is finer, D_{10} , of 82 - 90 μm , a D_{50} of 142 - 155 μm and a diameter for which 90% of the sediment is finer, D_{90} , of 239 - 259 μm (Figure 3.9). The density of the sand grains is 2650 kg m^{-3} and the bulk density of the sand is 1350 kg m^{-3} . The previous work conducted by Macdonald (2010) indicated that this type of sand was ideal for modelling suspended and bedload sediment transport and for eroding the current experimental substrate.



Figure 3.9 Grain size distribution curve of the suspended sediment in the flow as calculated using a Malvern Mastersizer 2000 laser diffractometer.

In order to compensate for sediment depositing in the pipework of the hydraulic flume during individual experiments and thereby maintain an approximately constant suspended sediment concentration in the main channel, up to 2.5 kg of sand was introduced into the water every 15 minutes during each experiment (see Table 3.8). Exp. 0 and Exp. 5 were running with sediment-free flow. Water samples were collected manually every 5-20 minutes, depending on the experiment, at about 30 cm from the downstream end of the mud bed in order to measure the suspended sediment concentration (SSC) (Table 3.8). The water samples were collected at approximately mid-depth, about 7 cm below the water surface. The SSC of all the experiments with suspended material was mostly well controlled in the range of 0.05% to 0.25% (Figure 3.10 & Figure 3.11).

Table 3.8 Difference among each experiment: sand addition amount, water sampling time, and velocity monitoring time.

| | Sand addition every 15 min (kg) | Water sampling | Velocity monitor (UDVP) |
|--|---------------------------------|--|--|
| Exp. 0: Clear water trial | 0 | null | null |
| Exp. 1: Terracotta hard-1 | 2.5 | every 5 min in 15-min run; every 10 min in 30-min run; every 20 min in 60-min and 120-min run; | every 7.5 min in 15-min run; every 10 min in 30-min run; every 20 min in 60-min and 120-min run; |
| Exp. 2: Terracotta hard-2 | 2.5 | | |
| Exp. 3: Terracotta soft | 2.5 | | |
| Exp. 4: Terracotta mid-hard with low flow rate | sand deposition in the flume | | |
| Exp. 5: Terracotta mid-hard | 0 | | |
| Exp. 6: Modelling hard | 1.5 | | |
| Exp. 7: Modelling mid-hard | 1.5 | | |
| Exp. 8: Modelling soft | 1.5 | | |

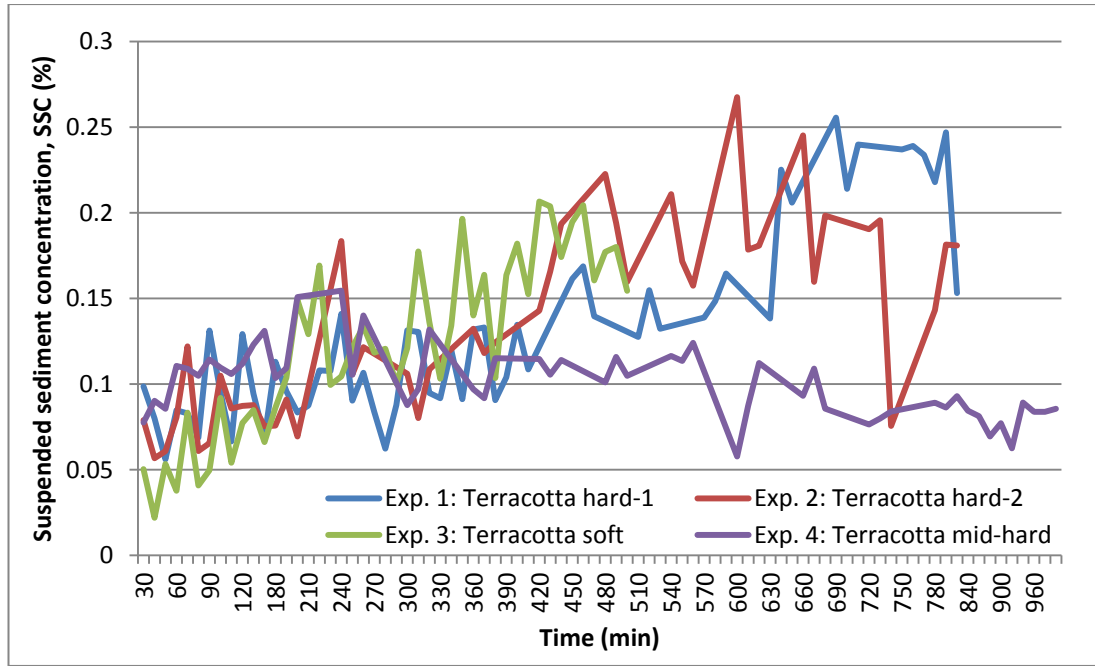


Figure 3.10 Suspended sediment concentration for experiments 1-4.

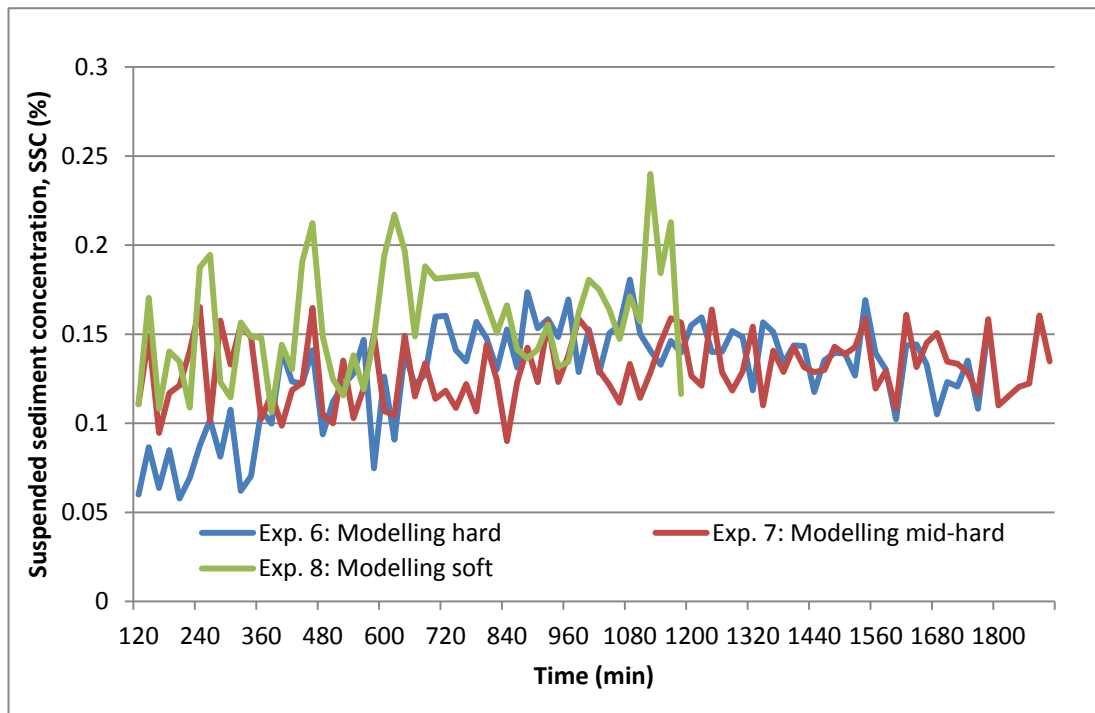


Figure 3.11 Suspended sediment concentration for experiments 6-8.

3.2.4 Flow velocity measurements by ultrasonic Doppler velocity profiling (UDVP)

Vertical profiles of downstream flow velocity were monitored by UDVP-DUO (Metflow-8A). The principle of the UDVP-DUO is to detect the reflection of the ultrasonic pulse when it hits the suspended particles in the flow (Best and Ashworth, 1994; Best et al., 1997; Best et al., 2001; Karcz, 1973; Kikuchi et al., 2006; Lhermitte and Lemmin, 1994; Rolland and Lemmin, 1997; Takeda, 1991; Teufel et al., 1992; Tokuhiro and Takeda, 1993). A total of ten 4 MHz probes were held vertically on a probe holder (Figure 3.12). Each experiment was stopped at intervals to record bed elevation and to obtain photographic records using a Canon 550D DSLR camera and 8-55mm lens (see Table 3.2 - Table 3.4). UDVP measurements were taken for a period of 60 seconds, five minutes into intervals of 15-minutes, ten minutes into intervals of 30-minutes, or twenty minutes into intervals of 1-hour (Table 3.8). The UDVP probes were located at the centreline position of the flume 1 cm downstream of the clay bed enabling measurement of a flow velocity profile above the clay bed. The diameter of each transducer probe was 8 mm. Probe 1 (the lowest probe) was placed above the bed floor by 6 mm, and the vertical span between two adjacent probes was 10 mm from centre to centre of the transducers. UDVP parameters are shown in Table 3.9. The raw data collected by UDVP was processed by a bespoke code within MATLAB. Figure 3.13 illustrates an example of the series of the vertical downstream velocity profiles of Exp. 1.

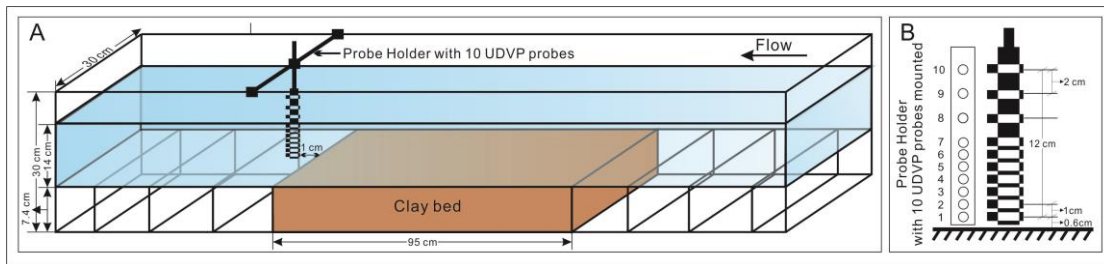


Figure 3.12 Schematic figure showing (A) the downstream, and (B) the vertical positioning of the ultrasonic Doppler velocity profiler's (UDVP) probe arrays

Table 3.9 Parameters for the UDVP used in the presented experiments

| | |
|-----------------------------------|-----------------------------------|
| Ultrasound frequency | 4 MHz |
| Number of cycles | 8 |
| Channel width | 1.48 mm |
| Channel distance | 0.74 mm |
| Number of repetition | 16 |
| V axis range | -675.4 – 668.9 mm s ⁻¹ |
| Measurement window | 5 - 101.2 mm |
| Number of bins | 128 |
| Multi-pixel time delay | 15 ms |
| Number of profiles per transducer | 500 |
| Ultrasound velocity | 1480 ms ⁻¹ |
| Transducer and probe diameter | 8 mm |
| Bin for analysis | 81 |

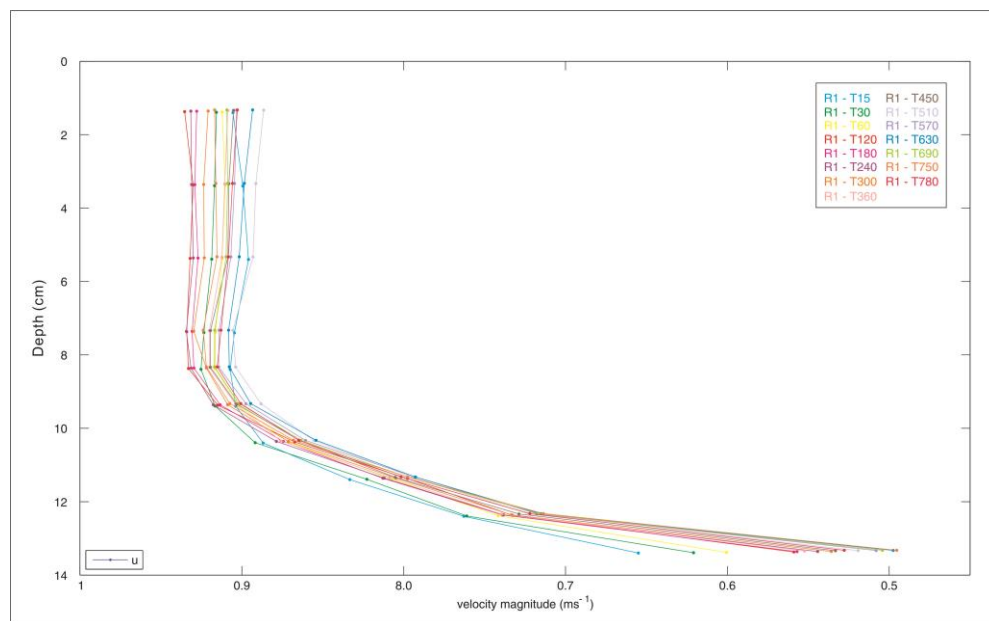


Figure 3.13 Downstream velocity profiles of Exp. 1 over time, taken at the channel centreline above the mud bed.

3.2.5 Topographic measurement using Seatek Ultrasonic Ranging System

An ultrasonic ranging system (from Seatek Instrumentation) (Figure 3.14) was used to investigate the bathymetry of the bedforms and determine morphological change of the clay bed under the influence of a unidirectional recirculating low concentration particulate suspension. The principle of the Seatek bedform profiler is that the transducers detect the pulse reflected by the channel bottom to qualify the distance between the head of the transducers and the surface of the objective. The operating frequency is 2 MHz. The data collected is transmitted back to the operating PC via an RS232 communication port and saved by associated software from the supplier (<http://seatek.members.atlantic.net/>).

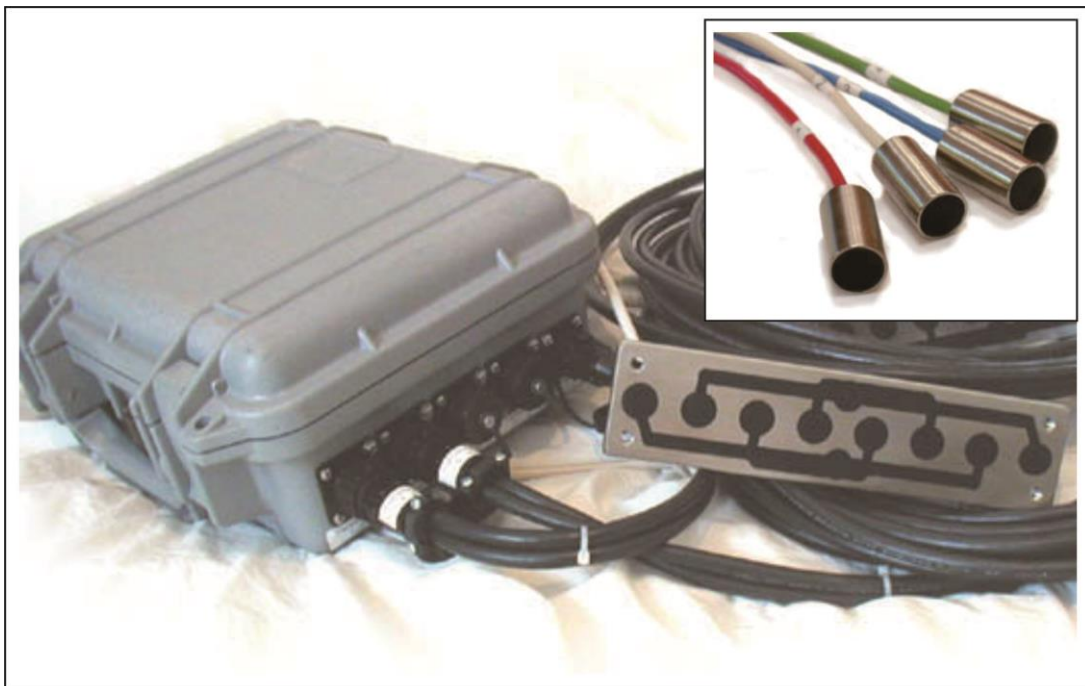


Figure 3.14 Seatek Ultrasonic Ranging System (5 MHz) with transducers. From Seatek Instrumentation.

The Seatek system used herein consists of twelve 5 MHz transducers arranged in a line transverse to the flume, with each transducer spaced 15 cm apart, as measured from the centre of one probe to the next (Figure 3.15A & B). The transducer array is mounted onto an XY traverse capable of moving the probes longitudinally (X) and across-stream (Y) with millimetric precision. For each bed scan, a Y value was fixed, with the probes running along the X-direction at 2 mm intervals. A second scan adjusted the position of the transducer array in the Y direction by 3 mm (Figure 3.15C). This

adjustment of the array in the cross-stream direction was repeated a total of 6 times in order to cover most of the clay bed and to examine the bed topography in detail; the individual scans were stitched together to produce a 2 mm (x) by 3 mm (y) grid (Figure 3.15B & C).

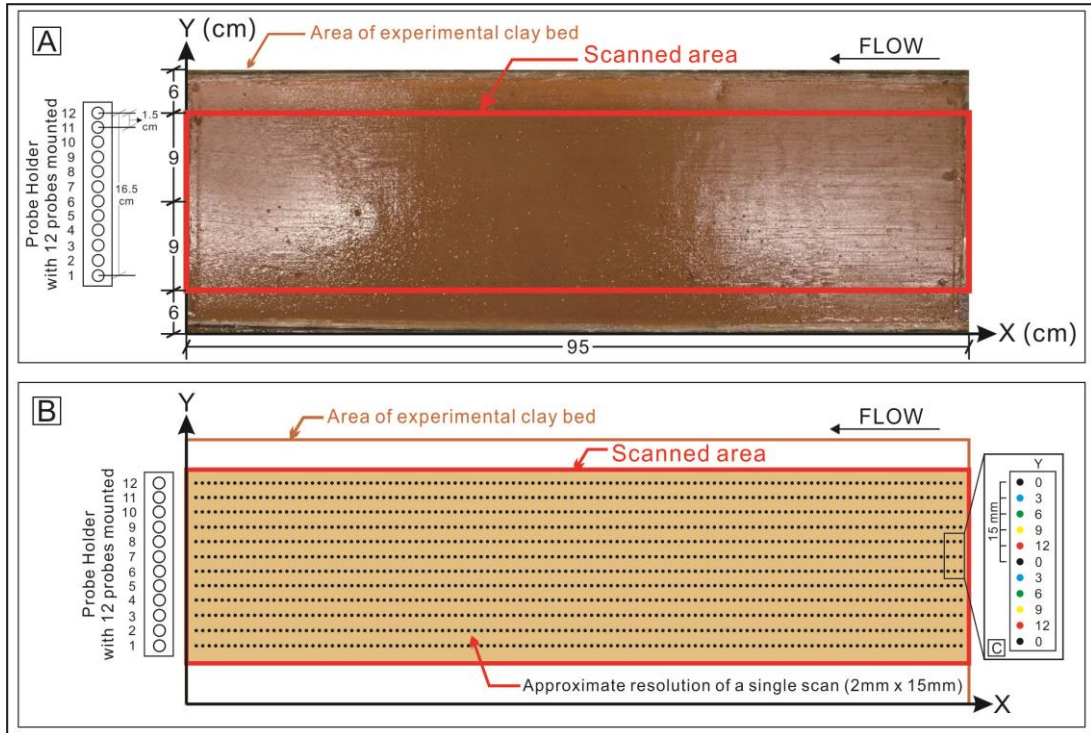


Figure 3.15 Plan view of arrangement for bathymetric profiling of experimental beds. A: All the data were collected within the red box by the Seatek system. The clay bed showed in A is the original flat bed before the start of the experiments. B: Schematic figure of the array of the Seatek sampling point on the clay bed. The resolution of a single scan is 2 mm x 15 mm. C: The probe holder moved in Y direction by 3 mm after each single scan to increase the sampling resolution. Such scans were repeated 6 times for each time interval.

Before running the Seatek array, the probes were placed just below the water surface and all bubbles on the base of the probe heads removed as these negatively influence data quality. The Seatek probe system was run twice in the clear water over the initial clay bed to confirm the status of the whole Seatek system is stable enough to provide valuable data. The temperature of the water was measured using a digital thermometer prior to starting each scan of the Seatek system. The water temperature varied between 8 – 12 °C during the scanning and differs from one scan to another. The temperature of the water initially is approximately 8 °C. It becomes warmer with time after the flume is filled up. During the scan, the temperature can increase to 12 °C. This temperature range is lower than the

limit, 20 °C, which the Seatek profiling system can accept. Although, previous studies show that the speed of ultrasound in water is a function of temperature, in freshwater the difference over this temperature range is only ~10-20 ms⁻¹, and the speed of ultrasound is ~1440 ms⁻¹ at 10°C, so the error is no more than ~1% (Al-Nassar et al., 2006; Bilaniuk and Wong, 1993). The results of the repeated scans above the original flat bed before the flume run also show that such small temperature differences barely alter the results of bed scanning.

Besides doing the bedform scans by using Seatek system, a series of photos of the whole clay beds were taken using a Canon 550D digital SLR that was mounted on a holder positioned directly above the beds. Four straight control bars with 10 control points on each of them were distributed around the edges of the clay bed in order to rectify the distorted images by using software named DxO ViewPoint.

3.2.6 Production of a fixed bed morphology

In order to accurately measure the flow field above and within the erosional features, a stable bed with unchangeable erosional features is required. Latex was chosen to make the copy of the experimental clay bed. The final bed formation of Exp. 8 was reproduced by using latex. First of all, a plaster-of-Paris cast was firstly made (Figure 3.16A). Secondly, the latex was dissolved by heating to 120 °C. Thirdly, the liquid latex was poured onto the plaster-of-Paris cast. After a half-day cooling down and solidification, a blue latex replica of the final Exp. 8 bed was ready to use. This latex replica was stable and unerodible under the effect of sediment-laden flow and therefore is ideal for detecting the flow profile within and above different erosional features during a flume run.

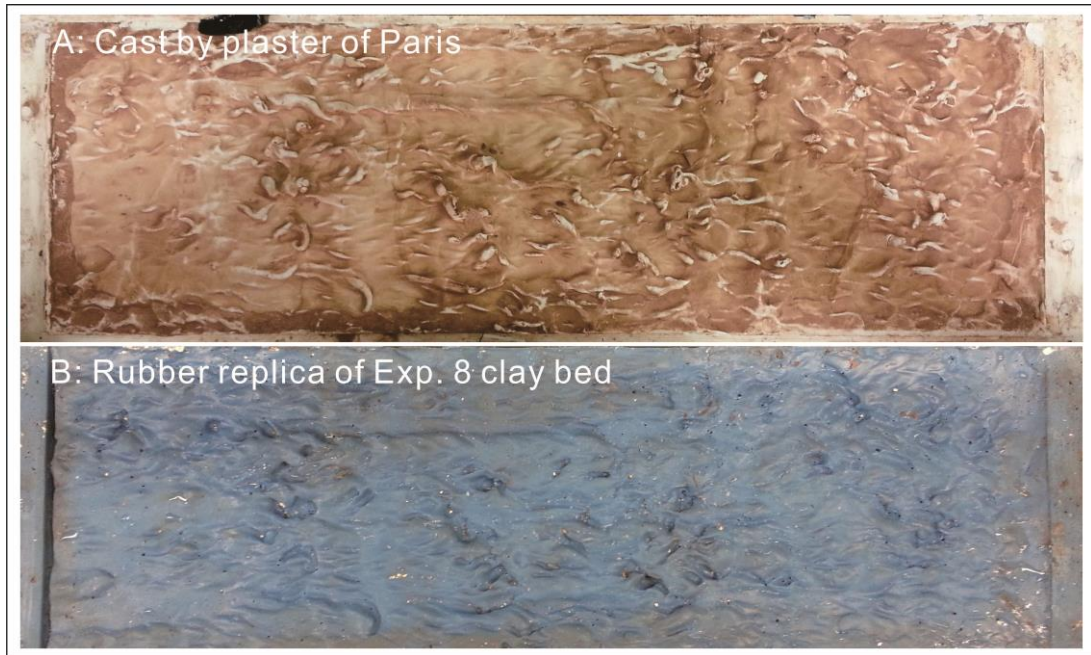


Figure 3.16 The cast made by the plaster-of-Paris and the replica of the final bed formation of Exp. 8 made using latex. A: cast made by the plaster-of-Paris; B: Latex replica of the final bed of Exp. 8.

3.2.7 3-D Flow velocity measurement by Acoustic Doppler velocimetry (ADV)

The Nortek Vectrino-II Acoustic Doppler velocimetry (ADV) (Figure 3.17) was used to measure the flow velocity within and above different erosional features that formed in the mud beds. The Vectrino-II profiler has a central transducer that emits ultrasound and four transducers that receive the reflection of the ultrasound from the bottom of the channel. In the experiments, it was mounted on a rack with the central transducer vertically towards the experimental bed surface. It can collect at-a-point three dimensional flow velocities at up to 100 Hz, with a vertical spatial resolution of 1 mm in the range from 4 cm to 7 cm below the centre transducer (Figure 3.17). The central transducer omits the pulse and the other 4 transducers detect the reflection of the pulse when it hits the seeding material in the flow or the surface of the sediment. The effective measurement coverage of the instrument is 3 cm above the bottom of the target area (Figure 3.17). Meanwhile, it can also measure the distance from the central transducer to the sediment interface at up to 10 Hz (Figure 3.18). The Vectrino-II ADV configuration is shown in Table 3.10.

Table 3.10 Vectrino-II ADV operating configuration

| | |
|-------------------------------|----------|
| Sampling rate | 100 HZ |
| Velocity range | 1.5 m/s |
| Range of first cell | 40 mm |
| range to last cell | 74 mm |
| Cell size | 1.0 mm |
| Number of cell | 35 |
| Transmit pulse size | 1.0 mm |
| Calibrated range | 40-74 mm |
| Power level | High |
| Bottom check sample rate | 1 Hz |
| Minimum depth | 20 mm |
| Maximum depth | 200 mm |
| Bottom check Cell size | 4.0 mm |
| Bottom check number of cell | 45 |
| File completion/sampling time | 60 s |



Figure 3.17 The Nortek Vectrino-II Acoustic Doppler velocimetry (ADV).
From Nortek AS, Norway
(<http://www.nortekusa.com/usa/products/acoustic-doppler-velocimeters/vectrino-ii>)

During the flume run, the Vectrino-II was mounted on a movable steel rack, and the downstream spacing between two sampling positions was 5 mm.

The sampling time for each position was set to 60 seconds. All the raw data obtained using the Vectrino-II were post processed by company software and plotted in Matlab using bespoke routines. Figure 3.19 shows a series of velocity profile above an erosion feature obtained using the Vectrino-II ADV. More results are provided and discussed in Chapter 7.

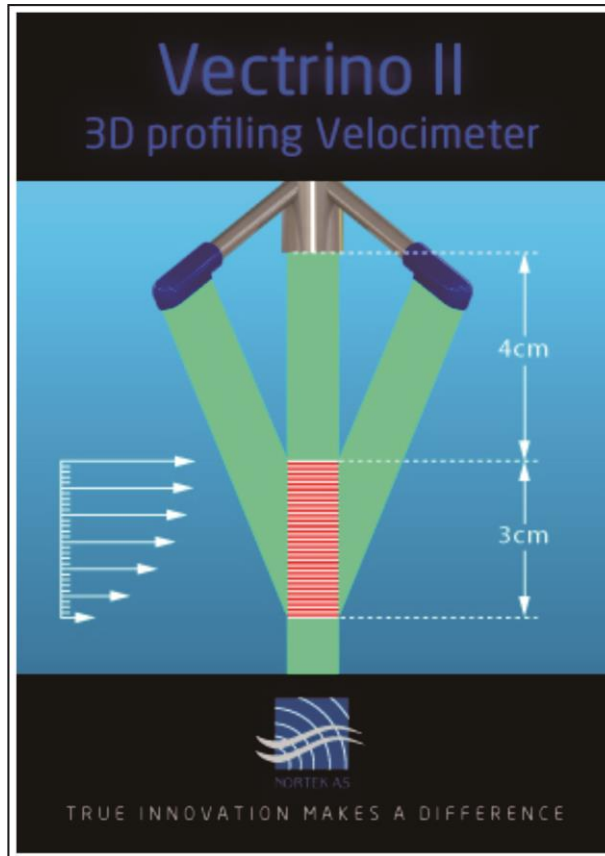


Figure 3.18 A schematic figure of the working principle of the Vectrino-II ADV. Only 2 of 4 receiver beams are shown in this figure. The included angle between 2 adjacent receiver transducers is 90 degrees. The red area shown in this figure is the effective measurement coverage, 3 cm. From Nortek AS, Norway (<http://www.nortekusa.com/usa/products/acoustic-doppler-velocimeters/vectrino-ii>)

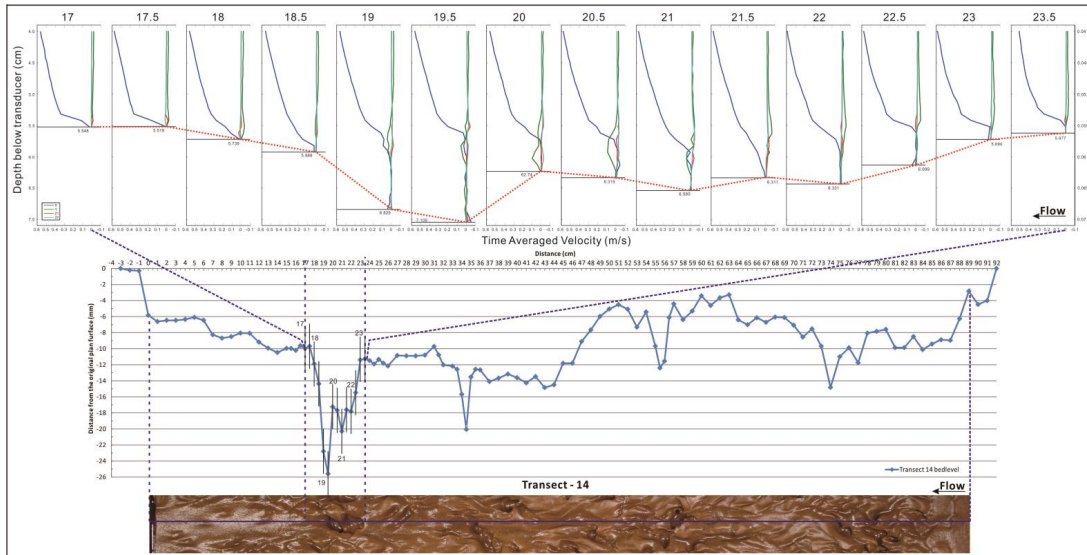


Figure 3.19 One series of the velocity profiles over and within an erosional feature measured by Vectrino-II ADV.

3.3 Summary

A series of methodological advances for the modelling of erosion in mud beds have been introduced here. Critically, these include measurement of both substrate and flow parameters, via vane tool derived shear strength, and UDVP-derived velocity profiles, respectively. In addition to these, bed profiling was utilized to measure the deformation, and then techniques were introduced to stabilize the bed, enabling later detailed measurement of fluid flow within and external to the erosive bedforms using a profiling ADV.

Chapter 4

Cohesive mud bed channel erosion: bedform dynamics and formative processes

4.1 Introduction

This chapter will introduce the results obtained from experiments using terracotta pottery clay. Six experiments, Exp. 0 to 5 have been conducted. Exp. 0 and 5 were conducted for examine whether sediment-free flow can produce erosive features on cohesive clay beds. Exp. 1 to 3 were run to figure out what role undrained shear strength of substrate played in the genesis and development of erosional features. Exp. 4 was conducted to investigate what kinds of erosional features can be produced under the condition of a low flow velocity, low suspended sediment concentration and a medium hard cohesive bed. The main objective of these experiments is to examine whether the classic flute marks and other erosional features produced in the plaster-of-Paris bed could be reproduced on the cohesive bed made by natural clay.

4.2 Erosion and bedform development on experimental cohesive mud beds

4.2.1 Experimental setup

The details of the experimental setup have been detailed in methodology chapter (Chapter 3). Here, the key points of Exp. 0 to 5 are briefly introduced again. Experiments 1 to 4 and two experiments, Exp. 0 and Exp. 5, with no sediment in the flow were conducted using terracotta pottery clay to investigate the development of bedforms on cohesive mud beds. The Strength of the experimental substrate varied between experiments (Table 4.2).

Fine-grained silica sand, the mean grain size, D_{mean} , of which is 129 μm , was used in experiments 1-4 (Figure 3.9 in chapter 3), and water sampling for suspended sediment concentration (SSC) calculation was conducted 2 to 3 times during each run (Table 3.7 & Figure 3.10 in Chapter 3). Flow velocity data were monitored and measured by UDVP. The water depth, H , was 14 cm over the false floor, $H_{1/2}$ flow velocity ($v_{H_{1/2}}$) over the mud bed was 0.90-0.95 ms^{-1} , and the flow velocity 0.6 cm above the mud bed was 0.50-0.65

ms^{-1} except Exp. 4 in which the flow velocity parameters are different from the first three experiments (Figure 3.13 in Chapter 3). The details of shear velocity and shear stress of Exp. 1, 2, 3 and 5 are shown in Table 4.1. Details of Exp. 4 with the medium clay bed will be given later in section 4.4. After each phase, plan view photos were taken and bathymetric bed-scanning was conducted using a Seatek Ultrasonic Scanning System. The raw data were then processed using Matlab to extract the quantified 3D bedform profiles.

Here the influence of substrate strength on erosion rates and bed morphodynamics is examined by adjusting the shear strength of the substrate whilst maintaining constant flow conditions. In order to adjust the shear strength of the clay, they were left to soak for different periods of time (see Section 3.2.3 in Chapter 3). The undrained shear strength of the experimental clay was measured using a hand vane meter (Figure 3.3 in Chapter 3).

The clay used in Exps. 1 and 2 was in its original condition and did not undergo pre-soaking prior to being placed into the flume. The initial undrained shear strength measured of the raw terracotta pottery clay before running was 19 kPa. The same clay was soaked to reach specific strength, 6.5-7 kPa for Exp. 3, and 9 kPa for Exp. 4, and Exp. 5, respectively (Table 4.2). During the preparation, the clay was exposed to air for less than an hour. After the tray was moved into the flume, the flume was filled over a period of 5 minutes to reach a water depth over the clay bed of 14 cm.

Table 4.1 Shear velocity u^* (ms^{-1}) and basal shear stress τ (Nm^{-2}) measured at 6 mm above the experimental bed in Exps. 1, 2, 3 and 5. For details of the position of the UDVP probes, please refer to Section 3.2.5 in Chapter 3.

| Exp. 1 (min) | shear velocity u^* (ms^{-1}) | Shear stress τ (Nm^{-2}) | Exp. 2 (min) | shear velocity u^* (ms^{-1}) | Shear stress τ (Nm^{-2}) | Exp. 3 (min) | shear velocity u^* (ms^{-1}) | Shear stress τ (Nm^{-2}) | Exp. 5 (min) | shear velocity u^* (ms^{-1}) | Shear stress τ (Nm^{-2}) |
|-----------------|---|--|-----------------|---|--|-----------------|---|--|-----------------|---|--|
| T30 | 0.059 | 3.460 | T30 | 0.066 | 4.386 | T30 | 0.042 | 1.784 | T30 | 0.050 | 2.454 |
| T60 | 0.059 | 3.537 | T60 | 0.069 | 4.794 | T60 | 0.044 | 1.968 | T60 | 0.059 | 3.455 |
| T120 | 0.068 | 4.625 | T120 | 0.071 | 5.029 | T120 | 0.041 | 1.706 | T120 | 0.056 | 3.146 |
| T180 | 0.070 | 4.957 | T180 | 0.070 | 4.932 | T180 | 0.043 | 1.833 | T180 | X | X |
| T240 | 0.074 | 5.431 | T240 | 0.071 | 5.028 | T240 | 0.042 | 1.772 | T240 | 0.061 | 3.669 |
| T300 | 0.073 | 5.322 | T300 | 0.075 | 5.563 | T300 | 0.046 | 2.128 | T300 | X | X |
| T360 | 0.061 | 3.701 | T360 | 0.073 | 5.401 | T360 | 0.056 | 3.147 | T360 | 0.063 | 3.982 |
| T420 | 0.073 | 5.383 | T420 | 0.074 | 5.489 | T420 | 0.069 | 4.740 | T420 | X | X |
| T480 | 0.074 | 5.528 | T480 | 0.077 | 5.963 | T480 | 0.073 | 5.398 | T480 | 0.058 | 3.322 |
| T540 | 0.076 | 5.828 | T540 | 0.076 | 5.720 | X | X | X | T540 | X | X |
| T600 | 0.077 | 5.873 | T600 | 0.078 | 6.114 | X | X | X | T600 | 0.059 | 3.538 |
| T660 | X | X | T660 | 0.081 | 6.518 | X | X | X | T660 | X | X |
| T720 | X | X | T720 | 0.084 | 7.088 | X | X | X | T720 | 0.058 | 3.370 |
| T780 | 0.076 | 5.705 | T780 | 0.082 | 6.730 | X | X | X | T780 | X | X |

Table 4.2 Strength of the experimental substrate for all experiments. Exp. 0: hard pottery clay bed; Exp. 1: hard pottery clay bed; Exp. 2: hard pottery clay bed; Exp. 3: soft pottery clay bed; Exp. 4: medium pottery clay bed; Exp. 5: medium pottery clay bed.

| | Terracotta pottery clay | | | | | |
|--------------------------------|-------------------------|-------|-------|-------|--------|--------|
| | Exp.0 | Exp.1 | Exp.2 | Exp.3 | Exp.4 | Exp.5 |
| | Hard | Hard | Hard | Soft | Medium | Medium |
| Undrained shear strength (kPa) | 19 | 19 | 19 | 6.5-7 | 9 | 9 |

Exp. 1 was stopped at 15-minute intervals in the first 300 minutes, 30-minute intervals from 300 minutes to 420 minutes, and then 60-minute interval from 420 minutes to the end at 780 minutes (Table 3.1 in chapter 3). Exp. 2 was a repetition of Exp.1 in order to assess the repeatability of bedform patterns. One difference compared to Exp. 2 were the time intervals between each run. The time intervals between successive phases in Exp. 2 were 60 minutes, except in the first 60 minutes, during which the time intervals were 15 to 30 minutes. All the other experimental conditions were the same as those of Exp. 1. The time interval of Exp. 3 is 30 min between most of the runs (Table 3.2 in Chapter 3). Exp. 4 was stopped at 30-min intervals in first 120 minutes, 60-min from 120 to then end of the experiment, 960 minutes (Table 3.2 in Chapter 3). In Exps. 1 and 2, 2.5 kg of fine-grained silica sand was introduced into the water every 15 minutes (Figure 3.9 in chapter 3), and water sampling was collected 2 to 3 times during each run (Table 3.7 & Figure 3.10 in chapter 3). In the rest of the experiments, 1.5 kg of sand was added into the flow because sand supply of 2.5 kg every 15 min was more than the sediment capacity of the flow induced the bed cover effect in the later stages of Exps. 1 and 2 (Table 3.7 & Figure 3.10 in chapter 3).

4.2.2 Mud erosion in sediment-free flows

Before conducting experiments under sediment-laden flow, an experiment (Exp. 0) was conducted using terracotta pottery clay and clear water flow without adding sand. This experiment explored whether bedforms on hard terracotta clay bed would initiate and develop under pure fluid stressing. Exp. 0 was run before the construction of the ~1 metre long clay tray which was used throughout experiments 1 to 8 (Figure 3.12 in Chapter 3). The clay

was placed in a slot between two sections of false floor and the surface of it was flattened to the same level as the surface of the false floor. The dimension of this clay bed was approximately 30 cm long and 30 cm wide. The clay used in this experiment was in its original condition with undrained shear strength of 19 kPa and was not soaked in the water in advance. This Exp. 0 was stopped at 15-minute intervals for the whole 120 minutes. Photos were shot twice after the first 15 minutes and after 60 minutes (Figure 4.1). After conducting Exp. 1 to Exp. 4, one experiments with medium hard terracotta pottery clay, Exp. 5, was been conducted for the same duration as the other experiments (Exps. 1-4) in order to further examine the absence of abrasion (Figure 4.2). The clay was pre-soaked in order to get the undrained shear strength of 9 kPa (Table 4.2).

After running the flume with clear water for 120 min, except for some small marks, the whole clay bed in the sediment-free experiments (Exp. 0 and Exp. 5) was almost unchanged and remained flat. Compared with the differences between the beds after the same period in Exp.1 and Exp. 2, the difference between two beds in the sediment-free experiments is very small (Figure 4.1). The condition of the clay bed in Exp. 5 shows that the sediment-free flow generally cannot alter a cohesive clay bed with this shear strength. In order to establish sediment-free conditions for Exp. 5, the whole flume system was cleaned thoroughly. Almost all the sand accumulating in the both ends of flume was cleaned out manually and high velocity flow was recirculating for removing the sands accumulating in the pipe system of the flume. Most of the sands were removed, but it is still impossible to clean every particle. Therefore, only a very few particles remained in the flume system. Never-the-less, this has not significantly affected the experimental results (cf. Figure 4.1 and Figure 4.2).

Compared with the erosion rate of Exp. 1 to 4, after the whole duration of Exp. 5, the experimental bed almost did not change except for a few small marks appeared in the down stream part of the clay bed after the first 30 minutes of the experiments (Figure 4.2). In the rest of nearly 700 minute long run, they did not develop, enlarge, or elongate to any other form over time and the rest of the clay bed barely changed in the whole 720-min run (Figure 4.2). These small marks might be produced by those few sand grains remaining in the flume system. The reason why they stopped developing might be because after each time interval, when the water was drained out, the remaining sands were drained out along with the water again and again

which meant that the quantity of the sands remaining in the flume became less and less.

In conclusion, the results from both sediment-free experiments, demonstrate that clay beds with shear strength of 9 to 19 kPa, show almost no change and the pure fluid stressing does not occur. In contrast, the experiments with suspended sediments indicate that sediment plays an important role in the genesis and evolution of erosional bedforms on cohesive clay beds.

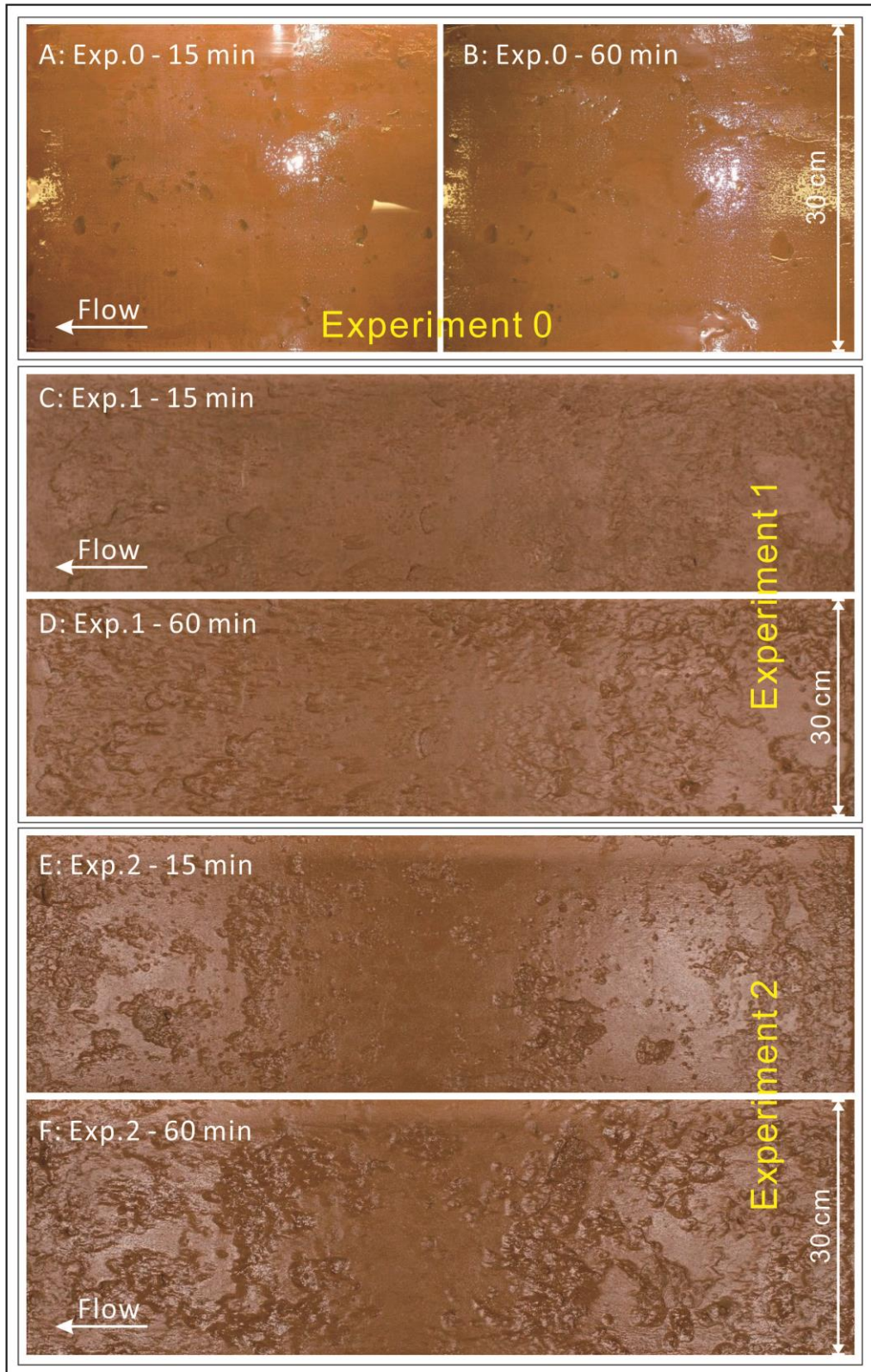


Figure 4.1 A & B: Planform images of pottery clay beds of Exp. 0 under the effect of recirculating clear water after 15 minutes and 60 minutes, respectively. C, D, E & F: Planform images of pottery clay beds under the effect of recirculating sediment-laden flow after 15 minutes and 60 minutes, respectively. C & D are clay beds of Exp. 1; E & F are clay beds of Exp. 2. All the beds are 30 cm wide. Flow is from right to left.

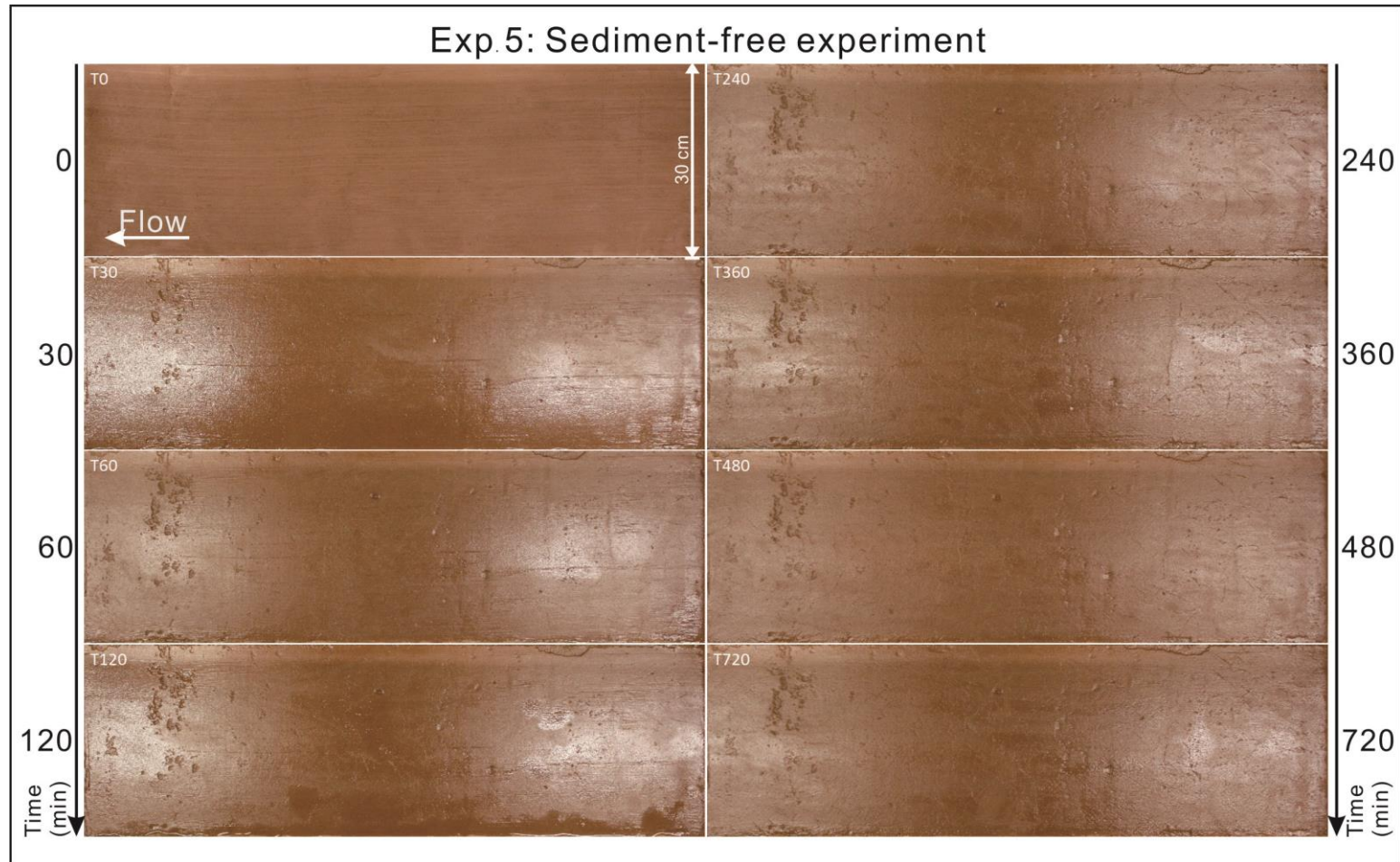


Figure 4.2 Experiment 5 conducted using sediment-free flow and terracotta pottery clay with undrained shear strength of 9 kPa. Flow from right to left. All the clay beds are 30 cm wide.

4.3 Overall development of clay beds in each of the runs with suspended sediment

4.3.1 Evolution of bedforms of Exp. 1 and Exp. 2

Exp. 1 and Exp. 2 were conducted under the same boundary conditions and with same experimental parameters. As mentioned before, the reason for conducting Exp. 2 is in order to verify; (1) whether the observed bed changes are repeatable, and (2) if different time intervals of flow running can affect bed erosion rate and extent. The bedforms monitored in each time interval demonstrate that the bed evolution and the erosional bedforms of the experiments are repeatable and reliable under the controlled experimental conditions (Figure 4.3 and Figure 4.6).

After the flume was run with sediment-laden flow for first 15 minutes, a clear change in the bed surface can be seen in both Exp. 1 and Exp. 2, in contrast to the previous clear water experiments (Figure 4.3). A large number of erosional marks are distributed throughout all the experimental clay beds, especially at both ends of the bed. Some marks could also be found in the middle part of the bed, but are not distributed as much as in both ends. At this moment, most marks have just been formed and still could not be identified as any kind of defined erosional features. The marks appearing within the first 15 minutes are very shallow with depths of 0.1 - 0.2 cm and varying widths. These erosional marks were mainly eroded downwards in the first 15 minutes. The rims of most of them were closed and relatively clear. The next 45 minutes witnessed the start of deepening and elongating of erosional marks. The bedforms in the T60-bed were obviously elongated from their previous forms as compared to the T15-bed (Figure 4.3). Some tiny approximate circular marks transformed to small shallow flute marks. Their former-closed distal rim broke to produce an open end with flanks flaring towards downstream. The depressions in their proximal ends deepened and the length of them elongated to 2 – 5 cm.

During T15 to T120, the small marks and shallow flute marks deepened, elongated and began to connect with each other to form compound features. With the elongation of the marks, the distal rims of most of the marks transformed from sharp to round. The stoss-side slope of these marks was gentler than the lee-side slope of them. Looking at the bedform planform at T120, the development pattern of the upstream end of the experimental mud bed presented different erosional rates compared to the downstream end of it (Figure 4.4). Most of the depressions in the upstream end presented clear

rims, no matter what kind of erosional features they were. Narrow straight flute marks and comet-shaped flute marks formed and connected with each other with time at the upstream end. The quantities of erosional features decreased from the upstream to the middle bed and increased in the downstream part again. The main features in the downstream part were short straight or sinuous parallel sided furrows, potholes and some complex compound features. After referring to these erosional features, the T120-bed can be considered as an embryonic form of bed erosion evolution.

The period from T120 to T480 can be regarded as the peak phase at bedform development with the most obvious changes of the mud bed configuration. The bed changed severely even in the 60 minutes from 120-min to 180-min run. The edge of the downstream end was seriously eroded, and then the erosion began to spread towards the upstream end. The outline of each kind of erosional feature became clear. A kind of wavy feature forms on the downstream part of the bed (Figure 4.4 & Figure 4.5: white squared areas), showing a prominent proximal rise with a steep stoss-side slope and gentle lee-side slope. In Exp. 1, although some of the waves were connected with each other, the separated heads of them were clearly visible (Figure 4.4: white arrowed areas). In Exp. 2, the wavy shape of them was more obvious near the middle of the bed, because most of these features are connected. The head part of the waves was only separated by short furrows (Figure 4.4: yellow curves). Meanwhile, the short sinuous furrows developed more with rounded parallel-sided rims. After 240-minutes, most of the adjacent solo short furrows started to link end to end by cutting through the space between them to form long sinuous furrows. The broad flutes combined with each other by cutting through the shared rims. The most remarkable features observed in T300-beds were that one straight long parallel-sided gully formed in the middle part of the bed and 3 such gullies developed in the middle of the bed and both sides of the bed near the glass walls. Such a situation might be caused by the effect of upwelling flow induced by the restriction of the experimental flow by the flume sidewalls (Albayrak and Lemmin, 2011; McLelland et al., 1999; Vachtman and Laronne, 2011). The next 60 minutes between 300-min to 360-min witnessed the sign of the start of polishing (planing off) of the erosional features that had formed in the first 300 minutes (Figure 4.5). The prominent parts of the erosional features, such as the knob of the wavy features, began to be polished. In the first 360 minutes, the mean vertical erosion of the experimental beds was approximately 0.8 cm. The broad shallow flutes at the upstream end combined with each other making narrower sinuous flutes.

In the Exp. 1 bed, some long parallel-sided furrows emerged on the bed which crossed the middle part of the mud bed (Figure 4.5 – T360 & T450). In Exp. 2, two straight wide grooves formed after T360. One is along the right hand side (as looking downstream) of the glass wall of the flume, and the other is at the central axis of the mud bed.

The beds were eroded severely in the 60 minutes from T360 and T420. The most dramatic change in these experiments happened in the 60 minutes between T420 and T480 (Figure 4.5). The changes started from the downstream end first, in which most of the flute marks disappeared. In Exp. 1, the projecting/crest part of flute marks had a tendency to be smoothed down after T360. The 60 minutes from T420 to T480 led to almost nothing remaining at the downstream end. In Exp. 2, only two relatively deeper grooves still remained. The upstream end was eroded as well, though erosion was not as great as that at the downstream end. Except for two big ribbon-like deeper flute groups, the right hand one and the left hand one along the glass walls of the flume and the one at central axis of the upstream end were eroded seriously.

From T480 to T660, the rate of erosion of the bed slowed down. The entire clay bed was polished to a very smooth surface again. After T660, the smooth bed almost stopped changing any more, although the sediment-laden flow still kept recirculating above it (Figure 4.6).

These experiments demonstrated that (I) cohesive mud beds barely erode under the influence of sediment-free flow; (II) the development of bedforms on these cohesive mud beds can be divided into 4 stages: (1) the initiation stage of erosion with the forming of small erosional marks; (2) bedform development stage with transformation from small erosional marks to shaped flutes or furrows; (3) bedform developed stage with bed full of developed flute marks and furrows; and (4) the final stage of progressive erosion and flattening of the bed due to it cutting down below the fixed points of the false floor, and eventually filling with sand; (III) the erosion rate of the two ends of the mud beds is higher than that of the middle part of the bed. On the other hand, the result of the two of experiments shows that the order of the mud bed change process is not an accidental event, but is repeatable.

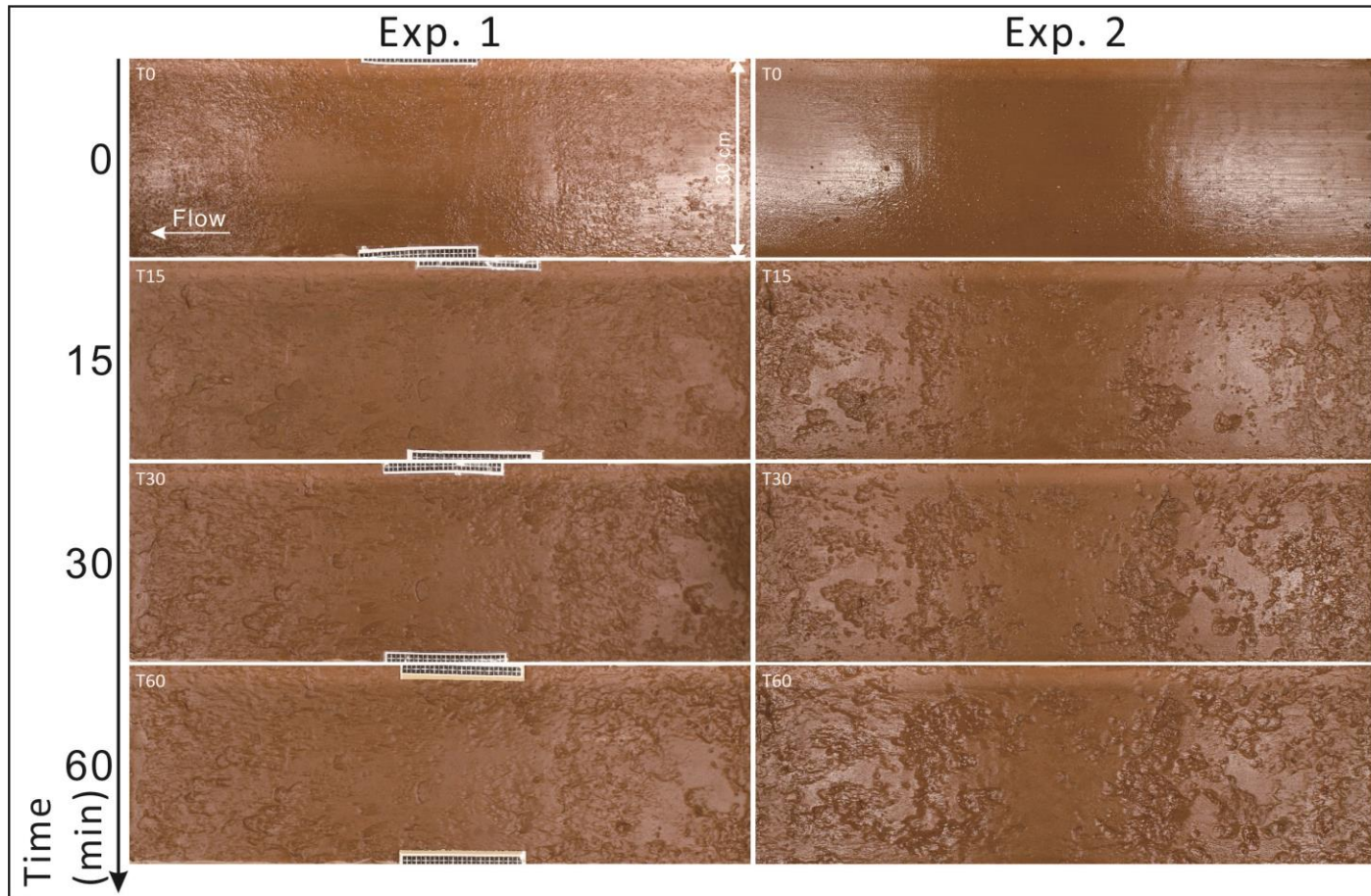


Figure 4.3 Experimental beds of Exp. 1 and Exp. 2: T0 to T60. Each label on beds of Exp. 1 contains 13 black squares with white crosses, each of which is 1.0 cm long and 1.0 cm wide. Flow from right to left. All the beds are 30 cm wide.

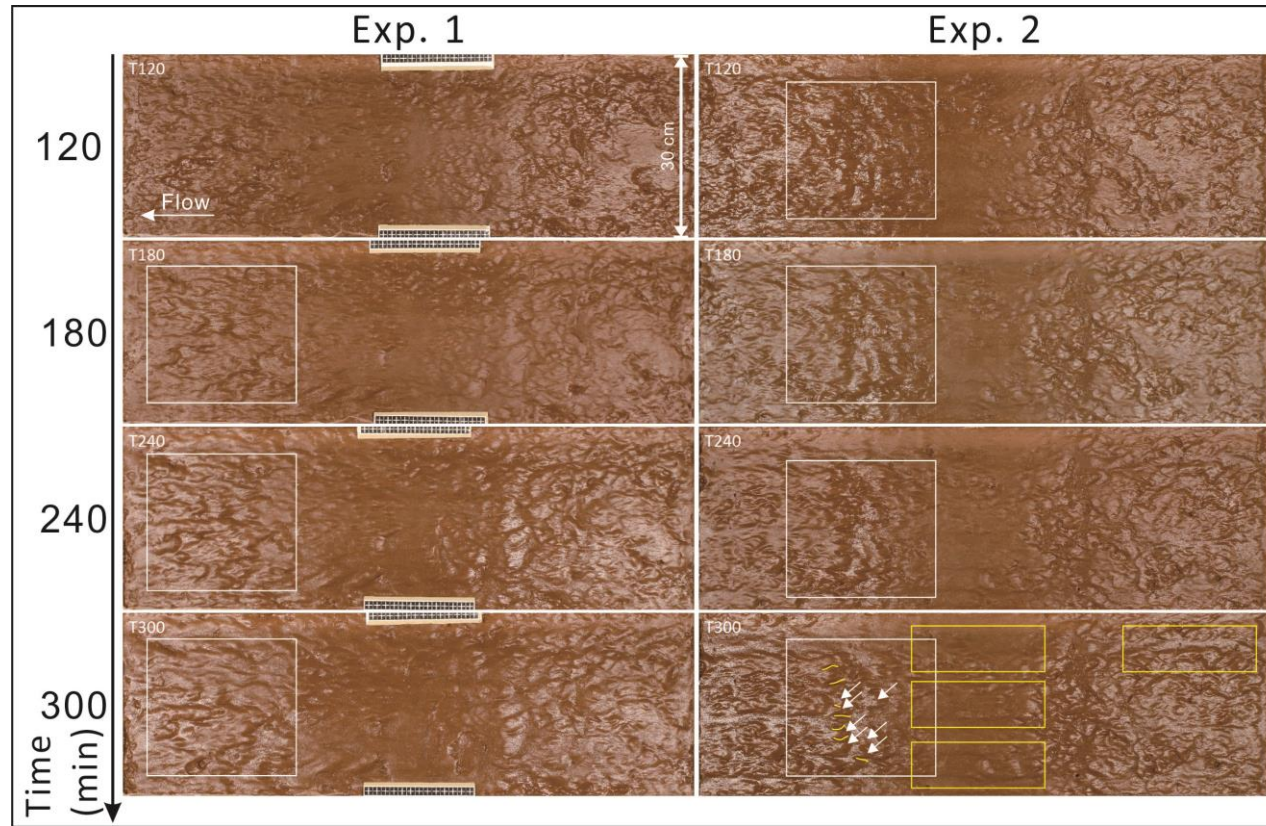


Figure 4.4 Experimental beds of Exp. 1 and Exp. 2: T120 to T300. Each label on beds of Exp. 1 contains 13 black squares with white crosses, each of which is 1.0 cm long and 1.0 cm wide. Flow from right to left. All the beds are 30 cm wide. The white squares tag the wavy features. The white arrows point the heads of wavy features. Yellow curves represent the short sinuous furrows on the beds. Yellow rectangles tag the gullies.

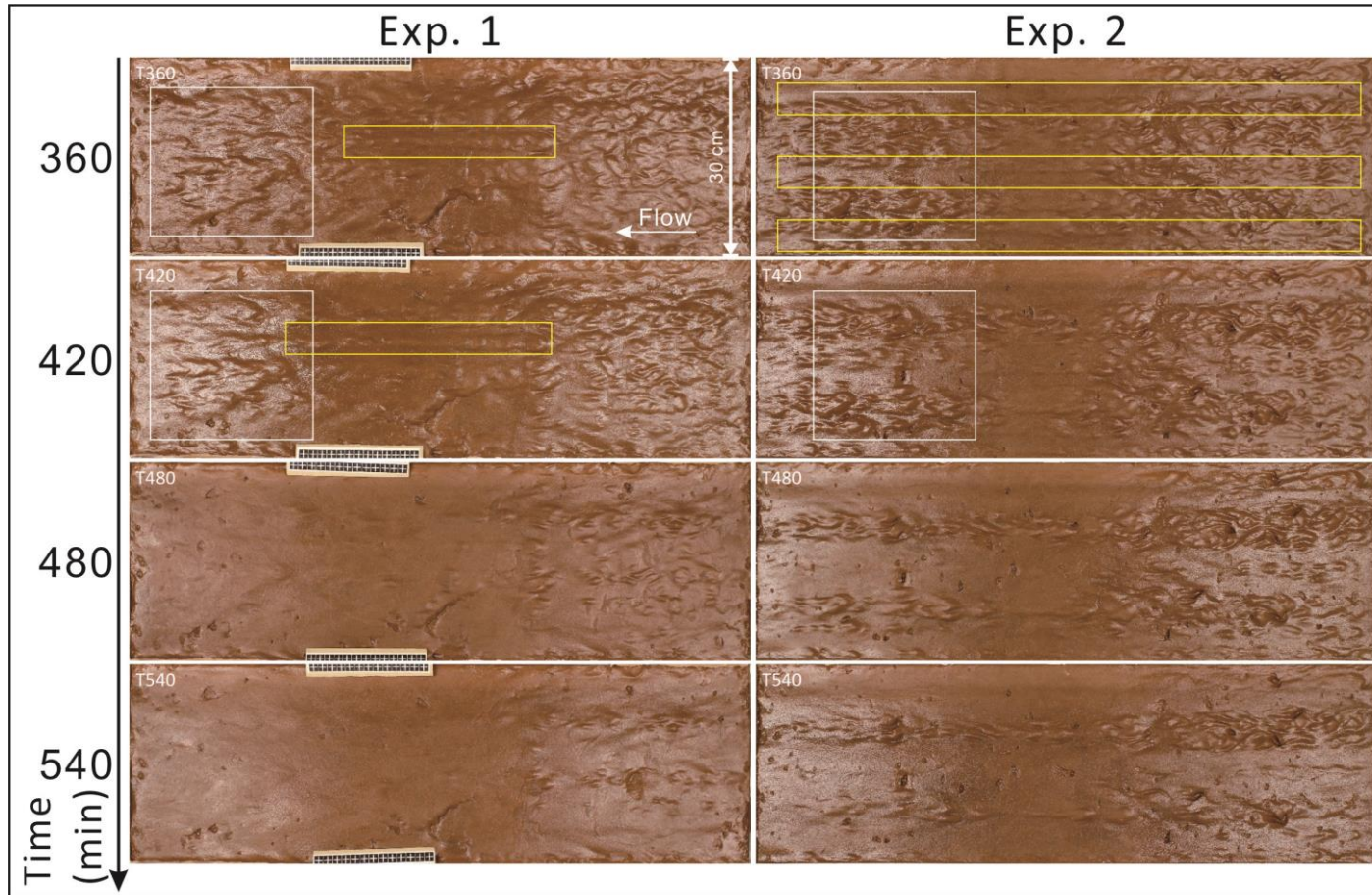


Figure 4.5 Experimental beds of Exp. 1 and Exp. 2: T360 to T540. Each label on beds of Exp. 1 contains 13 black squares with white crosses, each of which is 1.0 cm long and 1.0 cm wide. Flow from right to left. All the beds are 30 cm wide. The white squares tag the wavy features. Yellow rectangles tag the gullies.

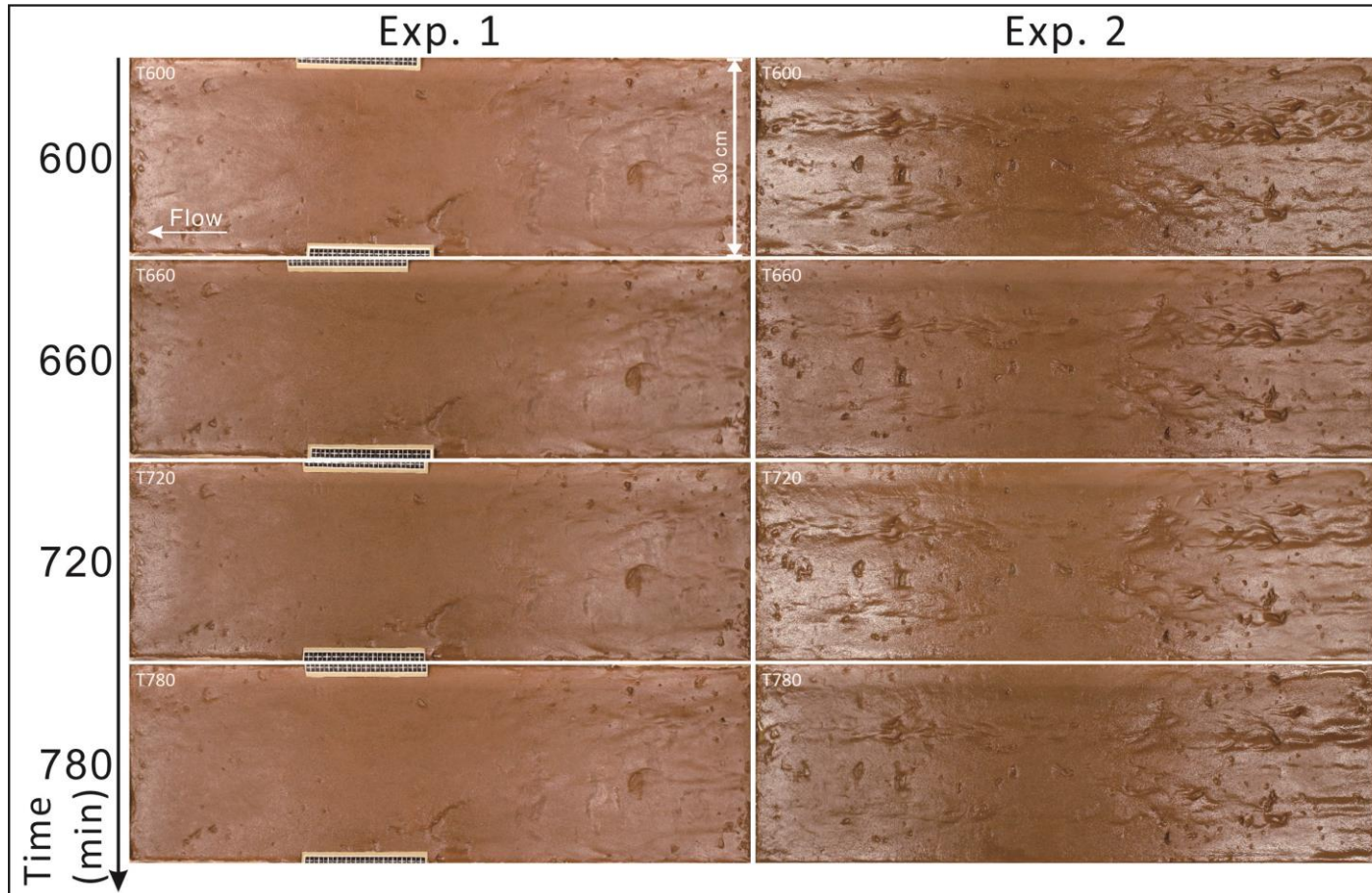


Figure 4.6 Experimental beds of Exp. 1 and Exp. 2: T600 to T780. Each label on beds of Exp. 1 contains 13 black squares with white crosses, each of which is 1.0 cm long and 1.0 cm wide. Flow from right to left. All the beds are 30 cm wide.

4.3.2 Comparison of bedform development over time

Exp. 3 was conducted using terracotta pottery clay as with the other experiments (Figure 4.7; Figure 4.9), but was soaked in water for 110 hours prior to moving into the flume. Therefore it was relatively weak after a long time soaking with an undrained shear strength of 6.5 to 7 kPa. A trowel was used to smooth the surface of the clay bed. However, owing to the 'soupy' condition, the surface is difficult to make completely flat.

The rate of change of the softer mud bed occurred in a shorter time period than on the harder mud bed. The whole evolution process of the soft mud bed completed in 480 minutes of experimental running, but that of the harder mud normally needs 600 minutes (Figure 4.7 to Figure 4.10). Nonetheless, the erosional features came into existence much later (after 120 minutes) than those on the harder substrate (after 30 minutes) and the range of features was much less than those on the harder mud bed. No tiny erosional marks or small flute marks formed on the soft mud bed during the very beginning of the experiments. Some wavy erosional marks grew at the downstream end and, meanwhile, some very small parallel sided straight or sinuous furrows showed on the upstream end of the mud bed after 120-min run (Figure 4.7 & Figure 4.9: red squared area). The form of the wavy erosional marks here are very similar to the wavy features observed in Exp. 1 and Exp. 2 after a time of 120 minutes (Figure 4.4). The prominent part of these wavy features had a relative steep stoss-side slope and gentle lee-side slope. The tail of these wavy features faded away to the same level of surrounding areas in the downstream direction and met the prominent part of the next wavy feature following it. Between adjacent prominent parts of the wavy features in the transverse direction, some furrows formed. These flutes and furrows kept cutting down and extending in the downstream direction after the first 180 minutes. These furrows vary from those appearing on the harder substrate. Their rims were rounded and extended slightly outwards instead of being parallel. The upstream proximal end of them was cusped and the downstream end was open, which is very similar to the shape of spindle-shaped flutes. However the depth of middle part of them was uniform. The small furrows widened and elongated to be curved or sinuous. However, the orientation of them was irregular, inclined inwards or outwards, but mainly parallel with the flow direction. Most of the erosional features are in isolated and simple form. In the later stage of experiments, some small deep hollows appeared, mainly on the upstream end of the mud bed with depths ranging from 0.5-1.0 cm. Some of them might be regarded as

potholes which might be initialized by the nonuniformity of the clay induced by manually flattening of the sediment.

In brief, the erosional features on the soft mud bed mainly contain following simple marks: (a) wavy erosional features, (b) small parallel-sided furrows, (c) furrows similar to spindle-shaped flutes, (d) isolated curved or sinuous furrows, (e) potholes. There are several significant differences from the erosional features on soft mud beds with harder mud beds: (a) no tiny erosional marks/pits formed during the beginning stage as observed on the harder clay bed; (b) no broad flutes developed; (c) no broad linear grooves formed as those seen in the harder clay beds; (e) erosional features were present mainly in isolated and simple forms.

Although the physical photos at each time point have already shown the general development process of the bedforms on the experimental clay beds, an elevation colour map of the clay bed for each time point measured by Seatek systems during every time interval demonstrates more quantitative variation in the erosion rate of the clay beds with different shear strength over time (Figure 4.8; Figure 4.10).

The elevation colour maps show that the initial state of Exp. 3 was not as flat as that of Exp. 1 and Exp. 2 (Figure 4.8 & Figure 4.10). The elevation of the downstream end of Exp. 3 clay bed was obviously lower than the remaining part of the bed (Figure 4.8). But this does not affect the investigation of the erosion rate of experimental clay beds with different strength. Throughout the whole evolution of the experimental clay beds of Exp. 1, 2 and 3, the most obvious is that the bed of Exp. 3 is much easier to erode than the bed of Exp. 1 and 2 (Figure 4.8 & Figure 4.10). The duration of the whole erosion process of Exp. 1 and 2 could last for 600 minutes until there was no obvious change happening on the clay bed. In contrast, the bed of Exp. 3 barely changed after only 300 minutes. The erosion rate and processes of Exp. 1 and 2 were very similar. Both beds started to erode even after a short time run, for example 15 minutes or 30 minutes (Figure 4.8). The most severe erosion happened at the downstream edges of both beds. The surface of beds near the downstream edge was cut down by 0.2 to 0.3 cm per 30 minutes in the first 60 minutes (Figure 4.8). The erosion amount decreased to 0.4 cm in the next 60 minutes and 0.1 to 0.2 cm from 120 minutes to 180 minutes (Figure 4.8). In the same period and the same location of the experimental bed of Exp. 3, the erosion rate in the first 120 minutes was 0.1 cm ever 30 minutes. The downstream edge was eroded by only 0.3 cm from 120 minutes to 240 minutes (Figure 4.8). The upstream

end of the clay bed is the area which was eroded slowest for all the beds of Exp. 1, 2, and 3. For all three experiments, after the flume had run for 60 minutes, the area close to the upstream edge was only eroded by 0.1 cm (Figure 4.8). In the following 120 minutes, from 60 minutes to 180 minutes, the upstream edge of the beds of Exp. 1 and 2 were eroded by 0.2 cm and 0.3 cm, respectively. Meanwhile, the downstream edge had been eroded by about 0.5 cm (Figure 4.7 & Figure 4.8). For Exp. 3, the erosion of the upstream edge was 0.3-0.4 cm, which is slightly greater than that of Exp. 1 and 2 (Figure 4.8). In overview, in the first 240 minutes of the experiments, the downstream area of the experimental beds was eroded slightly faster than the upstream area by 0.1 to 0.2 cm in each time point (Figure 4.8). The most obvious change in Exp. 1 and 2 happened between 240 minutes to 360 minutes. The development of bedforms on the T240-bed and T300-bed could be regarded as reaching the peak time with the most visible erosional features. But in the 60 minutes from 300 minutes to 360 minutes, most of the prominent parts of the features in the clay bed began to be polished by 0.2 cm (Figure 4.10). For Exp. 3, the peak time of erosional features forming was from 120 minutes to 180 minutes. In the next 60 minutes, the bed was polished by about 0.2 cm as happened in Exps. 1 and 2 (Figure 4.8). It took 180 minutes to polish the bed by 0.5 cm to the next stable stage for Exps. 1 and 2 from 360 minutes to 540 minutes and in Exp. 3, 120 minutes from 240 minutes to 360 minutes by 0.4 cm (Figure 4.9 & Figure 4.10). After 540 minutes for Exp. 1 and 2, and 360 minutes for Exp. 3, the experimental beds reached a stable stage with most of the prominent parts polished to a point where they have disappeared (Figure 4.9 & Figure 4.10). The beds of Exp. 1 and Exp. 2 were eroded by 0.8 cm to 1.0 cm in 540 minutes until reaching a stable stage (Figure 4.10). The variation of the bed of Exp. 3 is 0.6 cm in the whole period of 300 minutes before it reached the stable stage (Figure 4.10). The notable difference of the erosional process between the harder clay beds of Exp. 1 and 2, and the soft clay bed of Exp. 3 was that the Exp. 3 bed was eroded as a whole with similar erosional rate throughout the whole bed. It did not exhibit the erosion that was observed in Exps. 1 and 2 in which the erosion rate of the downstream end was slightly greater than that of upstream end.

This results show that (1) the strength of the substrate does affect the erosion rate of the cohesive clay bed with all the rest of parameters strictly controlled; (2) the soft mud bed was eroded entirely instead of regionally as happened in harder clay bed; (3) the erosional process of the soft bed was slightly faster than that of harder bed; (4) the total eroded volume of the soft

bed was larger than that of harder clay bed; and (5) different erosive features were observed to form on the soft bed relative to the harder beds, and a wider array of bedforms formed on the harder bed type.

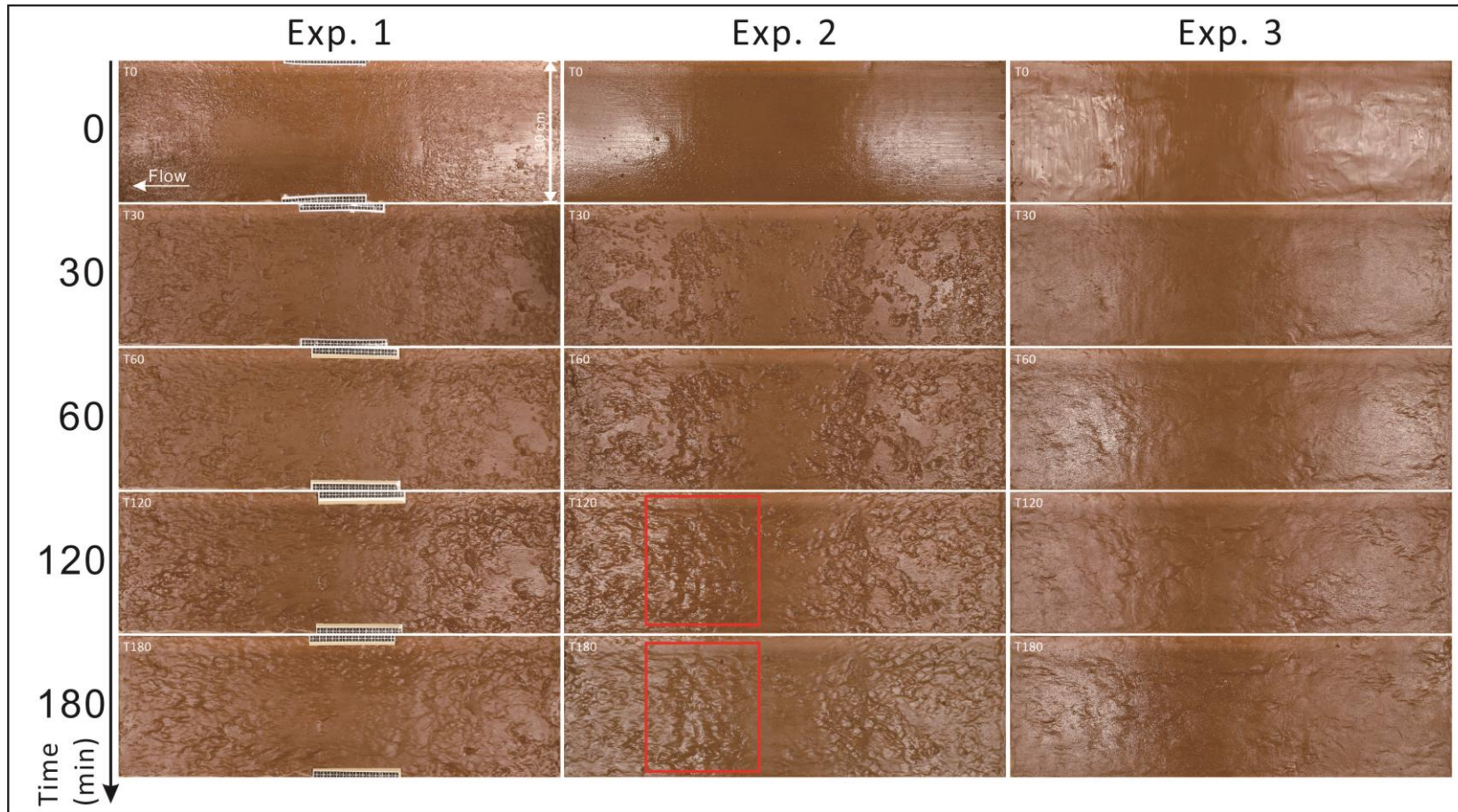


Figure 4.7 Comparison of the clay beds of Exp.1, Exp, 2 and Exp. 3: From the beginning of the experiments to 180 minutes experimental time (T0 to T180). Flow from right to left. Red boxes point the wavy features on the beds of Exp. 2. All the clay beds are 30 cm wide. The dimension of each black box in the scale bar is 1 cm x 1 cm.

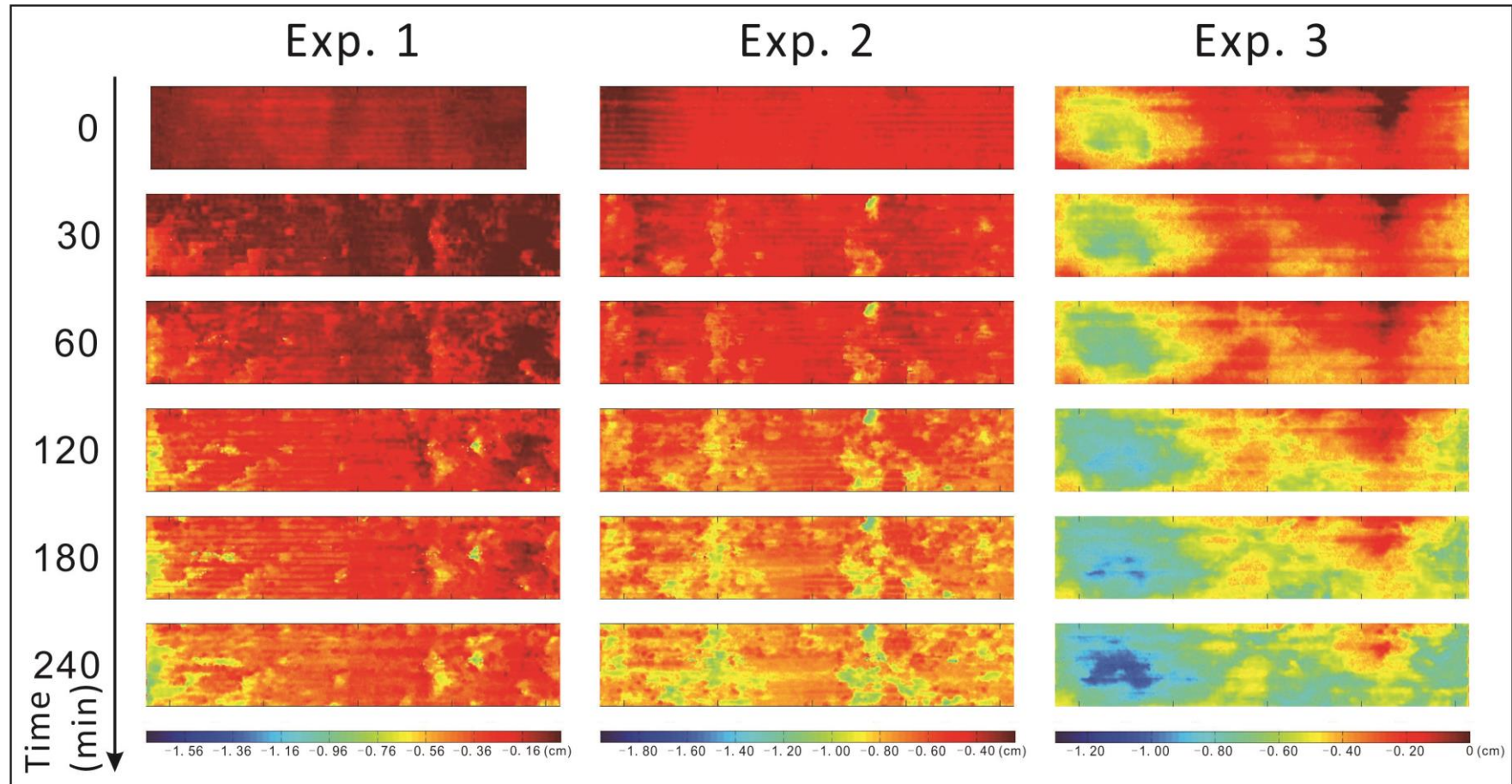


Figure 4.8 3D elevation plots of the experimental beds of Experiment Exp. 1, 2 and 3 (T0 to T240) showing bedform development with time (in minutes). Flow from right to left. Each bed is 90 cm long and 30 cm wide. The colour scale bar is in centimetre.

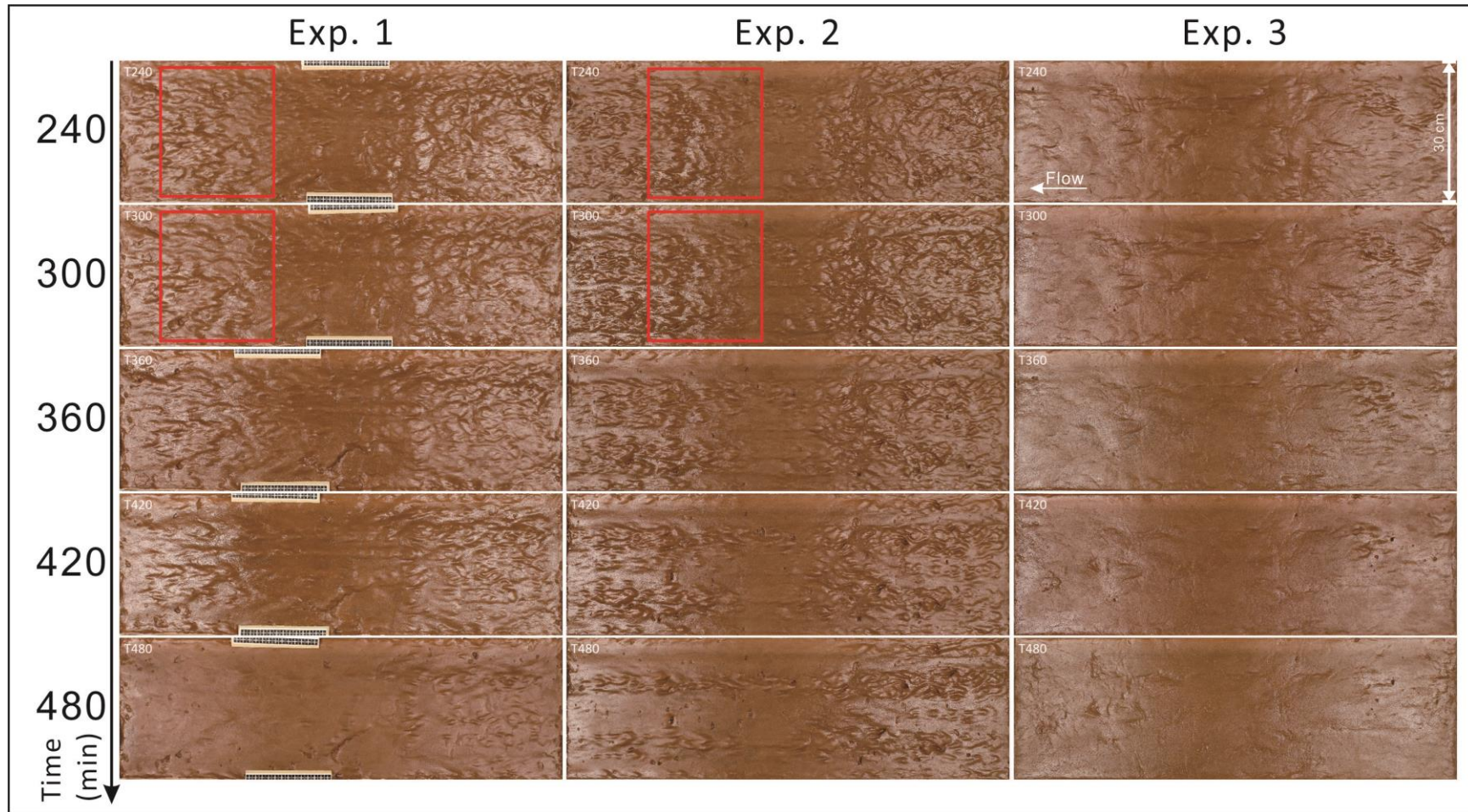


Figure 4.9 Comparison of the clay beds of Exp.1, 2 and 3: From 240 minutes to 480 minutes experimental time (T240 to T480). Red boxes point the wavy features on the beds of Exp. 2. All the clay beds are 30 cm wide.

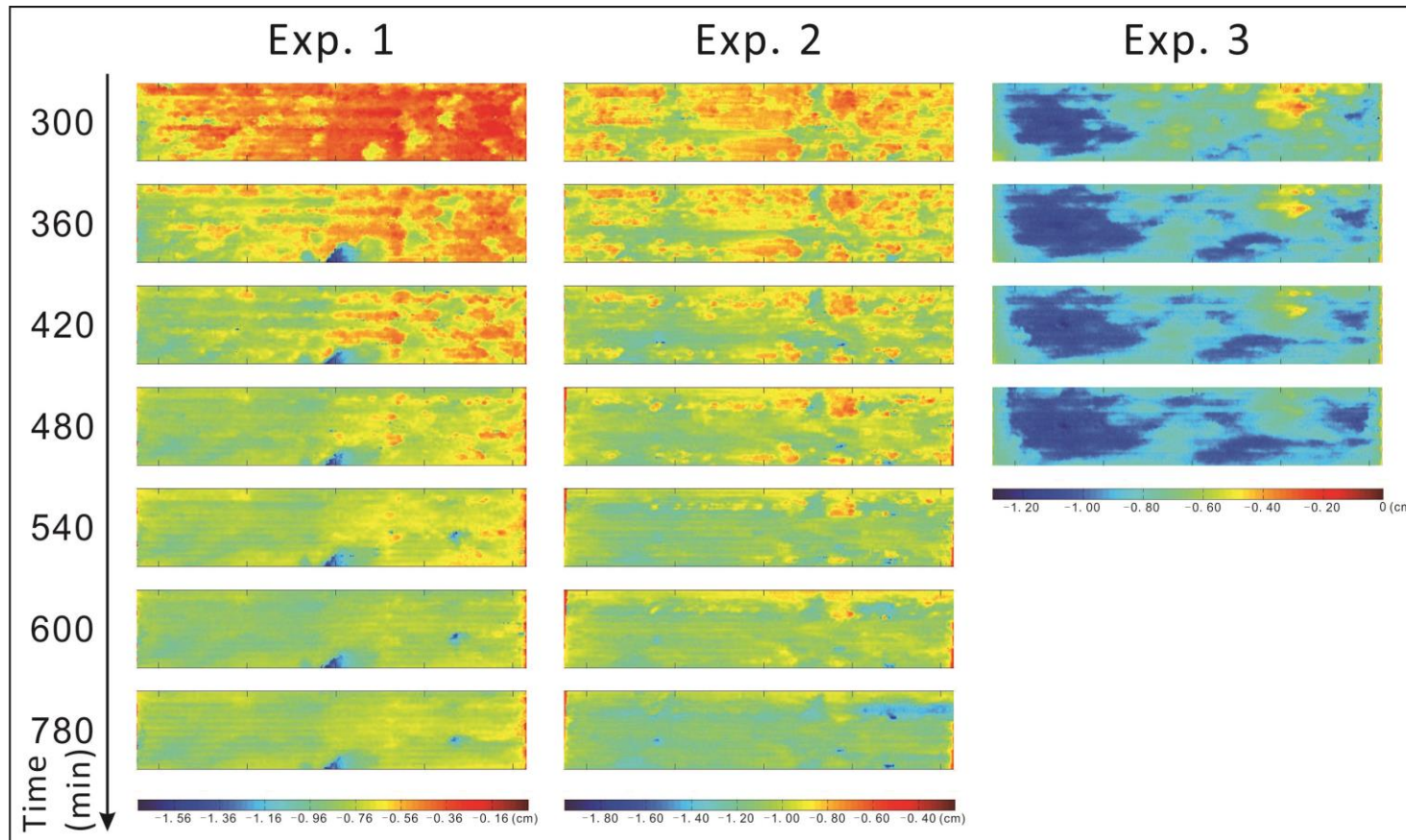


Figure 4.10 3D elevation plots of the experimental bed of Experiment Exps. 1, 2 and 3 (T300 to T780) showing bedform development with time (in minutes). Each bed is 90 cm long and 30 cm wide. Flow from right to left. The colour scale bar is in centimetre.

4.4 Bedforms in experimental cohesive clay beds

Tiny erosional marks and Potholes

Isolated tiny erosional marks initiate at the very beginning of the experiments and then evolve to other features with time. The shape of individual erosional pits (Figure 4.11a) is near circular with clear outline, diameters of 0.25 cm to 0.75 cm and depths ~ 0.1 cm. Most of them were too small and shallow to identify them as defined erosional features. Some relatively deeper pits appear to be symmetrical, whilst others can be observed to have an external tail or differences between the stoss and lee-side slopes within the boundary (Figure 4.11a). A bigger irregular area with a large number of tiny erosional marks in it was regarded as compound erosion marks (Figure 4.11b). The depth of them was ~ 0.2 cm. The shape of the individual tiny erosional marks within the area of the compound ones was indistinct, however the primary individual compound marks can still be clearly identified with clear outlines.

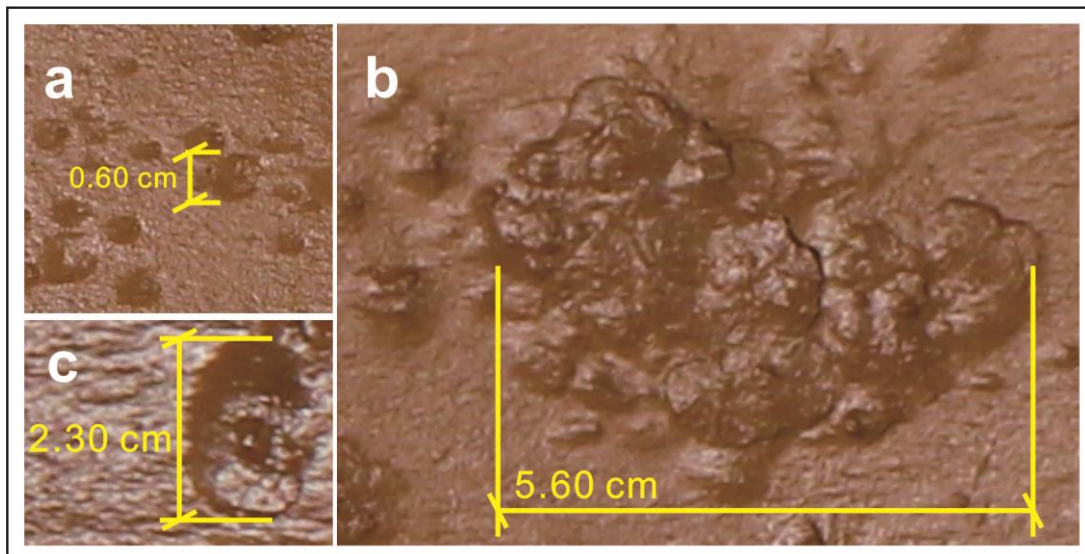


Figure 4.11 Example of tiny erosional marks and potholes formed in the experiments. a. several solo tiny erosional marks observed in Exp. 1 bed; b. compound erosional pits observed in Exp. 2 bed; c. a pothole observed in Exp. 1 bed. Flow from right to left.

Potholes in experimental clay beds were an approximate circular depression without a tail in any direction and were quite variable in terms of diameter. The potholes observed in the experimental beds were symmetrical saucer-shaped depressions, whose diameter is much greater than depth, with depths up to 0.20-0.25 cm. Figure 4.11c shows one of a few potholes on the

experimental beds that exhibits with a secondary smaller pothole on the bottom of the mother pothole. Potholes were relatively rare and were not widely distributed on the experimental pottery clay beds.

Flute marks

The solo flute marks were predominantly parabolic flute marks, but the proximal upstream end is more cusped than Allen (1971a) described (Figure 4.12). They are in approximate symmetric form in longitudinal orientation, but with no lateral furrows, or ridges at least in this initial stage. The lee side of the depression is obviously steeper than the stoss side. The length of the long axis, in the streamwise direction, of these parabolic flute marks is 1.5 ± 0.3 cm. **Flute marks with a median ridge** observed on the experimental bed were symmetric parabolic with a central prominent area (Figure 4.12b). However the central ridge line is not as clear as the ideal flute marks model given by Allen (1971a). **Spindle-shaped flutes** formed on the experimental beds with a cusped proximal rim with steep lee-side depression and parallel lateral rims flaring towards downstream. But, they were not widely distributed in the experimental beds (Figure 4.12c). **Comet-shaped flutes** were very similar with the comet-shaped flutes that formed on the plaster-of-Paris bed of Allen's work (Allen, 1971a, 1982). Although they were short, the length of them was still much greater than the width (Figure 4.12d).

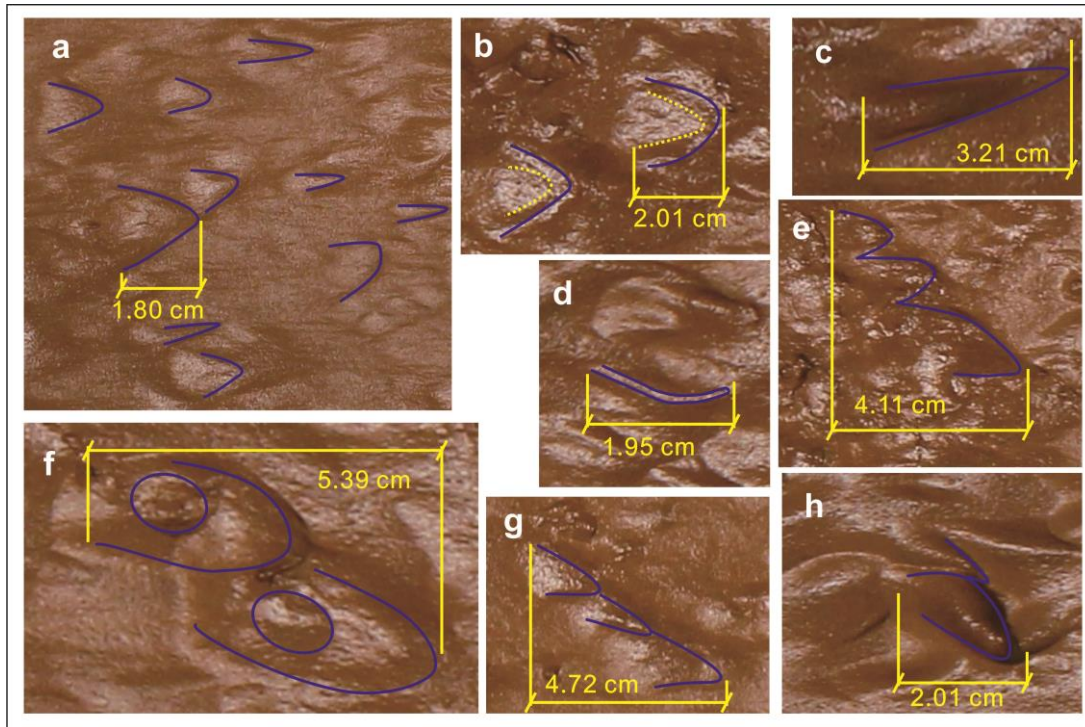


Figure 4.12 Typical forms of different type flutes observed in the experiments. a. Solo flute marks from Exp. 1; b. Flute marks with median-ridge from Exp. 2; c. Spindle-shaped flute marks from Exp. 2; d. Comet-shaped flute marks from Exp. 2; e. Compound flute marks from Exp. 1; f. Flute marks with internal structures from Exp. 1; g. Flute marks with external structures from Exp. 2; h. curved flutes with secondary external furrows from Exp. 2. Flow direction is from right to left.

Some bigger depressions can be observed, these formed by linking of adjacent solo flutes. In these kind of depressions, sometimes the outline of solo flutes can still be recognized. These bigger irregular depressions were treated as **compound flutes** (Figure 4.12e). The compound flutes do not have a typical shape. The width of them range from 1.4 - 2.6 cm (Figure 4.12e). In the category of compound flutes, **flutes with internal and external secondary structures** are two important forms (Figure 4.12 f & g), as described by Allen (1971b). **Flutes with internal secondary structures** formed in a variety of styles. Figure 4.12f illustrates two adjacent flutes containing smaller secondary structures - potholes. Other examples had smaller flute marks close to one rim inside the primary flute marks. **Flutes with external structures** included linear forms with one or two sub-flutes developed alongside one rim of the primary flutes (Figure 4.12g). **Flutes with secondary external furrows** (Figure 4.12h) appeared in the later stage of development of the mud bedforms. Most of them were asymmetric,

but still have a tail extending toward downstream. The depression on their upstream proximal end is much deeper than the flutes developed in the earlier stage of the experiments. The relative mean depth of them is 0.4-0.6 cm.

Furrows

A wide variety of different types of furrow were formed in the experiments: long parallel furrows, curved furrows, and sinuous furrows (Figure 4.13a & b). Some of them are associated with secondary structures. Some more complex composite features from multiple furrows were also observed, for example bifurcating furrows, and convergent furrows.

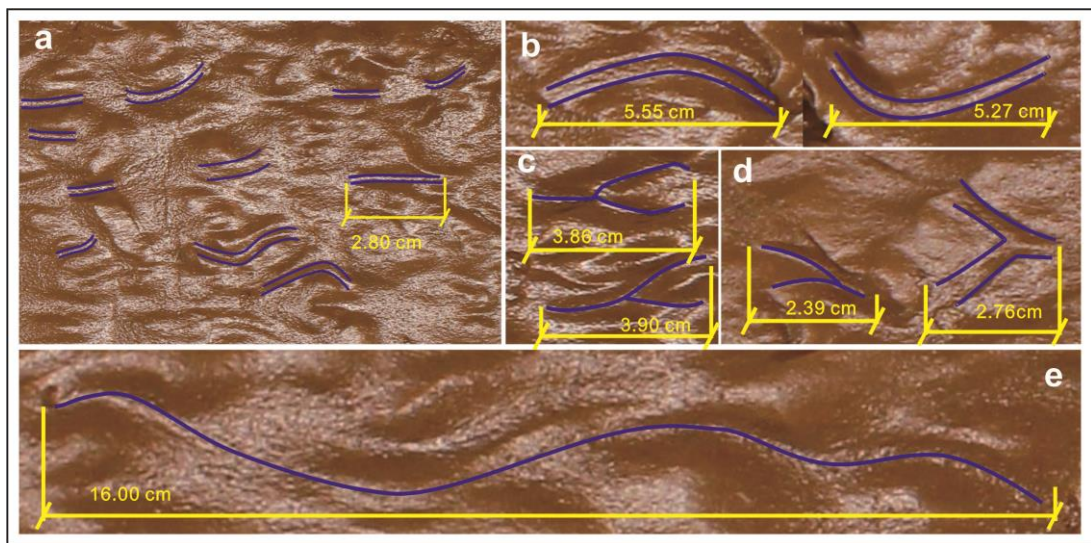


Figure 4.13 Furrows formed in the experiments. a. slight curved short furrows from Exp. 1; b. long curved furrows; c. compound convergent furrows; d. bifurcating furrows; e. long sinuous furrows. b-e from Exp. 2. Flow direction is from right to left.

From the initial stage of furrow formation in the experimental beds, most of them were long curved furrows (Figure 4.13b) with the length of them (1.0 - 16.0 cm) much greater than their width. Although the general orientation of furrows was towards the downstream, the furrows always curved or were sinuous to some extent with parallel-sided rims. Sinuous long parallel-sided furrows formed in the later stages of the experiments by the connection of a train of elongated curved furrows in line end to end (Figure 4.13e). Some relatively complex composite features were formed by the combination of multiple isolated furrows with time, such as convergent furrows or bifurcating furrows (Figure 4.13c & d). According to the definition of short furrows (Allen, 1982; Richardson and Carling, 2005), this kind of erosional feature was

missing in the current experiments. Almost no furrows were ellipse saucer-shaped depressions with length twice as long as their width. The strict straight furrows were also not found in the experimental mud beds.

Broad gullies

A series of features that can extend across the whole experimental bed were defined as broad gullies (Figure 4.14). Broad gullies that are mainly straight with irregular parallel-sided rims formed in Exp. 1 and Exp. 2, after ~300-min of run time (See Section 4.2.1). The length (30 - 80cm) and width (2 - 3 cm) of the gullies was always much greater than those of the furrows. The bottom surface of each broad gully is primarily flat and smooth with almost no defects. Normally, gullies developed on the longitudinal central axis of the bed or in the area close to the flume walls. It appears that the erosion rate is much higher than that in other bedforms. This feature might be caused by down-welling of secondary flow cells derived from anisotropy of turbulence caused in part by the presence of side walls (Albayrak and Lemmin, 2011; McLelland et al., 1999; Vachtman and Laronne, 2011).

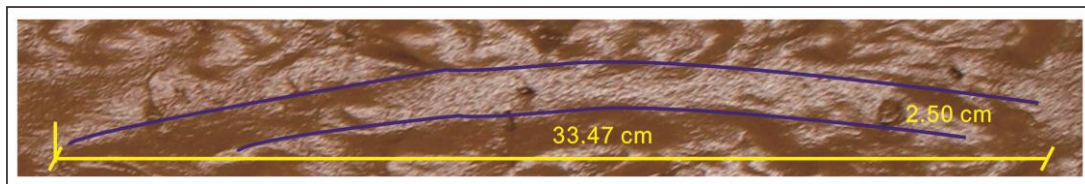


Figure 4.14 A long broad gully formed in Exp. 2. Flow direction is from right to left.

4.5 Experiments with medium hard clay bed

Exp. 4 was conducted using the medium hard mud bed with sand that had previously deposited in the pipe of the flume, and a lower mean flow velocity of about 0.8 ms^{-1} . The different settings of this experiment in comparison to Exps. 1 to 3, led to erosional features in the medium hard mud bed that were quite different to those on harder or softer clay beds. The details of the differences are described below (Figure 4.15).

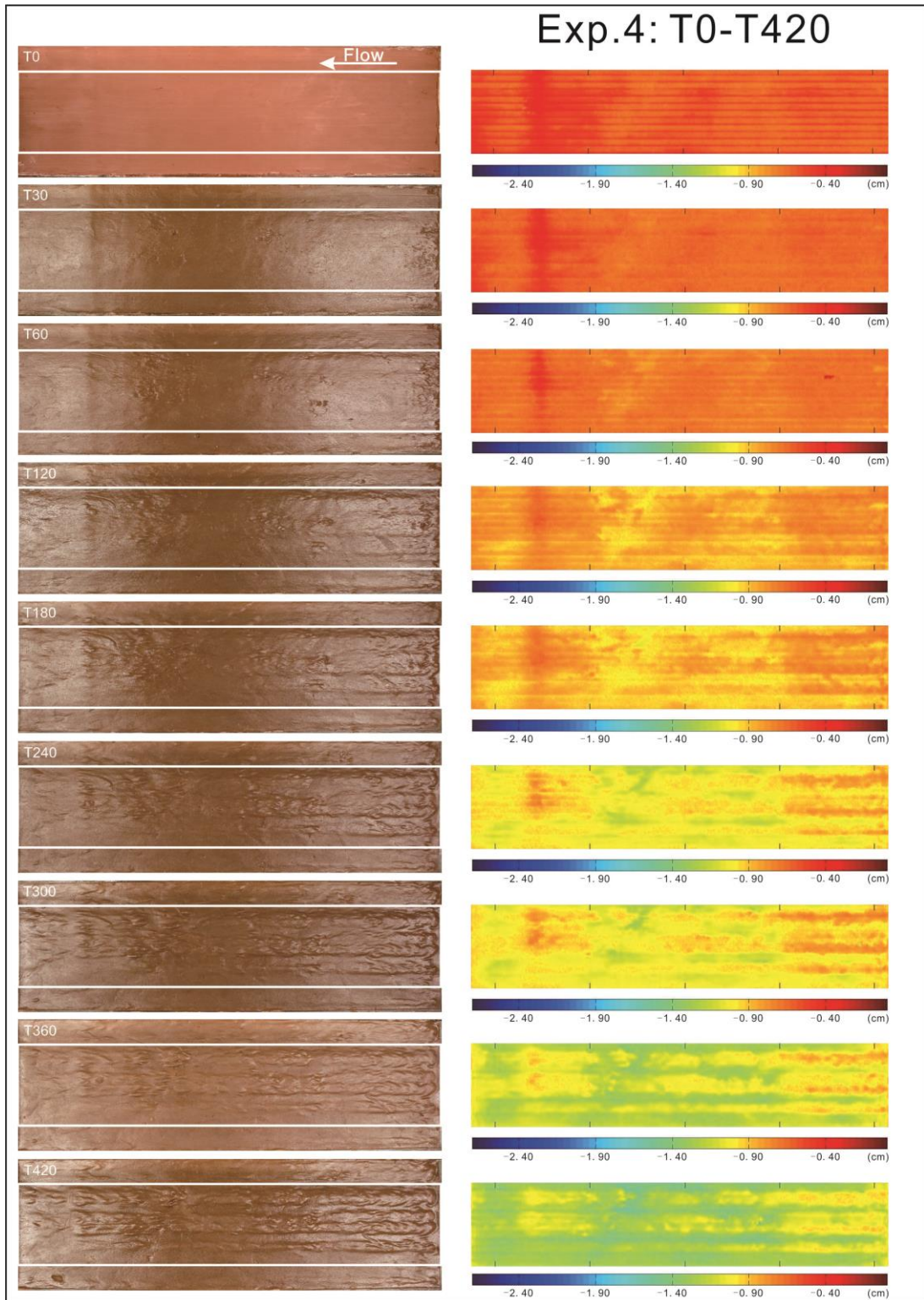


Figure 4.15 Plan view photographs and 3D elevation plots of the experimental bed of Exp. 4 (T0 to T420) showing bedform development with time (in minutes). Flow from right to left. The colour scale bar is in centimetre. The vertical scale bar is in centimetre.

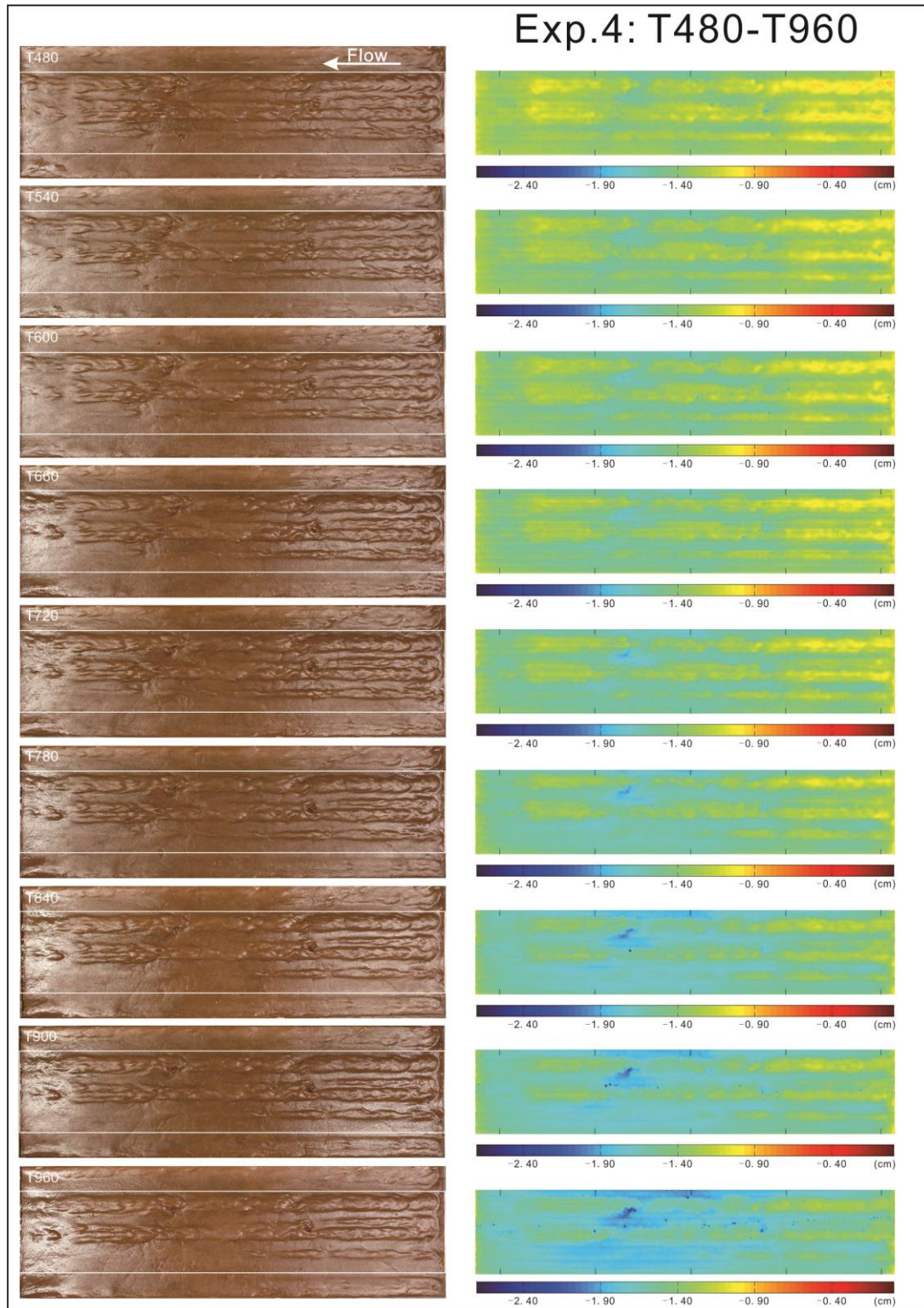


Figure 4.16 Plan view photographs and 3D elevation plots of the experimental bed of Exp. 4 (T480 to T960) showing bedform development with time (in minutes). Flow from right to left. The colour scale bar is in centimetre. The vertical scale bar is in centimetre.

Exp.4 was conducted with no extra sand addition in the total 960-min run (Figure 4.15 & Figure 4.16). The only source of sediment in the flow was the sand that had accumulated in the ends of the flume and the associated pipe work during the previous experiments. Though no extra sand was added, suspended sediment could still be in the flow during the run, and depositing on the mud bed after the run was paused. Comparing with the last runs with 2.5 kg sand addition every 15 min, the quantity of sand remaining on the mud bed of Exp. 4 was much less than those on the beds of Exps. 1 to 3, especially in the later stages and final stages of the experiments. In the final stages of Exp. 1, 2 and 3, all the experiments could not be continued owing to a thick sand layer covering the clay beds. This sand layer performed as a cover to protect the clay bed from further erosion. Exp. 4 was stopped due to the mud bed hardly changing after a relatively long time (total flow running time: 960 min) instead of when the mud bed was covered by thick sand layer.

Exp. 4 was conducted by using the mid-hard clay with undrained shear strength at about 9 kPa. The $H_{1/2}$ flow velocity is lower than in the previous experiments at 0.78 ms^{-1} and the near bottom flow velocity ranged from 0.48 ms^{-1} to 0.55 ms^{-1} (Figure 4.17). Flow velocity u (ms^{-1}), shear velocity u^* (ms^{-1}) and basal shear stress τ (Nm^{-2}) were measured during the experiments (Table 4.3 and Figure 4.18). The mean suspended sediment concentration was 0.1% by weight.

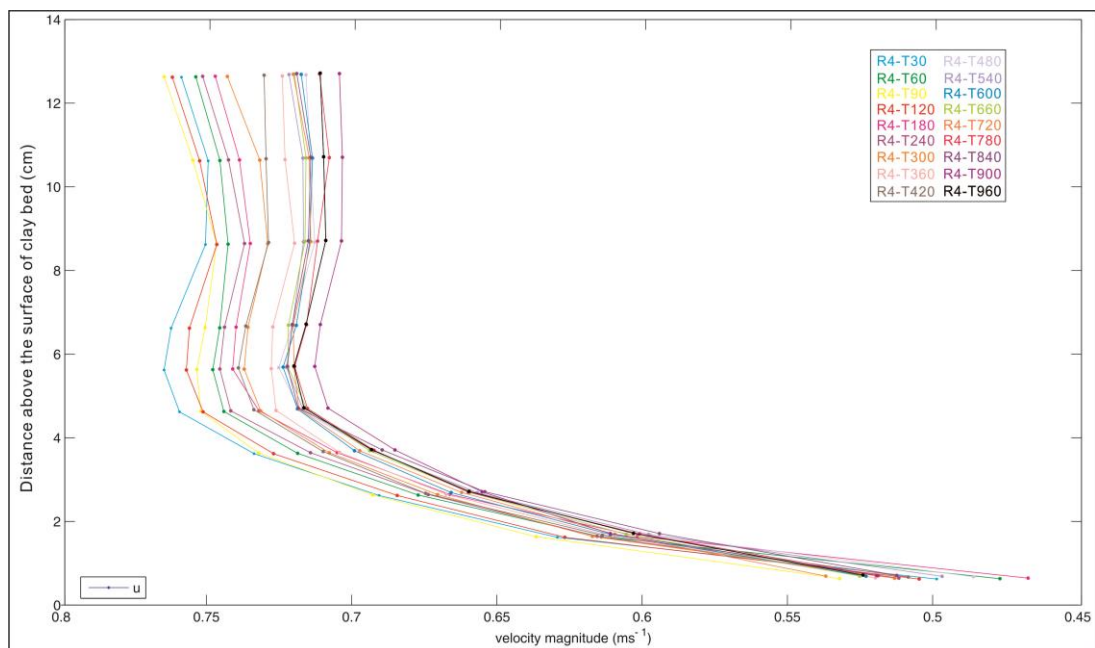


Figure 4.17 The velocity profiles of Exp. 4.

Table 4.3 Flow velocity u (ms^{-1}), shear velocity u^* (ms^{-1}) and basal shear stress τ (Nm^{-2}) measured at 6 mm above the experimental bed in Exp. 4. For details of the position of the UDVP probes, see Section 3.2.5 in Chapter 3.

| Exp. 4 (min) | velocity u (ms^{-1}) | Shear velocity u^* (ms^{-1}) | Shear stress τ (Nm^{-2}) |
|-----------------|--------------------------------------|--|---|
| T30 | 0.516 | 0.051 | 2.635 |
| T60 | 0.494 | 0.053 | 2.768 |
| T120 | 0.522 | 0.049 | 2.357 |
| T180 | 0.485 | 0.052 | 2.719 |
| T240 | 0.529 | 0.045 | 2.051 |
| T300 | 0.530 | 0.043 | 1.847 |
| T360 | 0.537 | 0.041 | 1.651 |
| T420 | 0.525 | 0.044 | 1.968 |
| T480 | 0.503 | 0.046 | 2.087 |
| T540 | 0.514 | 0.043 | 1.878 |
| T600 | 0.540 | 0.039 | 1.486 |
| T660 | 0.542 | 0.037 | 1.405 |
| T720 | 0.554 | 0.036 | 1.276 |
| T780 | 0.536 | 0.039 | 1.498 |
| T840 | 0.529 | 0.041 | 1.647 |
| T900 | 0.536 | 0.037 | 1.384 |
| T960 | 0.541 | 0.038 | 1.437 |

The most notable feature of Exp. 4 is the obvious linear erosional gutters with the relatively higher linear features alongside them on the clay bed (Figure 4.15 & Figure 4.16) which did not form in the Exps. 1 to 3, irrespective of the strength of the experimental bed was. They looked very similar to ridges and runnels (Carling et al., 2009), but the cause of these gutters is not clear. Except for the long linear erosional gutters, the other erosional features are not as variable as those that developed on the hard mud bed, or in natural bedrock channels. Only the following bedform types grew on the medium mud bed: (a) small flute marks with rounded ridge, (b) long curved furrows, (c) integrated linear erosional gutters (Figure 4.15 & Figure 4.16).

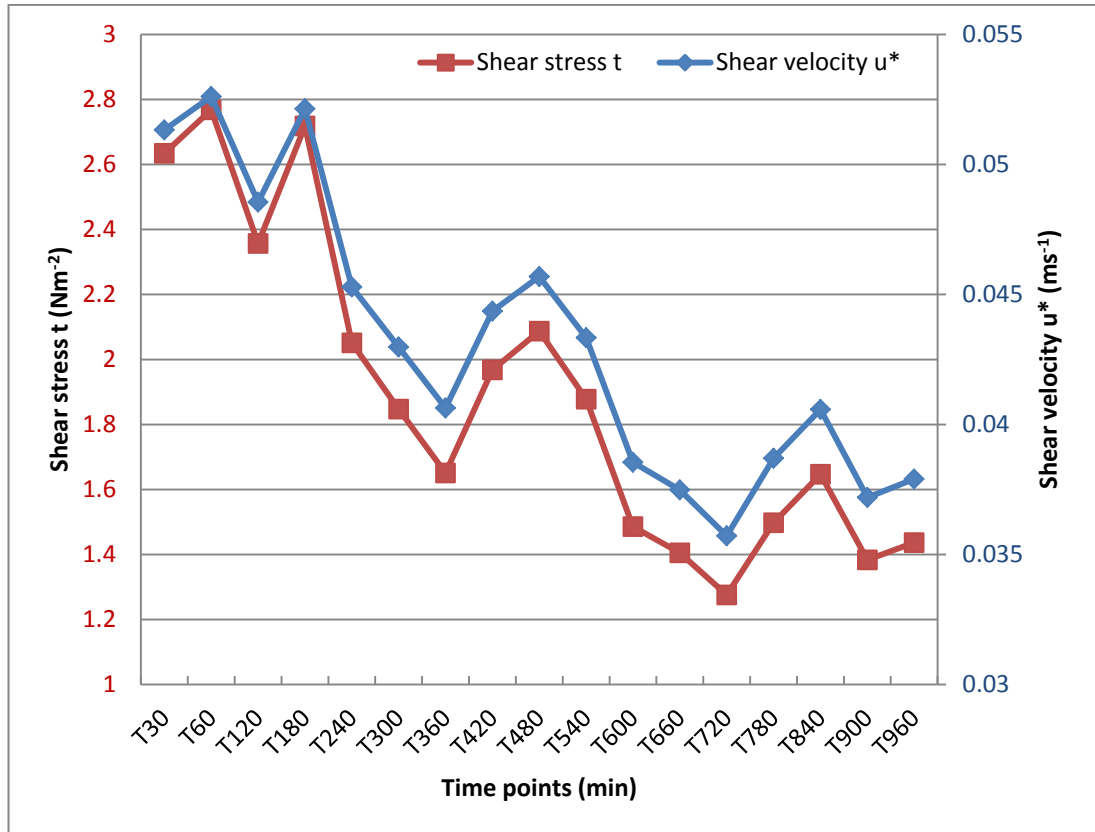


Figure 4.18 Shear velocity u^* (ms⁻¹) and basal shear stress τ (Nm⁻²) measured at 6 mm above the experimental bed in Exp. 4.

Instead of tiny erosional marks, potholes, or wavy erosional features as observed in previous experimental beds, small shallow flute marks with rounded rims formed in the initial stages of erosion of the clay bed. These flute marks would elongate and deepen to form furrows over time, and were 1.0-1.5 cm long, 0.6-0.8 cm wide. The depth of the deepest part of the proximal depression was 0.1-0.2 cm. For the linear straight erosional gutters mentioned before, both ends of them were open and the bottom of them is flat with uniform cross-section. However, they exhibit relatively prominent ridges between adjacent gutters, and the proximal upstream end of them had rounded surfaces and rims, whilst the downstream end rim was ambiguous or indistinguishable. Although erosional features developing in the upstream and downstream areas of the bed were different, they eventually integrated to form straight long ridges between the linear erosional gutters throughout the mud bed. Meanwhile, secondary erosional curved flutes with deep proximal depressions developed on the surface of these ridges. Nodular prominent parts with indistinguishable flaring tails are the dominant features in the downstream area, which could also be observed in the development stage of the erosional features in Exps. 1, 2 &

3. The experimental bed hasn't been covered by the sand layer during the later stage of experiments and therefore there was no cover effect to protect the substrate. However, even though there was no sand cover, the experimental bed tended to be a stable stage with smooth surface like in Exps 1 to 3. This suggests that there is a depth below the height of the false floor lip to which maximum erosion tends.

In summary, Exp. 4 delivered very different erosional features, dominated by linear straight erosional gutters throughout the whole experimental clay bed. These features formed at relatively lower flow velocity, lower basal shear stress, lower suspended sediment concentration, lower bedload sediment concentration and lower shear strength of the experimental substrate. This demonstrates the complex interaction between bed substrate properties and flow parameters, and suggests that different erosive bedforms initiate and develop in individual phase spaces that are defined by these bed and flow properties.

4.6 Discussion

The role of different processes in controlling erosional bedform genesis is poorly understood, and there is a limited understanding of the role of substrate properties in influencing this genesis in previous studies. A major limitation when comparing work with past studies such as those of Allen (1969); (Allen, 1971a, 1982) is that there is no shear strength data for the substrates used, and it is important to emphasise that such data is crucial in any future studies. The current physical experimental work on cohesive clay beds is intended to primarily reveal the relation between variety of boundary conditions and bedform genesis, including the role of sediment concentration in the flow and the influence of the undrained shear strength of the substrate. First of all, the experiments demonstrate that suspended sediment in the flow plays a key role in bedform genesis and development. The sediment-free experiments illustrated that cohesive bedforms would not generate and cohesive clay substrates with these shear strengths (9-19 kPa) and basal shear stresses ($1.2-7.1 \text{ Nm}^{-2}$) would not alter from fluid stressing alone. Instead abrasion is required for erosion to occur. Secondly, after introducing sands into the flow, different kinds of cohesive bedforms were produced and gradually developed over time. The evolution of bedforms in the experimental beds can be divided into 4 stages: initiation stage, developing stage, well developed stage, and final flattening stage. Two experiments, Exp. 1 and Exp. 2, indicated that the experimental results were

not random and were repeatable. Thirdly, Exp. 3 shows that substrate control plays a very large role in controlling both the rate of development and the nature of the erosive bedforms formed, and that shear strength plays a major role with variation of just a few kPa. Under the effect of sediment-laden flow, the genesis and evolution rate of bedforms in cohesive beds were highly dependent with the undrained shear strength of the experimental substrate. Soft beds needed longer time to generate the erosional forms than harder beds. The diversity of erosional forms and the quantity of each kind of erosional features in the soft clay beds were much less than that in the harder beds as well. The soft clay beds were eroded entirely instead of regionally in the harder beds. The erosional rate of the soft bed is slightly higher than that of the harder bed. What is common to all three experiments is that all experimental beds stopped being eroded after the surface was covered by a layer of sand, which is called the bed cover effect, which has been widely observed and studied in bedrock channels (Johnson and Whipple, 2010; Sklar and Dietrich, 1998; Sklar and Dietrich, 2004; Turowski, 2009; Turowski et al., 2008).

Additionally, experiments using different experimental conditions showed that under the integrated effects of lower flow velocity, very low sediment concentration, medium hard substrate, the experimental bed could produce very different bedforms, dominated by linear straight gutters with flat bottoms and non-uniform ridges between adjacent gutters. The cause of the genesis of these gutters is still unclear, but is probably caused by the secondary upwelling of sediment-laden flow caused by an isotropic variations in roughness and turbulence (Albayrak and Lemmin, 2011; McLelland et al., 1999; Vachtman and Laronne, 2011). The bed also developed to a stable final stage just as in Exp. 1, 2 and 3 that were affected by flow with far higher sediment concentration. However, notably, this stable final erosion stage was no longer induced by the bed cover effect, but instead appears to be related to a limiting erosion depth below the height of the fixed bed on either side of the clay bed.

The experiments produced flutes and a wide range of features such as potholes and furrows, which are collectively highly analogous to those that occur in bedrock river channels. They do not replicate the whole beds of flute marks like these that frequently occur in mud beds in nature and Allen's work (Allen, 1971a, 1982). This suggests that the substrate yield strength to applied shear stress ratio may be not in the correct range for classical flute formation in mud-beds. Given that the substrate appears to be in

approximately the correct range for sea-floor muds (see Section 2.4), given the available data, then this suggests that the applied shear stresses may not be in the right range, or other substrate properties such as the degree of bed compaction may not be analogous.

Chapter 5

Physical modelling of erosional bedrock bedforms

5.1 Motivation and research objective

Bedrock channels are an important but understudied type of river channel (Alexander, 1932; Bryant, 2008; Gjessing, 1967; Goodchild and Ford, 1971; Hancock et al., 1998; Johnson and Whipple, 2007; Richardson and Carling, 2005, 2006; Springer et al., 2006; Springer and Wohl, 2002; Tinkler, 1993, 1997a; Tinkler and Stenson, 1992; Tinkler and Wohl, 1998, 1998b; Whipple et al., 2000b; Whipple et al., 2000a; Wilson et al., 2012). Much of the erosion in bedrock rivers occurs through, and produces, a series of prominent bedform scour types (Richardson and Carling 2005). Our understanding of sedimentary processes forming these bedforms has been restricted by the slow rate of bedform development limiting field studies (Richardson and Carling, 2005; Tinkler, 1993; Wohl, 1998b). As a consequence fieldwork on bedrock channel erosion features has mainly concentrated on the geometric forms, and associated classifications (Richardson and Carling, 2005; Wohl, 1998b). Few flume-scale experiments have been conducted to investigate the evolution process of the features on the bedrock channels, because short-period erosion on bedrock produces very limited geomorphic change, and long-period experiments are typically unfeasible (Goodchild and Ford, 1971; Johnson and Whipple, 2007; Wilson et al., 2012). That is why, until now, there have been only few studies that have simulated the process of erosional bedform genesis and development in experimental analogue bedrock channels (Johnson and Whipple, 2007).

A new way of modelling bedrock bedform processes on realistic time-scales is required. Here the specific case of physical-erosion dominated bedforms in non-carbonate rocks is examined. For these systems, physical modelling requires a substrate sufficiently hard that it does not undergo erosion except by abrasion, and yet enables erosion to occur sufficiently rapidly that genesis and evolution can be studied in the laboratory.

5.2 Experimental setup and background

The experiments were undertaken using a clay bed composed of modelling clay in an 8.75 metre long tilting and recirculating flume. The clay bed was positioned within a false floor, with the top surface of the bed flush to the

upper surface of the false floor. The section in which most data were collected was located 4-5 m from the flume inlet where the mud bed is located (see Figure 3.2). The experiments were run with a uniform flow, with a water depth of 14 cm, on a slope of 1/200. The in-flume mean flow velocity was set to 0.95 m/s and monitored periodically by UDVP (see Table 3.8). Flow direction is from right to left in all cases of the experimental results. Further details of the experimental setup are provided in Chapter 3.

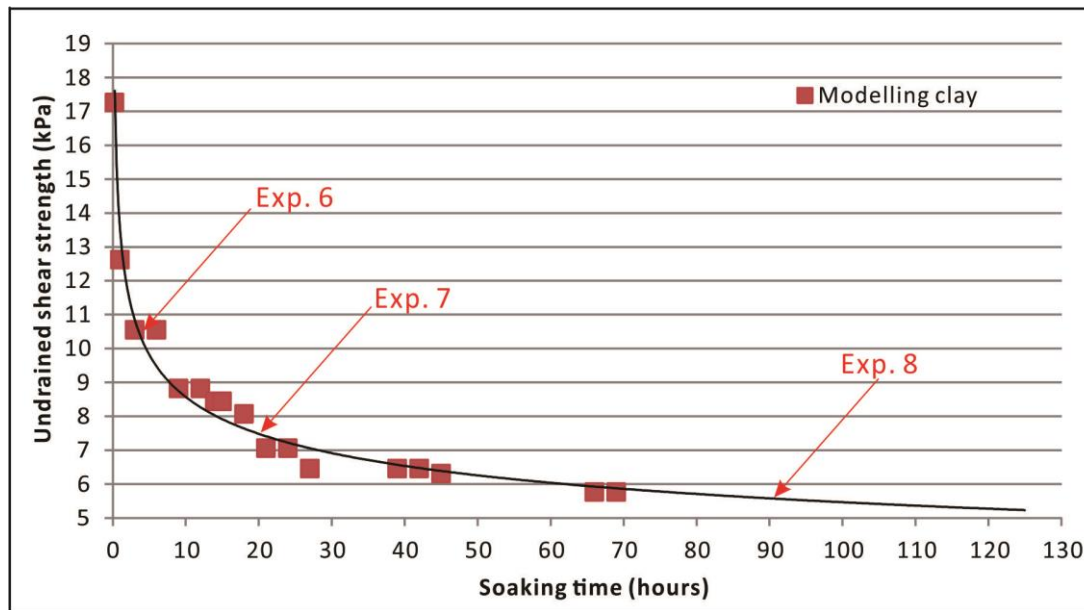


Figure 5.1 Undrained shear strength change with soaking time. Exp. 6: 10.5 kPa; Exp. 7: 7.5 kPa; Exp. 8: 5.5 kPa.

Three separate flume experiments, experiments 6 to 8, were conducted (Table 5.1, Figure 5.2 and Figure 5.3). There are 5 big and 4 small round preset defects on the initial bed of Exp. 6 (Figure 5.2). Exps. 7 and 8 started from the flat clay beds (Figure 5.2 & Figure 5.3). The bed substrate was composed of modelling clay, specifically SCOLA air-drying modelling clay. This material has a lower undrained shear strength than the terracotta clay used in experiments 1-4 (see Figure 3.8). The modelling clay is composed primarily of Illite-smectite (~40%) and kaolinite (~21%) clays, with quartz (~36%), and minor hematite (~4.5%) (see Table 3.5). The undrained shear strength of the modelling clay can be easily controlled by soaking in water (Figure 5.1). The initial undrained shear strength of Exp. 6, 7 and 8 are 10.5 kPa, 7.5 kPa and 5.5 kPa, respectively (Figure 5.1).

Table 5.1 The experimental time intervals for the sediment-laden experiments

| Time | T0 | T30 | T60 | T120 | T240 | T360 | T480 | T600 | T720 |
|---------------|------|------|-------|-------|-------|-------|-------|-------|-------|
| Exp. 6 | √ | √ | √ | √ | √ | √ | √ | √ | √ |
| Exp. 7 | √ | X | √ | √ | √ | √ | √ | √ | √ |
| Exp. 8 | √ | X | √ | √ | √ | √ | √ | √ | √ |
| Time | T840 | T960 | T1080 | T1200 | T1320 | T1440 | T1560 | T1680 | T1800 |
| Exp. 6 | √ | √ | √ | √ | √ | √ | √ | √ | X |
| Exp. 7 | √ | √ | √ | √ | √ | √ | √ | √ | √ |
| Exp. 8 | √ | √ | √ | X | X | X | X | X | X |

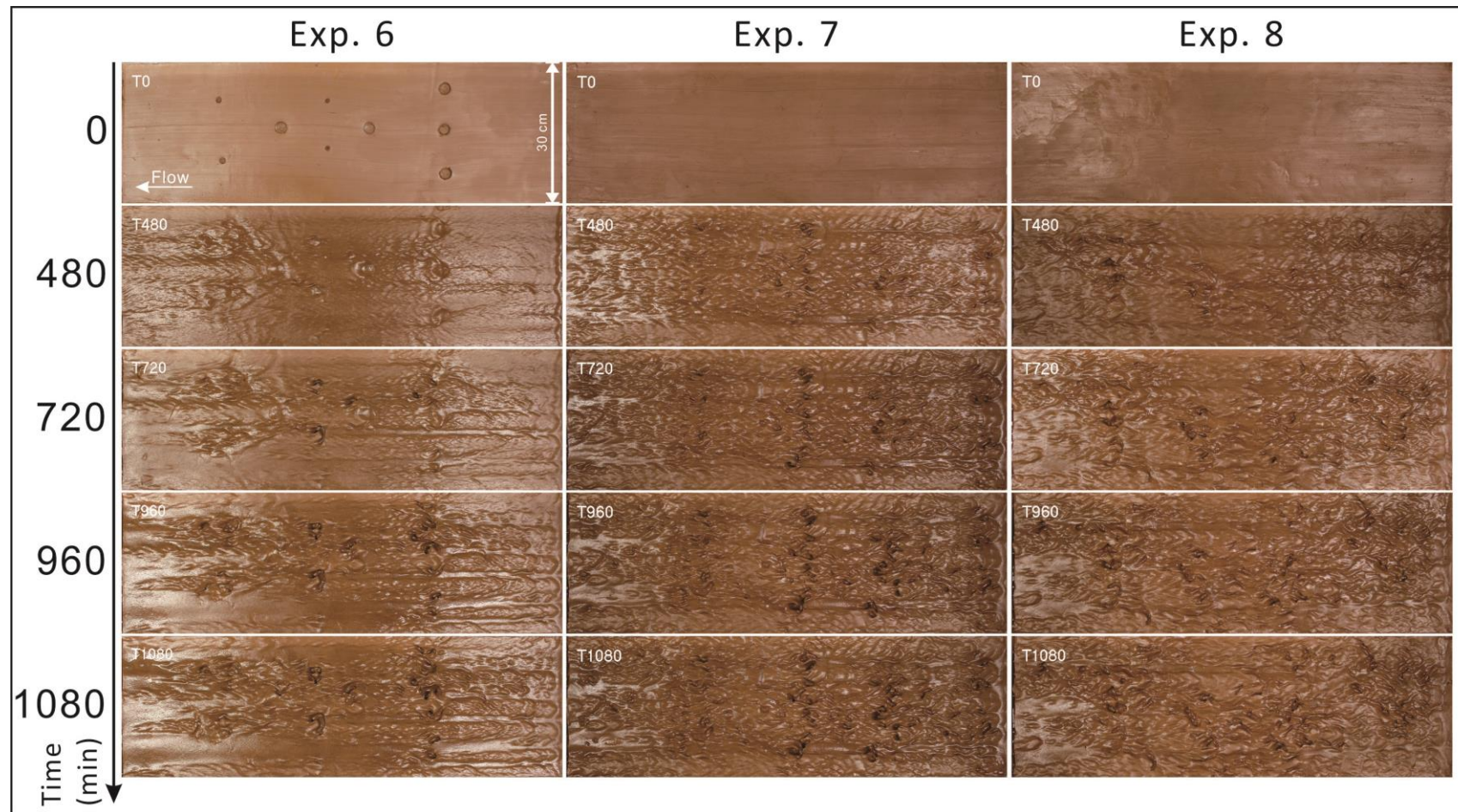


Figure 5.2 Experimental beds of Exp. 6, 7 and 8: T0 to T1080. The initial clay bed of Exp. 6. The big hollows are 2.4 cm in diameter and 0.3 cm in depth. The small hollows are 0.9 cm in diameter and 0.2 cm in depth. Flow from right to left. All the beds are 30 cm wide.

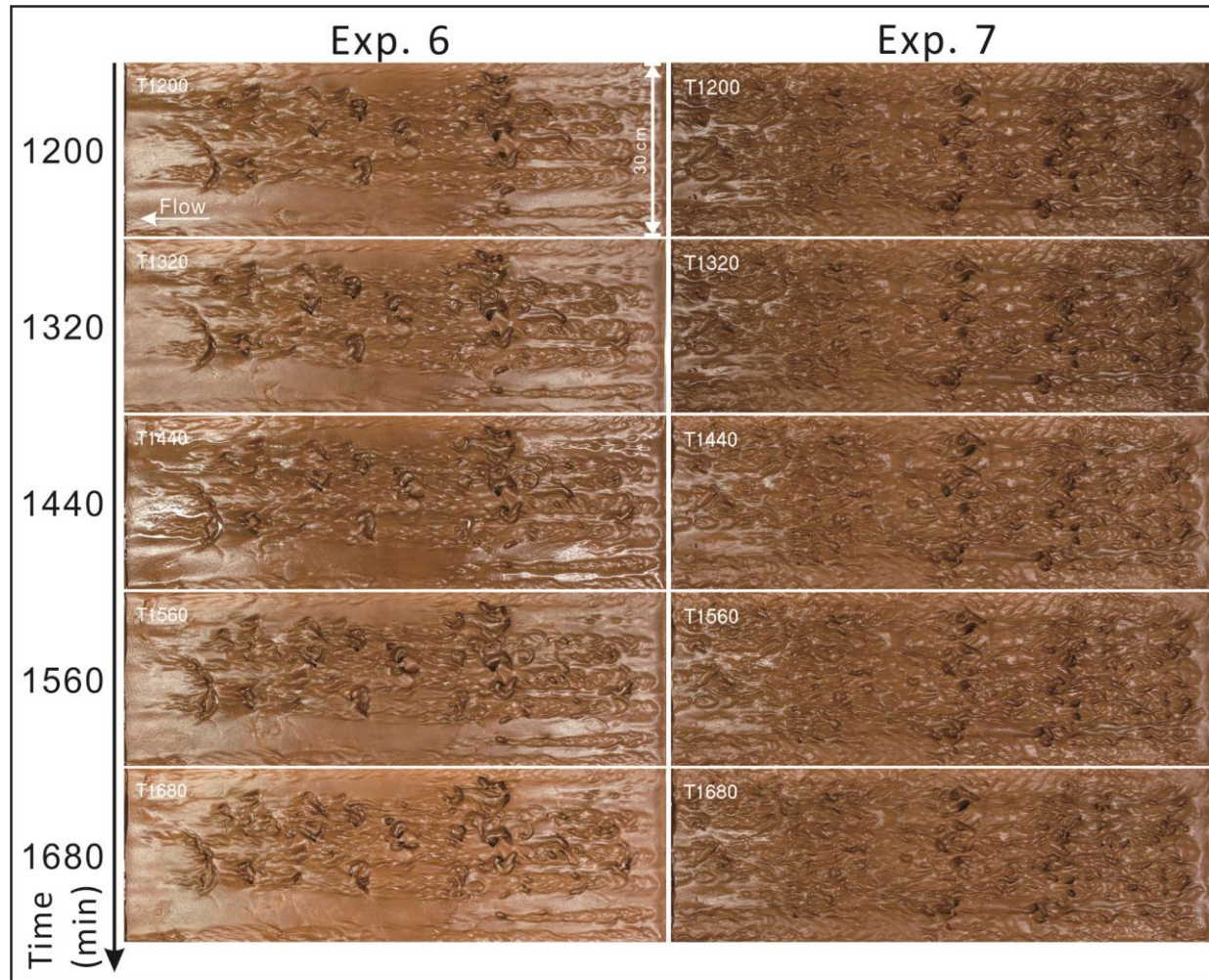


Figure 5.3 Experimental beds of Exp. 6 and 7: T1200 to T1680. Flow from right to left. All the beds are 30 cm wide.



Figure 5.4 Grain size distribution of the sediment added into the flow

The sediment added into the water is the same as that used in experiments 1 to 4. The grain size distribution has a D_{10} of 82-90 μm , a D_{50} of 142-155 μm , and a D_{90} of 239-259 μm (Figure 5.4). Sand was progressively lost whilst recirculating through the flume. In order to maintain a relatively constant sediment concentration, 1.5 kg of sand was added every 15 minutes. Water samples were collected manually every 15 minutes at about 30 cm downstream from the end of the mud bed, in order to measure the suspended sediment concentration (SSC). The collection depth was approximately 7 cm below the water surface. The SSC for experiments 6 to 8 was kept in a range between 0.1% and 0.25% (Figure 5.5).

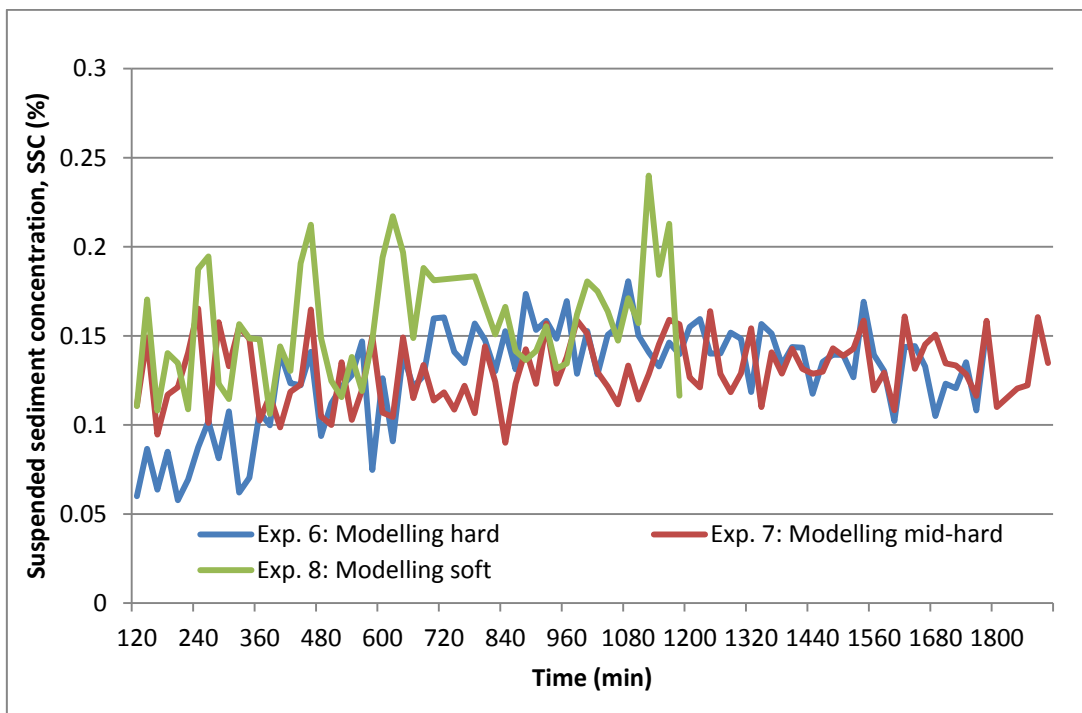


Figure 5.5 Suspended sediment concentration for Exp. 6, Exp. 7 and Exp. 8

5.3 Erosional bedforms observed in the experiments

A diverse array of erosive bedforms were identified within the experiments, and are described here. Comparison is made between these observed bedforms and natural erosive bedforms from bedrock rivers. In order to classify the forms, and for ease of comparison with natural erosive features, the typology of forms identified from bedrock rivers by Richardson and Carling (2005) is primarily used herein, with additional terms used as required.

5.3.1 The evolution of the experimental modelling clay beds

The evolution process and the erosion rate of the experimental modelling clay bed were quite different with those of the terracotta clay bed. However, in terms of the comparison of changing maps of Exps. 6, 7 and 8, it is very apparent that the erosion rate of the modelling clay bed is related with the undrained shear stress of the substrate as same as the situation of the terracotta pottery clay bed. For the hard modelling clay bed, the bedform barely altered until after 960 minutes and stopped to be eroded after 1440 minutes (Figure 5.6: Exp. 6). For mid-hard bed, the bedform started to change from 720 minutes and resisted to be eroded after about 1320 minutes (Figure 5.6: Exp. 7). The erosion of the softest experimental bed of Exp. 8 began from the 480th minutes and ended after 960 minutes, which was much earlier than Exp. 6 and 7 with experimental substrates with higher undrained shear strength (Figure 5.6: Exp. 8). This once again proves that the undrained shear strength of the substrate is one of the important parameters which effects the erosion rate of the cohesive bedforms.

All three experiments using modelling clay bed produced a huge array of the erosional features, all of which contained more apparent hollows than those produced on terracotta pottery clay beds. And further more, the geometries of them were very close to the sculpted forms observed on natural bedrock channels. Details of the geometry of the erosional features and the comparison between the erosional features produced by the experiments using modelling clay bed and the natural bedrock sculpted forms will be given exhaustively in the following sections. All examples were chosen from the experimental beds of the Exps. 6, 7 or 8 of different time interval. Therefore, it is impossible to indicate the spatial location of each of them here. However, the evolution of most of them will be discussed and the approximate locations of the final forms of them will be provided in the Chapter 6.

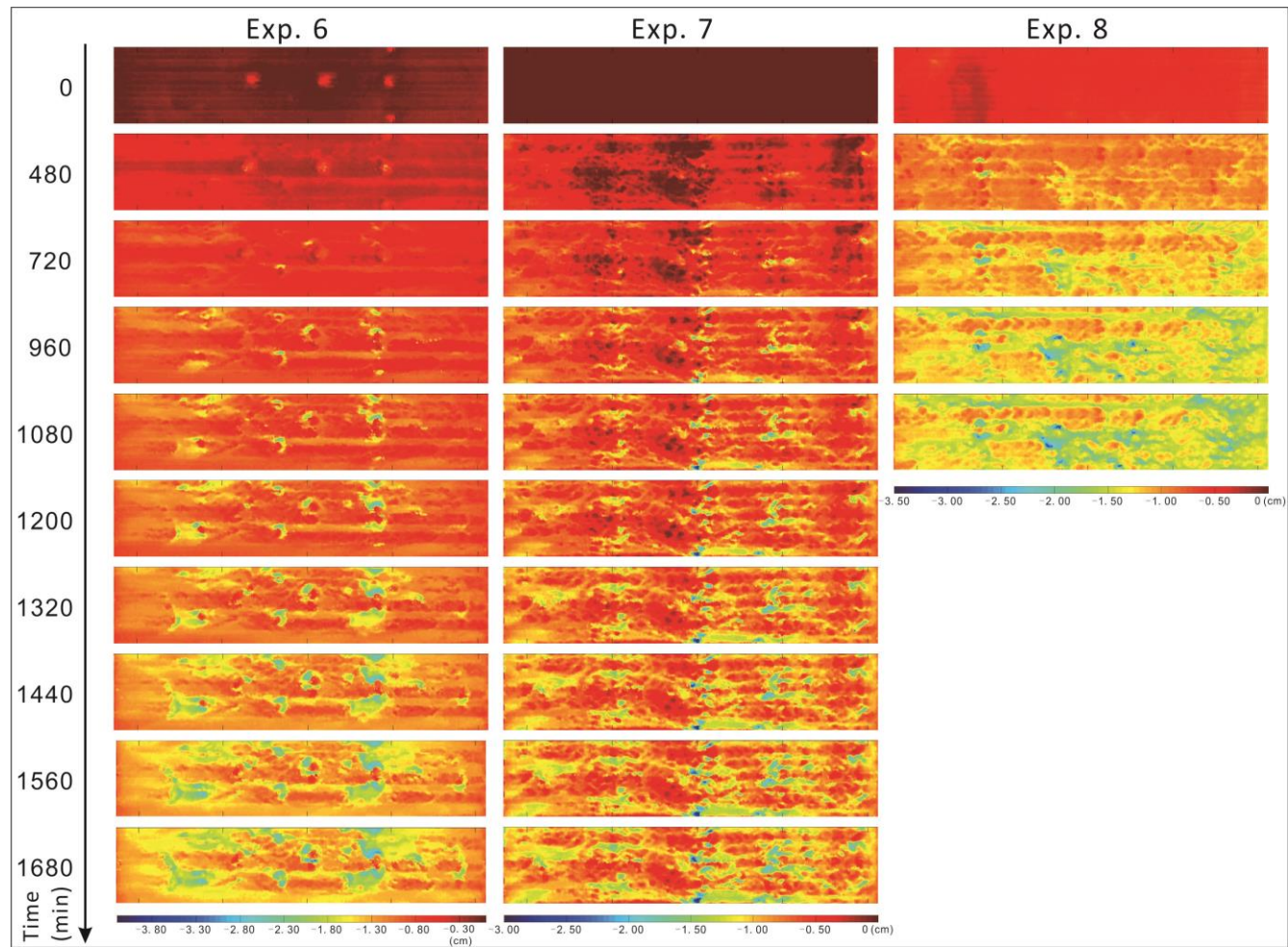


Figure 5.6 3D elevation plots of the experimental beds of Experiment Exp. 6, 7 and 8 showing bedform development with time (in minutes). Flow from right to left. The colour scale bar is in centimetre. The vertical scale bar is in centimetre.

5.3.2 Potholes

As described in Section 2.3.2, potholes are the most common abrasion sculpture on bedrock channels (Alexander, 1932; Allen, 1971a, 1982; Elston, 1917, 1918; Ives, 1948; Maxson and Campbell, 1935; Richardson and Carling, 2005; Wohl, 1992, 1993; Wohl and Ikeda, 1998; Zen and Prestegard, 1994). They are normally round to elliptical cavities in plan view whose depth is more than a quarter of their width (Alexander, 1932). Round to elliptical outline in plain view is the standard form of the simple pothole which can be found in the natural bedrock stream bed (Richardson and Carling, 2005). Except that, potholes can also be observed in many other regular or irregular shapes in plain view as well. Some of them have entry or exit furrows and some others are open instead of having a close rim. The others are in irregular shape with different secondary features on the bottom or lateral wall inside of them. In natural situations, potholes are observed on both the stream bed and the lateral boundary of rivers. The later ones are called lateral potholes. However, owing to the limitation of the experiments, no lateral potholes were produced during the current experiments. In subsequent parts of this chapter, all potholes referred to are located on the plan surface of the mud bed.

Potholes are the most visible erosional features on the experimental mud bed utilising modelling clay; in agreement with natural bedrock channels (see Section 2.3.2). The potholes observed in the experiments can be classified in to the following categories according to the previous classification (Richardson and Carling, 2005): i) Simple potholes; ii) Spiral furrowed potholes; iii) Potholes with exit furrows; Potholes with extended exit furrows; v) Potholes with both entry and extended exit furrows; vi) Open potholes; vii) Spiral-furrowed potholes with a spiral rib; viii) Potholes with horizontal furrows; ix) Potholes with lateral external secondary furrows; x) Complex potholes / convoluted potholes; xi) Hierarchical potholes; xii) Circle shape paired potholes, and xiii) Approximate-symmetrical paired potholes with both entry and exit furrows.

I. Simple potholes:

- **Standard round potholes (SRP)**

This kind of isolated, quasi-round potholes with vertical incision, giving a cylindrical form, is not very common in the experiments. They can be observed on the bed as a part of more complex features, or sometimes in the early stage of the experiments. These potholes typically evolve into other

forms, since as they widen and deepen their quasi-round top opening is rarely stable. The diameters of the potholes in Figure 5.7A & B are about 1.20 and 1.35 cm, with depths of approximately 0.50 and 0.80 cm, respectively. The radius of the top opening is usually slightly bigger than that of the internal radius of their base, but they are still regarded as cylindrical. The diameter of their top opening enlarges with time and may extend in a specific direction, usually in a streamwise direction, to form exit furrows. As a consequence, the rims of solitary potholes cannot maintain their quasi-round geometry. Hemispherical potholes were also present but could only be found in the initial stages of bed evolution; these would incise with time to become cylindrical potholes.

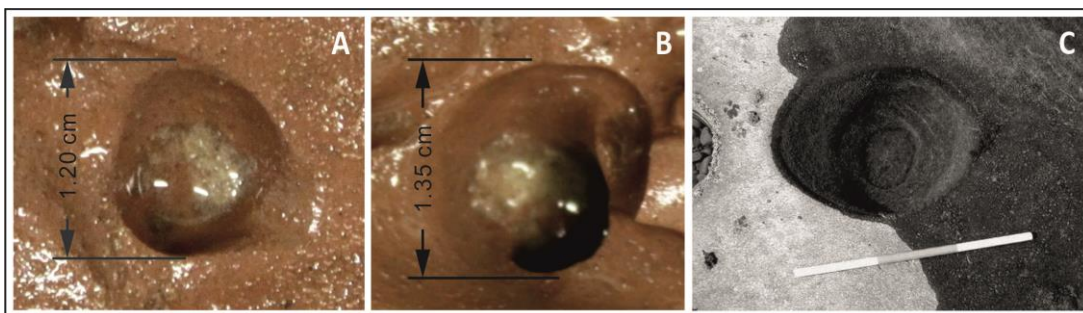


Figure 5.7 Standard round pothole (SRP). A and B demonstrate simple potholes in Exp. 7. C is a simple pothole from the River Lune (Halton), UK (from Richardson and Carling (2005)) with a length : width ratio of 1.35. The bedrock is fine-grained sandstone. The scale bar in C is 60 cm long. Flow from right to left in all images.

- **Spiral furrowed potholes (SFP)**

The experimental potholes in Figure 5.8 are typical spiral furrowed potholes (Alexander, 1932; Allen, 1982; Ängeby, 1951; Baker and Pickup, 1987; Diffendal, 1982; Gjessing, 1967; Glasser and Nicholson, 1998; Jennings, 1983; Kor and Cowell, 1998; Kor et al., 1991; Maxson and Campbell, 1935; Morgan, 1970; Shaw, 1996; Wohl, 1992). The flow direction is from right to left in all of the images. The example in Figure 5.8A is 4.9 cm long and 2.9 cm wide. The geometry of this kind of pothole is neither cylindrical nor hemispherical, instead the potholes contain stratified inner walls, and sometimes a boss in the central region of the basal surface. The upper surface is still broadly round, although the interaction of the spiral with the upper surface can complicate the degree of roundness. These potholes may develop from small round potholes, and the spiral may be caused by the grinder effect of the flow in the pothole (Alexander, 1932). This kind of inner profile of the pothole is thought to be induced by the movement of the

sediment-laden flow within the pothole (Figure 5.8D) (Alexander, 1932; Lugt, 1983). Sediment-laden flow whirls downwards within the pothole along a given track. Once it reaches the bottom of the pothole, the flow rotates upwards along another track. Over time the trace of erosion is left in the inner wall of the pothole, and a boss projection probably forms and is located at point 'd' in Figure 5.8D (Alexander, 1932).

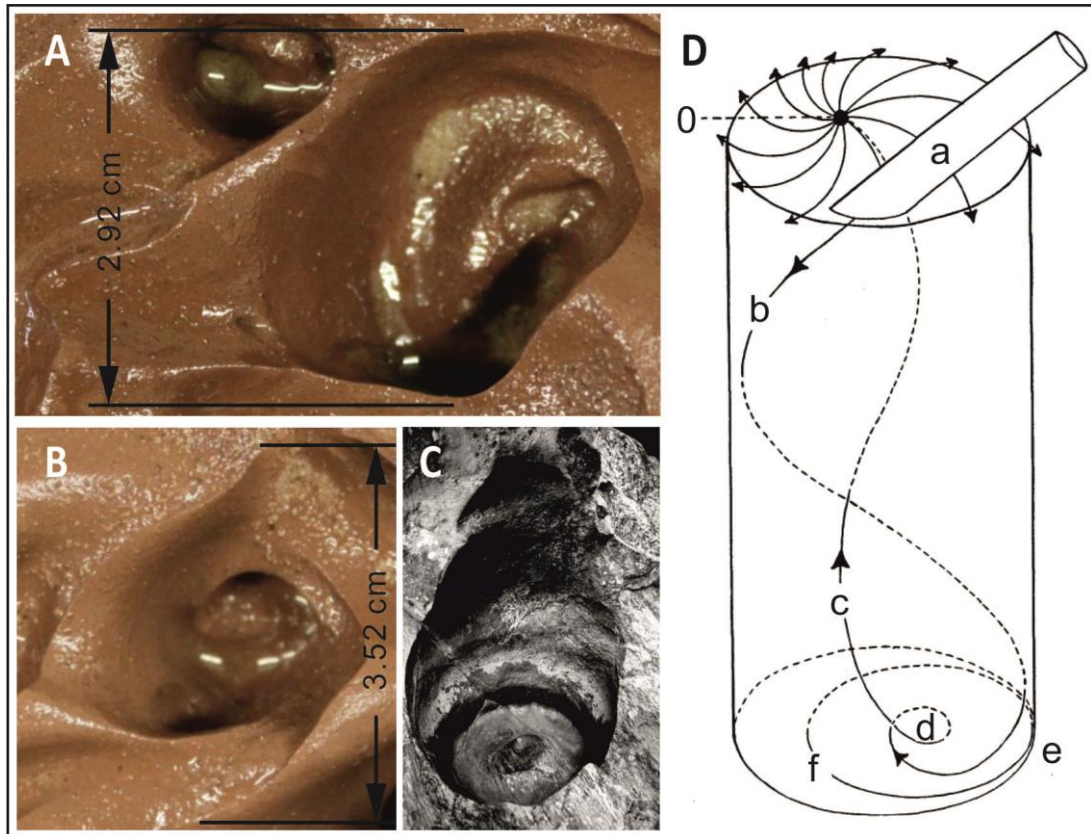


Figure 5.8 Spiral furrowed potholes (SFP). A and B illustrate SFP in Exp. 6 and 7, respectively. Flow from right to left. C shows a spiral furrowed pothole with a central boss in Nam Mae Chaem (Ob Luang), Thailand (from Richardson and Carling (2005)). D is a schematic diagram to show how the wall and the bottom of a spiral furrowed pothole erode by sediment-laden flow (from Alexander (1932)).

- **Pothole with exit furrows (PwEF)**

Potholes with exit furrows (Figure 5.9) are one of the most ambiguous potholes because they look very similar to typical flute marks widely found in mud deposits (Alexander, 1932; Allen, 1971a, 1982; Kor and Cowell, 1998; Lugt, 1983; Morgan, 1970; Richardson and Carling, 2005). PwEF normally have a round rim at the upstream end and a radial rim in the downstream direction. The rims of them are still closed in planview. The stoss-side slope of them is a little gentler than the lee-side slope. However, the most obvious

difference between PwEF and flutes is that the closed round rim can still be seen in the downstream half of the depression of PwEF, although it may be a little unclear in some cases. On the other hand, PwEF do not have any kind of median-ridge which flutes sometimes exhibit. The furrows associated with these features may be abraded by the sediment-laden flow escaping from the depression of the pothole in the downstream direction (Allen, 1982; Kor and Cowell, 1998; Morgan, 1970; Richardson and Carling, 2005). Sediment-laden flow travelling within the hollow brings the inner trace to the pothole, sometimes.

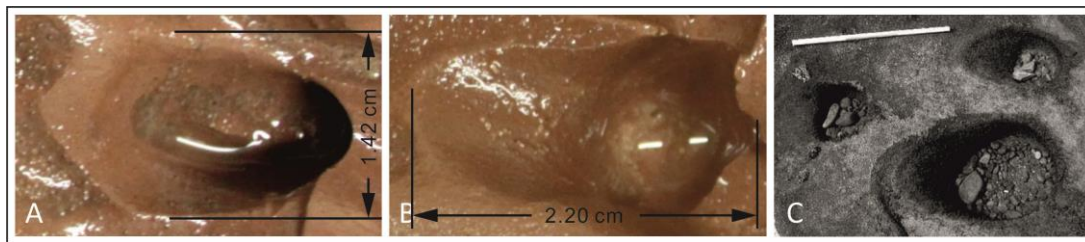


Figure 5.9 Potholes with exit furrows (PwEF) A and B are PwEF from Exp. 7 and Exp. 8, respectively. C are PwEF in the River Lune (Halton), UK (from Richardson and Carling (2005)). The scale in C is 60 cm long. Flow is from right to left in all cases.

- **Potholes with extended exit furrows (PwEEF)**

Potholes with extended exit furrows (Figure 5.10) are the most common potholes developing on the experimental bed. Unlike PwEF, the downstream ends of exit furrows of PwEEF are not always closed and the lengths of the exit furrows are much bigger than the diameters of the primary potholes. The exit furrows usually exhibit a curved profile in the stream-wise direction with lengths more than twice as long as their widths. They are still considered to be potholes because they were developing from individual hollows located at the upstream end which are much deeper than the rest of the bedform. The rims of PwEEF are parallel curved and extended downstream. In some cases, they are closed (Figure 5.10A & B), although sometimes, the downstream end rim is not as clear as their upstream end one. The downstream closed ends of these bedforms are generally convergent to a certain point whose shape is apparently different from their upstream ends and affected by the adjacent erosional features. In other cases, the exit furrows are totally open with two parallel lateral curved rims (Figure 5.10C & D). PwEEF are not classified as flutes because they are not parabolic in shape in plan view and they do not have any other features of flutes except the distinguishable stoss-side tail. Individual potholes can probably develop

into potholes with extended exit furrows, or open potholes with time, if they don't connect with adjacent bedforms to form complex features.

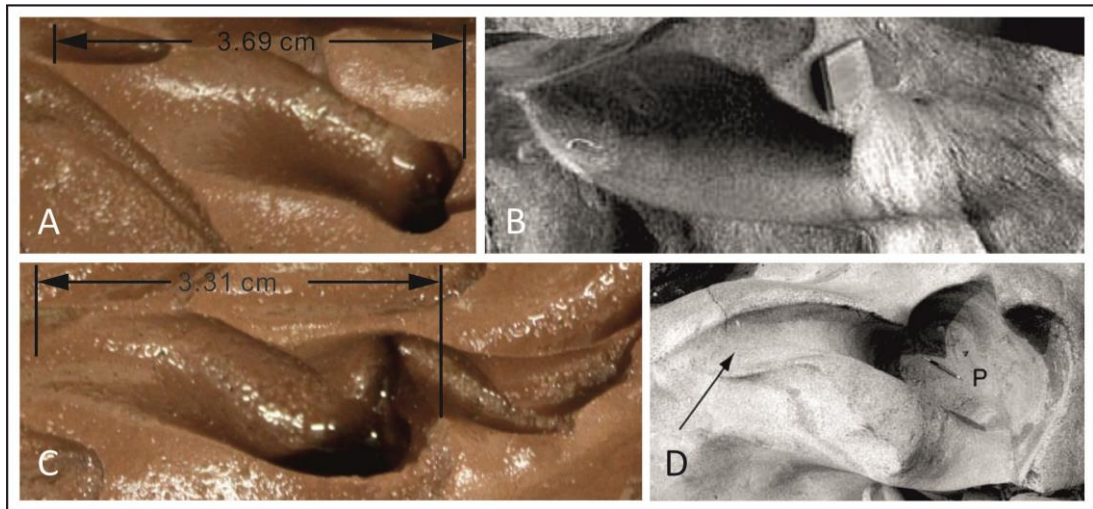


Figure 5.10 Potholes with extended exit furrows (PwEEF). The exit furrows of this kind of pothole are much longer than in PwEF. A and C are two PwEEF obtained by Exp. 7. B and D are two observed in the field (from Richardson and Carling (2005)). C and D are compound potholes with extended exit furrows. The pothole in A is 3.69 cm long and 1.59 cm wide. The exit furrow of C is 2.20 cm long. Pen is for scale. Flow direction is from right to left in all images.

- **Pothole with both entry and exit furrows (PwEnEF)**

Potholes having both entry and exit furrows at the same time (Figure 5.11) can be regarded as an integrated form of pothole. This is a pothole with a long curved entry furrow (Alexander, 1932; Allen, 1982; Gjessing, 1967; Sato et al., 1987) and exit furrow. It probably develops from a small pothole, in front of which a curved furrow elongates and eventually connects with the pothole, introducing more water into the pothole and accelerating the incision. The diameter of the pothole in Figure 5.11A is 0.63 cm. The entry and exit furrows are 3.2 cm and 1.8 cm, respectively.

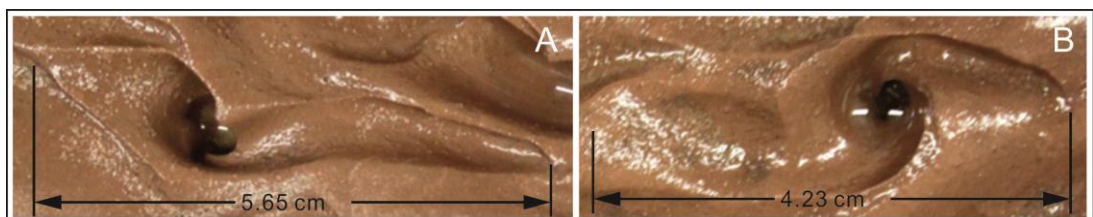


Figure 5.11 Potholes with both entry and exit furrows (PwEnEF) in Exp. 7.

- **Open potholes (OP)**

Open potholes are a special kind of pothole that have an open end in plan view (Figure 5.12). The open end of OP is almost as wide as the diameter of the primary hollow. They usually lack the lee side edge and have an entire open end whose dominant orientation is towards the downstream direction. On some occasions, their upstream end rims are also not closed; these might be cut through by other marks in front of them, for example, an entry furrow. The rim of these potholes is different from potholes with exit furrows or flutes. Except for the upstream end, the rest of their rim is relatively parallel instead of closed like that of PwEF or flutes with parabolic profile in plan view. Figure 5.12A shows an example observed in the current experiments (Exp. 7) which is 2.85 cm long and 1.54 cm wide. The length of the potholes is usually no less than 2 times the width.

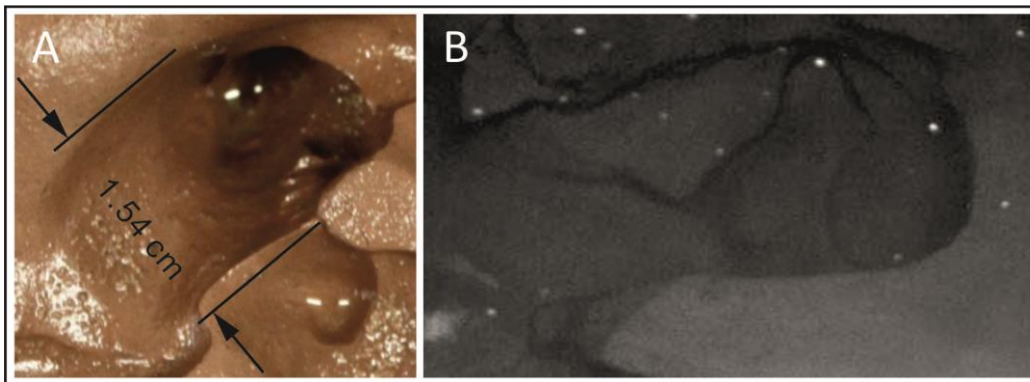


Figure 5.12 Open potholes (OP). A was observed in Exp. 7 and was 2.85 cm long and 1.54 cm wide. B is an OP from the River Lune (Halton), UK. It is 120 cm long with a diameter of 60 cm (from Richardson and Carling (2005). Flow from right to left in both images.

II. Compound potholes (CpdP)

Compound potholes are defined as potholes with internal or external secondary structures (Lorenc et al., 1994; Nemeč et al., 1982; Richardson and Carling, 2005). They can be subdivided into the following kinds.

- **Spiral-furrowed potholes with a spiral rib (SFPwSR)**

On the experimental mud bed, a lot of erosional marks have entry spiral ribs (Figure 5.13) which are widely observed in natural bedrock channels (Alexander, 1932; Allen, 1982; Ängeby, 1951; Baker and Pickup, 1987; Diffendal, 1982; Gjessing, 1967; Glasser and Nicholson, 1998; Jennings,

1983; Kor and Cowell, 1998; Kor et al., 1991; Maxson and Campbell, 1935; Morgan, 1970; Richardson and Carling, 2005; Shaw, 1996; Wohl, 1992). The spiral rib can be considered as a little curved furrow extending towards the upstream direction adjacent to the upstream rim of a pothole. The head of the spiral rib is usually cusped or approximately-cusped and points dominantly in the upstream direction. It rotates anti-clockwise along the rim of the pothole towards the downstream direction. The length and width of the spiral rib are normally far less than the primary pothole that it is connected with. Early workers suggested that these may be formed by the Coriolis force driving a downward-spiralling flow (Alexander, 1932; Lugt, 1983), however the Coriolis force is insignificant at the scale of these features both in the laboratory and the field (Dingman, 1984). Besides the spiral rib feature, this kind of pothole generally has an inner spiral furrow which is thought to be incised under the effect of the downward-spiralling flow. Sometimes, near the top open rim of potholes, a secondary spiral furrow with cusped ridge can be observed within the pothole (Figure 5.13B). In the current experiments, the spiral ribs rotate mainly in anti-clockwise direction, but the primary potholes that many of the ribs are adjacent to contains exit furrows, which develop usually slight curved in clockwise direction. The rib of Figure 5.13A is about 0.50 cm long and the whole length of the pothole is more than 5 times as long as the rib. The rib of the pothole demonstrated in Figure 5.13B is 1.05 cm long, that is only 1/6th of the length of the primary pothole that it is adhered to.

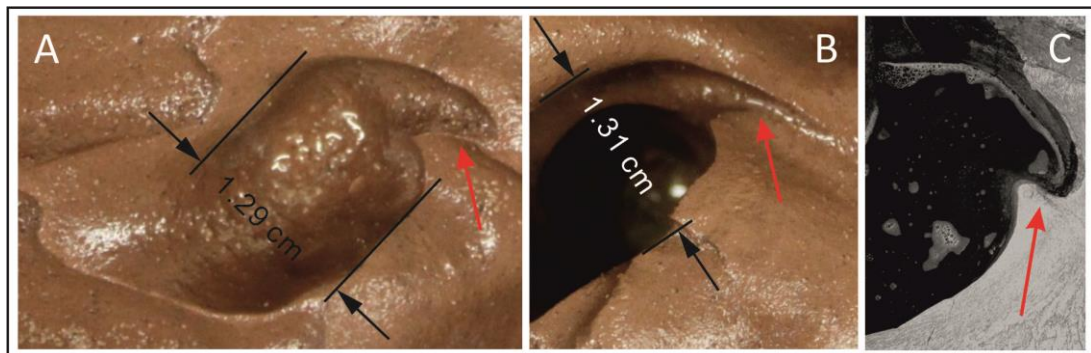


Figure 5.13 Spiral-furrowed pothole with a spiral rib (SFPwSR). The spiral rib (red arrowed) is a little entry furrow which is much smaller than the scale of the primary pothole. A and B are from the central part of the bed in Exp. 7; A is about 1.29 cm wide and B is 1.31 cm wide. C is observed in Woolshed Creek, Australia. The pothole is ~1.5 m (from Richardson and Carling (2005)). Flow is from right to left in all cases.

- **Potholes with horizontal furrows (PwHF)**

Potholes with horizontal furrows are defined as potholes with horizontal furrows on the inner wall (Figure 5.14) (Gjessing, 1967; Lorenc et al., 1994; Nemec et al., 1982; Richardson and Carling, 2005). PwHFs are distributed widely throughout all the experimental beds and are one of the most common forms observed. The size of PwHFs is very variable in the experiments. The horizontal furrows usually occur from the inner wall of the upstream end and flared outwards. PwHFs in the experiments usually have sharp overhanging flank rims as well. These features make the potholes look like overhanging flute at the upstream end. The difference is that overhanging flutes cut downwards and translate upstream, whilst the inner horizontal furrows of PwHFs develop along the lateral inner wall of primary potholes. This form can be regarded as a special secondary structure (Glasser and Nicholson, 1998; Lorenc et al., 1994; Nemec et al., 1982; Richardson and Carling, 2005).

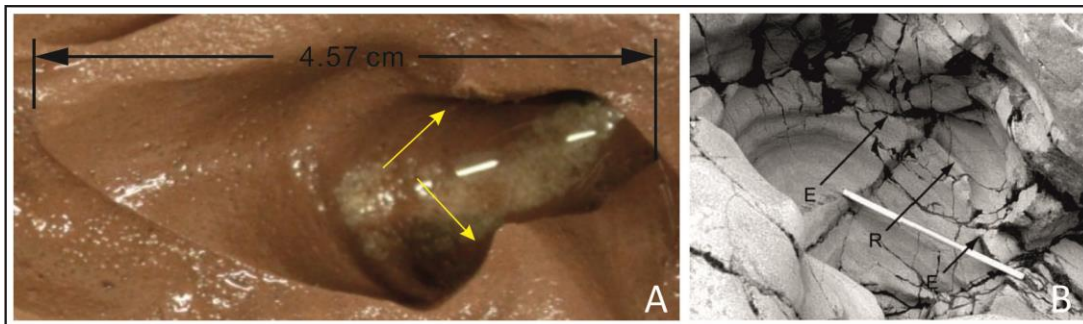


Figure 5.14 Potholes with horizontal furrows (PwHF). These tend to form in deeper potholes. A observed in Exp. 8, represents experimentally derived features. B shows a complex pothole with horizontal furrows in the River Lune (Tebay), UK. The arrows show the rims of a PwHF; Flow from right to left. The scale is 60 cm long (from Richardson and Carling (2005)).

- **Potholes with external secondary furrow (PwESF)**

Potholes with external secondary furrow (Figure 5.15) are the one of the most common kinds of feature on the experimental beds. A wide range of primary pothole types produce these features, marked by a secondary adjacent lateral furrow. The majority of these secondary lateral furrows in the experiments are located on the right hand side (as looking downstream) of the primary potholes, with some on the left hand side.. The widths, lengths and depths, are all smaller than the primary potholes. The direction of external secondary flow principally depends on that of the primary potholes. The pothole showed in Figure 5.15A is 2.4 cm in length and 1.1 cm in width. However the lateral furrow adjacent to it is only 1.78 cm long and 0.7 cm

wide (at the distal widest opening). In most of the cases, the upstream ends of the secondary furrows are curved and cusped. The ends of them are always open with the radial flank towards the downstream direction. In some situations, the lateral furrows are almost the same size, or are even bigger than the pothole in plan view (Figure 5.15B & C). In other situations, potholes have more than one lateral furrow, formed on either one side, or both sides, of the primary pothole (Figure 5.15A).

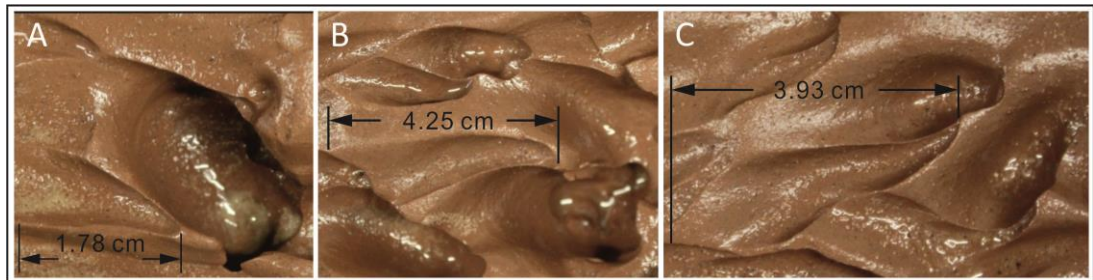


Figure 5.15 Potholes with external secondary furrow (PwESF). The primary pothole in A is 2.4 cm long and 1.3 cm wide from Exp. 6; B and C are from Exp. 7. Flow direction is from right to left.

III. Complex potholes (CoP)

Complex potholes (Jennings, 1983; Lorenc et al., 1994; Nemeč et al., 1982), herein, are defined as a relative irregular area formed by the combination of many different kinds and sizes of potholes with internal or external secondary features (Figure 5.16). Some CoPs are a group of some connected adjacent solo potholes and compound potholes. They are no longer in a regular form. Some of them developed regularly on the experimental substrate and can be subdivided into the following types: Hierarchical potholes, Circle shape paired potholes, Quasi - symmetrical paired potholes with exit furrows. Examples of complex potholes are shown in Figure 5.16; they can become quite extensive, for instance the whole depression area of Figure 5.16A is 9.46 cm long and 6.70 cm wide.



Figure 5.16 Complex potholes (CoP). A & B are CoP observed in Exp. 6 and 8, respectively. C is a compound lateral pothole in Nam Mae Chaem (Ob Luang), Thailand (from Richardson and Carling (2005). Flow from right to left. Notebook is for scale.

- **Hierarchical potholes (HP)**

Hierarchical potholes (Figure 5.17) are potholes with more than one secondary feature within them, some of which may contain their own lower-level secondary features (Diffendal, 1982; Kale and Joshi, 2004; Lorenc et al., 1994; Nemeč et al., 1982; Whipple et al., 2000a). This set of secondary forms make the primary potholes exhibit several different levels of secondary features. In the experiments, although HPs are not as common as the other bedforms, at least one or two can still be observed; Figure 5.17 shows some of them. In this irregular depression of Figure 5.17A, entry furrows, lateral furrows, exit furrows and the boundary of different features can all be distinguished.

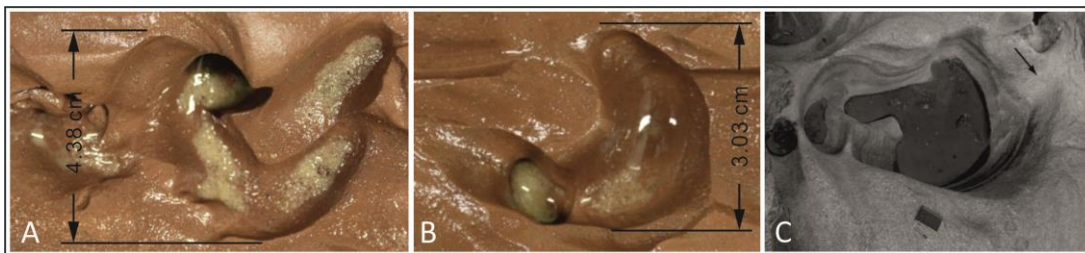


Figure 5.17 Hierarchical potholes (HP). HPs contain at least two classes of pothole. The most obvious part is that there is a great variety in internal scour depth within them. A and B are two HP in Exp. 6. Flow from right to left. C is the HP observed in the real bedrock surface, Nam Mae, Chaem (Ob Luang), Thailand. Flow from top to bottom. The notebook (15 cm long) is for scale. (from Richardson and Carling (2005).

- **Horseshoe-shaped paired potholes (HSPP)**

Horseshoe-shaped paired potholes (Figure 5.18) are a very unique kind of pothole in the experiments. One experiment beds, they mainly formed in positions where there were initial bed defects; they developed in the

downstream position of every set defects on the flat mud bed in Exp. 6. Solo simple potholes did not form as expected in the locations of these set defects. Instead, at the very beginning, two shallow curved furrows formed from both sides. The points where these furrows initiated from were located nearly on both ends of the centreline of the set round defect in the cross-section direction. They developed in parabolic profile towards the downstream direction with the original set defect gradually fading. Meanwhile two quasi-symmetric potholes with exit furrows developed along the track of the two shallow furrows mentioned above. These two potholes are not separated. Their deep round upstream ends were normally connected with each other, but the downstream ends were independent. The size of them was larger and deeper than the other potholes. The size of Horseshoe-shaped paired depends on the size of the set defect they initiated from.

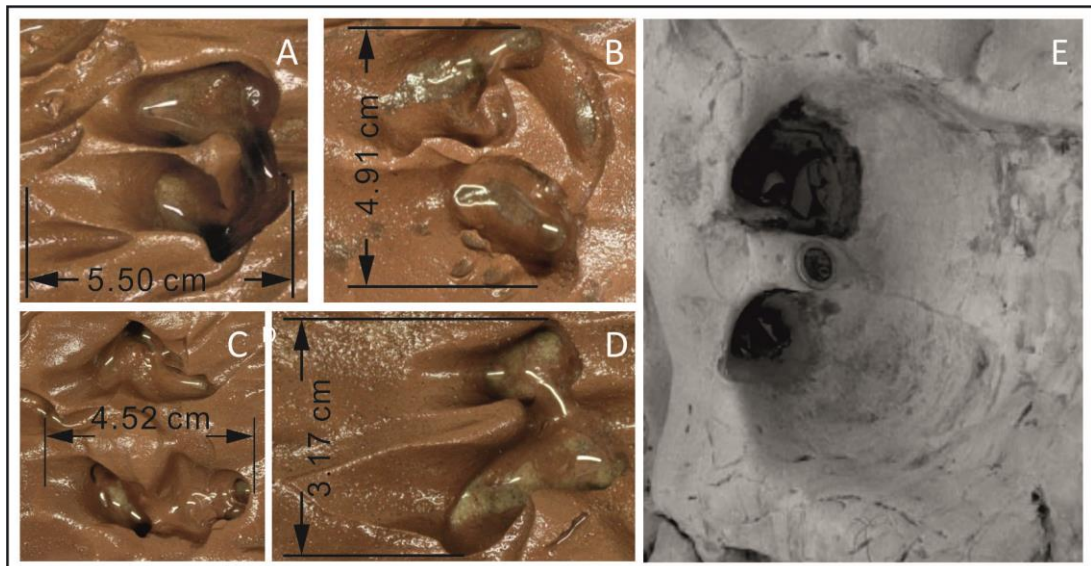


Figure 5.18 Horseshoe-shaped paired potholes (HSPP). A and B are observed in Exp. 6; C and D are observed in Exp. 8. Their dimensions range from 4 – 6 cm in width, and from 5 – 8 cm in length. The depth ranges from 0.4 cm to 2.9 cm. Figure 5. 15A is 4.10 cm wide 5.50 cm long and 2.3 cm deep. Flow direction from right to left. E: paired lateral potholes in Wadi Hazazon, Israel. Upstream to the right. Dolomite. Coin for scale. (from Richardson and Carling (2005))

- **Approximate-symmetrical paired potholes with both entry and exit furrows (ASPPwEEF)**

Approximate-symmetrical paired potholes with both entry and exit furrows (Figure 5.19) developed on every experimental bed no matter whether there

were set defects on the original flat bed or not. The whole set of them contains two potholes with exit furrows and median furrows between them as the centre axis of the whole system. They were actually a pair of potholes with external secondary furrows. One has a lateral furrow on its left side and the other one has lateral furrow on its right side. Two adjacent lateral furrows connected with each other with no shared rim to form the median furrows of the whole set of potholes. The reason why they are considered as a set instead of a kind of regular compound pothole is because the profiles of two potholes are nearly axial symmetrical. Each of them had a deep primary pothole at its upstream end, and an exit furrow whose flanks are not parallel like normal simple PwEF. The vertices of these two potholes point in different directions. For example, if the central axis is in stream wise direction, one points towards top right corner of the photo and the other one bottom right corner. One flank of the exit furrow extends towards the downstream as usual. However the other furrow turns to be convergent with the regular one. Briefly, the outer flank of the exit furrows always turn towards the central axis in order to converge with the inner one. In the beginning stage of the experiments, there were not any kinds of ASPPwEEF occurring on the mud bed. They only began to grow after the first one-third period (about 600 minutes running time) of experiments. There is nothing special in the location of where they develop. Although the above mentioned CSPs are partially symmetrical and have exit furrows as well, the cause of formation and the form are totally different from ASPPwEEF.

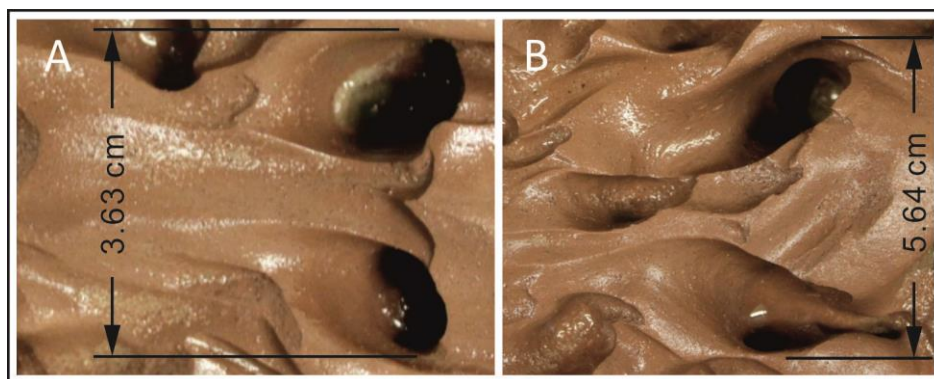


Figure 5.19 Approximate-symmetrical paired pothole with both entry and exit furrows (ASPPwEEF). This system contains two asymmetrical potholes with both entry and external furrows which connect with each other and form on a central axis of the whole system. A and B are observed in Ex. 7. Flow from right to left.

5.3.3 Longitudinal features

Compared with potholes, the other principle kinds of erosional marks in bedrock stream substrates are longitudinal features (Allen, 1969, 1971a, 1974, 1982; Baker, 1973; Baker and Kale, 1998; Baker and Pickup, 1987; Blank, 1958; Dzulyński and Sanders, 1962; Friend, 1965; Gupta et al., 1999; Hancock et al., 1998; King, 1927; Maxson, 1940; Maxson and Campbell, 1935; Richardson and Carling, 2005; Shaw et al., 2000; Shepherd and Schumm, 1974; Shrock, 1948; Tinkler, 1993, 1997a; Whipple et al., 2000a; Wohl, 1992, 1993; Wohl and Achyuthan, 2002; Wohl and Ikeda, 1998). Flutes and furrows are relatively shallow compared with potholes; the depths of them are usually much smaller than their lengths (Richardson and Carling, 2005). Longitudinal furrows can be sub-divided into flutes and furrows.

I. Flutes

Flutes, also known as flute marks, are one of the most common kinds of typical abrasion forms on cohesive beds and bedrock channels (Allen, 1971a, 1982; Baker and Kale, 1998; Baker and Pickup, 1987; Gupta et al., 1999; Hancock et al., 1998; Maxson, 1940; Maxson and Campbell, 1935; Richardson and Carling, 2005; Tinkler, 1993, 1997a; Whipple et al., 2000a; Wohl, 1992; Wohl and Ikeda, 1998). The most important previous studies on flutes were conducted on the basis of plaster-of-Paris beds which produced flutes in many different forms in both regular and irregular order (Allen, 1971a, 1982). In these studies, a typical profile of a simple flute in cohesive environment was defined. A standard flute contains a depression on its upstream end with steep lee-side slope and gentle stoss-side slope. The stoss-side upstream-facing slope extends towards downstream direct and becomes indistinguishable. In plan view, a flute has a parabolic outline, round or cusped rims flaring towards downstream direction and becoming indistinguishable. A median ridge lies in the central axis of flute and 2 lateral furrows with cusped rims form along the lateral flanks of the primary flute (Allen, 1971a, 1982; Richardson and Carling, 2005). The downstream end of the flute is usually open. The form of the flutes looks like a ladle without the handle (Figure 5.21A).

In bedrock environments, the form of flutes is mostly similar to those in mud deposits (Richardson and Carling, 2005; Tinkler and Wohl, 1998a; Wohl and Merritt, 2001b). However, no lateral furrows are observed and median ridges are almost missing in natural bedrock substrates (Richardson and Carling, 2005). Various types of flutes that are almost identical with the flutes on natural bedrock channels were produced in the current experiments. They

can be divided into two categories based on their morphology: simple flutes and flutes with secondary structures. According to the proceeding studies, simple flutes can be sub-divided into broad and narrow flutes, deep and shallow flutes, flutes with median ridge, overhanging flutes, spindle-shaped flutes and sinuous flutes by their geometrical morphology (Richardson and Carling, 2005). The flutes with secondary structures contain flutes with internal and external structures, paired flutes, paired convergent flutes, lineations and en echelon flutes (Richardson and Carling, 2005). The most difference between the experimental results and natural sculpted forms is that the flutes forming in current experiments sometimes contains external secondary furrows or flutes along their flanks which do not exist in the natural flutes on real bedrock because after all (Richardson and Carling, 2005), because the experimental substrate used here is the modelling clay still with characteristic of cohesive material instead of real bedrock.

- **Broad and narrow flutes**

Broad flutes are those whose width is no less than their length (Figure 5.20A & B) (Allen, 1971a). Broad flutes were not widely distributed on the experimental bed. Figure 5.20A show two broad flutes forming in the experimental bed and Figure 5.20B is a similar one observed in real bedrock (Richardson and Carling, 2005). The interesting thing is that all these three broad flutes are slightly skewed relative to the flow direction which is from right to left either in the experiment or in the field. The bigger one in Figure 5.20A can even be seen to have an external secondary furrow developing along its northern rim. To some extent, they look like mud ripple in the current experiments.

The narrow flutes, on the contrary, whose length is bigger than their width, are more like the standard flutes model in terms of their parabolic outline in plan view (Figure 5.20C & D) (Allen, 1971a). In current experimental beds, their flanks flare downstream, although the central axis of most of the flutes is skewed a few degrees relative to the flow direction (the lower flute in Figure 5.20C). This is probably because the features are affected by flow from other features leading to an overall asymmetry, or flow isn't perfectly uniform, though it ought to be in such a channel.

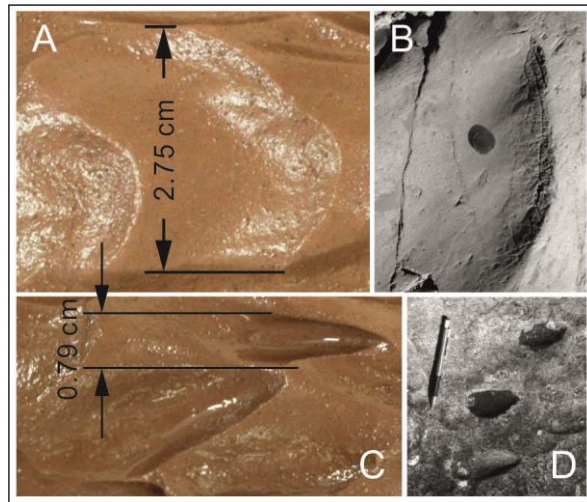


Figure 5.20 Broad and narrow flutes. A shows broad flutes formed on an experimental substrate of Exp. 7. They are 2.75 cm wide and 1.09 cm long. B is a natural broad flute in Wadi Hazazon, Israel. Limestone. Coin is for scale (from Richardson and Carling (2005)). C and D are the narrow flutes in experiments and natural bedrock, respectively. The small one in C is observed in Exp. 7, which is 1.77 cm long and 0.79 cm wide. Flow from right to left. (from Richardson and Carling (2005))

- **Deep and shallow flutes**

According to previous studies, there is no definite limit between deep and shallow flutes (Richardson and Carling, 2005). They were defined by direct observation. In plan view, both of these two kinds are parabolic in outline. The deep flutes, as the name implies, have a relatively deep depression in this proximal end. Figure 5.21A and B are deep flutes on an experimental substrate and natural bedrock, representatively. They are almost identical. Both of them have an internal structure (arrowed in Figure 5.21A and B). The depression of the natural one is about as long as the pen shown in the photo for scale. The only difference between these two is that the flanks of Figure 5.21A are flaring from the proximal end, but from a certain point, they are convergent and form a closed rim at the downstream end. This situation cannot be observed in Figure 5.21B whose flanks become indistinguishable at the downstream end.

In contrast, the depression of the shallow flutes is not as apparent as that of the deep ones. The broad and narrow flutes in Figure 5.20 are all shallow flutes. Figure 5.21C is a typical shallow flute forming on the experimental bed. However, Figure 5.21D can be regarded as an extreme case of the shallow flutes. Its proximal depression is nearly invisible. Only from the parabolic outline and big median ridge/part, can it still be recognized as a

shallow flute. Compared with the depression of shallow flutes, the depression of the deep flutes looks more similar to a pothole.

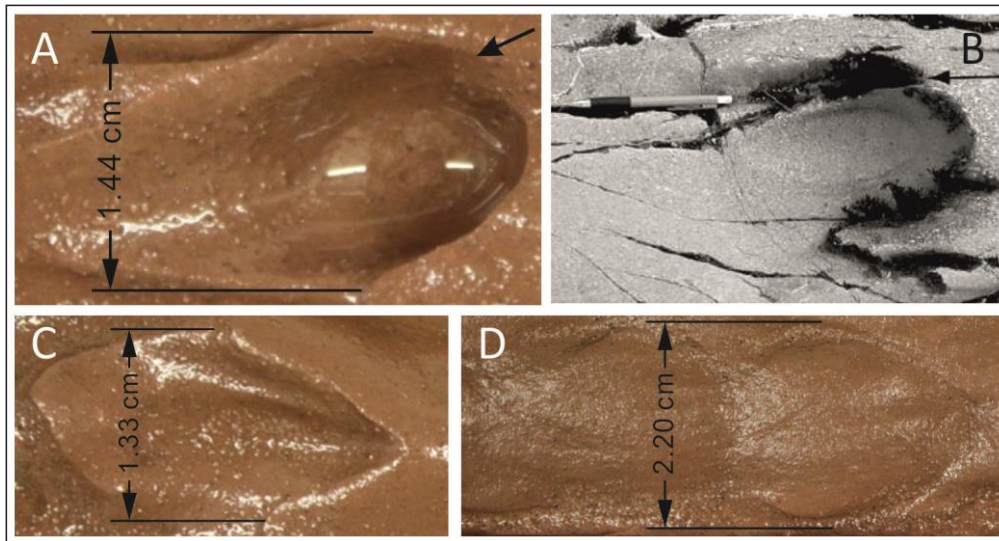


Figure 5.21 Deep and shallow flutes. A. deep flute in Exp. 6; B. deep flute in the natural environment (from Richardson and Carling (2005); C. shallow flute in Exp. 7; D. extremely shallow flute in Exp. 8. Flow from right to left in all cases.

- **Flutes with median ridge (FwMR)**

Median ridges are regarded as one of the typical features of standard flutes in cohesive mud deposits (Allen, 1971a). However, in the experiments with the modelling clay substrate, and in natural bedrock environments, median ridges are rare to see (Figure 5.22). The median ridges of the flutes in Figure 5.22A, B & C are very gradational and are not easy to see. Those in Figure 5.22D & E are obvious. The flute in Figure 5.22E on natural bedrock is the most similar one with the typical flute model raised by Allen (1971a) using plaster-of-Paris. Although the principal depressions of FwMRs in the current experiments were not obvious, The approximate parabolic flutes were still partly visible. The central axis of median flutes sometimes leaned to the central axis of the flutes by a few degrees instead of overlap of it.

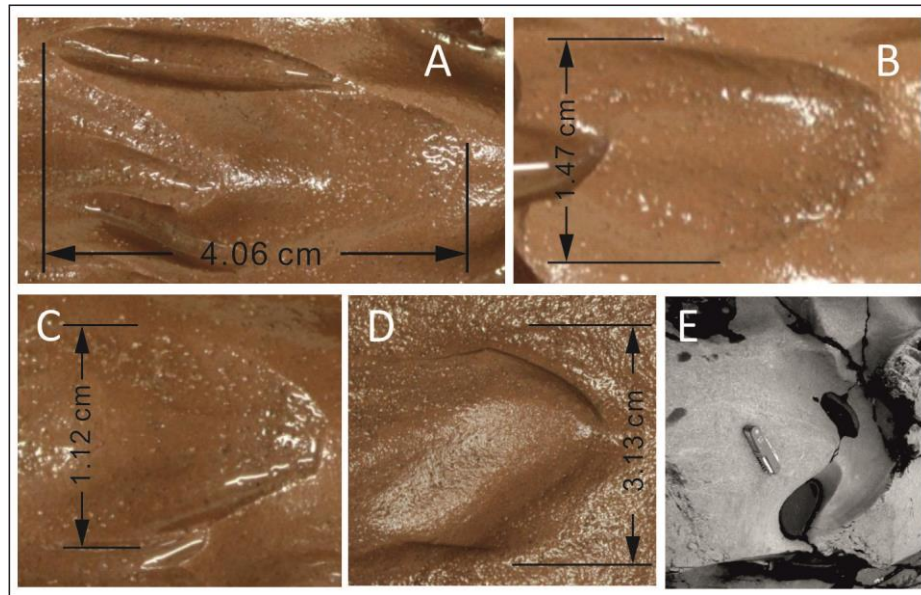


Figure 5.22 Flutes with median ridges (FwMR). A, B, C and D are flutes with median ridges selected from the experimental bed. A, , and C are observed in Exp. 7. D is in Exp.8. E is the one with two internal secondary structures observed in the River Lune (Tebay), UK. Knife is for scale. (from Richardson and Carling (2005).

- **Overhanging flutes (OF)**

The most obvious feature of overhanging flutes (Figure 5.23) is that the proximal rim overhangs its depression, which looks like the '**NIKE** logo:  in longitudinal section, if the flow is from left to right (Hancock et al., 1998; Maxson and Campbell, 1935). Overhanging flutes were not common in the experimental bed. Although they seem easy to recognize compared to the other kinds of flutes, actually, it is not easy to distinguish them from potholes with exit furrows. Some potholes do not cut downwards vertically. It is hard to define the critical point between the hollow of potholes and the depression of the overhanging flutes, especially when the up-facing slopes are similar. Figure 5.23 demonstrates two overhanging flutes in the experimental bed. Except for these two, a number of others can be found in the experiments, but in all cases the depression was cut downwards to eventually form a pothole with time. Consequently, the overhanging rims are not maintained in the process of the experiments. The morphological change will be discussed later in Chapter 6.

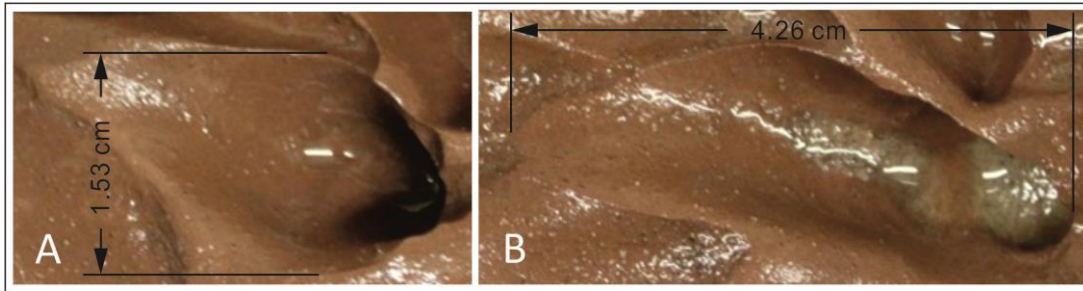


Figure 5.23 Overhanging flutes (OF). A: 1.53 cm in width; B: 4.26 cm in length. Both A and B are observed in Exp. 7. Flow from right to left.

- **Spindle-shaped flute (SF)**

Spindle-shaped flutes are those whose length is several times longer than its width (Figure 5.24) with a sharp/pointed proximal end rim (Allen, 1971a; Baker and Pickup, 1987; Maxson and Campbell, 1935; Tinkler and Wohl, 1998a). They usually do not have lateral furrows and median ridges. Their principal furrows are usually shallow (Allen, 1971a) and the rims are round or cusped. In the experiments, the length: width ratio of them is about 3:1 to 5:1. They were not always strictly symmetrical in form in plan view; some of them were slightly curved or sinuous. They were mainly affected by other kinds of adjacent erosional marks. Figure 5.24A shows one of the straight spindle-shaped flutes in the experiments. Previous studies suggest that spindle-shaped flutes are scour marks initialized from small defects in the rock (Richardson and Carling, 2005). However, in the current experimental substrate, most of them are initialized from a flat bed.

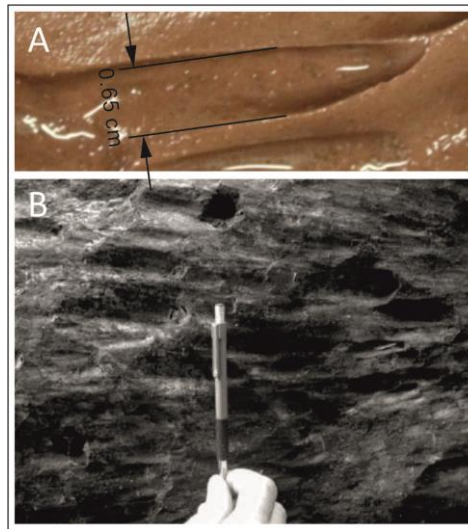


Figure 5.24 Spindle-shaped flutes (SF). A is a typical spindle-shaped flute in Exp. 7. B is a group of SF observed in volcanic rock in Huai Nang Rong, Thailand. Flow from left to right. Pen is for scale (from Richardson and Carling (2005).

- **Comet-shaped flutes (CSF)**

Comet-shaped flutes are actually sinuous flutes (Figure 5.25) (Allen, 1971a, 1982). They are asymmetric instead of parabolic in form in plan view. Most of the flutes in the experiments can be categorized as comet-shaped flutes. They sometimes form independently and sometimes along the flank of other erosional marks. They may be regarded as secondary structures of other erosional features. Their principle furrows are usually shallow and the proximal pointed ends are sharp as those of spindle-shaped flutes. The difference between comet-shaped flutes and spindle-shaped flutes is that the latter are usually straight in plan view and flaring strictly towards the downstream, but the former is sinuous in plan view like comets and sometimes skewed to the flow direction. However, comet-shaped flutes cannot be considered as sinuous spindle-shaped flutes. Some of them are not as narrow as spindle-shaped flutes and have wider distal ends.

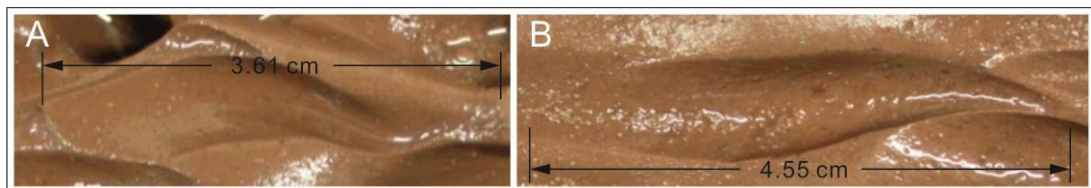


Figure 5.25 Comet-shaped flutes (CSF). CF is kind of sinuous narrow flute with cusped proximal ends. A is in Exp. 7 and B is in Exp. 8. Flow from right to left.

- **Flutes with internal secondary structure (FwISS)**

Flutes with internal secondary structure (Allen, 1971a) are not as common as flutes with external secondary structure in the current experiments. It may be because the scale of flutes forming in the current experiments is too small to contain smaller visible internal secondary structures. Only a few can be observed (Figure 5.26). On the other hand, some of the furrows adjacent to the principle flutes can potentially be confused with lateral furrows. Whether they are lateral furrows or internal secondary structures is hard to say, because the height of their rim is difficult to measure and compare with the rim of the primary flutes. The internal secondary structures are not limited within the range of furrows. Potholes can also be observed developing in a range of flutes. However, the problem is what the right order of these marks forming is. It is hard to say whether the pothole formed first and then the exit furrows formed, or if the flutes formed first and then a pothole developed in its principal proximal depression area, by only observing the final experiments results. The development of complex erosional features will be discussed in Chapter 6.

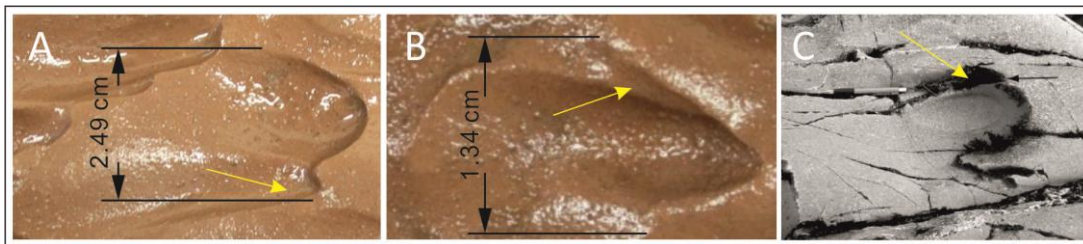


Figure 5.26 Flutes with internal secondary structure (FwISS). The internal secondary structures are usually small furrows within the outline of the flutes. A and B are FwISS Exp. 7 with internal secondary furrows on one side of their flanks (yellow arrowed). C contains a flute close to its upper rim (pointed by the pen) in Borrow Beck, UK. Flow from right to left. Pen is for scale (from Richardson and Carling (2005)).

- **Flutes with external secondary structure (FwESS)**

Most of the flutes in the experiments are classified as flutes with external secondary structures (Allen, 1971a), which form outside of the primary flutes (Figure 5.27A-D). Previous studies indicated that flutes with external secondary structures may be caused by a linear defect (Hancock et al., 1998; Richardson and Carling, 2005). However, in the current experiments, with the exception of experiment 6, there were not any pre-set defects. Figure 5.27E illustrates flutes with external secondary structures, arranged

into a linear set of small flutes in a row, in real bedrock (Richardson and Carling, 2005). The proximal rims of them connect with each other. They extend almost along the flow direction. If the biggest flute located on the top right corner is regarded as the primary flutes, the remaining flutes are getting smaller and smaller along the defect. The experiments indicate that the occurrence of the external secondary structures does not depend on defects. Additionally, the size of these features is variable; sometimes, they are as big as or only a bit smaller than the primary flutes. In other cases, they are much smaller than the primary ones. Figure 5.27 shows some typical flutes with external secondary structures. All of them are primary flutes with more than one secondary flute on one side of its flank (usually the flute-right side when you face downstream). These secondary flutes share lateral rims with adjacent ones. In most cases in the experiments, the rims of the FwESS are cusped.

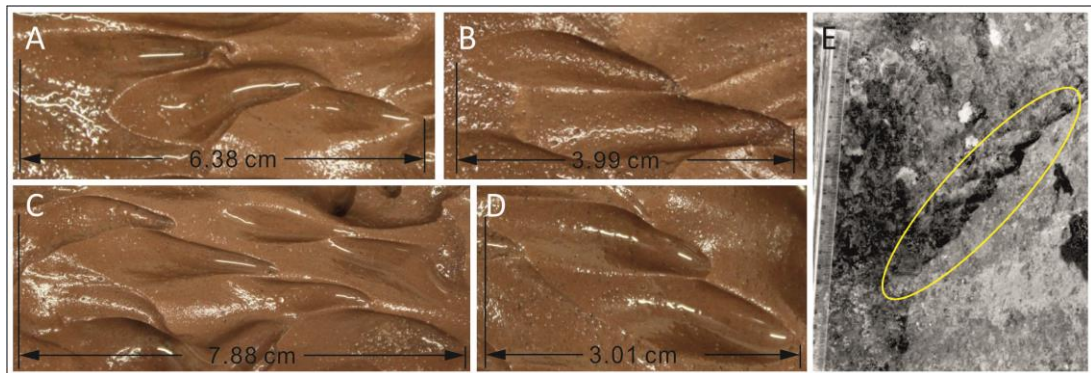


Figure 5.27 Flutes with external secondary structures (FwESS). A, B, C and D are several rows of flutes developing in Exp. 7. Normally the first flute in a row is regarded as the primary flute. The remaining flutes are the secondary ones. E is a row of small flutes (tagged by yellow ellipse) from the River Dee, UK. Flow from right to left. Ruler in centimetres for scale. (from Richardson and Carling (2005)).

- **Paired flutes (PF)**

Paired flutes (Figure 5.28) are two short flutes developed in pairs that share one of their lateral rims (Richardson and Carling, 2005). The separate flutes in paired flutes are approximately symmetric with respect to the shared lateral rim which can be regarded as the median axis if the paired flutes are considered as a whole. Generally, in the whole set, in other words, the median ridge of them developed in line with the flow direction. However, two separate flutes were sometimes divergent or convergent with each other. On the current experimental bed, paired flutes occasionally have open proximal

ends (Figure 5.28B), which is the distal end of a furrow ahead of it. This will be discussed in Chapter 6 later. Nevertheless, the features of the paired flutes are very distinct. Some paired flutes are a pair of short curved flutes. They are slightly rotated and were not strict symmetrical (Figure 5.28A).

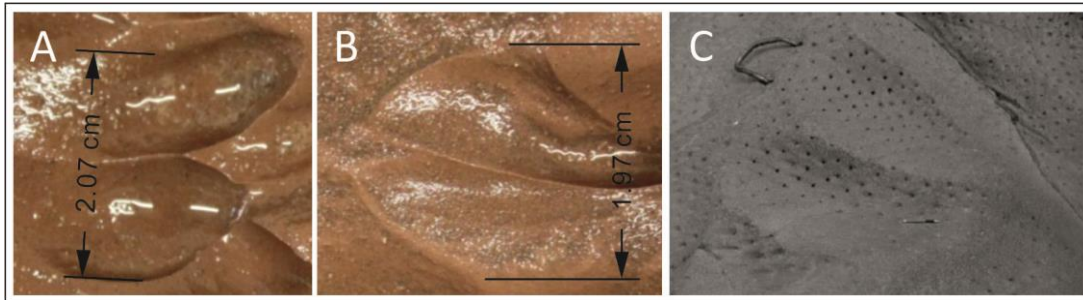


Figure 5.28 Paired flutes (PF). A and B are PF from Exp. 7 and 6, respectively. Two solo flutes which share a flank rim comprise paired flutes. These two flutes are symmetrical or approximately symmetrical. C is a paired flute developed in Nam Mae Chaem (Ob Luang), Thailand. Flow from right to left. Pen is for scale. (from Richardson and Carling (2005)).

- **Paired convergent flutes (PCT)**

The profile of paired convergent flutes (Figure 5.29) are new features which do not fit into any of the existing categories in the literature. They are slightly similar to that of approximate symmetrical paired potholes with exit furrows (ASPPwEF) (Figure 5.29). PCF contains two narrow flutes, a broad median ridge and a pair of secondary furrows developing on the distal half of the median ridge. If the PCF is considered as a whole, it looks like a big flute with open ends. However, at the location of the furrows in PCT, the ASPPwEF have two potholes. On the other hand, the outline of PCF is slightly convergent at the distal end rather than flaring. Two furrows are slightly curved and convergent inwards with cusped rims. Both of them contain an external secondary furrow located adjacent to the inner side of the short furrows. These two secondary furrows are partially lateral furrows and are actually raised on the distal part of the median ridge of the PCF. They share one rim with each other whose altitude is bigger than the other rims. This kind of furrow was not reported to be observed in the field before. Hence, whether this kind of special furrow can form on real bedrock is still questionable.

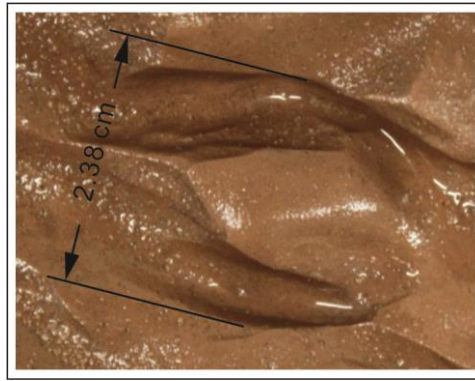


Figure 5.29 Paired convergent flutes (PCF). Two symmetrical slightly curved flutes with lateral secondary furrows and a big median ridge form a PCF. The whole system is observed in Exp. 7, which is about 2.38 cm wide. Flow from right to left. (from Richardson and Carling (2005)).

- **Lineations**

Lineations consist of a group of small flutes and short furrows with small scale ridges between adjacent marks (Figure 5.30). They have rarely been observed in the field (Figure 5.30B) (Richardson and Carling, 2005). In current experiments, they can only be observed in the initial stage of experiments. At this stage, all the marks were shallow, short and straight and both ends of them were open. The rims of them were approximately parallel and round. The spaces between two of them look like round ridges. Most of them were orientated dominantly parallel to the flow direction, as with those observed in the field. However, in the experiments there were still a few of them that were curved or sinuous and oblique to the flow direction. According to the hypothesis of previous studies, this kind of mark forms from the distal parts or extension of the spindle-shaped flutes which develop from small defects. These small defects are regarded as finally polished with only the small distal furrows of initially large features remaining in the bedrock (Richardson and Carling, 2005). However, in the experimental bed, similar marks were found in the initial stage of the experiments after 240-min rumming of Exp. 7, instead of towards the end stage. They almost look like fluid stressing features. In the last stages of the experiments, though there are many marks that remain in the experimental beds, most of them did not arrange themselves in rows and parallel to the flow direction, and the features are not that shallow. The rims of them are partially polished by sediment-laden flow, but some of them are still cusped. Therefore, lineations are considered as the initial form of the erosional furrows instead of the final form, based on the current experiments.

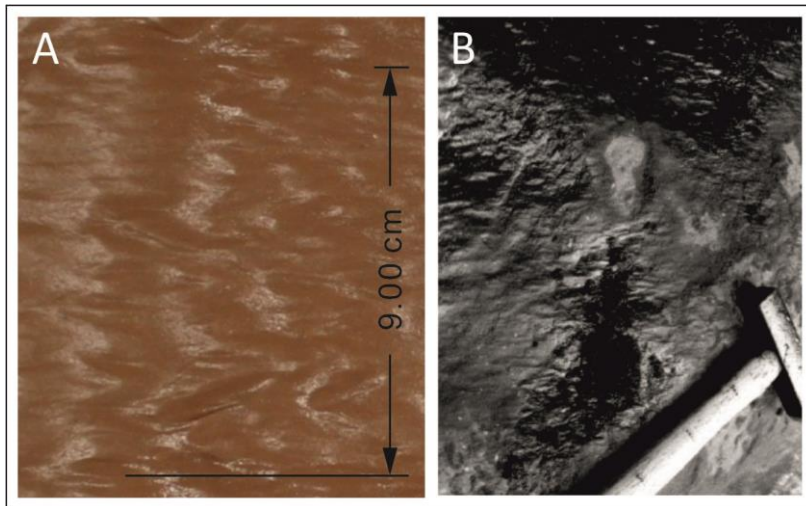


Figure 5.30 A. Lineations as seen on the bed of Exp. 7. These short flutes and furrows are about 1.0 - 1.5 cm long and 0.2-0.4 cm wide. B shows lineations in the field, from the River Dee, UK. Flow from right to left. Hammer is for scale. (from Richardson and Carling (2005)).

- **En echelon flutes**

En echelon flutes (Figure 5.31) are a group of deep flutes that assemble in a special 'Y' mode in plan view. This kind of flute is rare to see either in the field or in the experimental beds. Figure 5.31A is the only set of en echelon flutes in the experimental bed. It developed in a small area of the proximal part of the mud bed. This en echelon set contains only 6 flutes. Most of them are short flutes with approximately parabolic profile in plan view. The principle depressions of each of them are relatively deep compared with surrounding marks. Some of them share rims which are cusped. The lee-side slopes of them are steep and the stoss-side sides are much gentler and become difficult to distinguish.

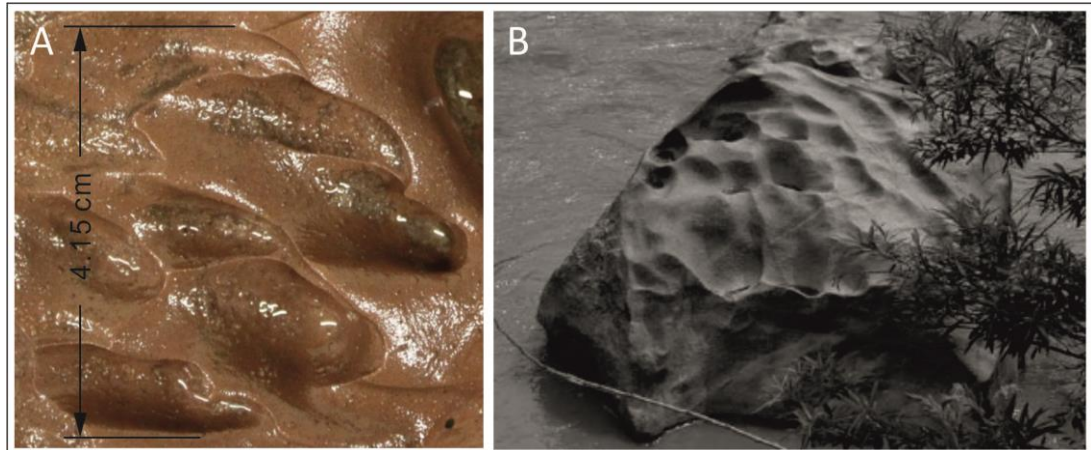


Figure 5.31 A shows a set of En echelon flutes formed in Exp. 7. Each of the flutes is about ~1.0-2.5 cm long, ~1.0-1.5 cm wide and ~0.8 cm deep. Flow is from right to left. B shows en echelon flutes in Nam Mae Chaem (Ob Luang), Thailand. Flow from bottom right to top left. The rock projection is about 4 m across (from Richardson and Carling (2005)).

II. Longitudinal furrows

Furrows (Figure 5.32) are the other common longitudinal abrasion marks in cohesive beds and bedrock channels. According to the definition of a typical furrow, the distal end should be the mirror image of its proximal end (Allen, 1969, 1971a, 1974; Baker, 1973; Blank, 1958; Dzulynski and Sanders, 1962; Friend, 1965; King, 1927; Richardson and Carling, 2005; Shaw et al., 2000; Shepherd and Schumm, 1974; Shrock, 1948; Wohl, 1993; Wohl and Achyuthan, 2002). The rims of furrows are normally parallel and round or cusped. Both ends of furrows are closed, for example, short furrows are elliptical in plan view (Figure 5.32). In the other situation, the rim of them is open like long parallel sided furrows. They can be straight, curved or sinuous. The key difference between furrows and flutes is that furrows are symmetric in both cross-sectional and longitudinal profile. The experimental bed witnessed the evolution of the replica of most of the furrows occurring in the field. The classification of furrows is similar to that of flutes. The normal longitudinal furrows include short and long furrows, narrow and deep furrows, open and closed furrows, furrows with round or cusped rims, straight and curved furrows, sinuous furrows, parallel-sided furrows, shear zone furrows, bifurcating furrows, convergent furrows, regular and irregular compound furrows, and expanding furrows. The non-longitudinal furrows contain reversed furrows, hummocky furrows, obstacle marks, and bladed

forms (Richardson and Carling, 2005). Most kinds of them can be produced in the experiments reported here.

- **Short furrows**

Short furrows (Figure 5.32C) usually have closed elliptical rims in plan view. Their depth is less than their length. Typically, they are not as deep as potholes, although potholes are sometimes elliptical in plan view. The cross section of a short furrow is a 'U' shape. The inner wall and the bottom of the furrow are usually smooth (Allen, 1971a; Richardson and Carling, 2005). The depth of the depression is variable, although the depth of a shallow furrow is no more than a quarter of their length (Figure 5.32A, C & D), and conversely for deep furrows (Figure 5.32B) (Richardson and Carling, 2005).

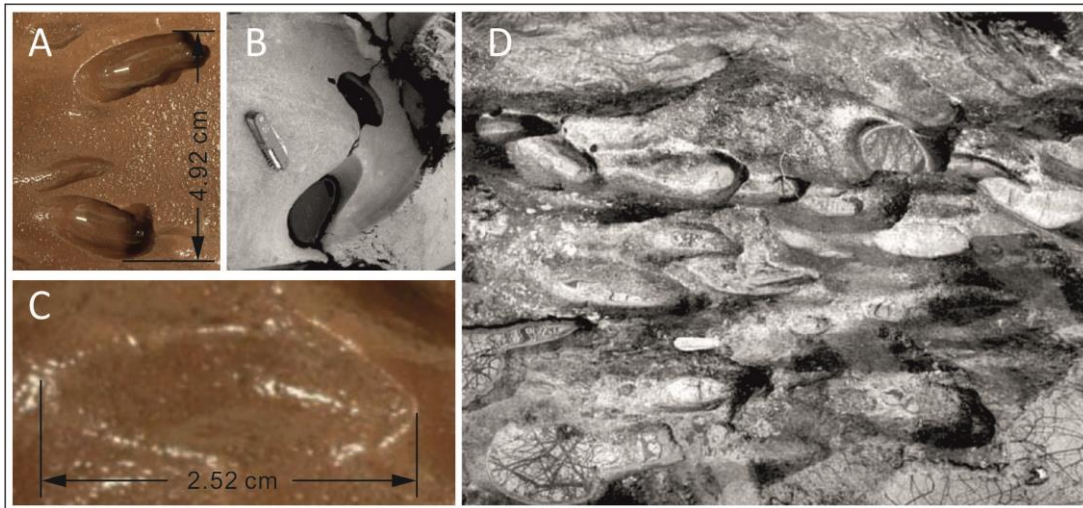


Figure 5.32 Straight short furrows (SSFrw). A and C are straight short furrows in Exp. 7. Furrows in A are 2.5-2.95 cm long and 1-1.15 cm wide. B and D are those in the field, River Dee, UK. Flow from right to left. Knife is for scale. (from Richardson and Carling (2005)).

Curved short furrows (Figure 5.33) were also observed on the experimental bed, although infrequently. They are not long and straight and symmetrical in plan view. The proximal end still points in the upstream direction, but the distal end slightly rotates and points no longer directly towards the downstream end. However, overall the dominant orientation is longitudinal in the downstream direction. The ends of them are not always closed, for example, the curved furrow in Figure 5.33A has a closed proximal end and an open distal end. Except for the round rim of the proximal end, the rest of the side rims are almost parallel.

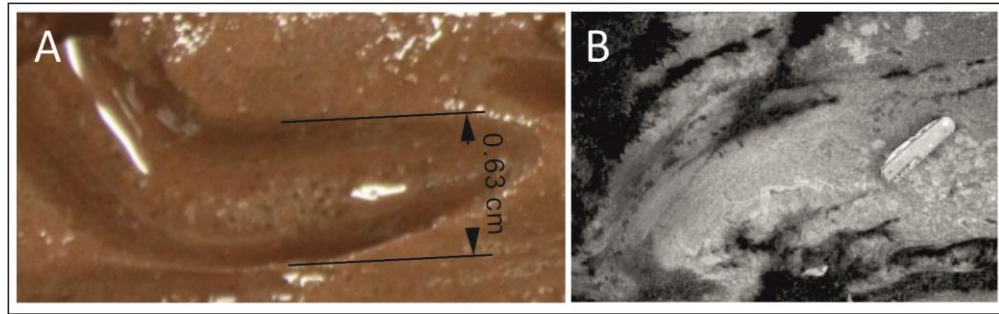


Figure 5.33 Curved short furrows (CSFw). A and B are curved short furrows in Exp. 7 and in the natural bedrock channel respectively. A is about 2.33 cm long and 0.85 cm wide. Flow from right to left. B. Knife is for scale. (from Richardson and Carling (2005)).

Figure 5.32 & Figure 5.33 also demonstrate cusped (Figure 5.32A, B D) and non-cusped short furrows (Figure 5.32C & Figure 5.33B). The rim of cusped furrows is sharper than non-cusped. However, it is hard to define the limit between the cusped and non-cusped furrows. In the current experiments, cusped short furrows were more widely distributed on the harder mud beds (Exp. 6 & 7) than on the softer mud beds (Exp. 8). Therefore, in real bedrock channels, the frequency of cusped furrows may be greater than that of non-cusped furrows.

- **Parallel sided furrows (PSFw)**

Parallel-sided furrows (Figure 5.34) (Allen, 1971a) can be simply considered as long furrows. In fact, most of the furrows have parallel sides except short furrows. The reason for short furrows missing parallel sides is just because they are too short to show the straight part of the sides. Once the size of the furrows exceeds the short elliptical profile, the sides of furrows are mostly parallel, no matter whether the furrows are straight, curved, sinuous, reversed or any other form.

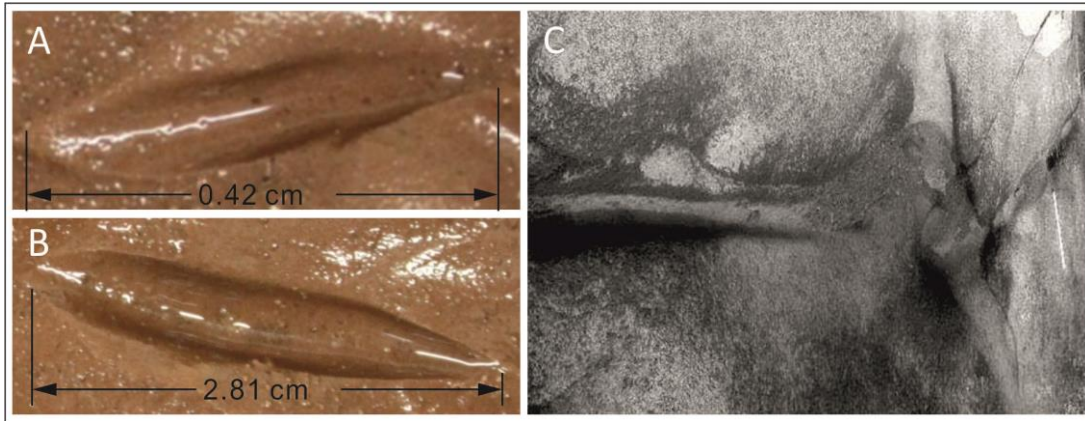


Figure 5.34 Straight parallel-sided furrows (SPF_{rw}). Straight furrows have parallel flank rims which are round or cusped. A is from Exp. 8 and B is from Exp. 7. Flow from right to left. (from Richardson and Carling (2005)).

The straight parallel sided furrow is the most typical kind of long furrow (Figure 5.34) (Allen, 1971a). The length of them is at least as twice long as their width. Both side rims of them are parallel with each other. The ends of them are either closed (Figure 5.34) or open (Figure 5.34C & Figure 5.35A). The rim of them is cusped (Figure 5.34B & Figure 5.40) or non-cusped (Figure 5.34A & C), and this depends on the stage of erosion and on the adjacent topography, which will be discussed in detail in Chapter 6. The cross section of it is still a smooth 'U' shape like that of short furrows (Richardson and Carling, 2005). Except for the proximal and distal closed ends, the depth of the rest of them is approximately uniform. The distal end of straight parallel sided furrows points approximately downstream (Figure 5.34C & Figure 5.40), although a few of them are slightly oblique to the flow direction (Figure 5.34A & B).

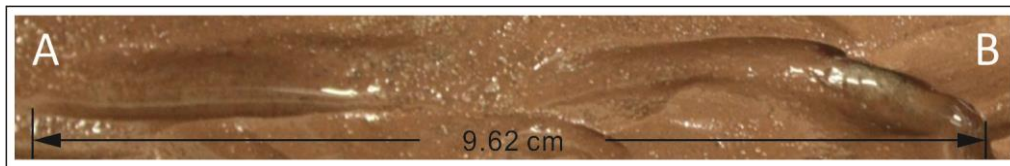


Figure 5.35 Cusped and non-cusped parallel-sided furrows (CPSF_{rw} or NCPSF_{rw}). A: non-cusped straight parallel sided furrow; B: cusped curved parallel sided furrow. They are from Exp. 7. Flow from right to left.

The opposite of straight parallel-sided furrows are sinuous parallel-sided furrows (Figure 5.36) (Wohl and Achyuthan, 2002). The length of them is

various and ranges from 1 cm to more than several tens of centimetres (Figure 5.36). The dominant orientation of them is longitudinal with either proximal or distal ends that curve away from the flow direction, and a sinuous furrow body. Although the furrows are sinuous, the rims of them are still parallel. The ends are either open or closed which is affected by the topography of the surrounding area. The slope of both ends is gentle and the rims are either round or cusped. The walls and the bottom of them are usually smooth without secondary structures or defects. The inner lateral wall in the middle part of them is steep. Some long sinuous furrows were developed from the connection of the curved or sinuous short furrows. Therefore the depth of them is sometimes not uniform.

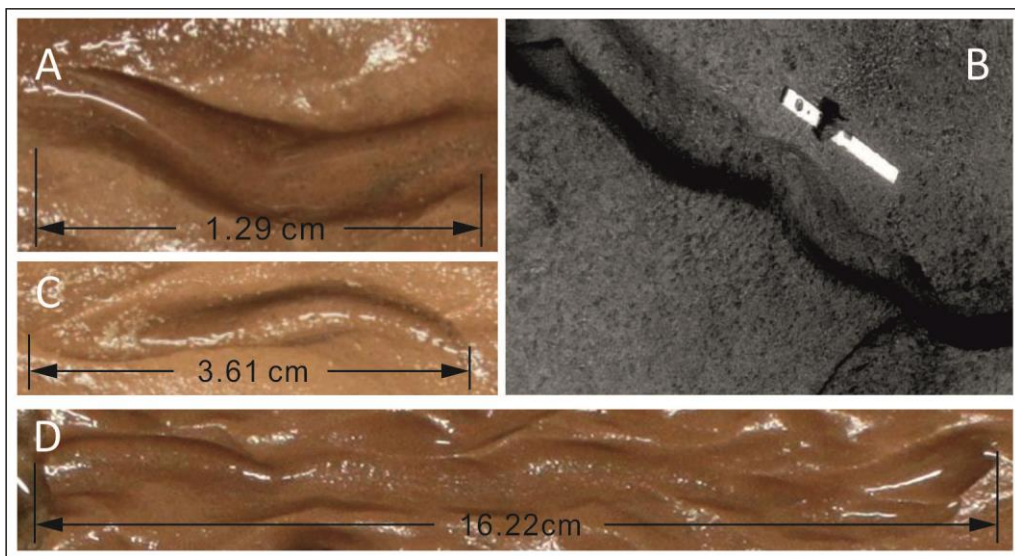


Figure 5.36 Sinuous parallel-sided furrows (SPSFrw). A, C & D: examples of features observed in Exp. 8, 7 and 6, respectively. Flow from right to left. B was observed in River Lune (Halton), UK. Flow from bottom right corner to top left corner. The scale is 60 cm long. (from Richardson and Carling (2005)).

- **Shear zone furrows (SZFrw)**

Theoretically, shear zone furrows (Tinkler, 1997a) should not occur in these experiments, because they were conducted without any obstacles on the bed. The formation of shear zone furrows purportedly needs the support of such obstacles which can produce a flow separation zone/shear zone behind it. It is rare in the field (Figure 5.37C) (Richardson and Carling, 2005; Tinkler, 1997a). Figure 5.37C demonstrates a simple and small shear zone furrow in the field which forms behind a large rock that is acting as an obstacle. The shear zone furrows occurred in pairs in the experimental bed and show some similarities to the example observed in the field (Figure 5.37A, & B). Although there are no pre-set obstacles on the bed, erosion created an elevated protuberance that evolved into an obstacle (Figure 5.37 A & B, area circled). Right behind this, elevated region two adjacent sinuous furrows developed. Both of them have closed proximal ends and open distal ends and share one rim. The water flowed over the obstacle and entered into the flow convergent zone triggering the formation of the shear zone furrows. However, the reason for why they occur in pairs in the experiments is not clear.

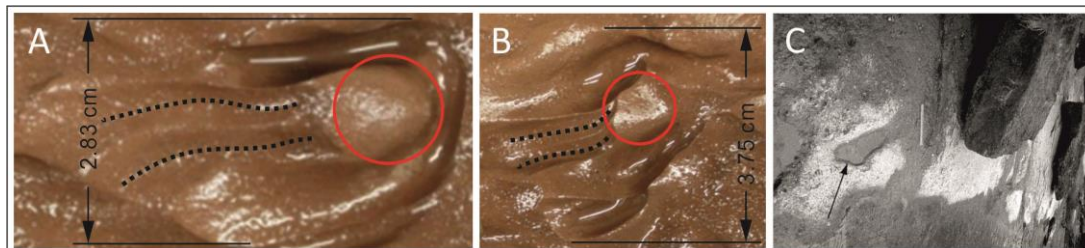


Figure 5.37 Shear zone furrows (SZFrw). Flow from right to left. A & B are shear zone furrows in Exp. 7; the red circles mark the position of an elevated region that may have acted as an obstacle to the flow. C is one found in a real bedrock channel, from Birk Beck, UK. Flow from top to bottom. The scale is about 30 cm long. (from Richardson and Carling (2005)).

- **Bifurcating furrows (BFrw)**

Bifurcating furrows (Figure 5.38) are furrows that divide into two longitudinal branches in the downstream direction, and are orientated dominantly along the flow direction (King, 1927; Richardson and Carling, 2005). According to previous studies, the dividing point would be a relatively gentle and rounded raised part (Figure 5.38D) (Richardson and Carling, 2005). They were not well distributed in the experiments, maybe because there were not many

relatively raised parts that formed in the experiments. Figure 5.38A, B & C are the only examples of bifurcating furrows. The primary furrows are not particularly clear but are still partially visible (Figure 5.38A & B), however the raised dividing points are prominent. The raised area in Figure 5.38A looks like those shown as the obstacle in Figure 5.37. The dividing points of Figure 5.38B, C & D meet the essential criteria of a gentle and rounded raised part for the formation of bifurcating furrows. The size of the bifurcating furrows in Figure 5.38A & B is relatively small compared with the one shown in Figure 5.38C. Figure 5.38C is a very special case of bifurcating furrows. The primary furrow is obviously broader than two following branches. It divided from the raised protuberance to two narrower branches. These two branches are actually composed of a series of straight, curved or sinuous parallel-sided furrows. They are divergent from the dividing point and flare dominantly towards the downstream direction. If each of the branches is considered as an isolated series of furrows, they are irregular compound parallel-sided furrows with irregularly spaced depressions (Wohl, 1993). The length and width of each small furrow is very similar, ranging from ~2-5 cm long and 0.5-1.5 cm wide.

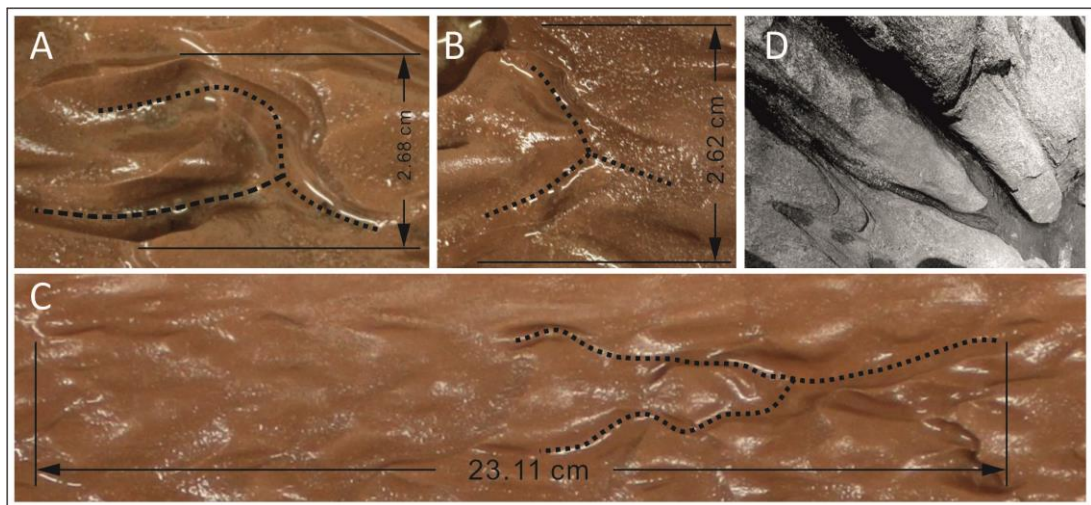


Figure 5.38 Bifurcating furrows (BFrw). A, B & C: bifurcating furrows in the experiments; A is observed in Exp. 7; B and C are in the bed of Exp. 8. Flow from right to left; D: Bifurcating furrow in the field, Woolshed Creek, Australia. Flow from top right to bottom left (from Richardson and Carling (2005)).

- **Convergent furrows (CFrw)**

Convergent furrows (Figure 5.39) can be regarded as the opposite case of bifurcating furrows, although this concept was not defined by preceding studies. This kind of furrow is a new type of furrow, and has not been reported

from the field, and are rarely observed in the experiments. Therefore, they can be considered as a new form of furrows. The convergent furrows herein contain a pair of furrows (Figure 5.39) which extended towards the downstream and eventually merged to be one furrow. The two isolated furrows are curved parallel-sided furrows. The left side wall of them is apparently steeper than the right side wall. The left rim (as looking downstream) of the convergent furrow in Figure 5.39 is cusped but the right one is round.

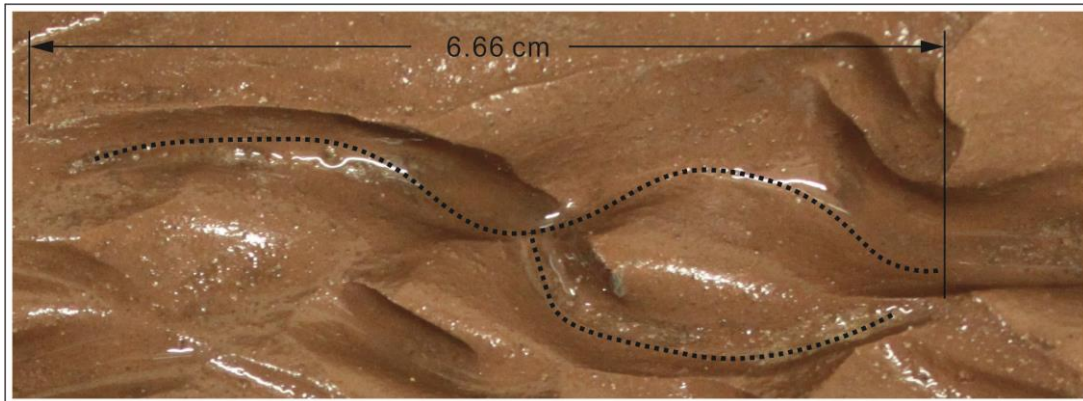


Figure 5.39 Convergent furrows (CFrw) in the bed of Exp. 7. Flow from right to left.

- **Group of parallel-sided furrows (GPSF)**

Previous studies defined groups of parallel-sided furrows as a lot of individual furrows with regular transverse spacing among them (Allen, 1969, 1971a; Baker, 1973; Blank, 1958; Dzulyński and Sanders, 1962; King, 1927; Shepherd and Schumm, 1974; Wohl, 1993). Normally, this kind of group occurs on a high-energy intertidal rock platform in an estuarine environment (Allen, 1987). The experiments conducted show a number of differences to this definition, notably the quantity of individual flute in the GPSF is not massive, the transverse spacing among furrows is irregular and the shape of individual furrows is not uniform (Figure 5.40A). Although they show differences to those observed in estuarine environments, they may correspond to the groups of parallel-sided furrows observed on channel margins which are irregular and less extensive (Figure 5.40B).

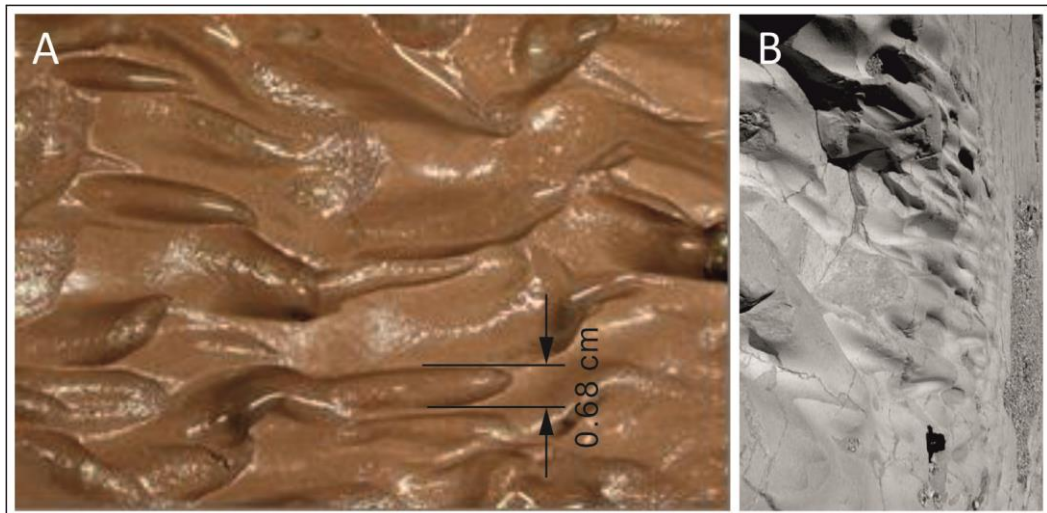


Figure 5.40 Groups of parallel-sided furrows (GPSF). A: GPSF obtained in Exp. 7. Flow from right to left. B: GPSF in the field, Wadi Hazazon, Israel. 20 cm wide camera bag is for scale. Flow from right to left (from Richardson and Carling (2005)).

Compound parallel-sided furrows can simply be regarded as a row of individual simple parallel-sided furrows with similar profile or features. In most of the cases, they are no less than two furrows, have undulating rims and floors, and are arranged in a row that is approximately linear. A longitudinal spacing or raised part occurs between a furrow and its upstream/downstream neighbours (Richardson and Carling, 2005). Compound parallel-sided furrows can be sub-divided into regular compound furrows and irregular compound furrows.

- **Regular compound furrows (RCF_{rw})**

Strictly speaking, regular compound furrows are defined as a linear series of similar furrows linking end to end but being separated by cusped crests between each other (Figure 5.41B) (Richardson and Carling, 2005). Nevertheless, if they are defined as adjacent furrows that are laterally offset replicas of the upstream one (Richardson and Carling, 2005), the curved furrows in Figure 5.41A can be classified as regular compound furrows, although they are not strictly identical. Regular compound furrows were almost missing in the experiments, except for the one shown in Figure 5.41A.

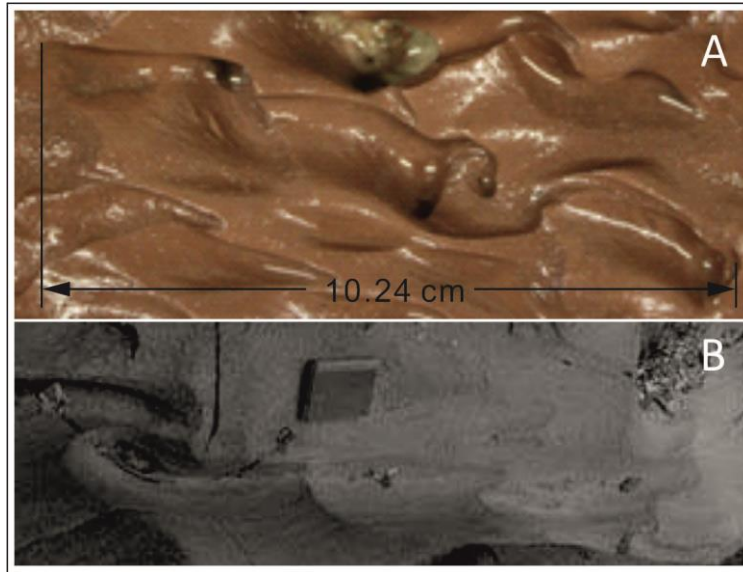


Figure 5.41 Regular compound furrows (RCF_{rw}). A RCF in Exp. 7; B: RCF in the field, from Than Rattana, Thailand. Flow from right to left. The notebook (15 cm long) is for scale (from Richardson and Carling (2005)).

- **Irregular compound furrows (IRCF)**

Irregular compound furrows (Figure 5.42A & B) were easier to observe in the experiments compared with regular compound furrows. The difference between irregular and regular compound furrows is that adjacent individual short or parallel-sided furrows are not in similar repeated forms and do not connect end to end. In Figure 5.42A & B, a longitudinal spacing can be observed between two furrows in the longitudinal direction. The individual ones in the series of irregular furrows could be short straight furrows, curved parallel-sided furrows, or sinuous parallel-sided furrows (Kor et al., 1991; Richardson and Carling, 2005; Shaw, 1996). The depth, the form of the rim of each furrow may differ. Irregular compound furrows are dominantly linear towards the downstream direction.

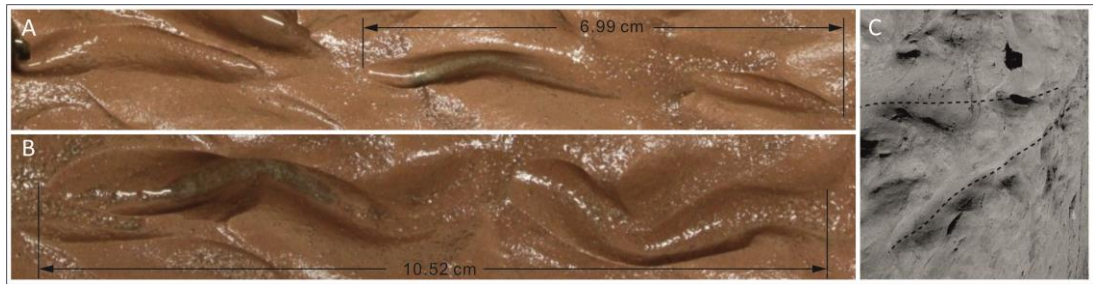


Figure 5.42 Irregular compound furrows (IRCF). A & B: IRCF in Exp. 7; Flow from right to left. C: IRCF in the field, Nahal Zin, Israel. Camera bag (20 cm wide) is for scale. Flow from top right to bottom left (from Richardson and Carling (2005)).

- **Expanding furrows (EF)**

Expanding furrows (Richardson and Carling, 2005) were rare in the experiments; Figure 5.43A, B & C illustrate the only three examples which can be classified into expanding furrows. They no longer keep the typical parallel-sided furrow shape. However, the proximal part of them is still in the shape of normal parallel-sided furrows, though sometimes it is curved or sinuous. The distal end of this kind of furrow expands to be an irregular closed depression. Expanding furrows have two forms according to previous studies (Richardson and Carling, 2005). One is a funnel-shaped furrow (Figure 5.43D), and the other are bulbous furrows (Figure 5.43E). Figure 5.43A is more like a funnel-shaped furrow and Figure 5.43B & C are very similar with bulbous furrows having a big round depression at the distal end.

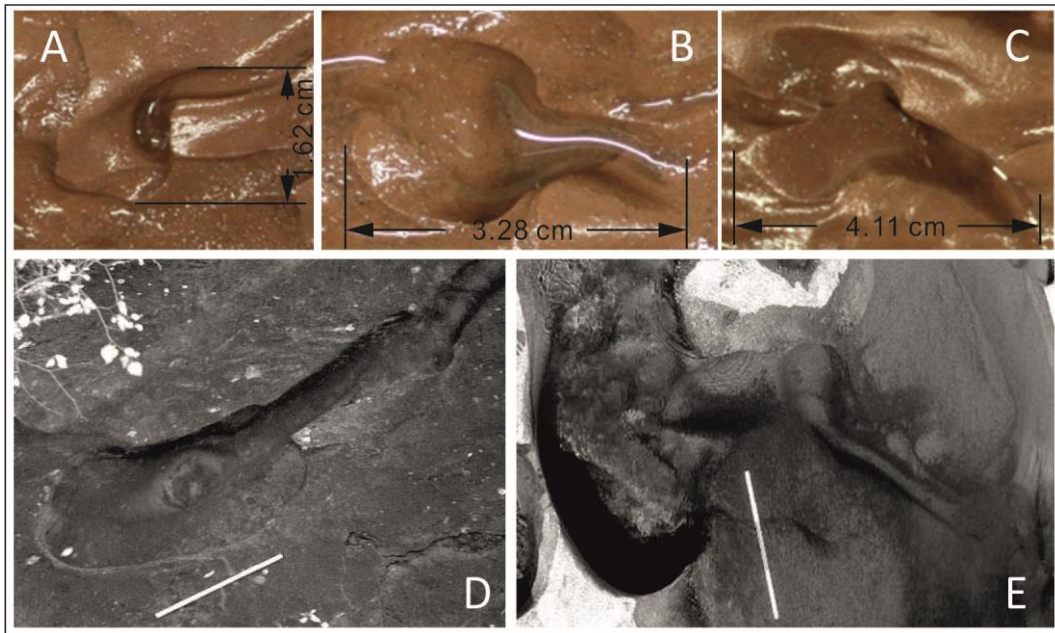


Figure 5.43 Expanding furrows (EF). A, B & C: EF in the experiments. A and B are in Exp. 7; C is in Exp. 8. Flow from right to left. D: Funnel-shaped furrow in the field, Stakeley Beck, UK. Flow top right to bottom left. The scale is 60 cm long. E: Bulbous furrow in the River Lune (Halton), UK. Flow from right to left. Scale is 60 cm long (from Richardson and Carling (2005)).

5.3.4 Non-longitudinal furrows

All of the above mentioned furrows are longitudinal furrows that develop dominantly along the flow direction. Non-longitudinal furrows mean any other furrows that do not evolve along the flow direction. The form and the orientation of them dramatically vary from longitudinal furrows, principally affected by the flow and the morphology of special areas. The main kind of non-longitudinal furrows in the experimental beds is reversed furrow (Richardson and Carling, 2005).

- **Reversed furrows (RF)**

In the field, reversed furrows are thought to occur in the lee side of rock projections due to the effect of recirculating flow in the lee side of the projection (Figure 5.44D, E, F & G)(Richardson and Carling, 2005). In the experimental beds, reversed furrows are observed, however, they are not located in the lee side of anything like rock projections. The furrows reverse in front of raised areas and they incise directly downwards and extend transversally around these protuberances. In the experiments the right end (as looking downstream) of them is closed and the left end is open; the rims are approximately parallel. The depth of the right closed end is slightly

deeper than the left open end. The slopes of the stoss and lee sides are similar; both of them are steep in Figure 5.44A, but gentle in Figure 5.44B. The genesis of these two examples of reversed furrows may be similar, related to obstacle marks, as discussed in section 6.2.4. A similar situation to those observed in real bedrock, is illustrated in Figure 5.44C; the furrows are located in the lee-side of an erosional mark, the raised area in front of them can be regarded as the projection which induced the formation of these reversed furrows. The flow direction within the reversed furrows in the experiments will be introduced in Chapter 7.

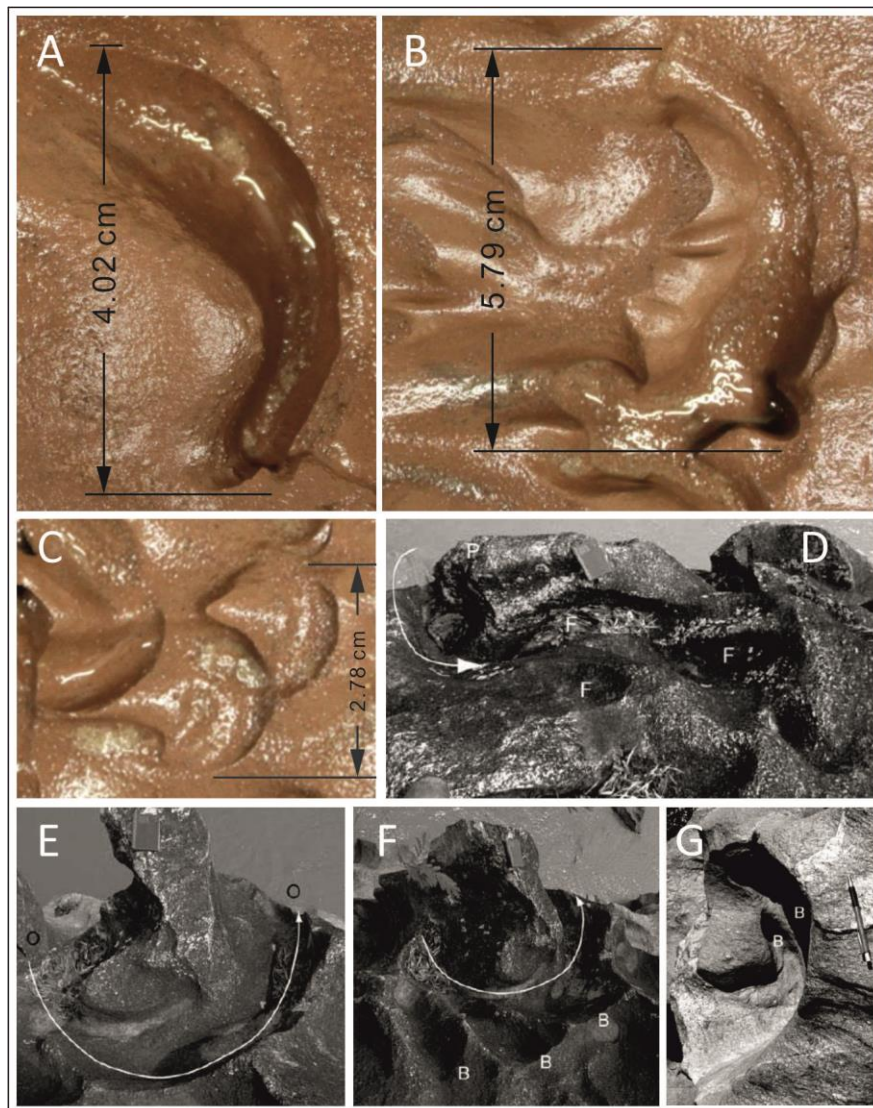


Figure 5.44 Reversed furrows (RF). A, B & C: reversed furrows in experimental bed. A is in Exp. 8; B and C are in Exp. 6. Flow from right to left. D to G: RF in the field from Nam Mae Chaem (Ob Luang), Thailand; flow from top to bottom (from Richardson and Carling (2005)).

5.3.5 Convex and undulating surfaces

Apart from potholes, flutes and furrows, a few convex and undulating surfaces form on experimental beds as well. Hummocky forms are the most important forms in this category (Richardson and Carling, 2005). The most common kind of hummocky form in the experiments is sharp-crested hummocky forms (SCHF). This kind of form looks like standard ripples and dunes on cohesionless substrates, but with obvious sharp crests (Figure 5.45). This is why some of these forms are named pseudo-ripples and pseudo-dunes (Figure 5.45) (Ängeby, 1951; Baker and Kale, 1998; Hancock et al., 1998; Richardson and Carling, 2005; Whipple et al., 2000a; Wohl, 1992).

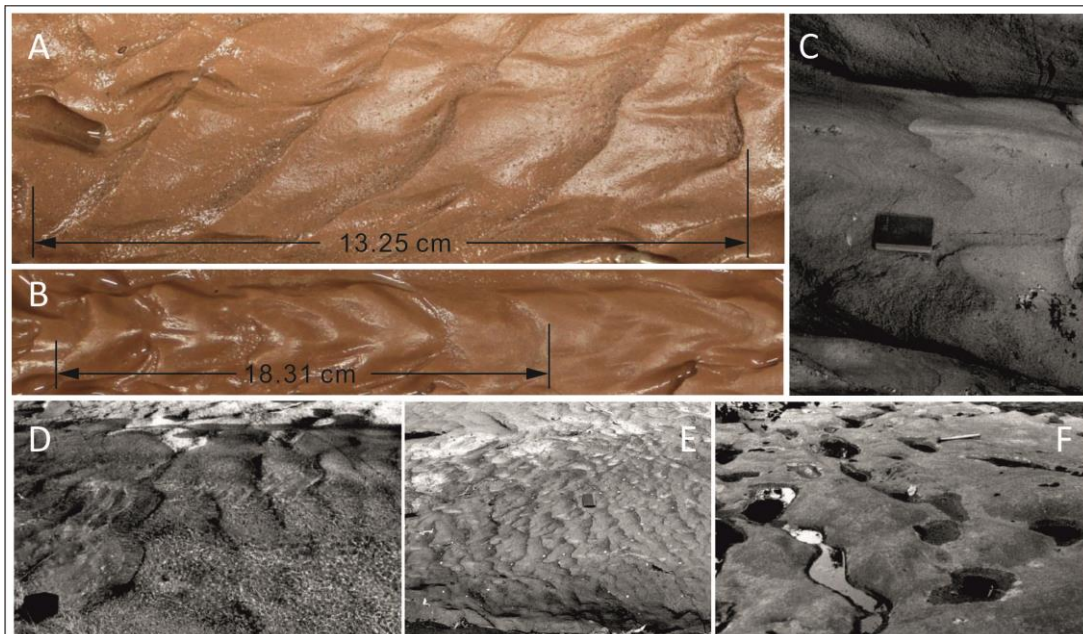


Figure 5.45 Hummocky forms (HF). A-B: Regular trains of sharp-crested hummocky forms (SCHF) obtained in Exp. 7 and 8, respectively. Flow from right to left. C to F: HF found in natural bedrock surfaces (from Richardson and Carling (2005)).

● Sharp-crested hummocky forms (SCHF)

The sharp crests are the key feature of the SCHF. The crests developed non-longitudinally and divide the convex form into two part, stoss side and lee side. The slope of the lee side is often steeper than that of the stoss side. In the experiments, the sinuous crests are parallel to each other and the form of the convex parts is similar. The convex forms are arranged in rows with regular spacing and orientation parallel to the flow direction (Figure 5.45A-D) producing regular trains of SCHF (Richardson and Carling, 2005).

- **Bladed forms (BFm)**

Bladed forms are the other common convex forms in both the experimental beds and in natural bedrock channels. The bladed forms here principally refer to the projections between two adjacent concave forms. For example, the shared rim of two flutes or furrows, or the cusped crest between two connected flutes or several secondary flutes in a compound form (Figure 5.46). Bladed forms do not have a standard form. Briefly, they are the sharp connection crest of any two adjacent concave marks on the substrate.

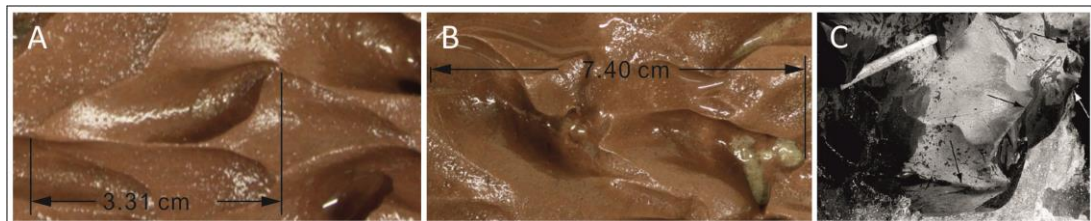


Figure 5.46 Bladed forms (BFm). A & B: Bladed forms observed in Exp. 7 and 8, respectively. Flow from right to left; C: Bladed forms in a real bedrock surface from River Lune (Tebay), UK. Flow from top right to bottom left (from Richardson and Carling (2005)).

5.3.6 Composite forms

Composite forms are the combination of the concave forms and convex forms (Richardson and Carling, 2005). The most common composite forms are obstacle marks and hummocky forms with linear depressions. Within the range of concave or convex features, secondary structures can form and develop. In current experimental bed, no hummocky forms with linear depressions could be observed and only obstacle marks were found.

- **Obstacle marks (OM)**

Obstacle marks (Figure 5.47) are one of the most common and important composite forms in the field (Allen, 1965, 1974, 1982; Baker, 1973; Dzulyński and Sanders, 1962; Dzulyński and Walton, 1965; Karcz, 1968; Lorenc et al., 1994; Peabody, 1947) and also well developed on the experimental beds. In the field, obstacle marks are scour marks caused by the recirculating flow when flow meets projections on the substrate. These scour marks develop to be current crescents in the bed. In the experiments, obstacle marks consist of a raised projection with a round stoss side surface and a current crescent reversed furrow upstream of it. The current crescent is parallel-sided in plan view with open or closed ends. This form corresponds with the definition given by proceeding studies (Peabody,

1947). They are created by the secondary flow structures in front of the raised projection. They tend to form behind a small defect which could be pre-set or initiate from a pothole or other incipient small scale concave features. When the flow met the stoss side wall of these concave forms and was stopped by it, the flow direction changed and went sideways along the wall. The small scale non-longitudinal furrow developed first. Both ends of it rotated towards the flow direction. The slopes of both the stoss-side and lee-side walls are steep or sometimes even vertical. The inducement of this phenomenon and the details of the development of obstacle marks will be discussed in Chapter 6 and the relative flow pattern will be given in Chapter 7.

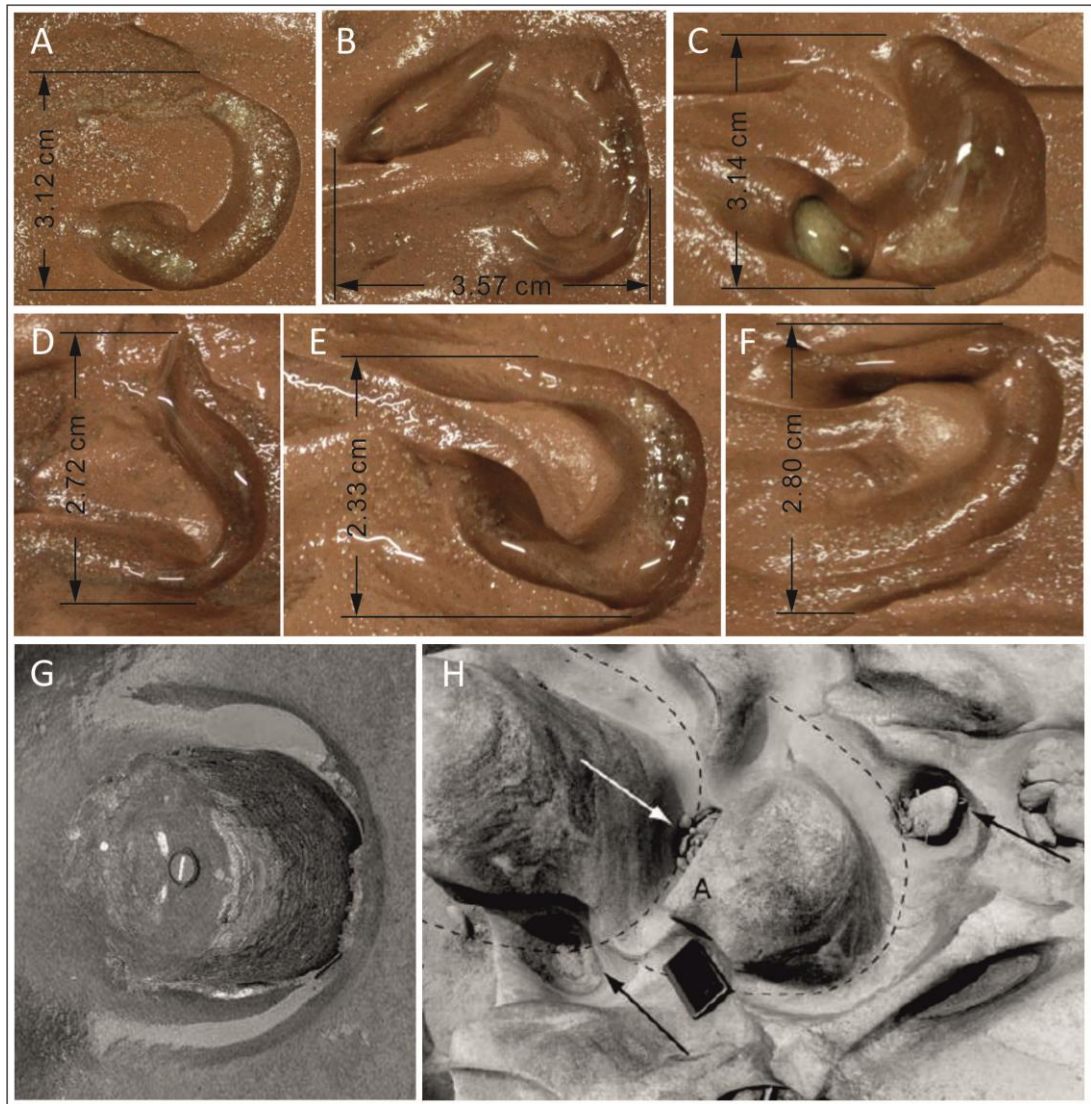


Figure 5.47 Obstacle marks (OM): Current Crescent (CC). A & F: Obstacle marks with secondary sculpting; B, C, D & E: Obstacle marks with internal secondary structures; A, C, D, and E are observed in Exp. 6; B and F are in Exp. 8 and 7, respectively; G & H: Obstacle marks in the field. G was observed from Sichiri-gawa, Japan. H was observed from Nam Mae Chaem (Ob Luang), Thailand. Flow from right to left (from Richardson and Carling (2005)).

Some others, such as runnel with cusped margins, runnel with alternating scour, oblique sloping furrows, overhanging concave surface, and solution pits were not observed in the experiments. The experiments had an initial flat original bed and there were not any tools or lateral surfaces, and consequently, this may account for the absence of some features. Perhaps unsurprisingly, solution pits did not form, given that the experimental bed substrate was not dissolvable.

5.4 Discussion

Three separate experiments (6-8) all produced an array of erosive bedforms that reproduce many features observed in bedrock river substrates. These include many types of potholes, flutes and furrows formed in natural bedrock channels. The degree of similarity is so strong that many of the bedforms are almost identical with the typical samples observed in the field, including: spiral-furrowed potholes with a spiral rib, potholes with extended exit furrows, potholes with both entry and exit furrows, open potholes, spindle flutes, flutes with internal or external secondary structure, paired flutes, en echelon flutes, short furrows, sinuous parallel-sided furrows, irregular compound parallel-sided furrows, expanding furrows, sharp-crested hummocky forms, and obstacle marks. All of the above forms were observed to originate from either flat beds or a bed with initial set defects. The size of each feature is variable, ranging in some cases from less than one centimetre to tens of centimetres. Such variability is likely in part a product of the growth and development of other bedforms which will then influence the downstream and lateral flow conditions. This complex interaction between the bed, the flow, and flow pathways for abrading sediment are examined in Chapter 6 and 7. Some of the variability in type and size of bedforms in the experiments may also be due to the different undrained shear strengths of the substrate between the three experiments. However, although these three experiments were conducted on mud beds with different undrained shear strength, the erosional features raised on them share a lot in common. In particular, no matter how large the undrained shear strength is, all the experiments reproduced similar potholes, flutes, furrows and other non-longitudinal forms, and almost every kind of abrasion forms observed in the real bedrock channels can be produced on the experimental beds. By far and away the greatest difference between the three experiments is the evolution rate. As noted earlier, the presence or absence of initial defects did not appear to play a major role in influencing the final form of the experimental bed. Experiment 6 was started from a mud bed with some small imposed defects, whilst the other two experiments (7 and 8) initiated from a smoothed plain mud bed.

A small number of features were recognised in the experiments that have not been observed and / or defined from natural bedrock substrates. These features include potholes with external secondary furrows, approximate-symmetrical paired potholes with both entry and exit furrows, comet-shaped flutes, and paired convergent flutes. Although these forms have not been

noted in real bedrock channels, they have been described from cohesive fluvial substrates (Allen, 1971a, 1982).

The experiments still lack quite a few sculpted forms that have been observed on bedrock substrates. These include: breached potholes (Ives, 1948; Lorenc et al., 1994; Whipple et al., 2000a; Wohl and Ikeda, 1998), coalesced potholes, natural arches, lateral potholes, parallel-sided furrows with levees, chute furrows, chimney furrows, runnels with cusped margins, and runnels with alternating scour, among others. The possible causes for the lack of these forms within the experiments are unclear. In some cases it may be that insufficient experiments have been undertaken to observe all of the possible forms; certainly some forms that were observed were restricted to only a single, or just a handful of examples. Other cases are a function of the experimental setup, in particular only a planar bed was utilised, and therefore lateral features could not be replicated. Other features may require enhanced heterogeneity in the sediment bed. In the present experiments every effort was made to make the substrate as homogenous as possible, however the degree of spatial variation in bed properties is not known in detail. None-the-less, many natural bedrock substrates will likely show a much wider degree of heterogeneity as a product of primary facies changes, later diagenesis, and / or features such as fractures and faulting. One aspect that is clear is that there are limitations to the temporal range of bedform development that can be explored with the present experimental setup. This temporal limit is a product of two distinct processes. Firstly as the bed erodes, a lip develops between the false floor and the mud substrate, and with time the bed becomes progressively protected from the main flow and suspended sediment starts to settle out and cover the substrate. Secondly, the narrow flume utilised here is characterised by wall effects, in turn setting up distinct secondary flow cells, that eventually form gutters where cells meet and bed shear stress is highest (see Chapter 4). The influence of these processes could be reduced in future work by increasing the length of the mud-bed, and by using a wider flume. None-the-less, the limits such as they are of the present experimental methodology should not be over emphasised, the experiments still reproduced all of the basic forms observed in bedrock substrates, and the vast majority of specific bedforms identified by past workers. Furthermore, the degree of similarity between experiment and field examples is very high, and at times exceptional.

5.5 Summary

These experiments reveal a new methodology that enables a wide range of bedrock sculpted forms to be replicated in the laboratory, within relatively short timescales (hours to tens of hours). The degree of similarity between the experimentally derived erosive forms and natural bedrock sculpted forms is extremely high, suggesting that the cohesive mud bed used in the experiments is a suitable analogue for bedrock substrates. The experiments demonstrate that the huge array of different bedforms reproduced in the laboratory can all be formed solely as a result of abrasion, since there is no cavitation or plucking. This suggests that whilst cavitation and plucking may enhance bedrock channel erosion they are not a pre-requisite for the formation of these structures. The ability to reproduce all these features in the laboratory enables their genesis and evolution to be examined in detail (Chapter 6), and their flow dynamics and interaction with the main body of the flow to be studied (Chapter 7).

Chapter 6

The evolution of erosional bedforms on bedrock

6.1 Introduction

In the previous chapters, the classification, typical morphologies and characteristics of the erosional features on the experimental analogue bedrock substrates have been demonstrated in detail. The general background of the experiments has been described in the previous chapters. Briefly, compared with one of the most successful previous physical modelling experiments on recreating bedforms in experimental analogue bedrock channels (Johnson and Whipple, 2007), all the experiments used recirculating instead of non-recirculating flow, modelling clay instead of a cement mixture, and finer grain size particles as suspended and bedload sediments transported by water flow. The resulting experiments are able to replicate a far more extensive range of bedforms than have been previously produced (see Chapter 5).

Froude number (Fr) in the current experiments ranges between 0.85-0.89 due to the minor differences in water depth which is controlled manually during experiments. According to previous studies, the ideal Fr number should be controlled around 1 due to natural river morphology being self-adjusted to around the critical condition (Grant, 1997; Shepherd and Schumm, 1974). However, some previous work has indicated that higher Fr numbers are present in flooding cases in the natural environment or in simulations bedrock erosion by physical experiments (Johnson and Whipple, 2007; Tinkler and Parish, 1998; Wohl and Ikeda, 1997). Comparison of experiments with a variety of Fr numbers show that no matter whether the flow was subcritical, critical or supercritical, the Fr number has minor effects on the formation of bedforms on bedrock channels, although this hypothesis still needs to be validated (Johnson and Whipple, 2007). The results of the current experiments (Chapter 5) further demonstrate that Fr numbers that are below critical, do not hinder the development of a wide array of erosive bedforms. Therefore, under such conditions with the boundary conditions essentially equal, apart from the undrained shear strength of the experimental modelling clay which is controlled, the evolution of erosional features with time can be explored, this aspect is examined in this chapter.

6.2 Evolution of erosional features on experimental analogue bedrock

The principal kinds of erosional features created by flume-scale experiments were potholes, flute marks, longitudinal furrows, non-longitudinal furrows, convex and undulating surfaces and composite forms with a variety of secondary structures. Most of the erosional features initialized from the plane clay beds of Exp. 7 and Exp. 8, with the exception of a few of them that formed in the clay bed of Exp. 6, that started with some preset defects. Examples of bedforms formed from preset defects include circle-shaped paired potholes and straight short furrows, these will be discussed later. All flow hydraulics and processes in this chapter are inferred based on the direct observation of the bedform evolution and previous studies on flow motion (Alexander, 1932; Allen, 1969, 1971a, 1971b, 1973a, 1982; Wilson et al., 2012).

6.2.1 Potholes

Potholes broadly distributed throughout the whole experimental clay bed no matter how strong the undrained shear strength of the experimental bed was, although the undrained shear strength of the clay bed affected the rate of change of development of each kind of bed feature. Potholes of similar forms could be observed on clay beds with different strengths. Experiments 6 to 8, especially Exp. 7, exhibited evolution sequences of potholes with the most kinds of secondary structures, which have been introduced in Chapter 5.

Standard round potholes

Both of the potholes shown in the Figure 6.1 are relatively typical round potholes from the few standard potholes observed in the bed of Exp. 7. The location of the pothole in Plot A was close to the upstream end of the clay bed, and the one in Plot B was at the middle part of the upstream area of the clay bed. The process of development of these two potholes was similar. The whole evolution duration could be divided into an initial stage, formation stage, and a mature stage. The initial stage of the pothole in Plot A is the first 240 minutes and that of the pothole in Plot B is the first 360 minutes of experiments (Figure 6.1). In this stage, no sign of the formation of potholes can be observed from the clay bed. The photos of the bed at the 120th minute interval (T120) in Plot A and the 240th minute interval (T240) in Plot B, only illustrate some narrow and shallow linear erosion features on the surface of experimental bed, which were only about 1 to 2 mm in width. On

the bed of T240 in Plot A and T360 in Plot B, obvious hollow areas have emerged. Water flow entered into these hollows and created lateral rims towards the downstream direction (Figure 6.1: yellow arrows in Plot A: photo T240 and Plot B: photo T360). At this time point (T240), the hollows were still lack of both proximal and distal rims.

The next 120 minutes, from the 240th minute to the 360th minute in Plot A and the 360th minute to the 480th minute in Plot B, is the transition phase from the initial stage to the formation stage. These 2 hours witnessed the formation of the initial round form of the potholes. The proximal rims formed and the depth of hollows increased. The round closed downstream inner wall of the potholes could be observed. The possible flow paths can be inferred from the form of the rims of the potholes at this time point. The water current should have entered the pothole from point **a**, and separate into two parts when it reached point **b**. One part of flow moved along the outer lateral rim towards the downstream and the other reversed backwards and downwards into the hollows of the potholes (Figure 6.1). The case of Plot B is more complicated than the case of Plot A. The flow Plot B separated more than once. When the reversed flow passed point **b**, it separated into 2 sub-flows again. The curvature radius of the outer sub-flow is obviously bigger than the inner one (Figure 6.1: Plot B – photo T480 to T1320). The inner sub-flow separated one more time when it reached point **d** (Figure 6.1: Plot B – photo T480). One of them kept twisting downwards into the pothole and the other moved slightly backwards to form a small secondary structure on the proximal inner wall. The formation stage of the pothole in Plot A lasted for 600 minutes to the 960th minute and that of the pothole in Plot B lasted for 840 minutes to the 1320th minute. In this formation stage, the potholes kept cutting downwards by separated vortices that, meanwhile, polished the inner wall to form the final round shape of the principal hollow of the potholes.

After entering into the mature stage, the shape and the depth of potholes did not alter a lot (Figure 6.1: Plot A – photo T960 to T1800; Plot B – photo T1320 to T1800). However, the diameter of the upper opening of the potholes still continued enlarging. The upper rim of the potholes also became polished to cusped and surrounding area of them got polished as well.

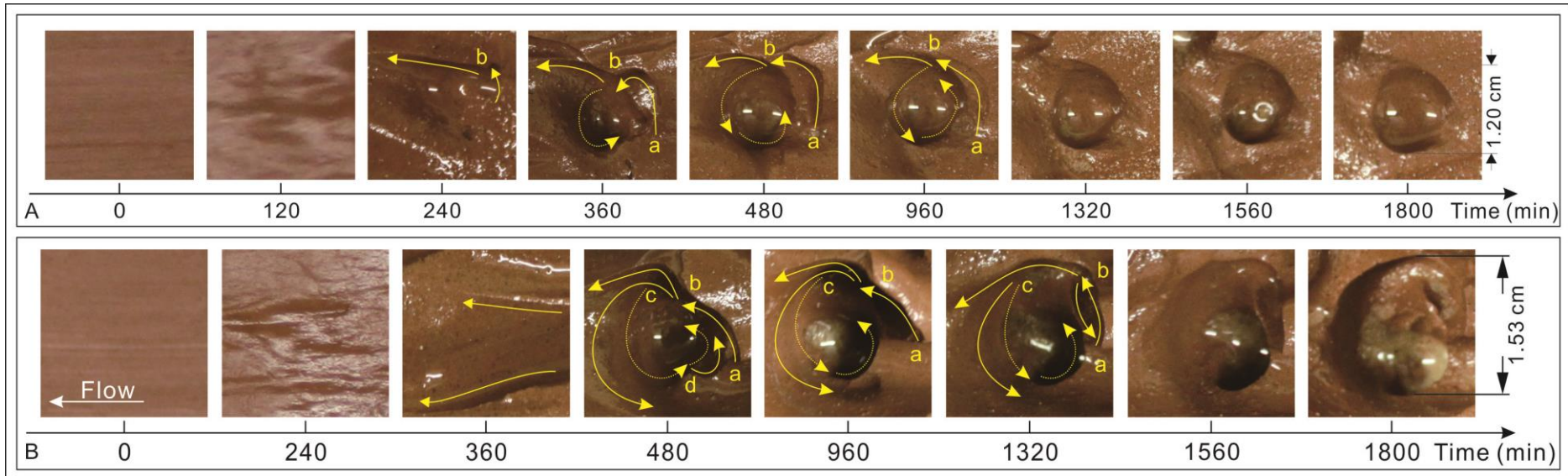


Figure 6.1 Evolution of standard round potholes. Both potholes were observed in the clay bed of Exp. 7. Flow from right to left. Yellow curved arrows refer to the possible path of secondary flow. a, b, c and d refer to flow separation points.

Spiral-furrowed potholes

Spiral-furrowed potholes were observed in the clay beds of both Exp. 6 and Exp. 7 (Figure 6.2). The pothole in Plot A, formed in the centre of the clay bed of Exp. 6 and the pothole in Plot B was located in the upper middle part of the clay bed near the right wall of the flume of Exp. 7, if looking downstream. The evolution sequence of these spiral-furrowed potholes can be divided into 3 stages as with the evolution of round potholes. The initial stage of pothole in Plot A was from the beginning of the experiment to 720 minutes and the pothole in Plot B was the first 360 minutes of the experiment. At the end of this initial stage, two sinuous furrows with deeper depressions in their upstream ends were observed on the clay beds.

The initial profile of spiral-furrowed potholes formed in the next 240-min run of Exp. 6 and 120-min run of Exp. 7. This means the formation stage started at Plot A – photo T960 and Plot B – photo T480 (Figure 6.2). From the inner structures of both potholes in Plot A and B, it appears that the flow moved along the right inner walls of the furrows forming in initial stage towards the downstream but separated into two flows at point **b** just as happened in the standard round potholes. One of separated flows produced a reversed spiral that incised downwards inside the potholes. This process of spiral incision created spiral furrows on the inner wall of the potholes. The inner wall was affected by flow along the left side of the potholes as well. Under the combined activity of the secondary vortices and flow along left inner wall, the extent of incision on the left-side inner wall was much greater than that of the right-side inner wall. This also aided the formation of lateral furrows on the inner wall. The formation stage of the pothole in Plot A lasted 480 minutes and the pothole in Plot B lasted for 1080 minutes. In this period, the spiral-furrowed potholes kept enlarging and deepening. The shape of the principal hollows of them changed from approximate ellipses to round. In the later stage of this formation stage, a small pothole formed close to the larger one from a previously formed shallow furrow (Figure 6.2: Plot A – photo T1440 and T1680).

After the formation stage, to the end of the experiments, was the mature stage. The rims of both of the potholes were altered to be cusperate. The hierarchical multi-tier spiral furrows could be clearly observed in the pothole. Sometimes, a boss could be observed in the bottom of them (Figure 6.2: Plot A – photo T1680). The reason why the existence of pothole in Exp. 6 developed much later than that in Exp. 7 is probably because the clay bed of

Exp. 6 had a higher shear strength and therefore took longer to be altered in comparison to Exp. 7.

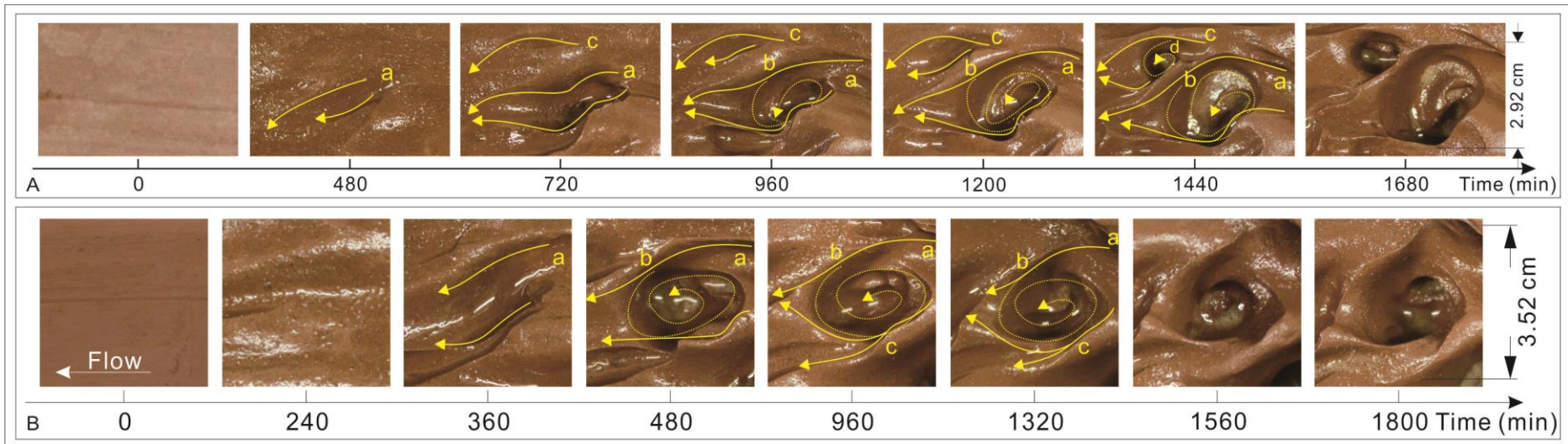


Figure 6.2 Evolution of spiral furrowed potholes. The pothole in Plot A was observed in the clay bed of Exp. 6 and the pothole in Plot B was observed in the clay bed of Exp. 7. Flow from right to left. Yellow curved arrows refer to the possible path of secondary flow.

Potholes with exit furrow

Compared with the two kinds of potholes previously introduced, the evolution of potholes with exit furrows was much simpler. The pothole with exit furrow shown in Figure 6.3 was observed in the upstream part of the clay bed of Exp. 7. The formation process contained three stages: initial stage, formation stage and a transformation stage. There was no mature stage because the form of pothole with exit furrow was not stable final ending shape of an erosional feature.

Almost nothing happened at the location where this pothole would develop in the first 720 minutes of Exp. 7 (Figure 6.3: photo T720). A simple flute formed in the 120 minutes between the 720th minute and the 840th minute with a shallow proximal depression and a clear upstream and lateral rim. But the downstream rim was not as visible as the upstream rim. Until the 840th minute, the pothole form could still not be distinguished. Therefore, the first 840 minutes of the experiments is defined as the initial stage of this pothole with exit furrow. The principal depression of the flute was cut downwards during the 240 minutes from the 840th to the 1080th minute, which brought the round form into the experimental bed (Figure 6.3: red ring in photo T1080). A secondary small pothole in the bottom of the bigger pothole could also be observed (Figure 6.3: yellow rings in photo T1080 and T1320). The pothole with exit furrow in the 1320th minute was regarded as its mature condition. The former principal hollow of the pothole elongated and became the exit furrow and the former smaller secondary pothole developed and enlarged to be the pothole with exit furrow. The smaller pothole and the exit furrow did not stop changing after the 1320th minute. A curved exit furrow formed and extended from one side of the smaller pothole in the bottom of the larger depression, the initial form of which was partly visible in the bed at T1320 (Figure 6.3: arrowed in photo T1320 and T1560). At the end of the experiments, the length of the bigger depression increased. The downstream part of the smaller pothole elongated downstream while the curved exit furrow widened. The final form of the smaller pothole with the exit furrow looked like the Yin-yang furrow (Figure 73 and 75 in P. 48-49 of Richardson and Carling (2005)). Therefore the period from the 1320th minute to the end of Exp. 7 was considered as the transformation stage of this pothole with exit furrow.

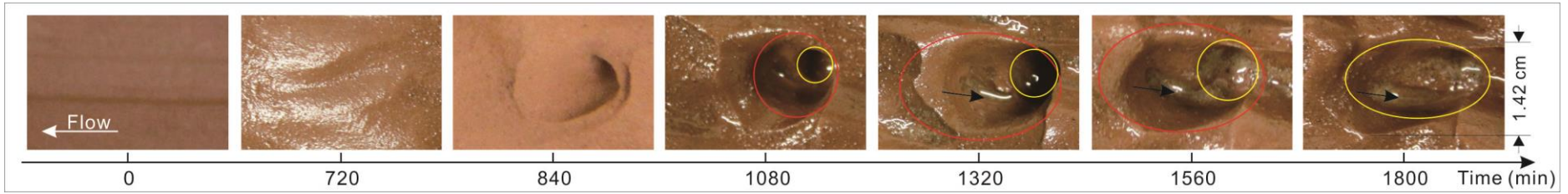


Figure 6.3 Evolution of a pothole with exit furrows. The pothole was observed in the clay bed of Exp. 7. Flow from right to left. Red ellipses refer to the bigger pothole; the yellow ellipses refer to a secondary small pothole that eventually changed the overall form to be a secondary furrow.

Potholes with extended exit furrow

In the current experiments, the extended exit furrow formed earlier than the principal hollow of the pothole (Figure 6.4). Both of the potholes with extended furrows in Figure 6.4 were produced by Exp. 7 and were located in the middle upstream part of the clay bed. The evolutionary processes of these two potholes were almost the same. Three stages of evolution are: initial stage of first 480 minutes of the experiments, formation stage of the next 480 minutes from the 480th to the 960th minute, and the last mature stage was from the 960th minute to the end of experiments.

In the first 360 minutes, only a sign of short shallow furrows emerged in the experimental bed (Figure 6.4: Plot A & B – photo T360). The depth of them was small and uniform. The short shallow furrow in Plot A transformed to be a narrow flute and that in Plot B developed to be a narrow curved parallel-sided furrow in the 120 minutes between the 360th to the 480th minute, respectively. The principal depression of the potholes needed more than 240 minutes to become partly visible (Figure 6.4: photo T480 - T720). Meanwhile the initial exit furrow with cusped lateral rims developed and deepened. The flow entered into the depression from the points arrowed in Figure 6.4 and moved along the lateral inner wall of the exit furrows. From the shape of the pothole in Plot A, the flow path could only be inferred along the lateral inner wall. Although the proximal hollow kept cutting downwards, no sign of vortices could be observed directly from Plot A. The deeper hollow in the upstream end of the furrow was probably produced by longitudinal near bed separation flow above the bottom of the hollow. In Plot B, in the location of the flow inlet, a deeper hollow formed as well, and signs of vortices could be observed. Together with the flow moving along the left inner wall from the inlet to the downstream, the vortices incised the hollow downwards and leftwards. In the bed at T960, the upstream ends of the features were obviously deeper than the other parts of the furrows. The photo at 1200 in Plot A shows the mature form of a well developed pothole with extended exit furrow, with a partly round pothole in the upstream end. After the 1200th minute, the surrounding area around the pothole was polished and the rim of this erosional feature changed to be cusped as happened with the standard round pothole A in Figure 6.1. The mature form of pothole in Plot B was observed in the final bed of Exp. 7. A part of the upper rim of the pothole developed to be partially round and the diameter slightly enlarged compared with that of T1200. The principal hollow was much deeper than the parallel-

sided exit furrow, the shape of which almost kept steady from T1200 onwards.



Figure 6.4 Evolution of potholes with extended exit furrow. Both of the potholes were observed in the clay bed of Exp. 7. Flow from right to left. Yellow curves refers to the possible paths of secondary flow within and around the potholes.

Potholes with both entry and extended exit furrows

Potholes with both entry and extended exit furrows were observed and produced by Johnson and Whipple (2007), although neither the entry or exit furrows were not as long and wide as the one shown in Figure 6.5 produced in the current experiments (Figure 3 e, f & g in Johnson and Whipple (2007)). The current pothole was observed in the lower area of the downstream part of the Exp. 7 bed, which was close to the right wall of flume. In the initial stage of the first 720 minutes of the experiments, only a sinuous shallow furrow formed in the clay bed, although the whole bed had already been incised by 0.5 to 1.0 cm. In the next 360 minutes, the erosion rate within this shallow furrow increased a lot and the depression was cut down by 0.5 cm. The cusped rim of the initial erosional feature was visible and a relative deeper part grew in the bend of the sinuous furrow (Figure 6.5: yellow ellipses in photo T1080). After the 1080th minute of the experiments, the evolution entered into the formation stage. The deeper area incised downwards into the clay bed by 0.5 mm in 240 minutes from the 1080th to the 1320th minute and became an initial pothole. Although the entry and exit furrows deepened as well, the erosion extent of them was much less than that of the principal pothole. The pothole continuously cut downwards with diameter enlarging from the 1320th minute to the end of the experiments. The form of the outer rim of the whole erosional marks did not change a lot from the 1080th to the 1800th minute. However the relatively deeper areas, including the principal pothole and the flute in the top right corner of each photo (Figure 6.5: blue ellipses), developed to be longer, wider and deeper over time.

The flow path could be interpreted from the form of the inner wall of the pothole. The flow should converge into the entry furrow first and then move along the depression of the entry furrow. When reaching the bend of the sinuous furrow, the flow separated into two secondary flows. One of them kept flowing forward towards the downstream and the other became vortices twisted downwards to incise the bottom of the deeper part of the sinuous furrow to initialize the principal hollow of the pothole (Figure 6.5: yellow dashed line in photo T1320). The radius of curvature of this spiral secondary flow increased with continuous running of experiments, which contributed to the widening of the primary pothole (Figure 6.5: yellow dashed curve in photo T1800).

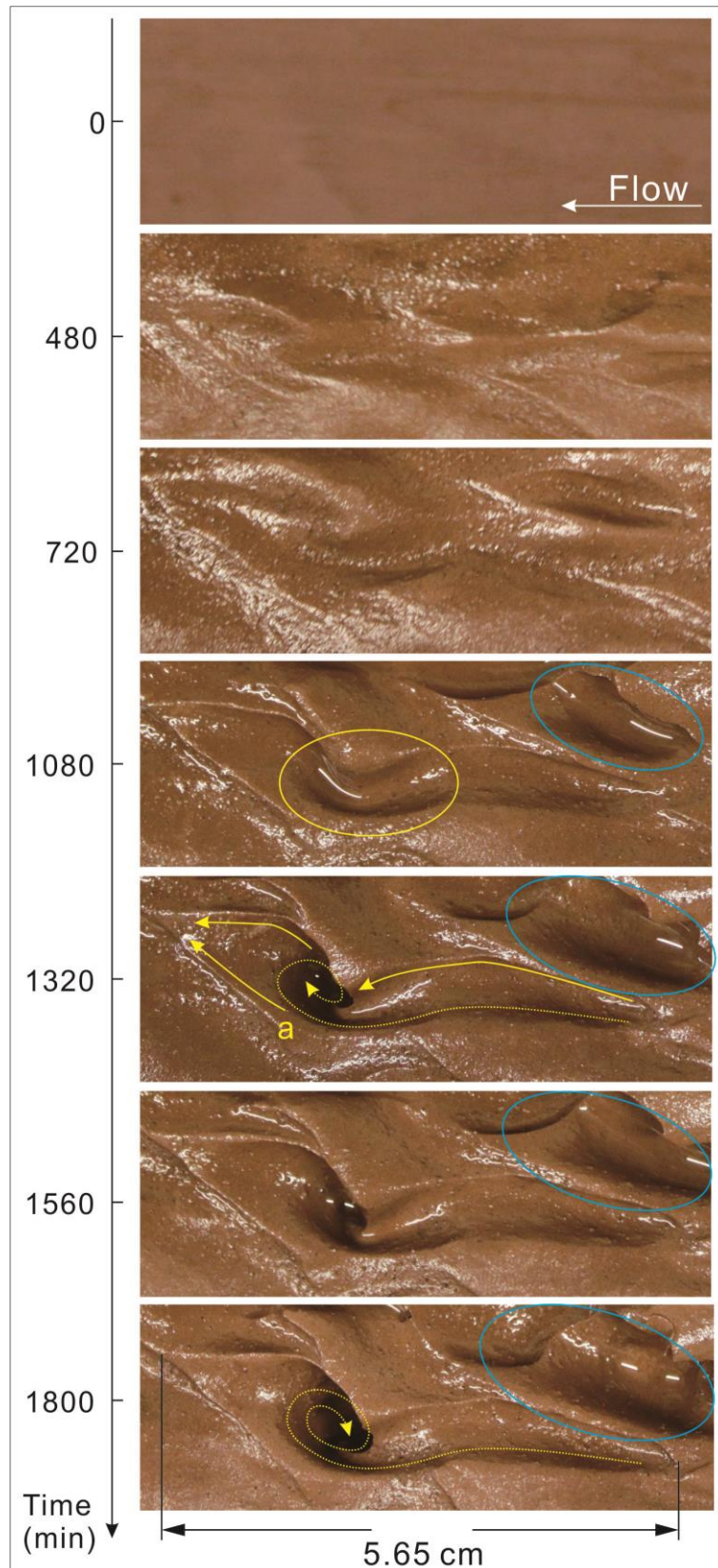


Figure 6.5 Evolution of a pothole with both entry and exit extended furrows. It was observed in the clay bed of Exp. 7. Flow from right to left. Yellow curves refer to possible paths of secondary flow within and around the potholes. Blue ellipse refers to the change of a smaller flute.

Open pothole

Open potholes were observed several times in experimental beds with different undrained shear strength. The one shown in Figure 6.6 was located in the middle part of the clay bed of Exp. 7. Figure 6.6 also illustrates the evolution sequences of two smaller potholes adjacent to the open pothole (Figure 6.6: red and blue ellipses). The primary outlines of the open pothole and one smaller pothole were forming simultaneously in the 120 minutes between the 360th and the 480th minute. A curved parallel-sided furrow with entry secondary furrow took shape from shallow marks and an obvious pothole formed in the bend of a slightly sinuous parallel sided furrow, respectively (Figure 6.6: photo T480). However, the principal hollow of the open pothole had not formed yet. The upstream depression of the bigger parallel-sided furrow was slightly deeper than the rest of the furrow. From the 480th to the 720th minute, this depression deepened while the width of this parallel-sided furrow increased. The shape of the rim of the small pothole, circled by the red ellipse in Figure 6.6, no longer remained in round and an entry furrow emerged ahead of it. Meanwhile, a flute with external secondary flute generated (Figure 6.6: blue ellipses in photo T720). At this time point, although the bigger parallel-sided furrow became broader and deeper, it still could not be regarded as a pothole, because the deeper depression could still not be distinguished from the rest of the furrow. The following 240 minutes witnessed the formation of the approximate round rim of the principal hollow of the open pothole (Figure 6.6: photo T720 to T960). In the photo at T960, the shape of the rim of the bigger pothole was slightly oval. The structure of this pothole illustrates the possible flow paths within the pothole. Flow might come from the entry furrow ahead of the hollow of the pothole and move along the right inner wall of the pothole. When it reached point **b**, a part of flow kept moving forward and the other part went downwards and reversed back towards the upstream end, which might be caused by flow convergence and wall resistant effects. These vortices incised downwards to deepen the main hollow of the pothole and modified the rim of the pothole to be round. This process lasted for the next 240 minutes and made the shape of the pothole rounder. Meanwhile the flutes in the blue ellipse eventually transformed to be a pothole and one much smaller pothole formed at the upstream end of the entry furrow, circled in the red ellipse. Until now the evolution had not finished. Over time to the 1560th minute, one more sub-stream might be separated from point **b** and appears to have reversed along the upper inner wall of the hollow (Figure 6.6: blue dash line in photo T1560). In the mean time, both of the upstream rims of the

pothole, tagged by the red and blue ellipses, were cut through. At this moment, the outlines of all the potholes were still partly visible. In the last 240-min of the experiments, the final form of the mature open pothole with entry furrow eventually formed. But the rim of the pothole, circled by the blue ellipse was totally polished and the round form of the former pothole could no longer be distinguished. For the smaller potholes, tagged with the red ellipse, the downstream end rim of the right pothole was removed and the left one became very shallow with the rim of it being barely observable.

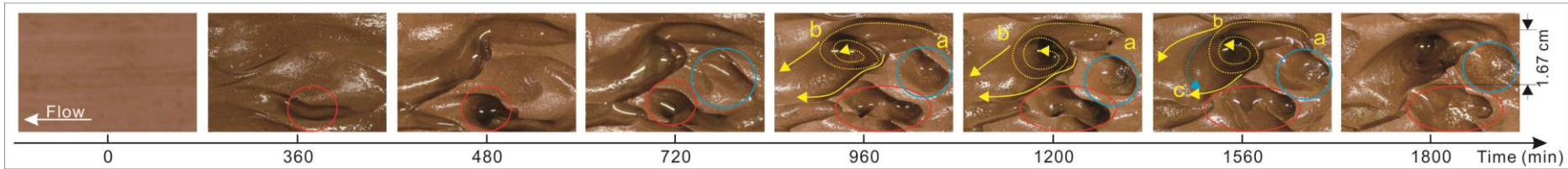


Figure 6.6 Evolution of an open pothole. The whole system was observed in the clay bed of Exp. 7. Flow from right to left. Yellow curves refer to the possible paths of secondary flow within and around the potholes. Red and blue ellipses refer to the change of the three small potholes.

Spiral-furrowed potholes with a spiral rib

The spiral rib of potholes could actually be regarded as a small secondary entry furrow ahead of the primary body of potholes. The relative bigger entry furrows of the pothole with both entry and exit furrow or the open pothole formed earlier than the formation of the principal hollows of the potholes. However, this much smaller spiral rib formed in the later stage of the development of this kind of pothole (Figure 6.7).

A shallow flute was forming in the upper middle part of Exp. 7 bed in the first 360 minutes. It transformed to the initial form of pothole between the 360th and 480th minute. At that point, the pothole had an irregular shape with a short but wide exit furrow. There was no obvious entry spiral rib that could be observed. In the upstream end, only a sign of the flow path could be seen, which could not even be regarded as an entry furrow (Figure 6.7: yellow arrowed in photo T480). In the 480 minutes between the 480th and the 960th minute, the principal hollow and the lateral spiral furrows on the inner wall had fully developed, but still not the spiral rib. The main circle shaped pothole was clearly showing in the bottom of the hollow. At the position of the flow inlet, the flow path altered to be an entry furrow from this moment (Figure 6.7: point **a** in photo T960). It needed 240 minutes to transform the approximately parallel-sided secondary entry furrow to a spiral rib (Figure 6.7: photo T960 to T1200). The rib had a cusped proximal end, which is slightly narrower than its downstream end that connected with the main hollow of the pothole. It would keep developing with time to have a closed proximal end like that observed in Figure 8A in Chapter 5 (Figure 6.7: photo T1800 point **a**). The enlargement of the main pothole did not stop from the 960th minute to the end of the experiment under the integrated effects of downwards vortices and flow along the left flank of the exit furrow which incised into the left lateral inner wall and made the left upper rim overhang over the main depression of the exit furrow.

Pothole with horizontal furrows

The erosional feature shown in photo of T1080 in Figure 6.8 was the final form of the pothole with horizontal furrows in the clay bed of Exp. 8. Below two overhanging lateral flanks, which are circled by two blue ellipses in Figure 6.8, there were two horizontal furrows on the lateral inner wall extending downstream. The final form of this pothole initialized from two adjacent deep flutes with an entry furrow on one of them (Figure 6.8: photo T480). The entry furrow, tagged by the green rectangle in the photo of T480 in Figure 6.8, developed to be a big flute, which was even bigger than the

one in the rear of this exit furrow, in only 120 minutes from the 480th minute to the 600th minute (Figure 6.8: green rectangular in photo T600). This large flute evolved to be the principal hollow of the final mature pothole. In the photo of T600, all three flutes were still separated with each other. Only the two in the upper part of the photo shared one rim. After a further 120 minutes, the inter-sections between the flutes were all thoroughly polished and removed. A mature form of pothole with horizontal furrows formed from the 720th minute (Figure 6.8: photo T720). From this moment to the 840th minute, the horizontal furrows below the left flank and on the inner wall of the rear part of the right flank could be observed (Figure 6.8: blue and red ellipses in photo T720 and T840). The horizontal furrow below the front right flank was not clearly visible until the formation of the final experimental bed (Figure 6.8: photo T1080). In the mean time, a broad parallel-sided entry furrow was produced, which probably introduced the water flow into the pothole to create these horizontal furrows on the inner walls of this pothole (Figure 6.8: yellow arrows in photo T840 and T1080).

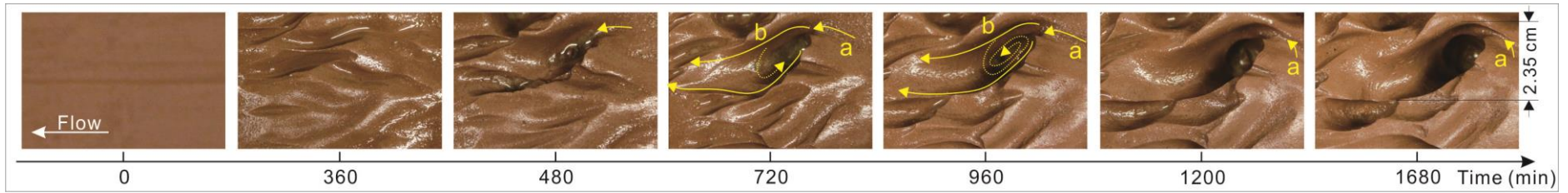


Figure 6.7 Evolution of a spiral-furrowed pothole with a spiral rib. It was observed in the clay bed of Exp. 8. Flow from right to left. Yellow curves refer to the possible paths of secondary flow within and around the potholes.

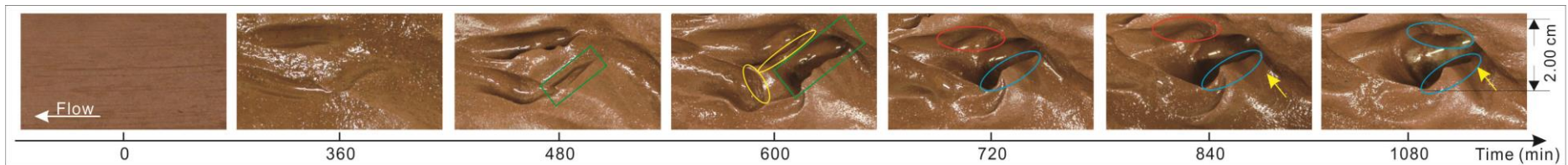


Figure 6.8 Evolution of a pothole with horizontal furrows. It was observed in the clay bed of Exp. 8. Flow from right to left. Green rectangle refers to an entry furrow. Yellow ellipses refer to the rims of marks. Red ellipse refers to a lateral furrow. Blue ellipses refer to the overhanging rim. Yellow arrows tagged to the inlet of flow.

Potholes with external secondary furrow

Potholes with external secondary furrow have not been reported in natural bedrock channels or in previous experiments simulating bedrock erosion. However, potholes with external secondary furrows are one of the most common kinds of bedforms on experimental beds. It is necessary to investigate the development process of it.

Figure 6.9 demonstrates the evolution sequence of a pothole with external secondary furrow on the lower centre part of Exp. 7 clay bed. The development of the external secondary furrow was synchronized with the evolution of the main pothole that it connected with. The initial forms of both the pothole and its external secondary furrow needed 600 minutes to take shape (Figure 6.9: photo T600). But at that moment, the external furrow still appears to be a normal independent flute, instead of a secondary structure of other bedforms. The next 120 minutes witnessed the formation of the principal round hollow of the main pothole. But the shape of external secondary furrow did not become obviously visible until the 960th minute. The flanks of it were cusped, slightly curved and flared downstream-wards. The depth of the secondary furrow deepened while the principal hollow kept elongating and enlarging over time. The form of the pothole in the photo of 960 in Figure 6.9 could be regarded as the mature form of a typical pothole with external secondary furrow. After the 960th minute, this kind of bedform did not stop evolving with the upstream end rim of main pothole being cut through and becoming irregular. Meanwhile, from the 720th minute to the 1680th minute, a short furrow evolved from a spindle flute.

Complex potholes

The complex pothole illustrated by Figure 6.10 developed from a short parallel-sided furrow forming in the early stage of Exp. 8. The upstream end of the short furrow was open, from which the flow could enter into the depression part of it (Figure 6.10: yellow arrowed areas in photo T480 and T600). Over experimental time, the upstream end was deepened by vortices that could be inferred from the form of erosional feature in photo of T840. By that moment, an obvious pothole formed in the upstream deeper end of the former short furrow, although the shape of it was not circular yet. Over the following 120 minutes from the 840th minute to the 960th minute, the shape of the proximal rim of the pothole altered a lot with small secondary furrows and potholes appearing on it. Those might be produced by the separation flow from the vortices. When they hit the wall of the primary depression, flow with sediment would try to incise into the wall to form some small secondary

structures on the outer rim of the primary pothole (Figure 6.10: photo T960). At the end of Exp. 8 (T1080), a much clearer form of a pothole with three secondary structures on its proximal end could be observed.

Hierarchical pothole

The hierarchical pothole in Figure 6.11 was observed in the clay bed of Exp. 6. Within the primary depression of the final mature pothole, there was one bigger secondary pothole with smaller secondary pothole in the bottom of the bigger one; two bigger adjacent short paralleled-sided furrows, and a smaller short furrow next to the smaller pothole in the bottom of the bigger secondary pothole (Figure 6.11: photo T1440 and T1680). The whole feature started to form after Exp. 8 was run for 960 minutes. Before that, only a curved shallow furrow could be observed (Figure 6.11: photo T720). The first secondary structure to form within the hierarchical pothole was the smallest pothole in the deepest part of the primary depression (Figure 6.11: photo T960). All flow coming from upstream (Figure 6.11: point **a**) converged into the deeper part, changed direction when touching the inner wall and incised downwards to form the smallest pothole (Figure 6.11: point **b**). In the bed at T1080, except for the deepest pothole, other kinds of secondary structures were still not observed. After the next 360 minutes, all the secondary structures were clearly shown by the experimental bed (Figure 6.11: photo T1440). That indicated that after 1440-minute running, a mature hierarchical pothole had eventually formed on the experimental clay bed. From T1440 to T1680, all the secondary structures kept enlarging while the round distal end rim of bigger pothole was destroyed (Figure 6.11: photo T1080 - 2). The rims of all the features became cusped because the surrounding area of this hierarchical pothole was polished by the sediment-laden flow.

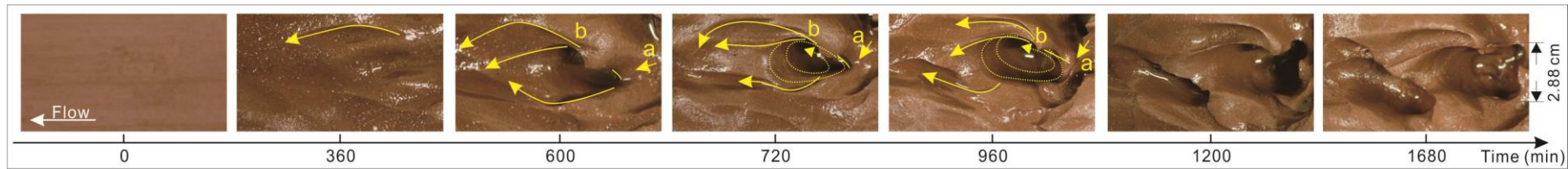


Figure 6.9 Evolution of a pothole with external secondary furrow. It was observed in the clay bed of Exp. 7. Flow from right to left. Yellow curves refer to the possible paths of secondary flow within and around the potholes.

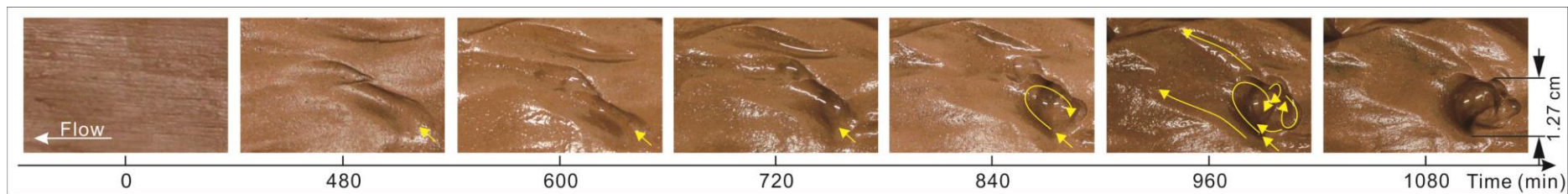


Figure 6.10 Evolution of a complex pothole. It was observed in the clay bed of Exp. 8. Flow from right to left. Yellow curves refer to the possible paths of secondary flow within and around the potholes.

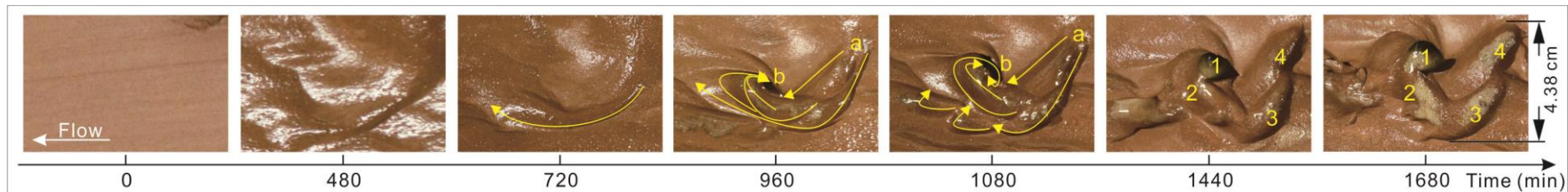


Figure 6.11 Evolution of a hierarchical pothole. It was observed in the clay bed of Exp. 6. Flow from right to left. Yellow curves refer to the possible paths of secondary flow within and around the potholes. 1 to 4 refer to the different secondary structures.

Horseshoe-shaped paired potholes

Figure 6.12 demonstrates horseshoe-shaped paired potholes, A and B, produced by Exp. 6 and Exp. 8, respectively. Paired potholes in Plot A are produced from a bed with a preset circle defect of 0.9 cm in diameter in Exp. 6. In contrast to the single flute created by the experiments conducted by Allen (1971a), two potholes with similar mirror form developed from the very beginning to the end of the experiments. The erosional marks shown in the photo of T360 did not show any defined types of bedforms in bedrock or cohesive substrates. Two tracks developed from the lateral rim of the preset defect. The profile of them looked like an initial form of a classic flute given by Allen (1971a). The area between two tracks was a raised part which has similarities with the median ridge of flutes (Figure 6.12: photo T360). From the 120th minute to the 480th minute, the former marks evolved to become two shallow sinuous furrows instead of a typical flute. From the 480th minute to the 600th minute and then the 720th minute, the two shallow furrows evolved to become sinuous flutes first and then potholes with exit furrows. The evolution process during this period moved into the typical pattern of the formation of potholes. Flow entered into potholes from an entry furrow ahead of the furrows or the flutes. Once the flow reached the bend of the furrows or the flutes, flow curved and moved spirally downwards to form the pothole. This spiral and down-cutting process would continue from the 720th minute to the end of the experiments.

Between two paired potholes with exit furrows, a rhombus projection formed with a partly sharp proximal end and cusps extended distal end. The flow should separate from the proximal end into the potholes. Once the flow passed the two lateral cusps at point **a** and **b**, they converged inwards simultaneously and moved downstream to create the extended cusps downstream part of the projection.

From 960 minutes, the area ahead of the projection started to be incised downwards and the obstacle between the two proximal ends was removed to become a channel to link two separated potholes (Figure 6.12: red dashed ellipse in photo T1320). At the same time, the paired potholes kept deepening and the exit furrows of them kept elongating, while the size of the rhombus projection reduced. Up to the 1320th minute, a mature form of circle shape paired potholes with exit furrows was present. After this, the clay bed was polished and most parts of the pothole rim were altered to be cusps.

A pair of horseshoe-shaped potholes showing in Plot B was initialized from the plane bed of Exp. 8 and evolved with a similar sequence, although the

form of each of the potholes was more complicated than those shown in Plot A. The left one of them in Plot B could be considered as a hierarchical pothole which contains more than one secondary smaller pothole within its larger primary depression. They share many features in common with those in Plot A and the evolution process of it was also almost the same as that in Plot A. Both of them have a pair of potholes of similar form and a projection with extended distal end in the median axis. Although a channel for connecting the two paired potholes had not been cut through yet, if the Exp. 8 continued, it might be created sooner or later. All the similarities of potholes in Plot A and B in Figure 6.12 indicate that horseshoe-shaped paired potholes could generate in any bed, no matter whether there were preset defects in the original beds or not.

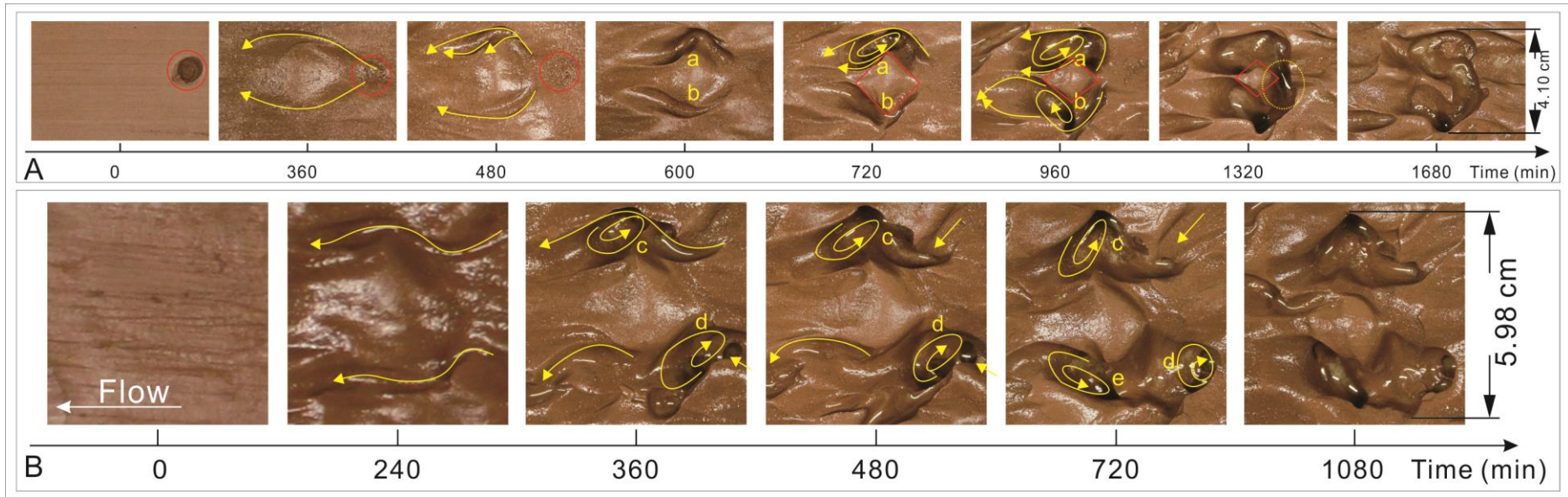


Figure 6.12 Evolution of circle-shaped paired potholes. Potholes in Plot A were observed in the clay bed of Exp. 6 and those in Plot B were in Exp. 8. Flow from right to left. Yellow curve refers to the possible paths of secondary flow within and around the potholes. Red circle refers to the preset defect. The red rhombus refers to the projection.

Approximate-symmetrical paired pothole with both entry and exit furrows

Pothole with both entry and exit furrows have been discussed before. In that case, both the entry and extended exit furrows formed prior to the formation of potholes in the bend position of the former sinuous furrow. And the length of entry or exit furrows was much bigger than the diameter of the pothole. In the current case, the hollows of the potholes were the most obvious features in the whole system. Entry furrows were relatively small, but were still in charge of introducing water into the pothole. The exit furrows were very short compared with the extended exit furrow in the former case.

Both of the pothole systems in Figure 6.13 were observed on the clay bed of Exp. 7. Potholes in Plot A were located in the upstream part of the bed and those in Plot B were in the middle part. The changing process of each of the pothole was very similar to those deep potholes mentioned before, although the timing of their appearance was different, with potholes in Plot A developing by the 840th minute and in Plot B by the 720th minute. All the deep hollows of the potholes were generated from deeper parts of sinuous furrows or flutes, and were incised downwards by secondary vortices which separated from the primary flow when it hit the downstream inner wall of the potholes. The other branch of secondary flow moved downstream to elongate the exit furrow.

The notable part in this case is that the upstream flow did all the actions including creating two furrows in mirror form, incising them to form potholes, forming short entry furrows and elongating exit furrows simultaneously and induced the formation of this kind of approximate-symmetrical paired pothole with both entry and exit furrows. This indicated that the flow pattern above the two potholes in the same system was almost the same except for the direction of the flow turning around in the initial shallow furrows. What affected this direction is still unclear. This may in part be a function of the morphology of the surrounding areas. The probability is that the bedforms ahead of these shallow furrows let to the flow moving into them and then the lateral walls of them guided the water moving along them in the downstream direction. Nevertheless, why they generated in pairs is still unclear.

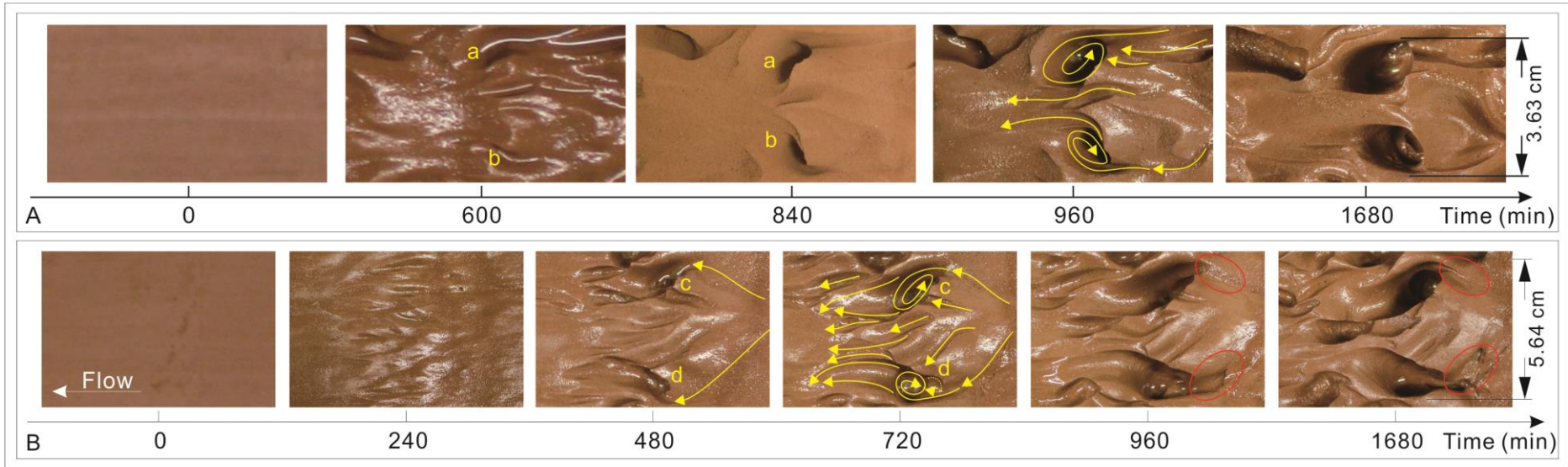


Figure 6.13 Evolution of approximate-symmetrical paired potholes with both entry and exit furrows. Both systems were observed in the clay bed of Exp. 7. Flow from right to left. Yellow curves refer to the possible paths of secondary flow within and around the potholes. Red ellipses refer to the entry furrows.

6.2.2 Flutes

The last section of the evolution of potholes has already illustrated some flutes as a transitional form during the formation of potholes. However, flutes were not only present as a transitional form but also as a final form. In this section, the development patterns of different morphologies of flutes in experimental beds are assessed in detail in order to reveal the evolution process of flutes in bedrock channels.

Simple flutes are those flutes without secondary and complex structures, the forms of which have been introduced in the Chapter 5. They can mainly be classified as broad and narrow flutes, deep and shallow flutes, flutes with median ridge, overhanging flutes, spindle-shaped flutes and comet-shaped flutes (Figure 6.14 to Figure 6.19).

Broad and narrow flutes

Broad and narrow flutes evolved in a relatively simple pattern. The formation rate of broad flutes was very slow compared with other erosional bedforms. No obvious form of them could be observed until the 960th minute (Figure 6.14: Plot A – photo T960). From the 960th minute to the end of Exp. 7, the shape of broad flutes was changed with little widening or elongating. The only change was that the rim of the flutes became more cusped which might be caused by the polishing effect occurring in the later stage of the experiments. For the narrow flutes, after 480 minutes, some shallow longitudinal marks appeared and evolved to be the initial form of flutes in the following 240 minutes (Figure 6.14: Plot B – photo T720). The flutes would reach their peak mature condition at the 960th minute of Exp. 7. Four standard narrow flutes were clearly exhibited by clay bed (Figure 6.14: Plot B – photo T960). Over time, flute 1 became slightly wider and the lateral flanks became clearer from the 960th minute to the 1200th minute, and then elongated and transformed to be a short furrow with round proximal end at the end of experiments. Although the rim of flute 2 became less and less visible from the 960th minute to the end of the experiments, it extended towards the upstream direction over time. For flutes 3 and flute 4, they enlarged a bit and developed towards the upstream direction as well from the 960th minute to the end of the experiments. What's more, the 600 minutes between the 1200th minute to the 1800th minute witness the formation of an entry furrow ahead of flute 3, no sign of which could be observed on the beds before the 1200th minute. This indicated that entry furrows don't always form prior of the formation of bedforms in the back of it.

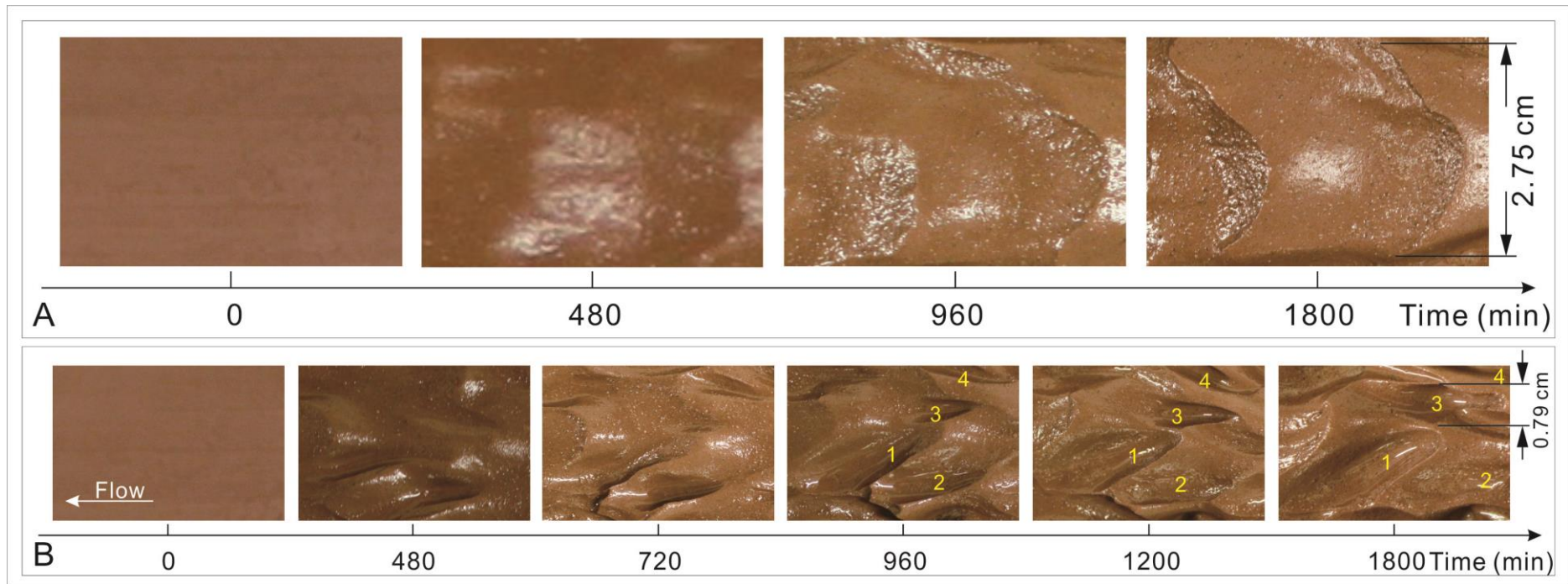


Figure 6.14 Evolution of broad and narrow flutes. Both of them were observed in the clay bed of Exp. 7. Flow from right to left. 1 to 4 refer to the number of narrow flutes.

Deep and shallow flutes

The deep flute in Plot A and the shallow flute in Plot B of Figure 6.15 were observed on the clay bed of Exp. 6 and Exp. 7, respectively. The genesis of the deep flute in Exp. 6 didn't start until the 960th minute. The formation of the flutes lasted from that time point to the end of the experiments. This deep flute evolved from a shallow flute to a deep one directly. At the same time, an internal lateral narrow furrow and an external furrow were forming alongside the deep flute (Figure 6.15: Plot A – photo T1440 & T1680). The shallow flute started to form from the 480th minute of Exp. 7 and the basic form of it became visible after the 960th minute (Figure 6.15: Plot B – photo T960). The following 240 minutes led to the development of all features of this shallow flute, including cusped rim, principal shallow depression, lateral furrow, lateral rim and an external furrow. The shallow flute in the photo of T1200 was considered as a standard shallow flute. From the 1200th minute forward to the end of the experiments, the proximal depression deepened a bit but was still not as deep as that in the deep flute while the primary shape of the flute did not change a lot.

Flutes with median ridge

Flutes with median ridge did not broadly distribute on the experimental beds. Only a few could be observed as introduced in Chapter 5. The evolution pattern of one of them is shown here (Figure 6.16). The basic form appeared on the bed after the 720th minute, within which a clear outline, shallow depression, and slightly prominent median ridge could be partly observed. The mature form of this feature formed in the following 360 minutes. At that moment, the rim of the flute was in perfect parabolic shape with an obvious median ridge on the middle axis of the flute (Figure 6.16: photo T1080). The defect on the distal end of the median ridge was the proximal end of a furrow. Although it was present a perfect form of flute with median ridge, it was not the final bedform observed on the clay bed of Exp. 7. Over the remaining experimental time, the flanks of this flute developed so that they no longer flared outwards and downstream-wards. They altered to slightly inwards which changed the shape of the flute from parabolic to partially horseshoe form. The depression of the flute became deeper and the rim of it became more cusped. Meanwhile, the proximal end of the median ridge was slightly flattened and the distal end of this flute was progressively eroded further more by the elongation of the furrow following it (Figure 6.16: photo T1680).

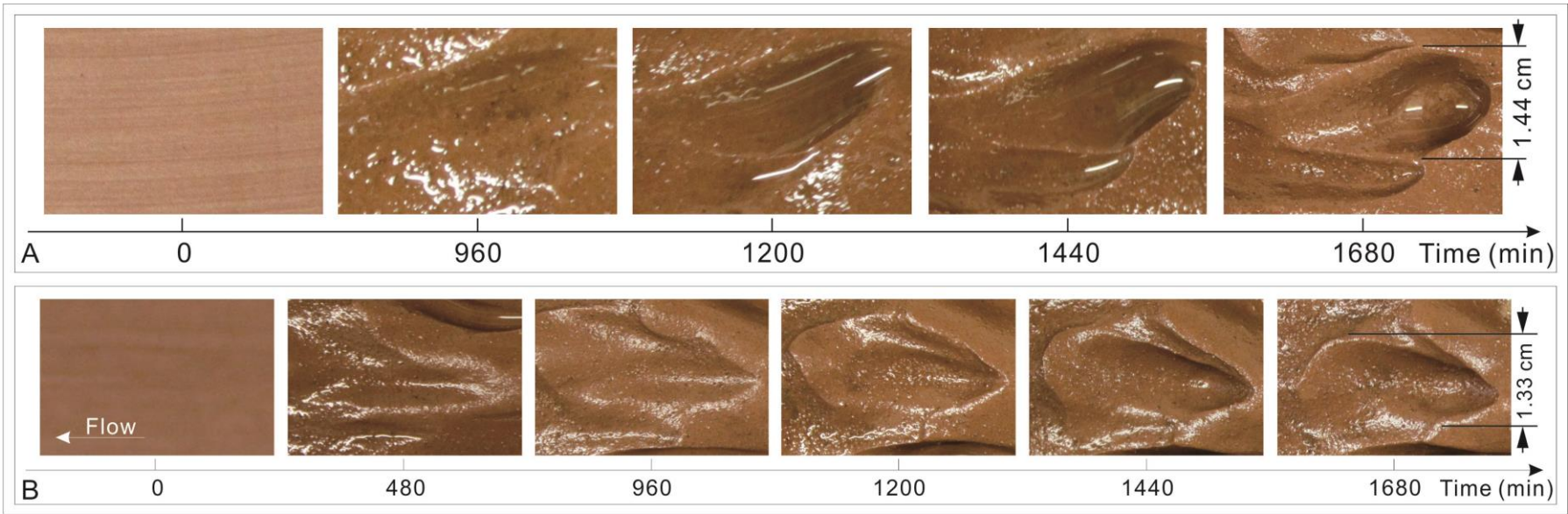


Figure 6.15 Evolution of deep and shallow flutes. Flute in Plot A is observed in the clay bed of Exp. 6 and that in Plot B is in Exp. 7. Flow from right to left.

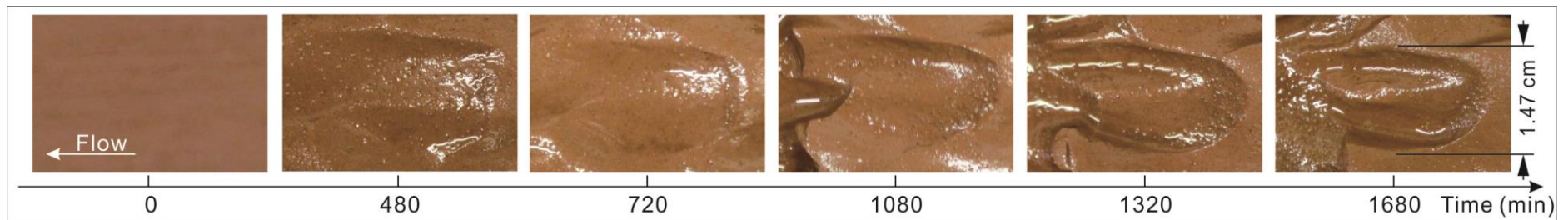


Figure 6.16 Evolution of a flute with median ridge. It was observed in the clay bed of Exp. 7. Flow from right to left.

Overhanging flutes

The feature of overhanging flutes is that the upstream end rim overhangs the principal depression of the flute below it. Therefore, overhanging flutes are normally a kind of deep flute. This was also one of the rare flutes on the current experimental beds, because many features can better be defined as potholes with exit furrow, rather than overhanging flutes. The flute shown in the photos at T1080 and T1440 in Figure 6.17 is good example of an overhanging flute. In the first 720 minutes, the flute developed from a simple sinuous mark as most of the flutes did. From the 720th minute, the upstream end rim and the right flank of the pothole were slightly overhanging over the principal depression. The proximal inner wall of the depression was incised headward further between the 1080th minute and the 1440th minute. This might be mainly caused by the effects of near bed secondary flow within the depression of the flute. The concave part on the proximal inner wall was covered by the lip of of the upstream end rim of the flute and is therefore hard to see in the photos in Figure 6.17 (Figure 6.17: photo T1080 & T1440). Because the small thickness and weakness of the overhanging part, it was destroyed and removed by sediment-laden flow in the last 360 minutes of the experiment. The whole bottom of the flute can be seen in the bed at T1800. A close-up view of the proximal inner wall of the flute shows that there was a small secondary hole on the proximal inner wall. This indicates that the incision of the proximal inner wall never stopped, even in the later period of experiments.

Spindle-shaped flutes

Spindle-shaped flute are a kind of extremely narrow flutes without a median ridge whose length is much bigger than their width. They are usually straight other rather than curved or sinuous. The size of them is normally small, such as the one on the Exp. 7 bed shown in Figure 6.18, which was only 0.65 cm in width. The outline of it formed after 720 minutes and the initial form of it was slightly sinuous with a sharp upstream end and cusped rim. The right flank straightened and the depth of it deepened from the 720th minute to the 960th minute. In the next 240 minutes, it kept deepening a bit and the upstream end became slightly rounder than that observed in the 720th and the 960th minute. The form at this time was considered as a mature form of spindle-shaped flute in the current experiments. It would change to be a furrow with further time.

Comet-shaped flutes

Comet-shaped flutes have not been reported to be observed in natural bedrock channels, but are one of the common erosional bedforms on cohesive substrates. Therefore, it is still important to examine their evolution here.

The flute shown in the photos of T720 to T1200 in Figure 6.19 was a typical comet-shaped flute in the current experiments. From the very beginning to the 720th minute, a form of normal flute evolved from a shallow lower zone observed in the bed of T480 (Figure 6.19: photo T720). At this moment, the area between the two yellow curves looked like a depression which would evolve to be the principal depression of the flute, the lateral flanks of which were tagged by two yellow curves in Figure 6.19. The short dashed curve in the photo of T480 was regarded to develop to be the lateral rim of a lateral furrow within the flute. The following 240 minutes demonstrated a quite different changing tendency of this flute. The movement of the flow should be as follows: water flow entered into the flutes from the inlet in point **a**, converged into the deeper part of the flute and moved sinuously along the right flank, and then spread broadly in the downstream part of the flute. Under the effect of this flow pattern for more than 240 minutes, a mature form of comet-shaped flute was present on the bed by T1200. In the following 360 minutes, the downstream part of the right flank was cut through by an entry furrow of a pothole adjacent to this flute (Figure 6.19: photo T1560 **c**). This entry furrow evolved from a smaller sinuous flute adjacent to the comet-shaped flute. Owing to the convergent effect of the flow, after the rim cut through, the flow entering from the inlet would no longer move on the surface of the comet-shaped flute, but moved downwards along this deeper furrow and incised forward and downward simultaneously until the end of Exp. 7 (Figure 6.19: photo T1800).

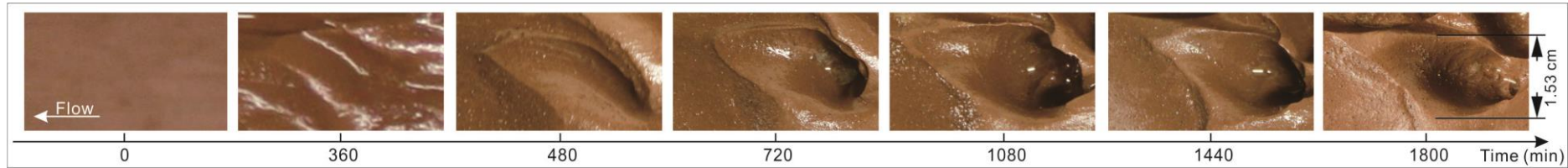


Figure 6.17 Evolution of an overhanging flute. It was observed in the clay bed of Exp. 7. Flow from right to left.

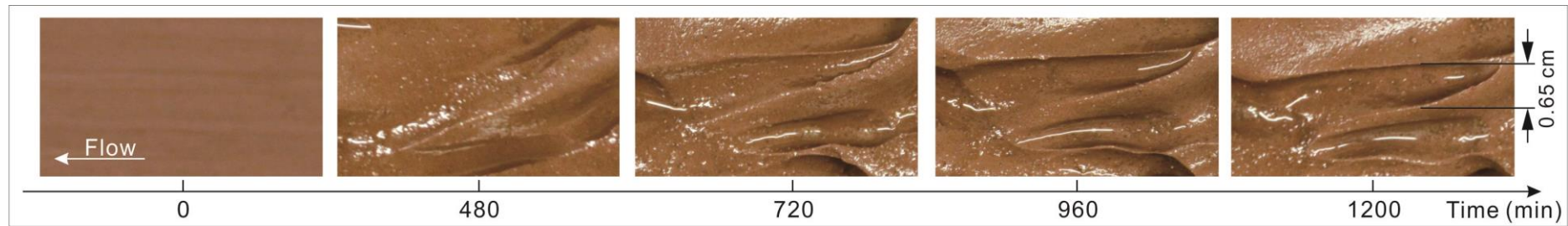


Figure 6.18 Evolution of a spindle-shaped flute. It was observed in the clay bed of Exp. 7. Flow from right to left.

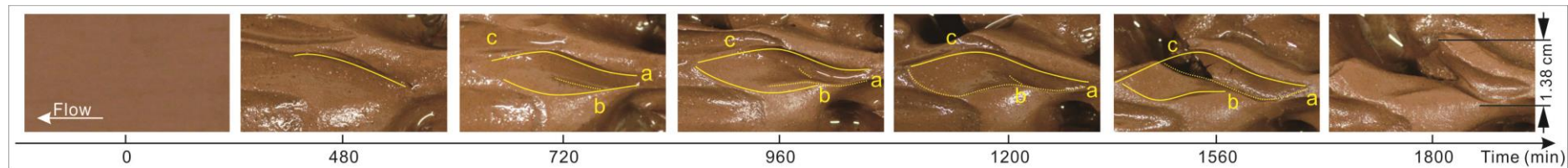


Figure 6.19 Evolution of a comet-shaped flute. It was observed in the clay bed of Exp. 7. Flow from right to left. Yellow curves refer to the shape of the flute.

Flutes with secondary structures were also broadly distributed on the experimental bed just like the potholes with secondary structures. These can be mainly divided into two kinds, flutes with internal secondary structures, and those with external secondary structures.

Flutes with external secondary structures

Flutes with external secondary structures can simply be considered as a linear series composed of more than two flutes with very similar form. Figure 6.20 well illustrates the evolution of a series of flutes with external secondary structures which is observed on the bed of Exp. 7. The flutes could not be observed until the 720th minute of experiments. In the early stage of the experiments, only an entry furrow or other marks and a shallow curved furrow was present on the clay bed (Figure 6.20: photo T480 – curve 1; T600 – curves 1 and 5). The curvature of curve 1 and 5 at T600 indicated that in this area, the direction of water flow might not be restricted to purely streamwise. Flow entered into the furrow from a sharp head at the right bottom corner towards the flaring tail at the upper left corner, and curved along the right inner wall of the furrows (Figure 6.20). A series of approximately parallel curved tracks with similar curvature of curve 1 and 5 appeared on the bed at T720. The following 240 minutes from the 960th minute to the 1200th minute witness the genesis of the flute with external secondary structures. The lower areas between the two adjacent tracks developed to be the principle depression of each secondary flute. The downstream part of the right flank of the former flute would become the left flank of the later flute. Four flutes with almost the same form developed arrayed linearly on the later experimental bed (Figure 6.20: photo T960). The form at this time was considered as the mature form of this kind of flute with external secondary structures/flutes. Flute No. 1 was regarded as the primary flute and the rest the secondary flutes. With time to the end of the experiments, the general form of them barely changes with only the shared crests of them slightly developing to be more cusped (Figure 6.20: photo T1200).

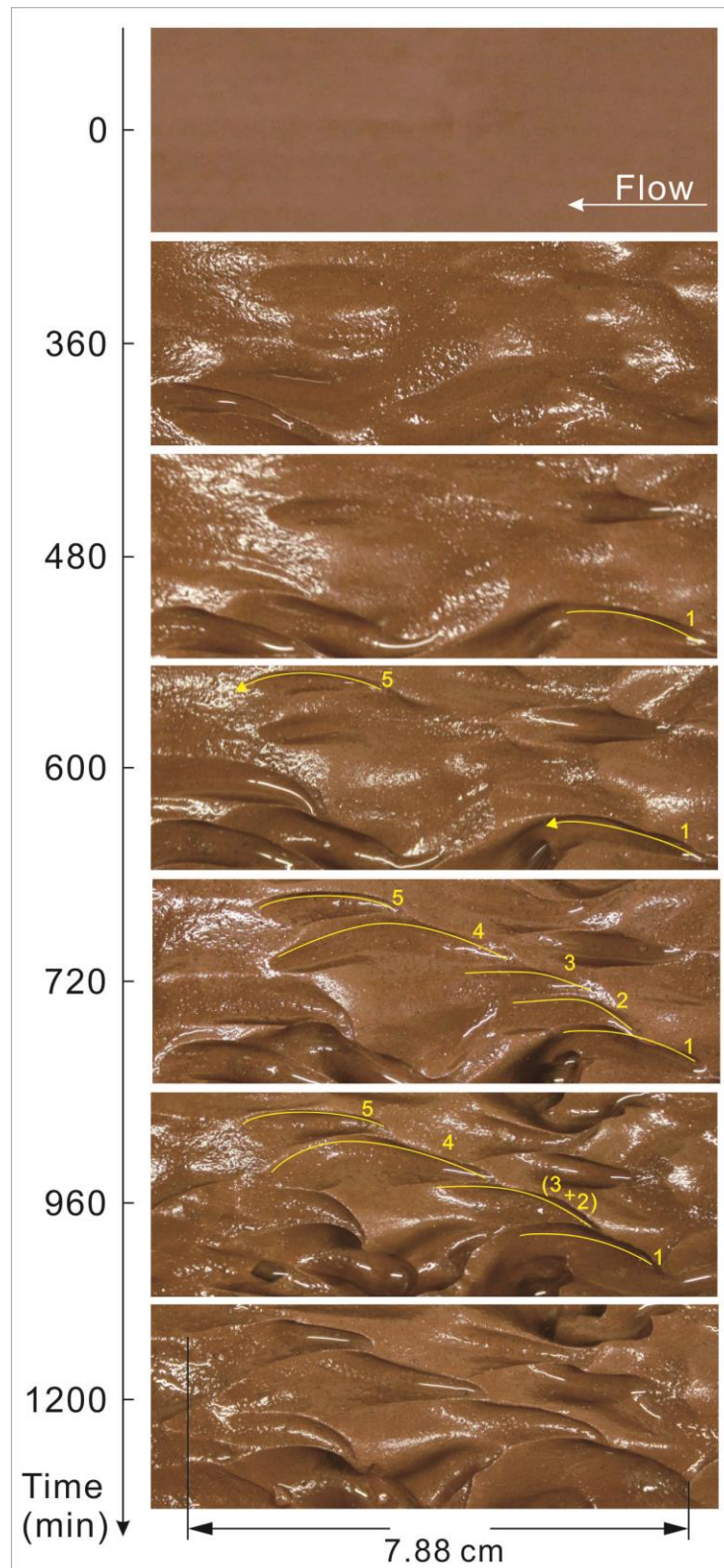


Figure 6.20 Evolution of flutes with external secondary structures. They were observed in the clay bed of Exp. 7. Flow from right to left. Yellow curves refer to the right rims of flutes. 1 to 5 refer to flutes. Curve 2 disappeared over time.

Flute with internal secondary structure

Figure 6.21 shows a flute with internal secondary furrow evolved from a pothole with external flutes on the clay bed of Exp. 7. A pothole was evolved from a shallow short furrow in 120 minutes (Figure 6.21: photo T360 and T480). The pothole is quite round with a short exit furrow extended from the left inner wall. By this exit furrow, there was an external secondary flute the length of which was about three times as long as the diameter of the pothole. The downstream rim of the pothole became indistinct and flared outwards and downstream-wards from the 480th to the 720th minute, and then totally disappeared in the following 240 minutes (Figure 6.21: photo T480 to T720 to T960). This induced the pothole transform to a flute with external secondary flute. From the 960th minute, the basic form flute with secondary structure formed, but the secondary structure at that moment was still an external structure. With further time, both the primary flute and the external flute were polished by sediment-laden flow. The profiles of both of them altered to be cusped and to the same level. Meanwhile, the former raised right rim of the secondary flute was removed as well. The remaining part of the rim of the secondary flute connected with the proximal and right rim to become a whole profile of the flute with internal secondary flutes. From that moment, the external secondary flute transformed to be an internal secondary flute.

Except simple flutes and flutes with secondary structures, some other kinds of flutes in special forms were also observed on the experimental beds. The evolution of some of them, such as paired flutes, paired convergent flutes, lineations forms and En echelon flutes is explained below.

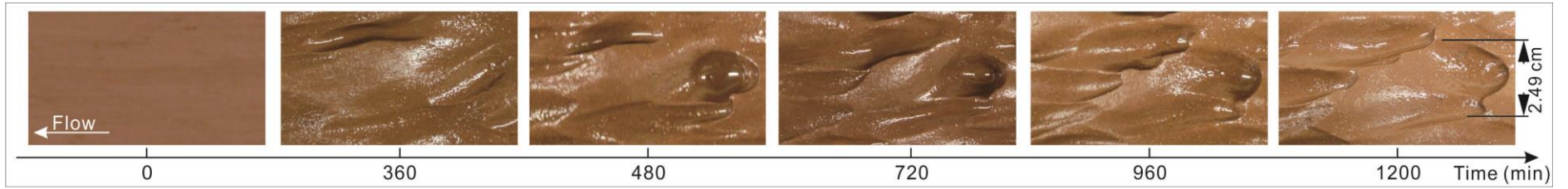


Figure 6.21 Evolution of flute with internal secondary structure. It was observed in the clay bed of Exp. 7. Flow from right to left.

Paired flutes

According to previous studies on bedrock bedforms, paired flutes very rarely seen in natural bedrock channels. Fortunately, one sample of paired flutes was produced by Exp. 6 (Figure 6.22). The formation of them mainly occurred in the last one-third period of Exp. 6 (Figure 6.22: photo T1320 to T1680). In the early bed of T960, a shallow lower zone (tagged by yellow closed curve Figure 6.22: photo T960) and a short furrow (tagged by red curve in Figure 6.22: photo T960) could partly be visible on the bed of Exp. 6. These erosive features would eventually evolved to be paired flutes. In the 360 minutes between the 960th to the 1320th minute, the short furrow cut through its downstream end, elongated and extended in a curved form towards the downstream direction. Finally, once the flow passed the deepest and narrowest part of the furrow and kept moving forwards, it created an expanded downstream zone in the rear of the narrow furrow. The clearer basic form became visible from the 1320th minute. The lower yellow closed curve and the expanded zone shown by the red curve finally formed similar profiles to paired flutes during 360 minutes from the 960th to the 1320th minute. In the last 360 minutes until the end of Exp. 6, the general form of paired flutes kept stable and the depth of them barely changed as well. The only change was the rim of them which became more cusped and obvious, from which it was easier to distinguish these special paired flutes from other erosional features (Figure 6.22: tagged by yellow rectangle in photo T1680).

Paired convergent flutes

Paired convergent flutes are not a typical erosional feature in either bedrock channels or cohesive substrates. Owing to the similarity between paired convergent flutes and approximate-symmetrical paired potholes with both entry and exit furrows that have already been introduced before, it is necessary to simply talk about it here. The main process of their formation was mainly happening in the last stage of Exp. 7, as with paired flutes. Until the 1320th minute, the initial final form of the two flutes did not show. What could be seen was that two sinuous furrows converged towards a certain convergent point. Flow moved from different paths to enter into these two furrows. Up to the 1560th minute, both of the proximal and distal ends of these two furrows curved inwards. Meanwhile a projection could be observed on the clay bed which was very similar to the rhombic projection observed in the system of approximate-symmetrical paired potholes. The lower zone ahead of both furrows and the projection became the inlet of the flow. Two furrows transformed to be curved flutes over time, the ends of

which curved inwards to converge towards the middle axis of the whole system (Figure 6.23: photo T1560 and T1680). Two small internal furrows appeared on both sides of the extended part of the projection (Figure 6.23: photo T1560 and T1680). Those might be caused by the secondary separation flow from the primary flow within two flutes (Figure 6.23: tagged by yellow ellipses in photo T1560 and T1680).

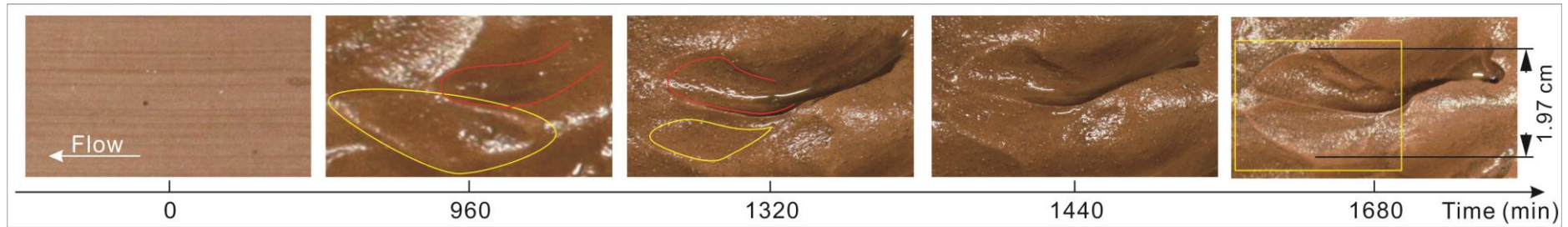


Figure 6.22 Evolution of paired flutes. They were observed in the clay bed of Exp. 6. Flow from right to left. Yellow closed curves refer to the left flute. Red curve refers to the right flute. Yellow rectangle refers to the final form of paired flutes.

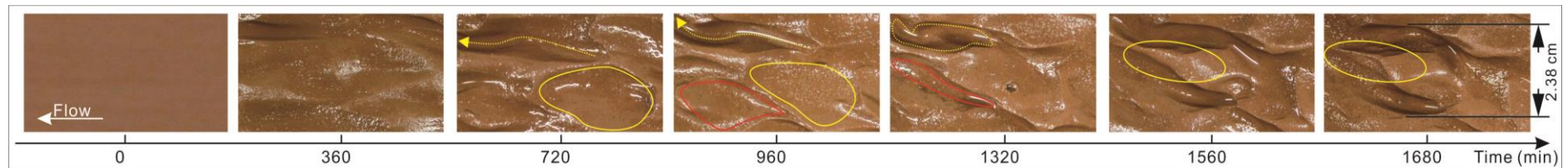


Figure 6.23 Evolution of paired convergent flutes. They were observed in the clay bed of Exp. 7. Flow from right to left. Yellow curves refer to the possible path of flow within the right flute. Yellow closed curves refer to a plan area. Red closed curve refers to the early form of the left flute. Yellow ellipse refers to the extended lee-side slope of the projection.

Lineations

A similar form to natural lineations was observed in the very beginning stage of the downstream part of the Exp. 7 bed (Figure 6.24: photo T240). It was not common, because most of the erosional features introduced before were primarily observed in the medium or later stages of experiments. After experiments running for the first 240 minutes, a large number of shallow small flutes or very short furrows were arrayed on the downstream part of the clay bed. Most of them were parallel or at least approximately parallel to the streamwise. From the evolution sequence of them, it could be learned that each small feature of this lineations could evolve to be many different kinds of erosional features, such as flutes with entry furrow, parallel-sided furrows, curved furrows, pothole with entry spiral rib, etc. (Figure 6.24: photo T480). Therefore, lineations can be regarded as a kind of transition form and stage instead of the final form of the erosional features on bedrock substrates.

En echelon flutes

Unlike lineations which were transitional forms, En echelon flutes were the final form which could be observed on the final bed of experiments. Figure 6.25 demonstrates a group of En echelon flutes sampled in the very upstream end of the clay bed in Exp. 7. They began to form from the 960th minute and have most of the components within the whole area developed after 1320 minutes of Exp. 7. In the early stage, this area was covered by lots of shallow sinuous furrows. Some deeper parts of shallow furrows evolved to be flutes first with shallower parts modified later. The rate of change during the last stage of experiments was much faster than that in the early stage in this area. Most of the secondary flutes within this area formed in the period from the 1320th to 1560th minute. Adjacent flutes shared their rims with each other and every single flute evolved to be a simple deep flutes (Figure 6.25: photo T1560). The En echelon flutes in the photo of T1560 were considered as the final stable state of them. The general form of them would not change a lot in the rest of experimental time (Figure 6.25: photo T1560 to T1800). Only depth kept increasing with time.

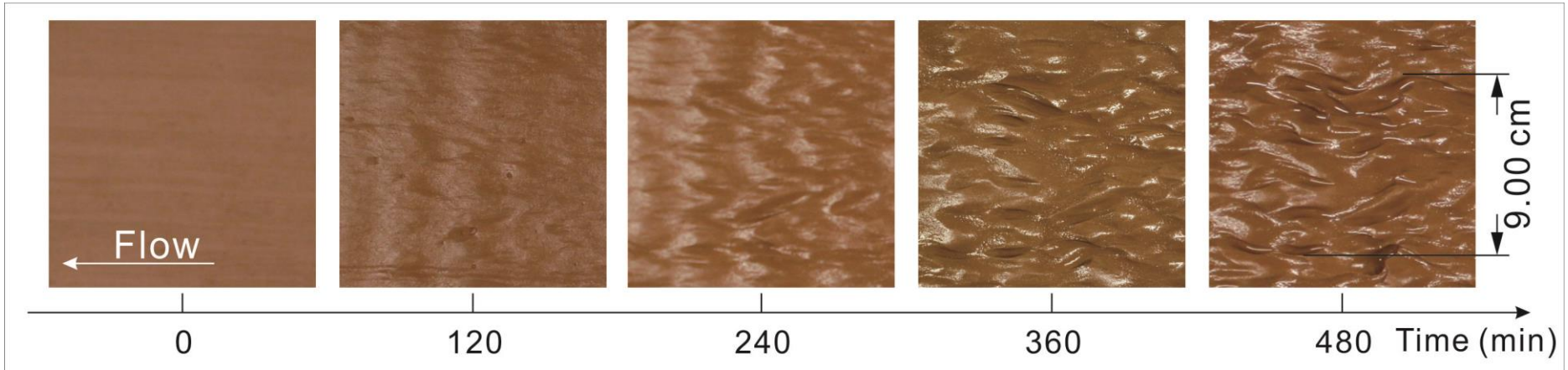


Figure 6.24 Evolution of lineations. They were observed in the clay bed of Exp. 7. Flow from right to left.

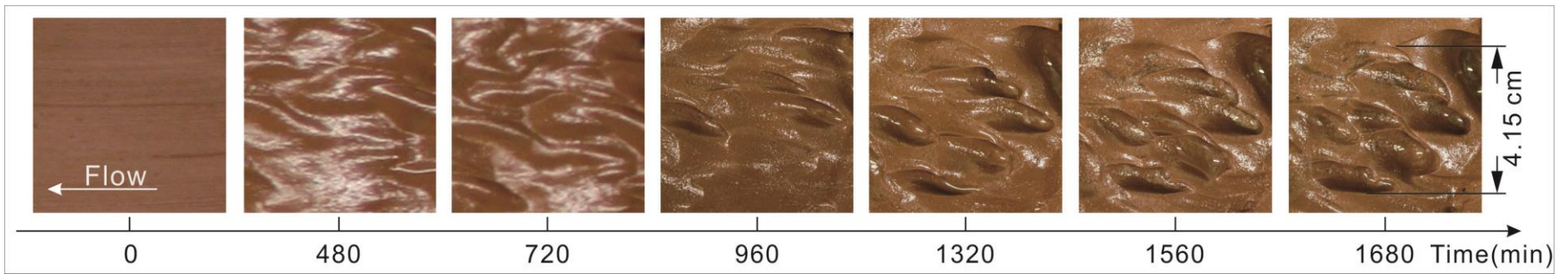


Figure 6.25 Evolution of En echelon flutes. They were observed in the clay bed of Exp. 7. Flow from right to left.

6.2.3 Longitudinal furrows

Longitudinal furrows are the other common erosional features in bedrock and cohesive substrates besides potholes and flutes. In the previous sections of this chapter, some short longitudinal furrows have been mentioned as initial forms or transition forms in the evolution sequence of many kinds of potholes and flutes. However, except being transitional forms of other erosional features, longitudinal furrows, could be present on the final bed of experiments, especially relatively longer and deeper longitudinal furrows. Herein, the evolution processes of different longitudinal furrows are given according to a classification by defined their complexity.

Simple longitudinal furrows contain straight and curved short furrows, and straight and sinuous parallel-sided long furrows. Most of these furrows could exhibit either cusped or non-cusped forms which depends on the flow dynamics above it, the condition of the substrates and the location of where they formed in the experimental bed.

Straight and curved short furrows

The pair of short potholes showing on the later stage of Exp. 6 were initialized from two lateral furrows that extended from the lateral rims of a preset defect in the clay bed, which was 2.4 cm in diameter and 0.3 cm in depth (Figure 6.26: photo T0). The initial form of this pair of straight short furrows was very similar with that of circle shape paired potholes which initialized from a preset defect on the bed of Exp. 6. Two lateral narrow furrows formed and extended downstream from two vertexes of the transversal symmetry axis of the preset round defect (Figure 6.26: photo T480). The right narrow furrow developed to a flute with external secondary flute by its left flank and the left one slightly widened and elongated towards downstream as well, but without secondary structures (Figure 6.26: photo T720). After a further 240 minutes, the right flute and the left narrow furrow evolved to be two potholes with exit furrows. The left flank of the right pothole and right flank of the left pothole were overhanging over the principal depressions of these two potholes which might be induced by the effect of vortices within the hollows. At the same time, the external secondary flute looked more prominent above the bed and became more curved. From the 960th minute to 1080th minute, the experimental bed became progressively more polished. The former prominent upstream end part of the external secondary flute was flattened. The former right potholes elongated to be short furrows with uniform bottoms and cusped rims under the effect of polishing. The mature form of the right short furrow had been completed by

that moment. At this time point, the left pothole was still in the form of a pothole with exit furrow with the hollow deepening, although the raised part of the right flank was flattened as well (Figure 6.26: photo T1080). The following 240 minutes contributed to the formation of the mature form of the left short furrow. Most parts of the rim of the exit furrow and all prominent parts close to it were removed thoroughly. The pothole elongated and deepened to a short furrow shape, developing a uniform bottom and cusped rim with the right short furrow (Figure 6.26: photo T1320). So far, the whole evolution process and final form of the straight furrow have been described. According to this, it can be concluded that, not only can other erosional features be evolved from furrows, but furrows can also be developed from other form and to be the final forms on the experimental bed.

Compared with straight short furrows in Figure 6.26, the evolution process of curved short furrows was simpler. The one shown in Figure 6.27 was formed under a simple elongation and combination process. The early form produced by Exp. 7 was a curved flute with sharp closed head and open flaring tail (Figure 6.27: photo T480 and T720). In the bed at T720, a curved shallow part was partly visible. The depth of this part was much shallower than the depth of the rear of the flute. The most important function of it in this evolution process was that it led to the flute incision headward. The proximal end of the flute incised the proximal wall, elongated along the track of this shallow part, developed a slight curvature towards the upstream end, and then eventually completed the formation of a curved short furrow (Figure 6.27: photo T960). Since a very deep hollow developed in the rear of this curved short furrow, this short furrow would become an entry furrow of this deep hollow over time to lead the flow entering into the hollow to deepen it (Figure 6.27: photo T1200).

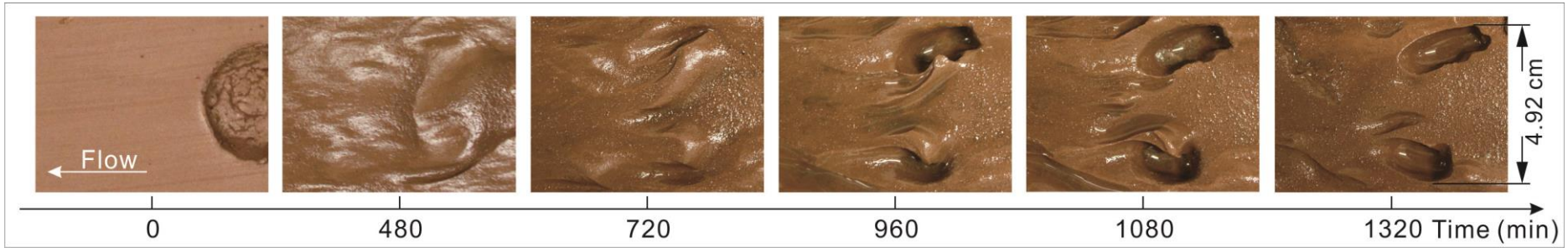


Figure 6.26 Evolution of straight short furrows. They were observed in the clay bed of Exp. 6. Flow from right to left.



Figure 6.27 Evolution of curved short furrow. It was observed in the clay bed of Exp. 7. Flow from right to left.

Straight and sinuous parallel-sided furrows

The forms of straight and sinuous parallel-sided furrows were the simplest forms of furrows on the experimental bedrock analogue beds. Although sinuous parallel-sided furrows look slightly more complex than straight ones, in fact, it was much harder to find straight parallel-sided furrows than sinuous ones in the experimental beds. This might be because both the flow direction right above the bed and the actual cohesive behaviour of the modelling clay beds are changeable. The flow direction at the proximal end of furrows depended on the morphology of the entrance zone and marks ahead of, and around furrows. However, in natural bedrock channels, long straight parallel-sided furrows are very common and this is not observed on the current experimental beds. This may be because the strength of the real bedrock is much greater than the modelling clay used herein, and the surface of real bedrock can not be altered in the short term by sudden changes of flow direction. Even so, a few straight furrows could still be observed on the experimental beds, such as the one in Exp. 7 shown by Figure 6.28, whose shape barely changed after the formation of the initial form after the first 600 minutes of flume running to the end of Exp. 7 (Figure 6. 2: photo T600 to T1080). Hence, any changeable characteristics of the modelling bed are not a weakness of the experiments.

The initial form of sinuous parallel-sided furrows, consisted of a shallow lower track in the early stage of the experiments (Figure 6.29: photo T360). After the first 360 minutes, flow converges into the lower zone and moves along it downstream-ward. From then on, the lower zone kept incising downwards and elongating along the track to transform it to be a mature sinuous parallel-sided furrow. The outer bank of the bend would move outwards and the inner bank would move inwards over time while the width of it increased simultaneously (Figure 6.29: photo T1080).

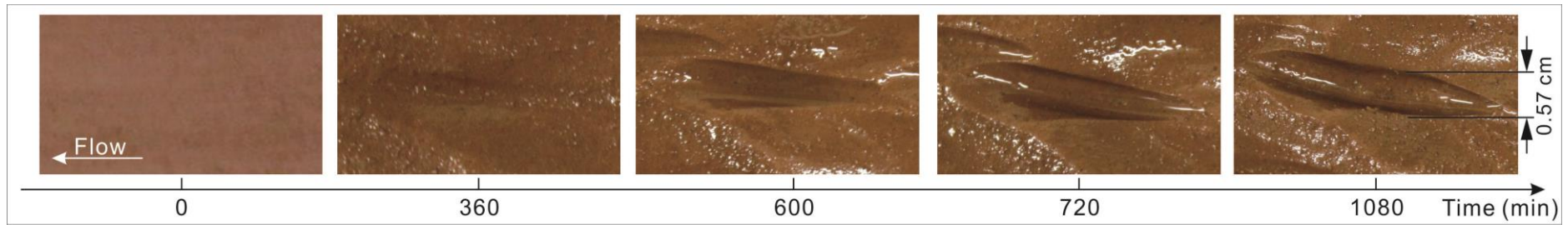


Figure 6.28 Evolution of a straight paralleled-sided furrow. It was observed in the clay bed of Exp. 7. Flow from right to left.



Figure 6.29 Evolution of sinuous parallel-sided furrows. They were observed in the clay bed of Exp. 7. Flow from right to left.

Cuspate or non-cuspate furrows

Whether furrows had cuspate or non-cuspate rims mainly depended on the integrated action of morphology of the surrounding area, flow condition and the stage of development of the experimental beds. Even a single furrow could have both cuspate and non-cuspate rims simultaneously (Figure 6.30). The furrow in Figure 6.30 was a long sinuous furrow observed in Exp. 7. Although it was not very consistent and was divided into two parts, upstream (Figure 6.30: **a**) and downstream (Figure 6.30: **b**), these were still considered as a whole and an entire sinuous furrow. The cuspate rim was always observed on the outer banks (Figure 6.30: tagged by yellow curves) and the non-cuspate on the inner banks (Figure 6.30: tagged by red curves). This was probably because flow preferred to move along the outer bank while most of the erosion effect applied on the wall of the outer bank. Consequently the inner banks were much rounder than the outer banks. On the other hand, the banks of the furrow in the downstream part were not as sharp as those of the upstream part. This might be due to the dramatic dissipation of flow energy after flow passed the middle part of the furrow.

On the other hand, as bedforms seen in the former section, non-cuspate rims were observed in the period of early and medium stage of experiments and cuspate rims always evolved from these non-cuspate ones in the later stage of experiments, due to the polishing effect. The applicability of this process, observed in the current experiments, to natural bedrock is difficult to determine because it is hard to say what evolution stage the natural bedrock bedforms are in.

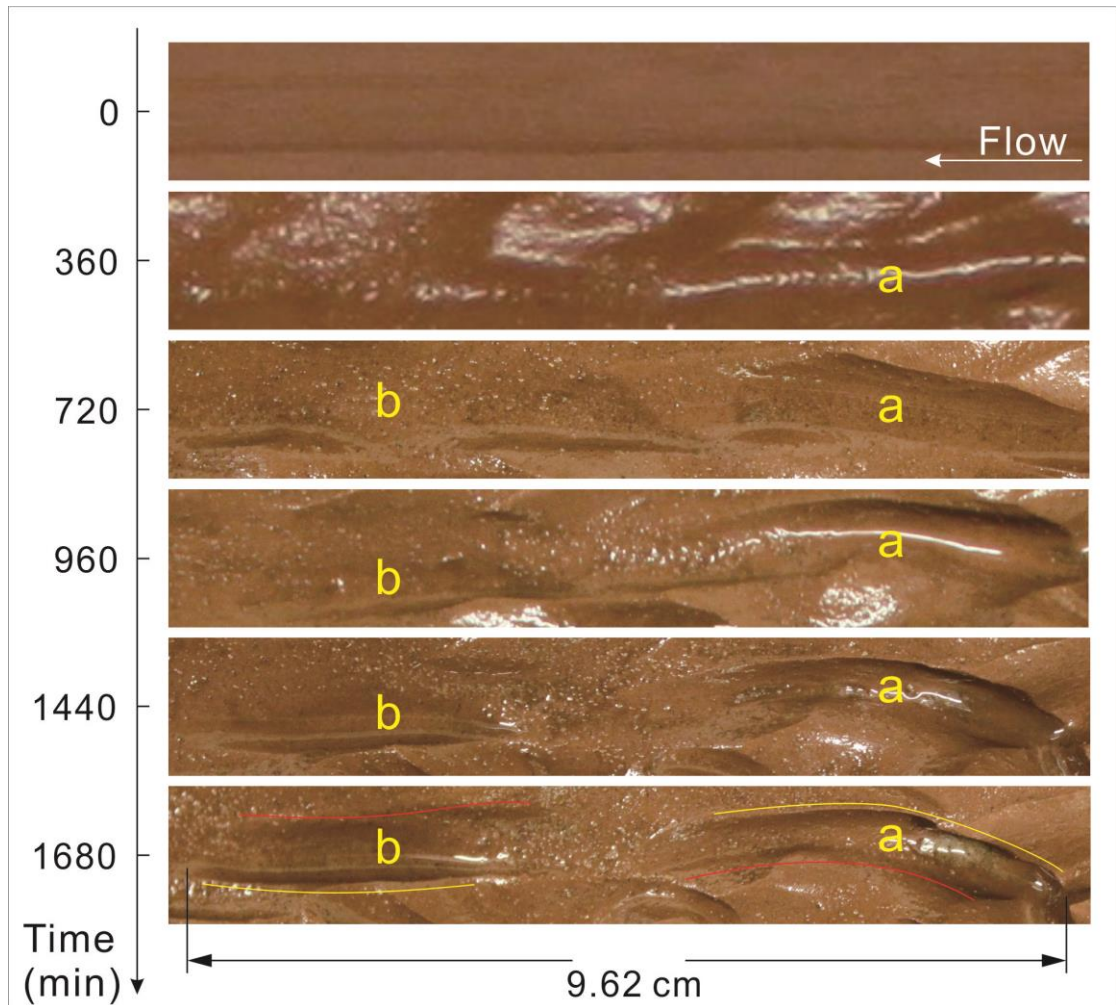


Figure 6.30 Evolution of cusped and non-cusped parallel-sided furrows. They were observed in the clay bed of Exp. 7. Flow from right to left. a and b refer to the upstream and downstream parts of the furrow, respectively.

After talking about simple forms of longitudinal furrows, some other special complex forms, including shear zone furrows, groups of parallel-sided furrows, bifurcating furrows, convergent furrows, regular and irregular compound furrows and expanding furrows, are introduced herein to investigate the evolution of them.

Shear zone furrows

The shear zone furrows defined in the current experiments are different from those defined by Richardson and Carling (2005) that has been discussed in section 5.3.2 in Chapter 5. In the current experiments, sinuous furrows initiated from the lee-side of a projection were defined as shear zone furrows. This kind of projection was normally a part of obstacle marks or from the center of a horseshoe-shaped furrow. The example given here was observed in a system of obstacle marks in Exp. 7 (Figure 6.31: photo T1320). Two shear zone furrows with a shared crest generated from the lee-side of a projection (Figure 6.31: tagged by red circle in photos T960 and T1200). From as early as T720, a projection with two shallow lower parts in the rear of it was partly visible (Figure 6.31: photo T720). All of furrows and projection were growing from the 720th minute to the 1200th minute. The projection became increasing obvious when the surrounding area was continuously incised. The formation of the two shear zone furrows was presumably due to the shear zone in the rear of the projection, within which secondary separation longitudinal flow with suspended sediments rotated backwards towards the upstream. This rotation of the secondary flow would erode the surface of the back of the projection headward. The proximal ends of the furrows then elongated upstream over time (Figure 6.31: tagged by yellow curves in photo T960 to T1320). With the interaction of the current flow over the projection which altered the form of the downstream part of the shear zone furrows, two shear zone furrows eventually developed and became visible on the final bed of Exp. 7 (Figure 6.31: photo T1320).

Group of parallel-sided furrows

A group of parallel-sided furrows observed in the final bed of Exp. 7 were evolved from the lineations observed in the bed of early stage of Exp. 7 (Figure 6.32 and Figure 6.24). Each single erosional mark in the lineations evolved to either straight flutes, spindle-flutes, comet-shaped flutes, curved parallel-sided furrows, or straight parallel-sided furrows (Figure 6.32: photo T480 to T960). In this period, these bedforms also changed forms from one to the other, for example, a short furrow would change to be a short flute and vice versa. In the later stage of the experiments, most forms tended to

transform to be parallel-sided furrows (Figure 6.32: photo T1320 to T1680). All parallel-sided furrows here were short furrows in elliptical form with cusped rims and approximately uniform inner bottoms. They were the mature form evolved from lineations and present on the final bed of Exp. 7. This evolution process fully accorded to the principles of continuity and convergence of bedrock bedforms, which indicates that a given type of bedform is polygenetic as it could evolve from different features through different routes (Richardson and Carling, 2005).

Bifurcating furrows

Bifurcating furrows on experimental beds could be divided into 2 types according to the scale. The bifurcating furrows in Plot A of Figure 6.33 were the smaller ones observed on the bed of Exp. 7 and the other in Plot B were a bigger system observed on the bed of Exp. 8. For the smaller furrows in Plot A, beds of early stage of Exp. 7 illustrate that two branches of this bifurcating furrow (yellow dashed curves) were actually formed much earlier than the main furrow (yellow curves) ahead of them (Figure 6.33: Plot A – photo T480 to T840). The channel linking the main furrow and two branches started to be observed from T960. From that moment, the whole system seemed to stop changing over time.

In the other case of bigger bifurcating furrows system, parts of the branches were also forming prior to the main channel ahead of them (Figure 6.33: Plot B – photo T360 to T720). The depression parts on the tracks of branches were affected by flow individually. On the bed of T360 and T480, no sign of a channel of main furrow could be found in the bed. In the area that would evolve to be a later junction of the main furrow and branches, there was a projection part (Figure 6.33: tagged by red circle in Plot B – photo T480). In the period between the 480th and 720th minute, the projection was entirely removed and that area became a lower zone. Meanwhile, a broad furrow was suddenly produced ahead of two branches (Figure 6.33: Plot B – photo T720). By the 960th minute, all furrows in this bifurcating furrows system became mature and more obvious (Figure 6.33: Plot B – photo T960).

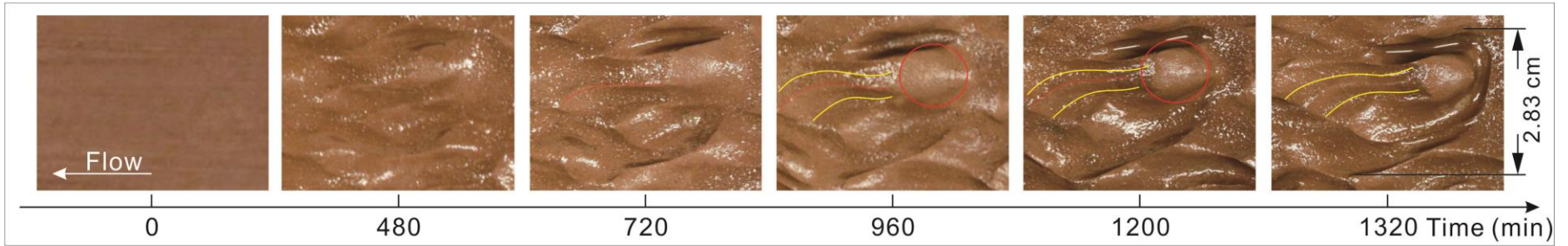


Figure 6.31 Evolution of shear zone furrows. They were observed in the clay bed of Exp. 7. Flow from right to left. Yellow curves refer to the possible paths of flow in the shear zone furrows. Red dashed curves refer to a shared crest of two shear zone furrows. Red ellipses refer to a projection on the bed.

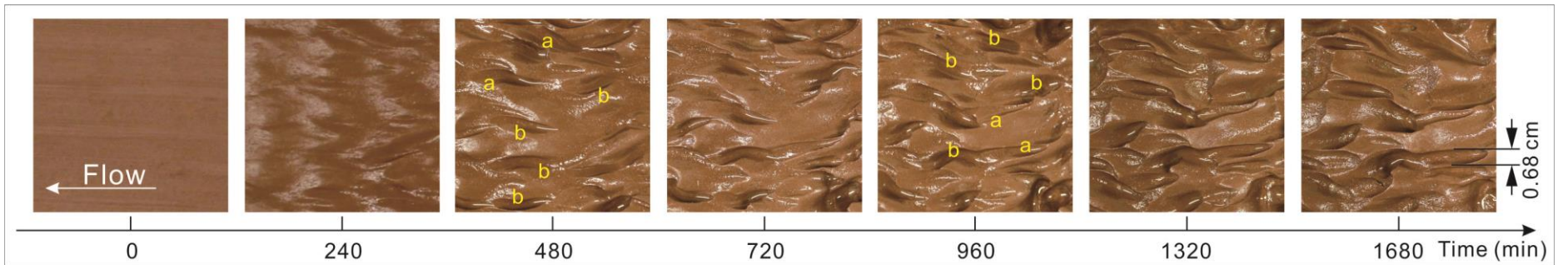


Figure 6.32 Evolution of a group of parallel-sided furrows. They were observed in the clay bed of Exp. 7. Flow from right to left. a and b refer to the individual marks on the experimental bed.

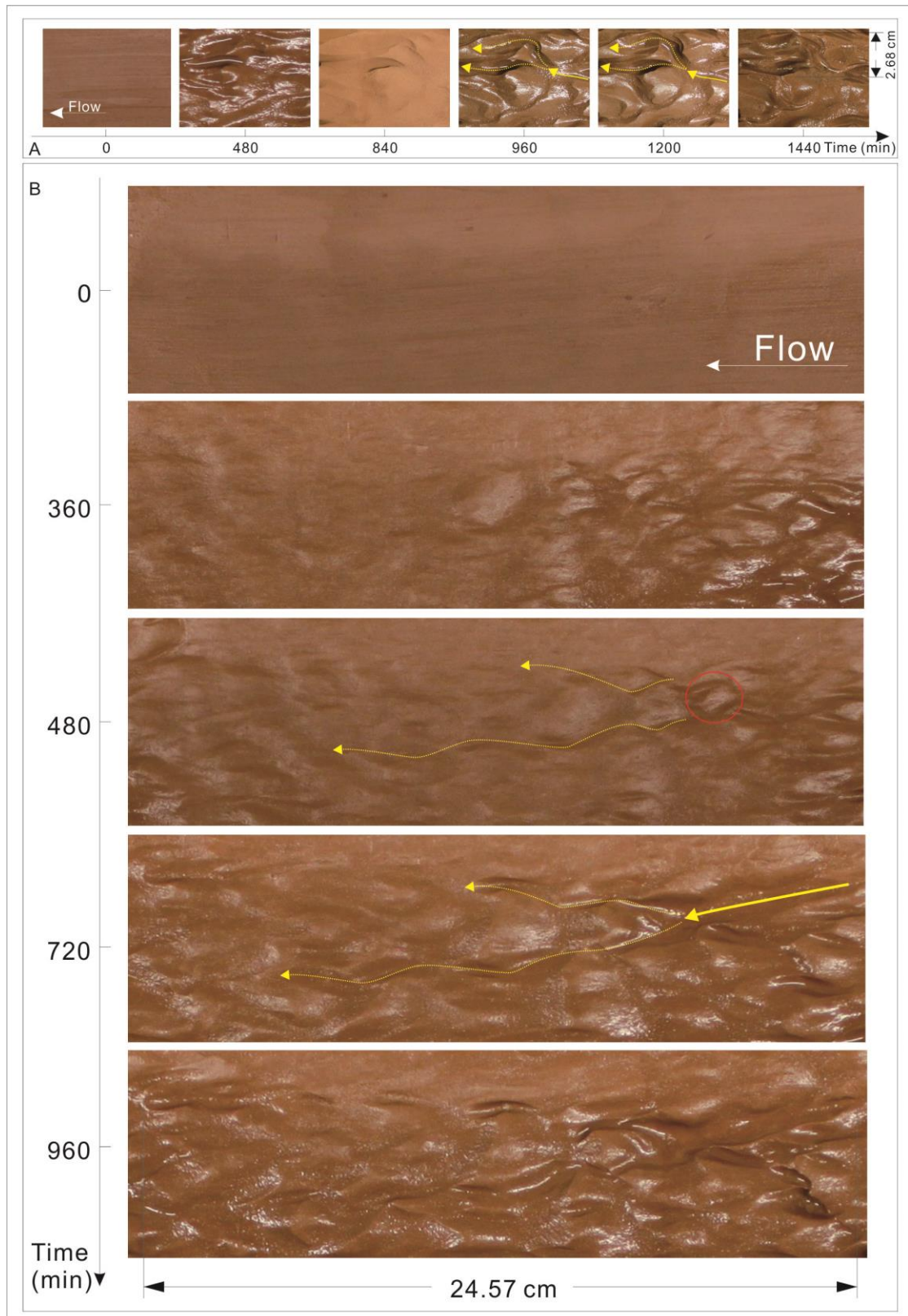


Figure 6.33 Evolution of bifurcating furrows. They were observed in the clay bed of Exp. 7. Flow from right to left. Yellow curves refer to the possible paths of flow within the primary furrow. Yellow arrowed dashed curves refer to branches. Red ellipse refers to a projection on the bed.

Convergent furrows

Convergent furrows are the opposite bedforms to bifurcating furrows. The most interesting part is that the bigger furrow which two branches eventually converge into formed obviously earlier than the two branches (Figure 6.34: photo T480 to T720). From the early stage of experiments, T480, a long partially parallel-sided furrow had already been produced by Exp. 7. The rims of its upstream part were parallel and cusped. The left side rim of the downstream part was obscure (Figure 6.34: photo T480). Moving forward to the bed of T720, the middle part of this long furrow became sinuous and curved towards the right side. A curved external secondary furrow formed by the right side of the bend of the long furrow. From this moment, the downstream part of the long furrow eroded faster than the upstream end part. A slope could be observed at the back of the bend area. From then on, the long furrow separated into two parts and the downstream part of it evolved to be an independent furrow. In the mean time, a short furrow started to form on the opposite side of the external secondary furrow (Figure 6.34: tagged by yellow dashed curve in photo T720). The basic form of the convergent furrows developed on the bed from the 960th minute. The furrow separated from the long furrow in the downstream part of this area developed its own proximal rim and eventually became a totally independent furrow. The small furrow on the left side kept deepening and developed around the projection (tagged by blue circle in Figure 6.34) to converge into the new independent furrow. Flow from the upstream part changed direction when met the projection and curved into the new independent furrow (Figure 6.34: photo T960 to T1080). So far, all components of convergent furrow appeared and a completed system of the convergent furrows with obvious cusped rims was eventually produced in the bed at T1440 (Figure 6.34: photo T1440).

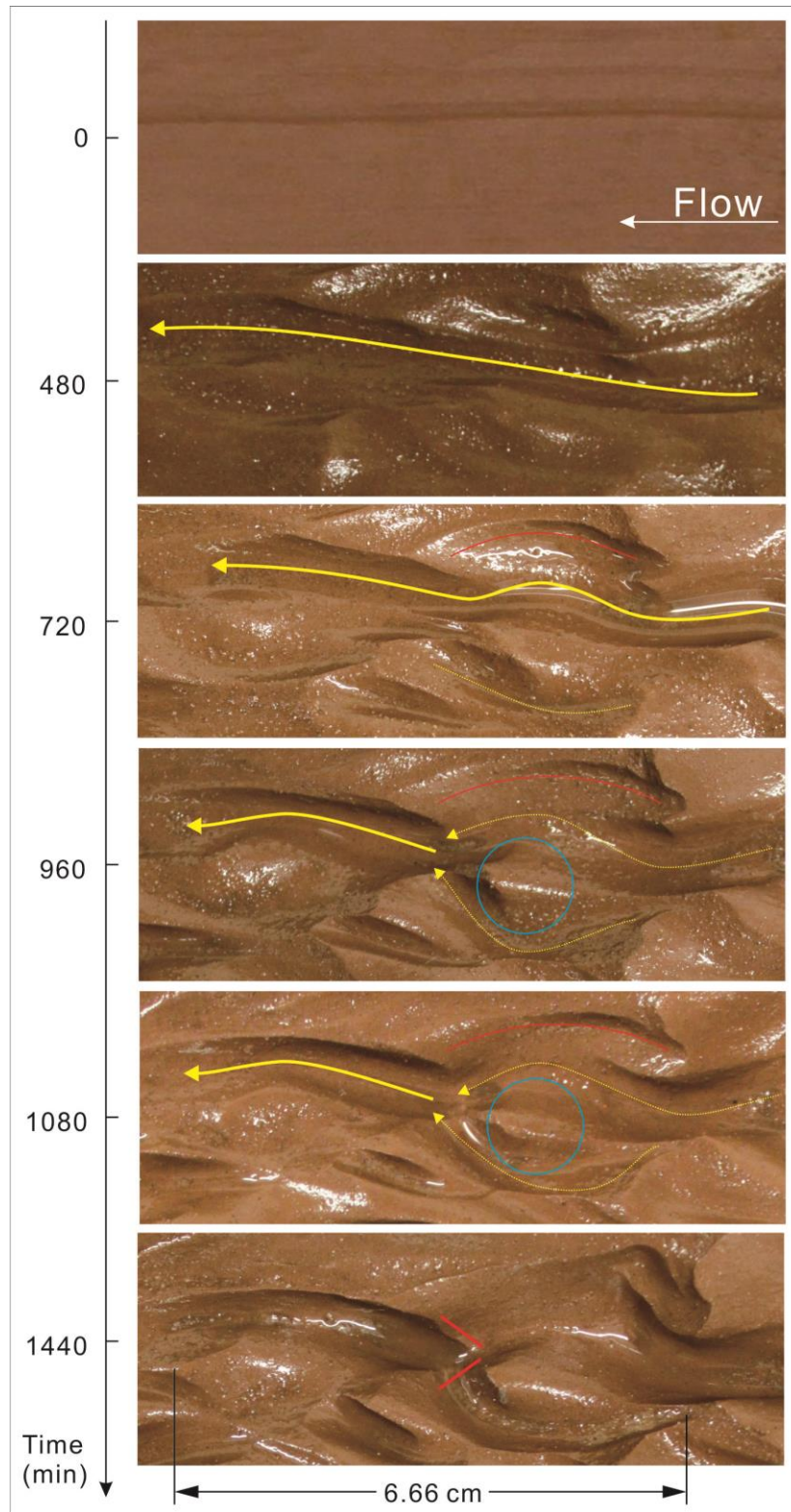


Figure 6.34 Evolution of convergent furrows: They were observed in the clay bed of Exp. 7. Flow from right to left. Yellow curves refer to the possible path of flow within the bigger sinuous furrow. Yellow arrowed dashed curves refer to branches. Red curves refer to a lateral furrow. Blue circles tag a projection and short red lines in Plot 1440 refer to inlets of flow entering into the primary furrow.

Regular compound furrows

The series of regular compound furrows in Figure 6.35 were observed in the later stage of Exp.7. The most downstream furrow was the first one to forming in the clay bed (Figure 6.35: 1 in photo T480). The other two furrows emerged one by one and became arrayed linearly from downstream to upstream. The flow path should change from the bed at T480 to the bed at T720 according to the trend of the furrows. The long furrow arrowed in the photo at T480 should be the original flow path leading water into furrow 1. It was cut by furrow 2 which also altered the flow path from the original path to a new one of yellow curve in photo T960 in Figure 6.35. A pothole formed in the proximal end of furrow 2 in the bed at T960 and a similar one formed in the proximal end of furrow 1 at T1320. Both of them were likely created by the effect of secondary vortices. Over time to the end of Exp. 7, the last furrow (No. 3) eventually formed. Although these three furrows were not in exactly the same form, they were very similar and might experience a similar formation process. For that reason, they were considered as regular compound furrows.

Irregular compound furrows

The irregular compound furrows observed in the experiments were the mature forms in the final bed of Exp. 7. These bedforms were initialized from two regular furrows (Figure 6.36: tagged by yellow rectangle in photo T480) and a long sinuous furrow (Figure 6.36: tagged by red rectangle in photo T480). The evolution process mainly occurred in the later 2/3 period of Exp. 7. On the bed at T480, two separate regular furrows were produced linearly on the bed and a broader sinuous furrow with non-cuspate rim emerged. In the following 240 minutes, the distal end of the former furrow and the proximal end of the later one were cut through to connect two separated regular furrows to be a long sinuous furrow. Meanwhile, both long sinuous furrows deepened (Figure 6.36: photo T720). The profiles of both the sinuous furrows tended to be increasingly clear from the 720th to the 960th minute. The next 480 minutes witnessed the formation of the cuspate rims for all parts of both furrows. After these changes, these two long sinuous furrows evolved to be increasingly similar and eventually formed mature irregular compound furrows (Figure 6.36: photo T1440).

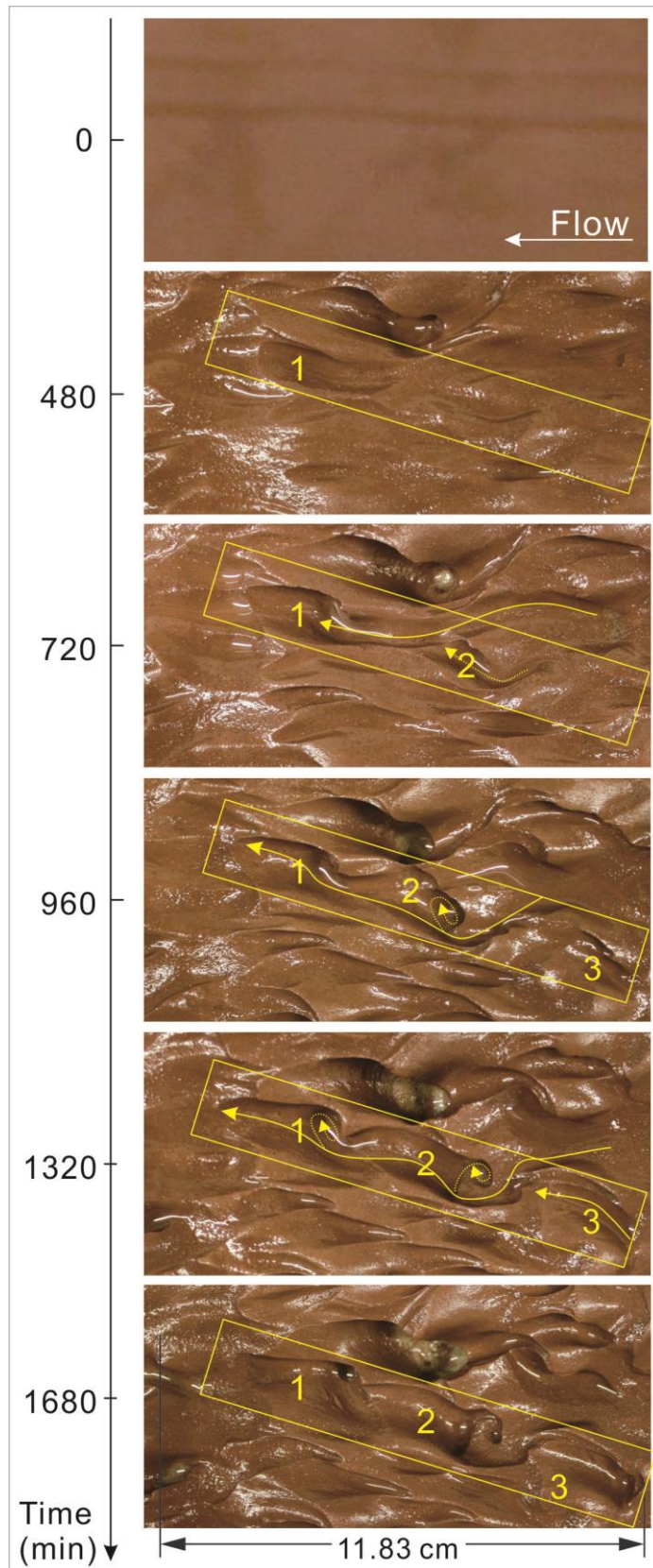


Figure 6.35 Evolution of regular compound furrows. They were observed in the clay bed of Exp. 7. Flow from right to left. Yellow rectangles refer to the formative process of these furrows. 1, 2 and 3 refer to the specific furrows.

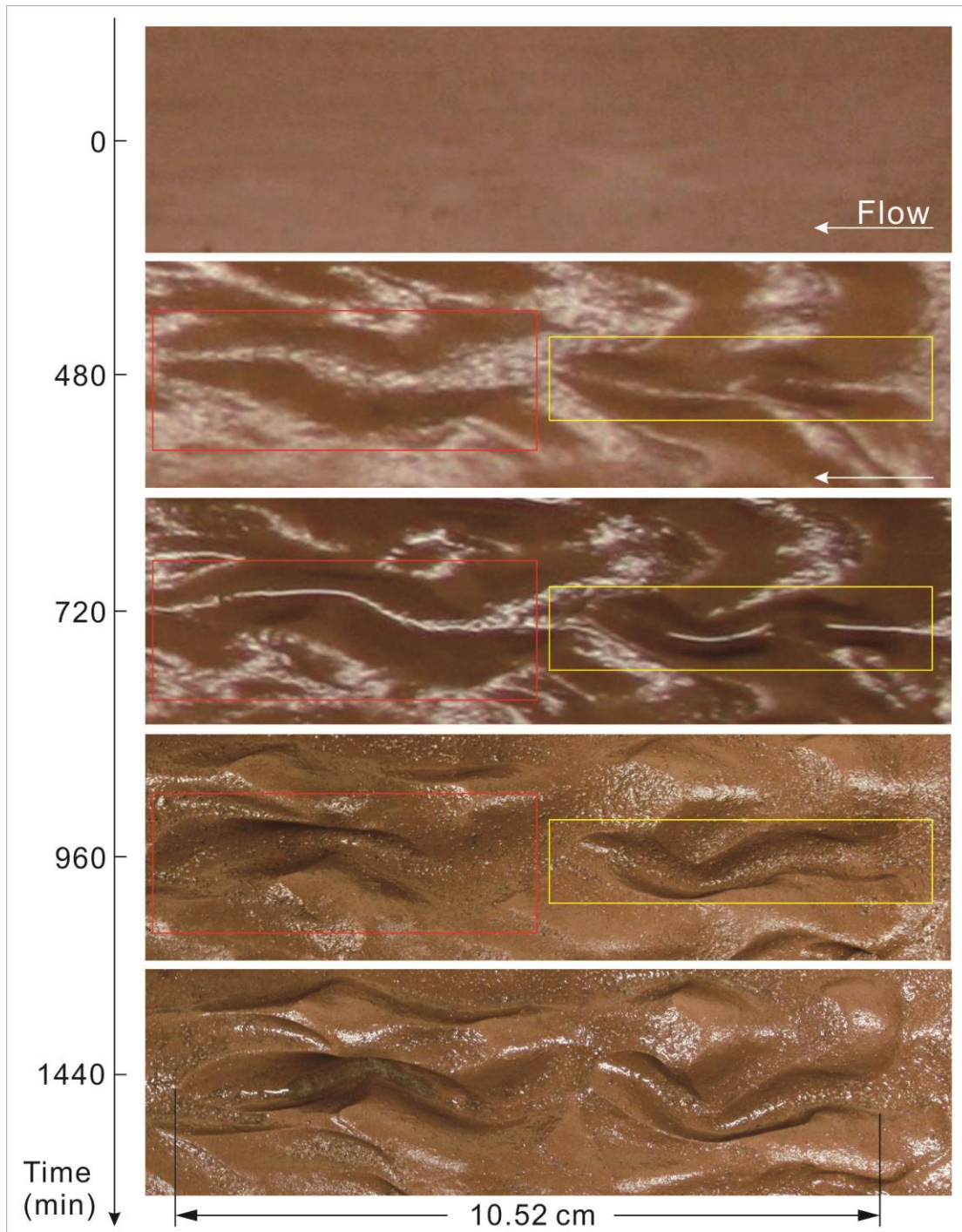


Figure 6.36 Evolution of irregular compound furrows. It was observed in the clay bed of Exp. 7. Flow from right to left. Yellow rectangles refer to the change of a pair of regular furrows and red rectangles refer to the change of a long sinuous parallel-sided furrow.

Expanding furrows

Expanding furrows are not common in either natural bedrock channels or the current experimental beds. The one illustrated in Figure 6.37 was one of only three observed in all the modelling clay beds. Until the 960th minute, the early form of this expanding furrow appeared to be a bifurcating furrow whose downstream part bifurcated into two branches (Figure 6.37: photo T960). However, it did not develop to be a bifurcating furrow according to their definition. The flow instead converged into one branch, the left one (Figure 6.37) whilst the other branch was abandoned. From the final form of this expanding furrow, the flow entered into the narrow forepart furrow from its sharp proximal end, and curved into one branch, widening the downstream end of the furrow to an expanding part and then spread out of it (Figure 6.37: photo T1320 to T1560). A separation flow would form in the last stage of the furrow formation and moved spirally downwards to create a secondary pothole in the junction of the narrow furrow and the expanding area (Figure 6.37: photo T1680). Meanwhile, the narrow furrow was eroded more headward and slightly elongated towards upstream and combined with the other furrow ahead of it to form a longer and wider furrow. This combined bigger furrow and the expanding area eventually comprised the final form of the expanding furrow on the clay bed of Exp. 7 (Figure 6.37: photo T1680).

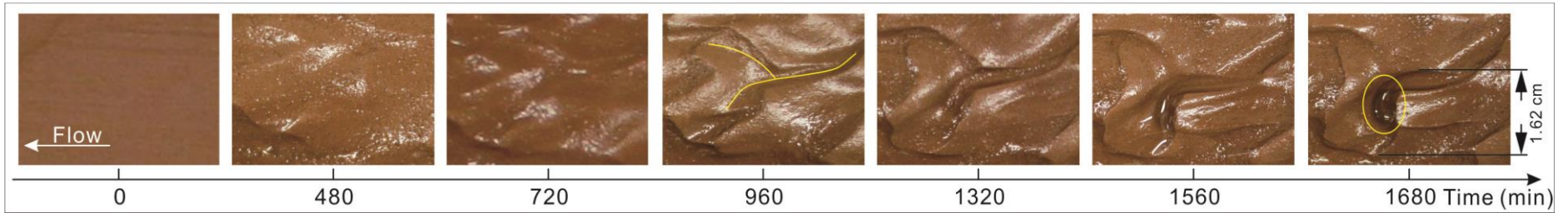


Figure 6.37 Evolution of expanding furrow. It was observed in the clay bed of Exp. 7. Flow from right to left. Yellow curves refer to the possible path of flow within the furrow. Yellow ellipse tagged the secondary pothole in the junction of the narrow furrow and expanding area.

6.2.4 Non-longitudinal furrows

Reversed furrows

Reversed furrows were the only non-longitudinal furrows produced in the current experiments. They exhibited different sizes and shapes in Exp. 6 and Exp. 8 (Figure 6.38). Comparison of the evolution of three series of reversed furrows, indicates that the reversing process of them normally occurred in the second half of experiments. The initial forms of the reversed furrows here were normal furrows. Headward erosion happened on all of them to elongate their proximal ends. However the elongation of their proximal end did not occur directly upstream. They were slightly curved at the early stage of their evolution (Figure 6.38: Plot A – photo T1200; Plot B – photo T960 and Plot C – photo T480). With time, the upstream ends not only curved but reversed by 90 to 180 degrees and sometimes connected with other furrows to partially form a half circle (Figure 6.38: Plot A – photo T1320; Plot B – photo T1320 and Plot C – photo T960). The downstream ends of them did not elongate or deepen a lot. The principal changes happened mainly along the reversed proximal end which developed by increasing depth and cutting through the proximal end. Once it reversed beyond 90 degrees, the flow moving along the reversed part might mix with flow directly entering from the upstream edge. The integrated flow could keep eroding the inner wall of the proximal end and even cut through it (Figure 6.38: Plot A – photo T1440; Plot B – photo T1200). From the form of the reversed furrows, the only thing that could be inferred was the flow path. But the reason for why the flow provided headward erosion and could reverse by so a big degree is still questionable and needs to be investigated by further work.

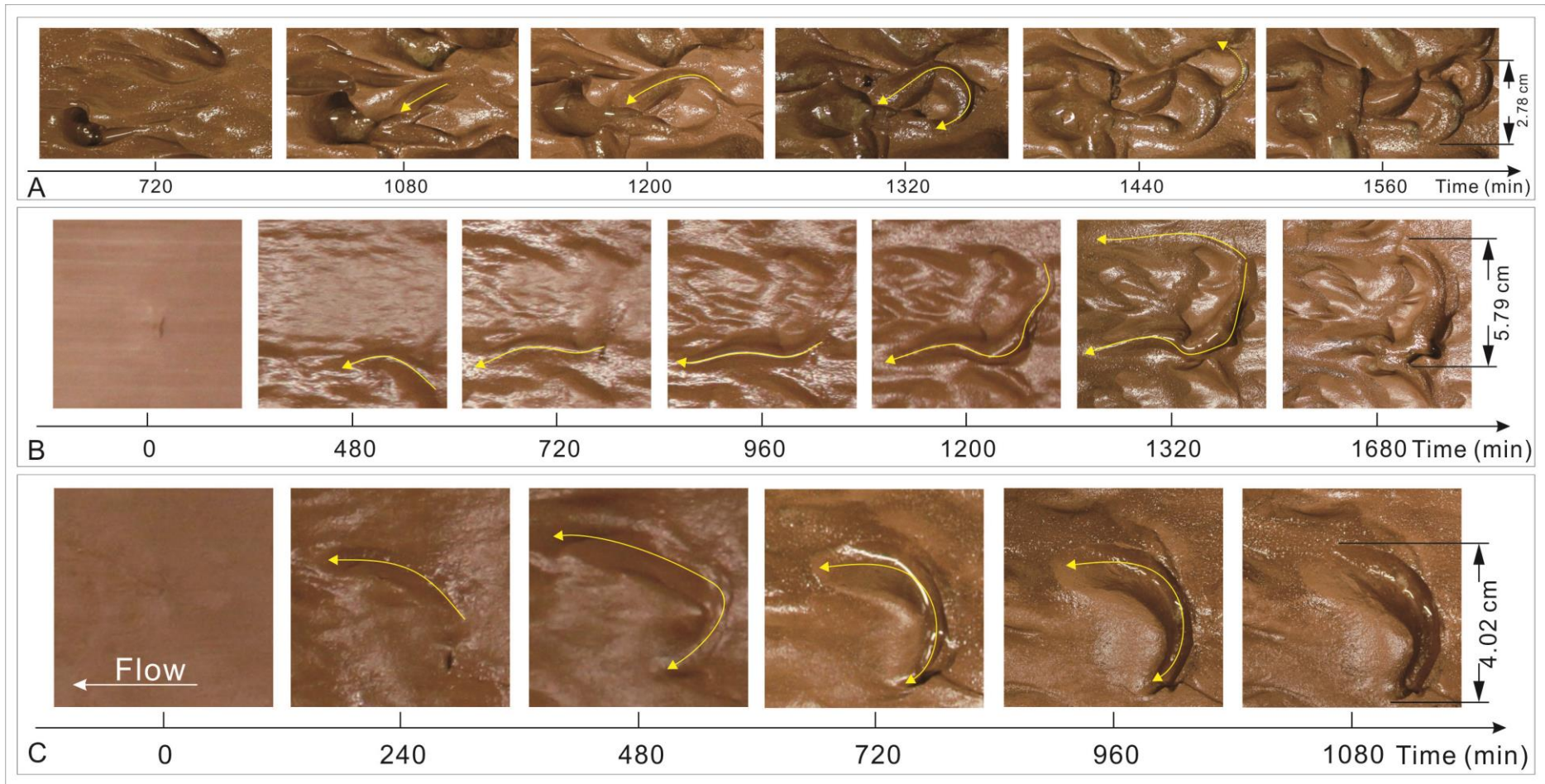


Figure 6.38 Evolution of reversed furrows. Furrows in Plot A and B were observed in the clay bed of Exp. 6, and C in Exp. 8 . Flow from right to left. Yellow arrowed curves refer to the possible paths of flow within the furrows.

6.2.5 Convex and undulating surfaces

Hummocky form

The hummocky form was convex and undulating form on the experimental beds like a mud wave (Figure 6.39). The structure of the hummocky form in Exp. 7 was very regular. During the whole duration of Exp. 7, the general structure of the hummocky form barely changed from the initial formation of them produced in the very beginning of the experiments. The regular form should be created under the effect of steady flow with small separated flows marked by a separation zone in its near bed layer (Richardson and Carling, 2005). This possibly indicates that both the condition of the clay bed and the flow structures above it were very steady and homogeneous (Richardson and Carling, 2005). This inference might also be applied to the hummocky form on the natural bedrock channels. If the condition of the substrate of the natural bedrock and the above flow, reach a certain equilibrium state, such kinds of regular hummocky form could probably be produced under the effect of a long-term continuous steady flow. Whether this inference is right or not needs to be validated by further work.

Bladed forms

Bladed forms observed in the current experimental beds were mainly the shared cusped crests of at least two different kinds of erosional features at the end of experiments (Figure 6.40). Most of the erosional features deepened and widened over experimental time. Two or more separated feature developed and got closer and closer while the area between them was getting smaller and progressively more cusped. It would eventually transform to be a cusped shared crest of two adjacent erosional features. Meanwhile, the former non-cusped rims and the inner walls of the erosional features were polished by sediment-laden flow to form cusped rims or overhanging rims. All these effects could induce the formation of bladed forms on the experimental beds and probably in natural bedrock channels. The formative process for bladed forms accords with the principle of development of sharp edges proposed by Richardson and Carling (2005).

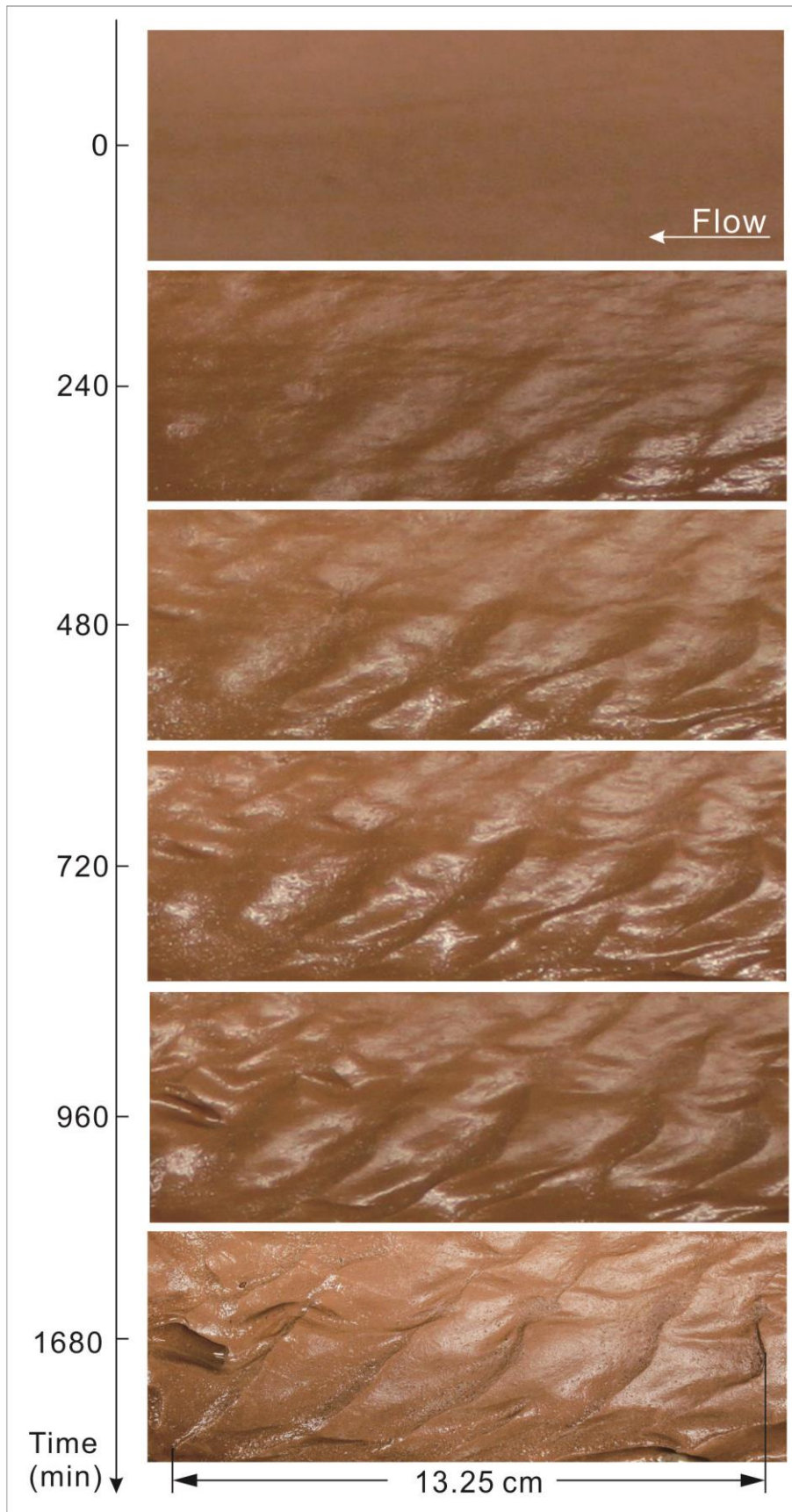


Figure 6.39 Evolution of hummocky forms. They were observed on the clay bed of Exp. 7. Flow from right to left.

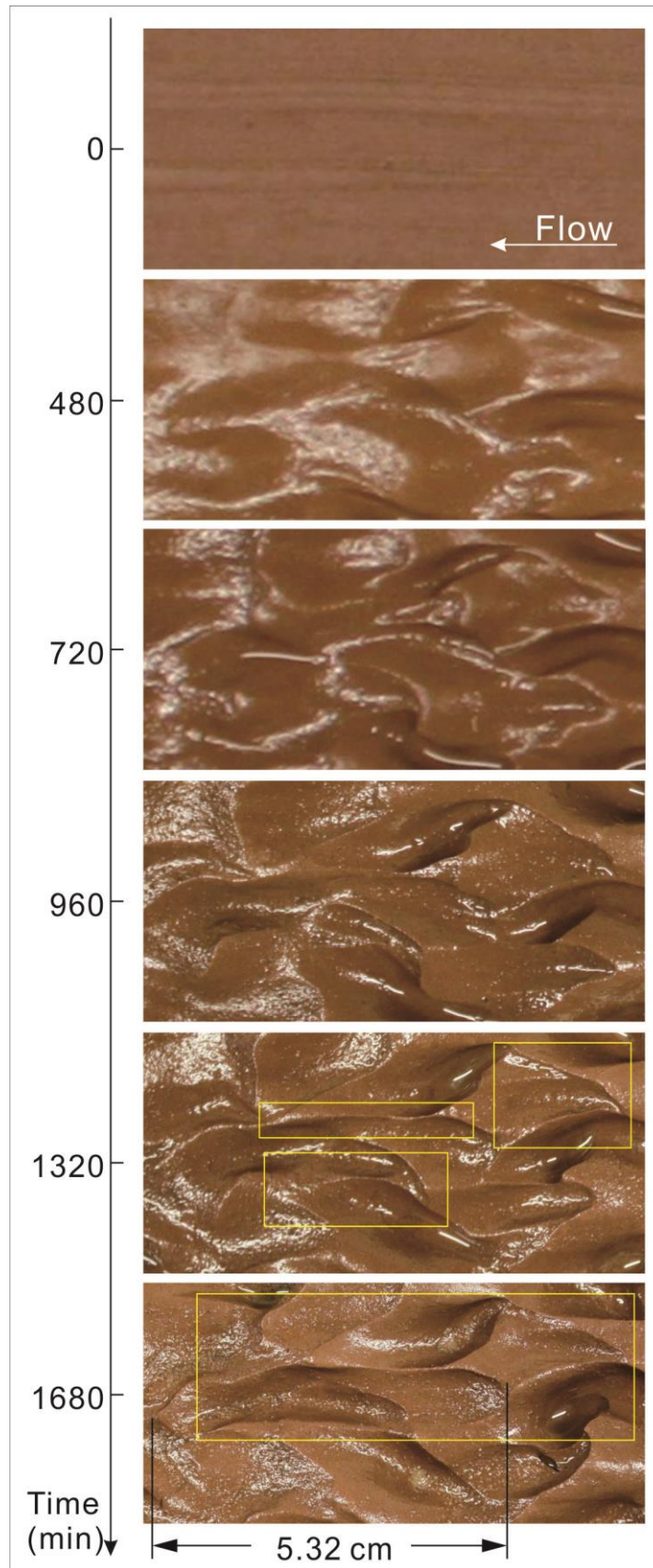


Figure 6.40 Evolution of bladed forms. They were observed in the clay bed of Exp. 7. Flow from right to left. Yellow rectangles refer to the main bladed forms in the later experimental bed.

6.2.6 Composite forms

Obstacle marks

Obstacle marks were the most obvious composite forms in the current experiments. They generated more than once and could be observed on any part of the experiment clay beds with different undrained shear strengths. Both the obstacle marks shown in Figure 6.41 were observed on the clay bed of Exp. 6, and both of them mainly formed in the later stage of experiments. During their evolution, the first part appearing on the bed was the projection. Normally, two sinuous furrows formed on both sides of a projection (Figure 6.41: Plot A – photo T1200; Plot B – photo T720). At mean time, one or a pair of shear zone furrows formed on the lee-side of the projection and extended downstream (Figure 6.41: yellow dashed curves in Plot A – photo T1320; Plot B – photo T1200). One curved furrow formed to the left side of the projection and extended around the head of the projection to the right side of it (Figure 6.41: yellow dash curves in Plot A – photo T1320; Plot B – photo T1200). It deepened and underwent headward erosion which cut through the path ahead of the projection and flattened the zone in the upstream part of the furrow. The furrow then formed a horseshoe form (Figure 6.41: Plot A – photo T1320; Plot B – photo T1200). So far, a mature form of the obstacle marks was completed. With time, the projection and the rims of the horseshoe form were polished to flat and the rims altered to cusped to become the final structure of the composite forms on the experimental beds (Figure 6.41: Plot A – photo T1680; Plot B – photo T1800).

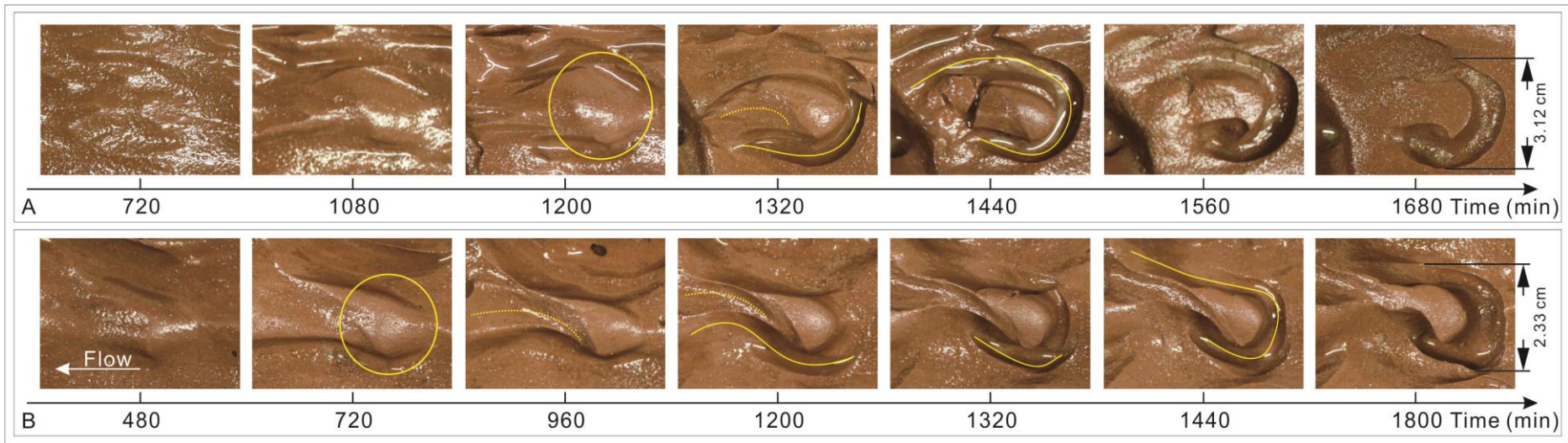


Figure 6.41 Evolution of obstacle marks. Both of them were observed in the clay bed of Exp. 6. Flow from right to left. Yellow curves refer to the possible paths of flow within the furrows.

6.3 Discussion

Comparison of the evolution of all types of erosional features on the experimental modelling clay beds reveals that the formation process of potholes were more complicated than those of the other two longitudinal erosional features, flutes and longitudinal furrows. The evolution of other erosional features could occur along with the evolution of different kinds of potholes or other features could be produced in the beds as a transition form in the sequences of pothole formation. The experiments showed that potholes tended to form at a position where local morphology forces flow to change direction to form secondary vortices. The most obvious examples were potholes forming at inflection points of curved or sinuous flutes or furrows (Figure 6.5 and Figure 6.12). Except for this, potholes preferentially formed in relatively lower zones ahead of which there was a shallow entry feature which could lead to flow entering into the lower zones and incising spirally downwards (Figure 6.2, Figure 6.4, Figure 6.6, Figure 6.7 Figure 6.13). In other cases, the wall resistance effects of features such as the lateral inner walls of furrows, or the stoss-side of flutes, led to potholes forming as flow was stopped and restricted, and then changed the direction to reverse and spiral downwards, producing incision (Figure 6.1, Figure 6.3, Figure 6.10, Figure 6.13). According to direct observation, it can be concluded that the principal driving force for generating potholes is the downwards secondary vortices separated from incoming longitudinal flow under the influence of variety of topographic features in surrounding areas, especially the area ahead of the proximal end of potholes. On the other hand, potholes could not only be the final form but sometimes the transition form in the evolution of other erosional features or the internal secondary structures of other features like regular compound furrows (Figure 6.21, Figure 6.26, Figure 6.35, Figure 6.37). Such an evolution process completely accords with the principles of continuity of bedforms and the constructive interference of flow structures of contiguous bedforms on natural bedrock channels (Richardson and Carling, 2005).

The longitudinal or approximately longitudinal forms, such as flutes and longitudinal furrows, did not need vortices to c deepen hollows in them. The evolution and the final forms of them mainly depended on the morphology and the characteristics of the location in the early stage of experiments where the longitudinal forms would eventually generate. They were also affected by the surrounding area or adjacent erosion features which could

alter the process of their evolution. A simple curved track with slightly lower area could lead the local near bed flow to form a short flute, spindle-shaped flutes, comet-shaped flutes or curved parallel-sided furrows (Figure 6.17, Figure 6.19, Figure 6.28 to Figure 6.30). The experiments also indicate that near bed flow prefers to choose the relatively lower path to move. After longitudinal forms emerged, flow tends to converge into the main depression of them while eroding them vertically and laterally at the same time. In a zone without adjacent erosional features, simple forms of flutes and longitudinal furrows could maintain their forms longer on the experimental bed. If the density of erosional features in an area was relatively large, adjacent forms could affect each other to form certain forms, for example, a curved short furrow developed by the linkage of a short furrow with its entry shallow furrow by cutting through the proximal rim of the short furrow and elongating upstream (Figure 6.27). Some adjacent furrows or flutes could even combine together to form more complex bedforms with sharp crests (Figure 6.20, Figure 6.22, Figure 6.25, Figure 6.32, Figure 6.35). Such processes are consistent with the principle of constructive interference of flow structures of contiguous bedforms (Richardson and Carling, 2005).

The effect of headward erosion was important in altering the form of bedforms. It happened frequently in the development of many bedforms, especially in the evolution of reversed furrows and obstacle marks. In these cases, the former proximal end walls kept eroding and then reversed inward instead of directly incising in the upstream direction. Subsequently, the flow condition within the reversed furrows became more complex and formed convergent horseshoe vortices. The convergent horseshoe vortices in these deep furrows then eventually transformed the shape of the sinuous furrows to a horseshoe shape with time.

Comparison of the diversity of bedforms produced on the experimental modelling clay beds of Exps. 6, 7 and 8 with different undrained shear strengths ranging from hard to very soft, shows that although all clay beds produced similar types of erosional bedforms, the clay bed of Exp. 7 with medium strength modelling clay demonstrated the richest variety of erosional bedforms in and on it (Figure 6.42). This indicates that modelling clay with undrained shear strength of 7-8 kPa, and a shear flow with a basal shear ranging from 4.5 to 5.8 Nm^{-2} , provides the best characteristics for analogue bedrock substrates for creating erosional bedforms and simulating the whole development process in order to investigate the genesis and evolution of bedrock bedforms in natural environments.

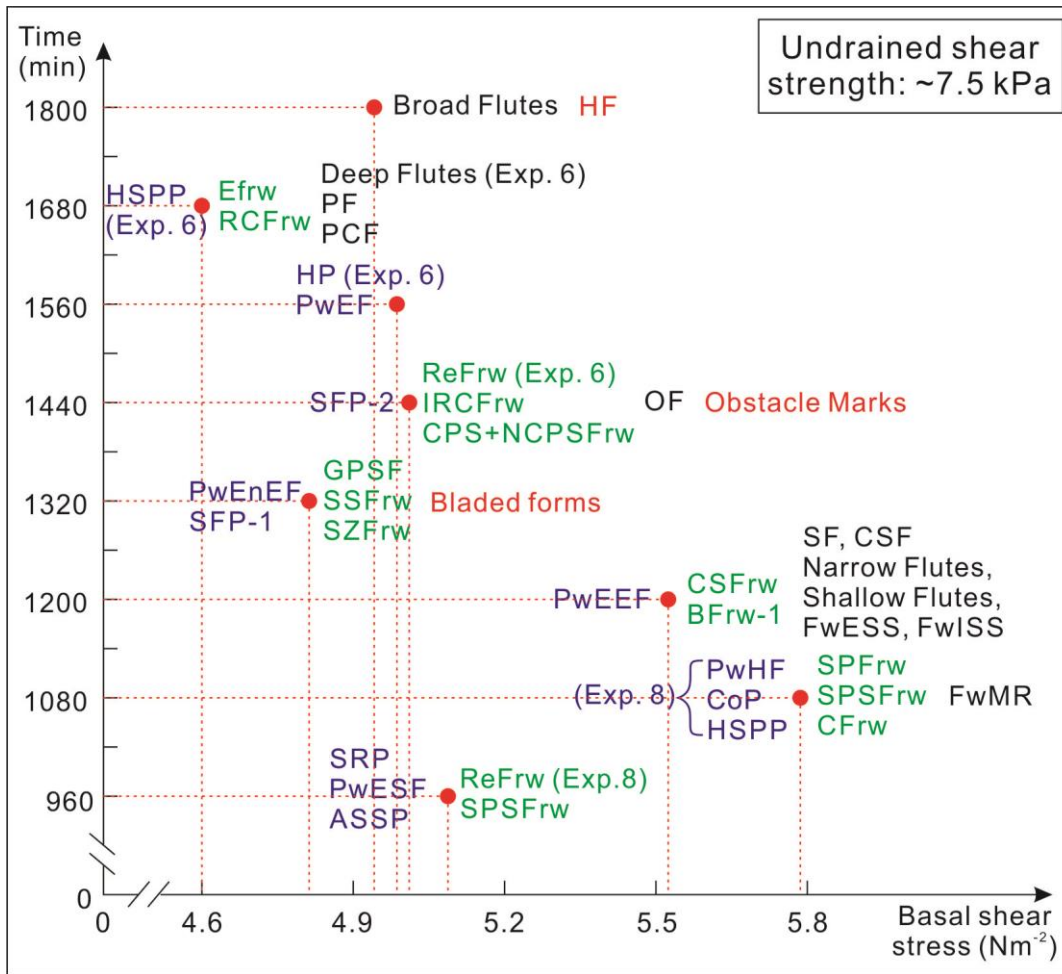


Figure 6.42 The distribution of all types of erosional features on the experimental modelling clay bed under different basal shear stress. The undrained shear stress of the clay bed is around 7.5 kPa.

Presumably a phase space exists between bed substrate and flow conditions where conditions are optimal for such bedform reproduction (Figure 6.43). Given the importance of abrasion to the process of bedform development then the key flow parameter likely relates to their impact velocity. Mean flow velocity is therefore likely related, although a near-bed parameter such as shear velocity, in turn related to the applied basal shear stress, may be more appropriate. The influence of sediment concentration on such a phase diagram is unknown, but at low concentrations may primarily determine the rate of bedform development, rather than the final form of such features.

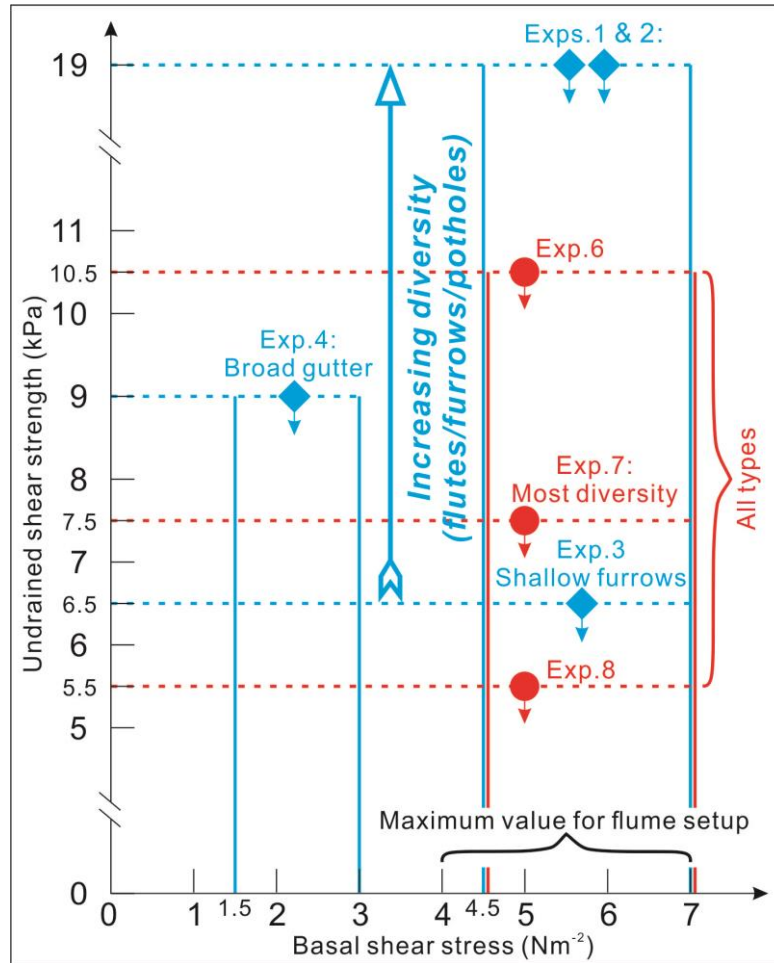


Figure 6.43 A phase space diagram of the relation between the bed substrate and flow conditions where conditions are optimal for current bedform reproduction. The blue diamonds refer to the experiments using the terracotta pottery clay. The red dots refer to the experiments using the modelling clay. The small downwards arrows refer to the decrease in the undrained shear strength of the beds with time. The big upwards arrow refers to the increasing diversity of the erosional features in the terracotta clay bed with undrained shear strength. ‘All types’ refers to all types of erosional features that could be produced by the modelling clay beds with any undrained shear stress.

6.4 Summary

Three experiments run using modelling clay beds created a large array of erosional bedforms and illustrated the specific evolution process of most common types of bedforms, including potholes, flutes, longitudinal furrows and other marks. The experimental results compensate for the lack of knowledge on the evolution of bedrock bedforms which is nearly impossible to obtain by conducting long-term continuously field observation or physical modeling simulation on real bedrock in the laboratory. The evolution sequences and analysis of transitional forms of certain bedforms illustrated

the possible flow paths of currents in and above erosional features. This helps to infer the flow transporting pattern and relevant hydrodynamics above these locations. On the other hand, the evolution process of experimental bedforms and the mature form of them contribute to partially validate some empirical principles applied to the natural bedrock morphology by previous studies, such as the continuity of forms, convergence of forms, constructive interference, and the criterion for the development of sharp crests (Richardson and Carling, 2005). Meanwhile, the experimental results demonstrated that with relatively lower Fr number, most of the bedforms could be successfully produced and the medium hard modelling clay bed is the most optimal solution to for these flow parameters, for the simulation of bedrock erosion.

Chapter 7

Flow structure within and above analogue bedrock bedforms

7.1 Introduction

Bedrock channels are common in the natural environment. However, most of the bedforms on bedrock channels observed in the field are necessarily exposed and are thus not submerged under formative water flows (Richardson and Carling, 2005; Whipple, 2004; Whipple et al., 2000b; Whipple et al., 2000a). This is largely because of the difficulty of measuring the morphology of bedrock channel bedforms beneath their formative flows. In addition, without realistic replica models of bedrock substrates, investigating flow structures over bedrock in the laboratory using flume-scale experiments is also difficult. This is because in order to measure the flow dynamics within and above the erosional features, the transducers of the ADV need to be plugged vertically into the water which would alter the flow field around and beneath the transducers. This flow field above the erosional features change would induce change in the evolution tendency of the bedforms beneath them owing to the sensitivity of the experimental substrates. Only a few experiments have reproduced bedrock features and investigated the flow dynamics and bedform evolution in the laboratory (Johnson and Whipple, 2007; Wilson et al., 2012). But the limitation of these previous experiments is that the range of erosional features produced was still very limited, restricting the ability to explore the related flow characteristics over them. Chapter 5 and 6 have shown that the current experiments succeeded in producing a huge array of erosional features that have prototypes in natural bedrock channels. A fixed-bed latex model of the final experimental bed of Exp. 8 allows investigation of the flow dynamics over, and within, different kinds of erosional features in analogue bedrock channels for the first time.

7.2 Experimental setup and background

A latex replica of the final bed of Exp. 8 was made to investigate the flow structures within and above the different kinds of erosional features (Figure 3.16 Section 3.2.7). Plaster-of-Paris was used to make the cast of the final bed of Exp. 8. After the plaster-of-Paris cast solidified, liquid latex was poured onto the cast and cured. The latex solidified with time and, with the

plaster-of-Paris removed, formed a stable replica of the experimental bed. The total running time of Exp. 8 was 1080 minutes, with the mean flow velocity set to $0.9\text{-}0.95\text{ ms}^{-1}$ (for the details of Exp. 8, see Chapter 3).

Thirty-nine deep erosional areas in the experimental latex bed were selected for velocity sampling. A Vectrino-II Acoustic Doppler Velocimeter (for details, see Section 3.2.8) was positioned vertically above the latex bed with a distance of about 6.5 cm between the head of the central transducer and the lowest location of the erosional marks. The central transducer emits a pulse towards the bottom surface of the bed, and the reflected signals from within the water column are received by 4 receivers to sample the 3D horizontal and vertical flow velocity data using the Doppler shift in the acoustic returns (for details, see Section 3.2.8). The flow velocity was sampled every 5 mm along streamwise direction (longitudinal direction) with the duration of each velocity sampling lasting 1 minute. The velocity profiles shown in this chapter are the average value over the 1 minute sampling time. The locations of these 39 areas are shown in Figure 7.1. Among these, 16 of them are selected to demonstrate the details of the flow structures above specific erosional features. Figure 7.2 illustrates the flow along a longitudinal section of the central axis of the clay bed and highlights selected areas of this transect with the flow velocity profiles obtained by the Vectrino above the features. The X-velocity (blue curve) refers to the longitudinal flow velocity, Y-velocity (green curve) refers to the transverse flow velocity and Z-velocity (red (Z1) and light blue (Z2) curves) refers to the vertical flow velocity obtained via the four beam Vectrino matrix. The x-axis in the figure of the elevation map represent the distance from the downstream edge of the clay bed, and the y-axis refers to the distance below the basal surface level of the original plane bed, which is at the same level as the false plastic floor around the latex bed. The x-axis of the velocity profile plot is the magnitude of velocity. For longitudinal velocity, positive values are indicative of flow direction towards the downstream and negative indicate (reversed) upstream flow. For transverse velocity, positive values reveal flow direction to a deviation to the left hand side and negative to the right hand side (looking downstream). For the vertical velocity, positive values are upward. For more details of the experimental setup for measuring the flow structures, in and above erosional bedforms, please see Chapter 3.

In the present experiments, most areas selected to undertake flow velocity measurements contained relatively deeper erosional marks. Flow direction was from right to left in all cases. Owing to the restriction of the experimental

bed conditions of Exp. 8, not all types of erosional feature mentioned and identified in Chapter 5 and 6 could be found and measured. Nevertheless, three or four typical samples of each kind of erosional features were selected from the 39 samples in order to show the typical flow structures over them. 3D flow field at all 39 XY positions was not measured simultaneously. The sampling positions were altered manually during the experiments. All positions were measured one by one. Potholes were the most common feature on the Exp. 8 bed. Considering the similarity of the flow field over the potholes, 5 samples were sufficient to illustrate the features of the within and over them. Flutes and longitudinal furrows were also common on the Exp. 8 bed and flows were also obtained over and within these features. Although only 16 areas are examined in detail here, these are sufficient to show a clear picture of the key flow structures within and above different kinds of erosional features on an analogue bedrock substrate, and these results can help to understand the evolution processes of a variety of the typical erosional features in natural bedrock and cohesive channels.

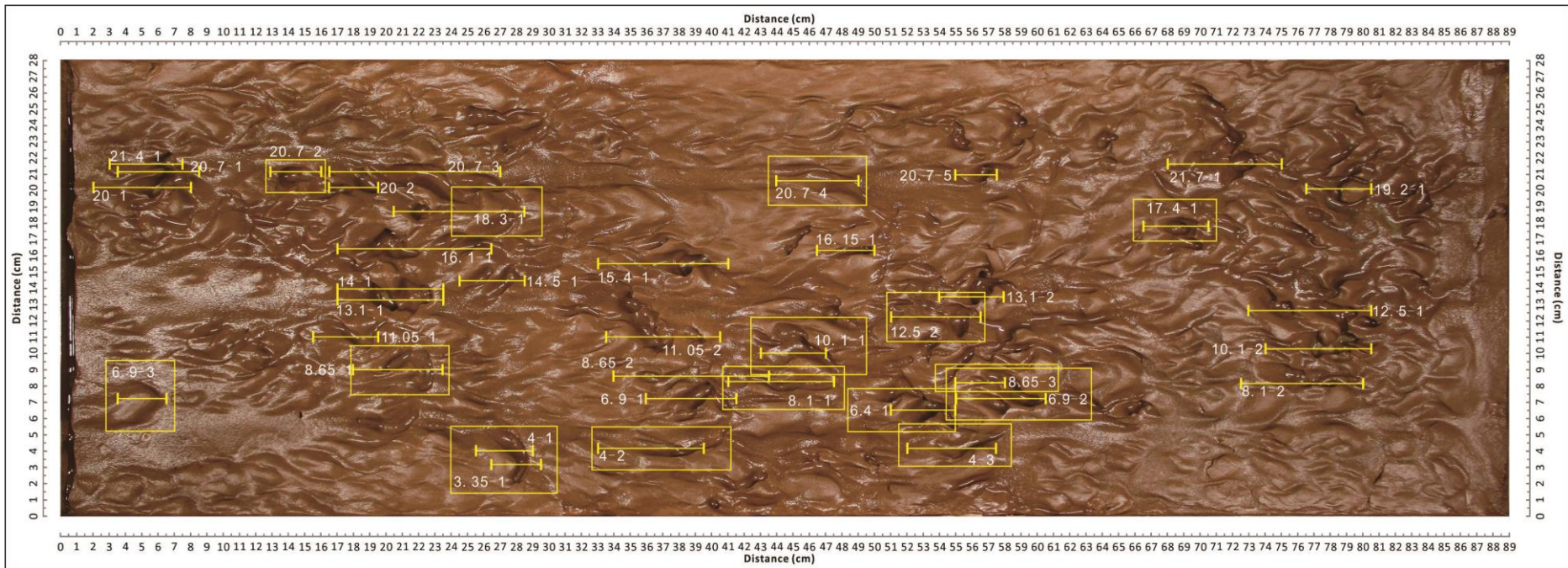


Figure 7.1 The locations of erosional marks in the experimental clay bed of Exp. 8 for flow velocity measurements by ADV. The flow structures above and within the areas indicated by the yellow rectangles and lines are discussed in this chapter. The yellow lines are parts of different transects, e.g. Line 6.9-3 located in the bottom left corner means the third sub-transect selected from the Transect-6.9. Flow is from right to left.

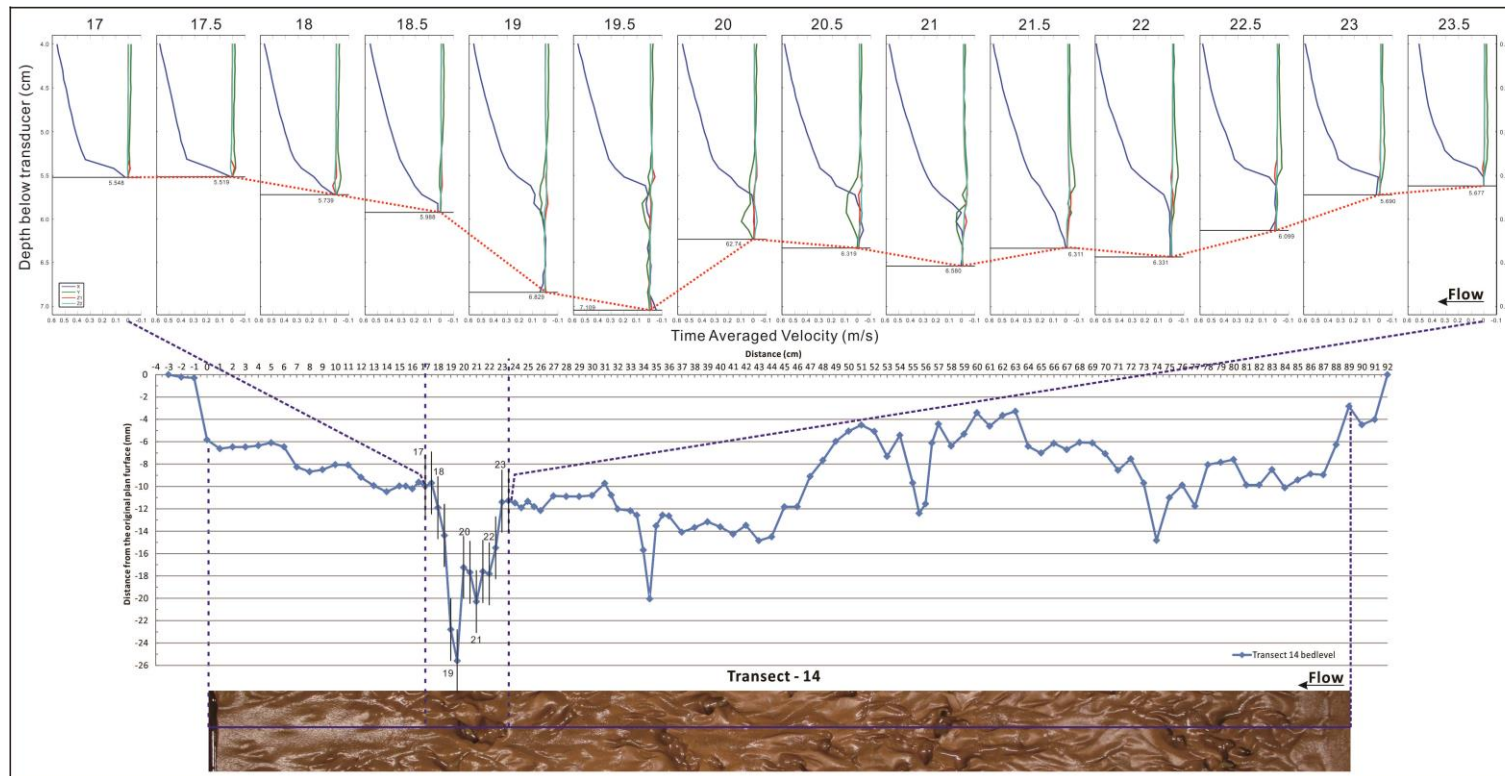


Figure 7.2 Elevation map of a central transect (Transect-14) and vertical flow profiles above selected erosional marks. The blue curves (X-velocity: receivers 1 & 3) in the plots of vertical flow profiles; represent the longitudinal flow velocities; the green curves (Y-velocity: receivers 2 & 4) represent transvers flow velocities; and, the red and light blue cures (Z1 and Z2 velocities) are the vertical velocity (Z1) estimates associated with receivers 1&3 (X) and (Z2) 2&4 (Y). In all the figures in this chapter, X-axis in elevation map illustrates the distance from the downstream edge. Y-axis shows the distance below the basal level of the original surface of the flat bed. The Y-axis of the velocity profile is the depth below the central transducer of the ADV. X-axis shows the time averaged velocity. Numbers above the profiles refer to the x position. Flow is from right to left. The clay bed is defined as left bank and right bank as looking downstream.

7.3 Flow structure above and within erosional marks in an experimental analogue bedrock channel

7.3.1 Potholes

Simple potholes

Potholes with a typical simple round shape in plan view and without secondary features could barely be observed on the final bed of Exp. 8. Most potholes in Exp. 8 had more complex forms and were largely distributed throughout the whole bed. Here one simple round pothole with an entry furrow is examined and flow field measured (Figure 7.3). The main depression of this pothole is located from sampling location 12.5 cm to location 14 cm. The diameter of its main body is about 1.5 cm with a depth of about 0.7 cm. The length of its entry furrow is 1.0 cm long.

The longitudinal velocity within the pothole was much lower than the velocity above of the pothole. Within the main body of the pothole, flow velocity magnitude ranged from zero to about 0.1 ms^{-1} (Figure 7.3: area between the black bottom line and red dashed line). From the opening of the circular edge of the pothole to the edge of the entry furrow of the pothole, the longitudinal velocity increased from 0.1 to near 0.3 ms^{-1} (Figure 7.3: area between the red dashed line and the blue dashed line). The velocity increased from 0.3 to 0.6 ms^{-1} with increasing distance from the edge of the entry furrow to about 7.0 mm above the deepest part of the pothole (Figure 7.3: area above the blue dashed line). The rate of increase of longitudinal horizontal velocity in each depth range was different, which is shown by the gradient of the x-curves (blue) of longitudinal velocity profiles. A close-up view of the parts of curves in the near bottom area reveals that the velocity values of the lowest parts of the blue curve are negative (Figure 7.3: blue curves in profile 13.5cm). This indicates a small flow separation zone was forming near the bottom of the potholes, which is likely to induce an anti-streamwise incision of the proximal inner wall of the pothole.

The green curves in the profiles refer to the transverse flow velocity in and above the pothole. This (secondary) transverse flow was lower in magnitude than the longitudinal velocity (which can reach 0.6 ms^{-1}), with a velocity no larger than 0.1 ms^{-1} . Notably, the deepest part of the pothole (Figure 7.3: profile 13.0) could be regarded as a transition in the transverse velocity profile pattern (Figure 7.3: orange dashed line). Towards the upstream direction from this position, location 13.0, the transverse velocity above the

level of opening of round depression was positive (flow right) and the magnitude was no larger than 0.05 ms^{-1} . However, the transverse flow past the deepest part of the pothole changed from positive to negative direction and the magnitude doubled to -0.1 ms^{-1} . The vertical velocity distribution above this area displayed a uniform pattern, being slightly negative (downwards) in the streamwise direction from upstream to downstream above the pothole.

In order to describe the flow direction more clearly, 0° is orientated downstream, positive to a deviation to the left hand side, and negative refers to the right hand side. The flow structures above the pothole can be concluded as following: The transverse and the vertical flow patterns remained uniform and both velocities kept to close to a zero value within the deepest part of the pothole. There is a very thin separation cell in the near-bed portions in the proximal end of the pothole with the flow above this shows a circular pattern, with flow moving towards left hand side at the proximal end and right hand side at the distal end. Considering the structures of all three components of the velocities, the direction of the resultant velocity above the pothole changed from approximately 8.1° of deviation from the downstream flow with nearly no vertical component at the proximal end, to approximately -29.7° and slightly downward at the distal end of the pothole (Figure 7.3: profiles 13.5 to 12.0). This change likely corresponds to lateral downwards erosion within the pothole and production of a more three dimensional form over time.

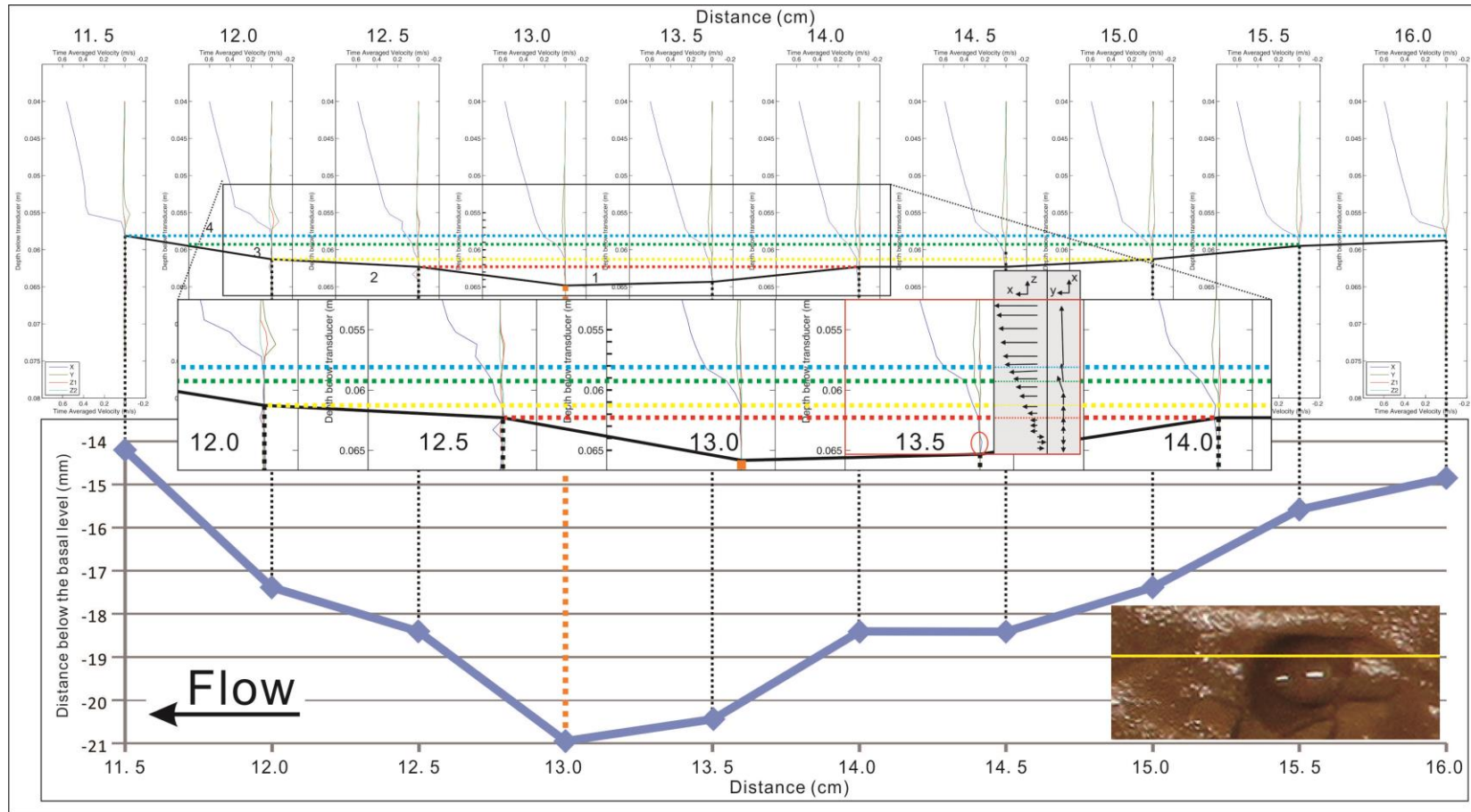


Figure 7.3 Flow structure above a simple pothole with entry furrow. The dashed line divided the water into several layers, which will be discussed in detail in the text. The gray boxes with arrows refer to the overhead view (x-y) and the side view (x-z) of the changes of flow direction with increasing height from the bottom. Flow is from right to left. This sampling area is numbered as Y20.7-2, which can be found in Figure 7.2.

Pothole with exit furrow

A pothole with short exit furrow is examined from the experimental bed of Exp. 8 (Figure 7.4). The diameter of the main pothole was about 1.5 cm long and 8.0 mm deep relative to the level of initial surface of the final bed of Exp. 8. The whole length of the pothole with exit furrow was 2.5 cm. The proximal rim of the pothole was slightly extended upstream. Within the pothole, a small secondary pothole could also be observed. The sampling location 68.0 was located right at this secondary pothole.

The flow velocity structure through the pothole with exit furrow is much more complicated than the flow field in and above the simple pothole discussed above (Figure 7.3). Above the surface of the surrounding area ahead of the proximal edge of the pothole, the curves of longitudinal flow velocity show typical logarithmic profiles (Figure 7.4: profiles 69.5 and 69). However, as flow enters into the principal depression area of the pothole, the flow field altered significantly. The changes of the flow velocity within the pothole can be divided into several stages longitudinally through the feature and the flow field can be divided into several layers mainly according to the most obvious changes of the longitudinal flow conditions. The whole sampling area can be divided into the upstream area, the principle depression, and the downstream area. The principal depression of the features can be sub-divided into the proximal part (lee-side slope/forepart), the deepest part and distal back end part (stoss-side slope/part).

The whole range of the sampling height of the flow can be considered within the range of the boundary layer thickness. It can be divided into the outer layer and the inner layer. The outer layer is the upper most portions of the sampling flow fields (Figure 7.4: the portions higher than the purple dashed lines). No matter how complicated the flow velocity structures are in the lower portions, in the outer layer, the longitudinal velocity increases steadily and gently with logarithmic profiles with increasing height above the bed and the structures of the transverse velocity and vertical velocity are regular. The lower portions below the outer layer is defined as the inner layer which can be sub-divided into the shear layer and the near bed sublayer (Figure 7.4: the portions between the purple dashed line and black basal line). In the near-bed sublayer, all velocity components are very small and very close to zero (Figure 7.4: portions between the black basal line and the red dashed line). The thickness of this layer ranges from 4 to 5 mm in this case of the pothole with exit furrow (Figure 7.4). The thickness of the shear layer in the current case ranges from 2 mm above surrounding areas to 8 mm above the

deepest part of the pothole (Figure 7.4: portions between the red and purple dashed lines). The most visible changes of the flow structure can be observed in the shear layer.

In the example presented here, above the lee-side slope of the proximal extension part of the pothole, the flow field could still be divided into several layers as before. In the near-bed sublayer, both of the longitudinal and vertical velocities were still low ($< \pm 0.05 \text{ ms}^{-1}$) with the transverse velocity magnitude increasing negatively with height above the bed, which means the transverse flow advecting flow towards left hand side if looking downstream. In the lower portions of the shear layer, the longitudinal flow velocity increases at a relatively low rate; increasing from nearly zero to about 0.05 ms^{-1} over a height of about 1.0 mm (Figure 7.4: green ellipse in profile 68.5). Higher in the flow, the longitudinal velocity further increases in the higher portions of the shear layer (Figure 7.4: the portions between the yellow and purple dashed lines in profile 68.5). The rate of increase in the longitudinal velocity in the higher portions of the shear layer is much higher than that of the lower portions in the shear layer. Flow increased from 0.05 ms^{-1} to 0.3 ms^{-1} in about 0.4 mm. The transverse velocity in the whole shear layer fluctuated slightly but generally remained negative. Within the outer layers the transverse velocity was around zero and became slightly positive when entering into the outer layer. Within the outer layer, the longitudinal velocity increased steadily at a low rate. In brief therefore, above this location of the bed, the flow direction is towards right hand side in the near-bed sublayer, and towards -26.6° in the lower shear layer. The flow direction changes to -7.4° in the middle shear layer, and then keeps changing anti-clockwise to almost the downstream direction in the higher shear layer and the outer layer.

Flow structure within the small secondary pothole at the bottom of the principal pothole was more complex than the location 68.5. The flow field above the location 68.0 featured a longitudinal flow velocity increased with fluctuation. However, above the location 68.5, the longitudinal flow kept increasing with different increasing rate without decreasing upward. The transverse velocity component above the location 68.0 was slightly negative and had smaller magnitude than that above the location 68.5. The outer layer above the location 68.0 presented almost the same condition as that of the location 68.5 with longitudinal velocity increasing slowly, and then eventually reaching 0.75 ms^{-1} . The integrated flow pattern above the location 68.5 was that there was a very small longitudinal flow separation cell in the

near-bed sublayer. In the lower portions of the shear layer, the direction of the flow was towards downstream with small up-welling. In the middle and higher portions, the direction of the flow altered to towards downstream and slight downward. The transverse velocity only presented slightly positive in the transition of the lower and middle portions of the shear layer.

With the flow keeping moving forward to the stoss-side slope of the exit furrow, the velocity structure changed back to the flow field situation similar with that above the location 68.5. The only difference is that the vertical velocity in the higher sub-layer of the shear layer above the location 68.5 was positive, but above the location 67.5, it was negative. This difference might be caused by the different morphology of the lee-side slope above the location 68.5 and the stoss-side slope of the exit furrow above the location 67. The different direction and gradient of the sampling areas might alter the vertical flow direction above it. Above location 67.5, the direction of the flow is as follows: directly towards downstream in the near-bed sublayer, towards approximately -14° and downward in the middle shear layer, and then reversing back towards mainly the downstream direction and a few degrees to right hand side in the outer layer.

After the flow kept moving further more onto the flat surface, the flow velocity structure returned back to a regular condition like that happening on normal flat river surface.

In summary, the changes of the flow direction in the different positions within the pothole with exit furrow indicated that above the location 68.5 the flow moved anti-clockwise with small up-welling, with the flow velocity increasing gradually in the vertical. The flow structure over the deepest part of the pothole, at the location 68.0, contained a very small longitudinal separation cell near the bottom whilst the flow changed direction towards downstream with relatively small up-welling or down-welling. The decreasing of the longitudinal flow components in each sub-layer might be induced by a negative pressure gradient as, which formed when the flow hit the wall. The flow was deflected by the distal inner wall of the pothole to produce a deflection flow which acted to decrease the longitudinal velocity. Above the location 67.5, the flow velocity changes its helicity with height, increasing once again. The slightly downward flow in the shear layer might be the component of the down-welling part of the vortices within the pothole.

A very similar flow pattern can also be observed in the other deep potholes with short exit furrows (Figure 7.5). This indicates that above the similar features, the flow structure is also similar. From another perspective, a

conclusion can be made that similar flow structure could produce similar erosion features.

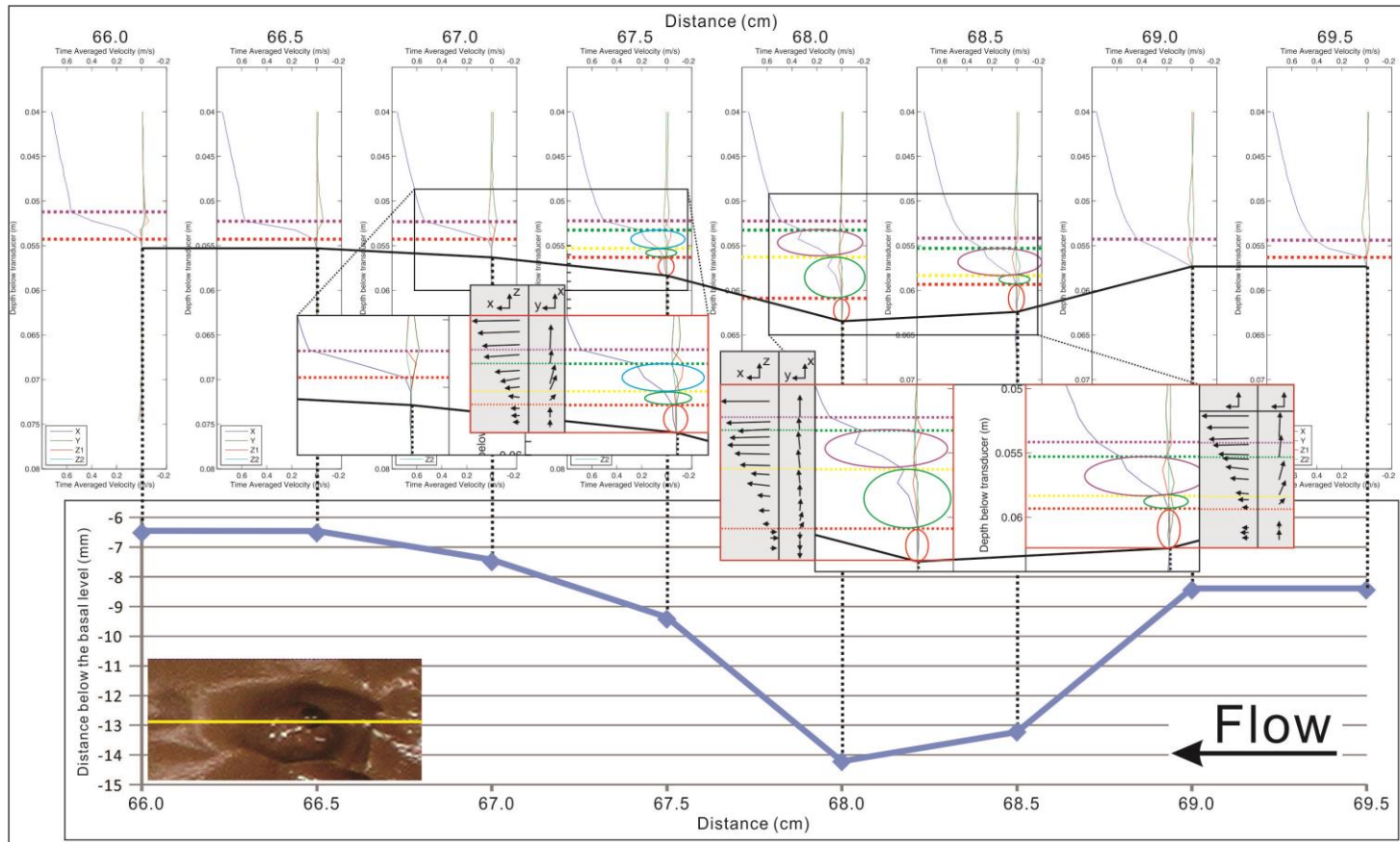


Figure 7.4 Pothole with exit furrow-1. Black line refers to the bottom level of the erosional feature; Areas between black line and red dashed line are the near bed bottom layers; areas above the purple dashed line are outer layers; areas between red and purple dashed lines are shear layers; yellow and green dashed lines sub-divided the shear layers into several sub-layers. The gray boxes with arrows refer to the overhead view (x-y) and the side view (x-z) of the changes of flow direction with increasing height from the bottom. Flow is from right to left. This sampling area is numbered as 17.4-1, which can be found in Figure 7.2.

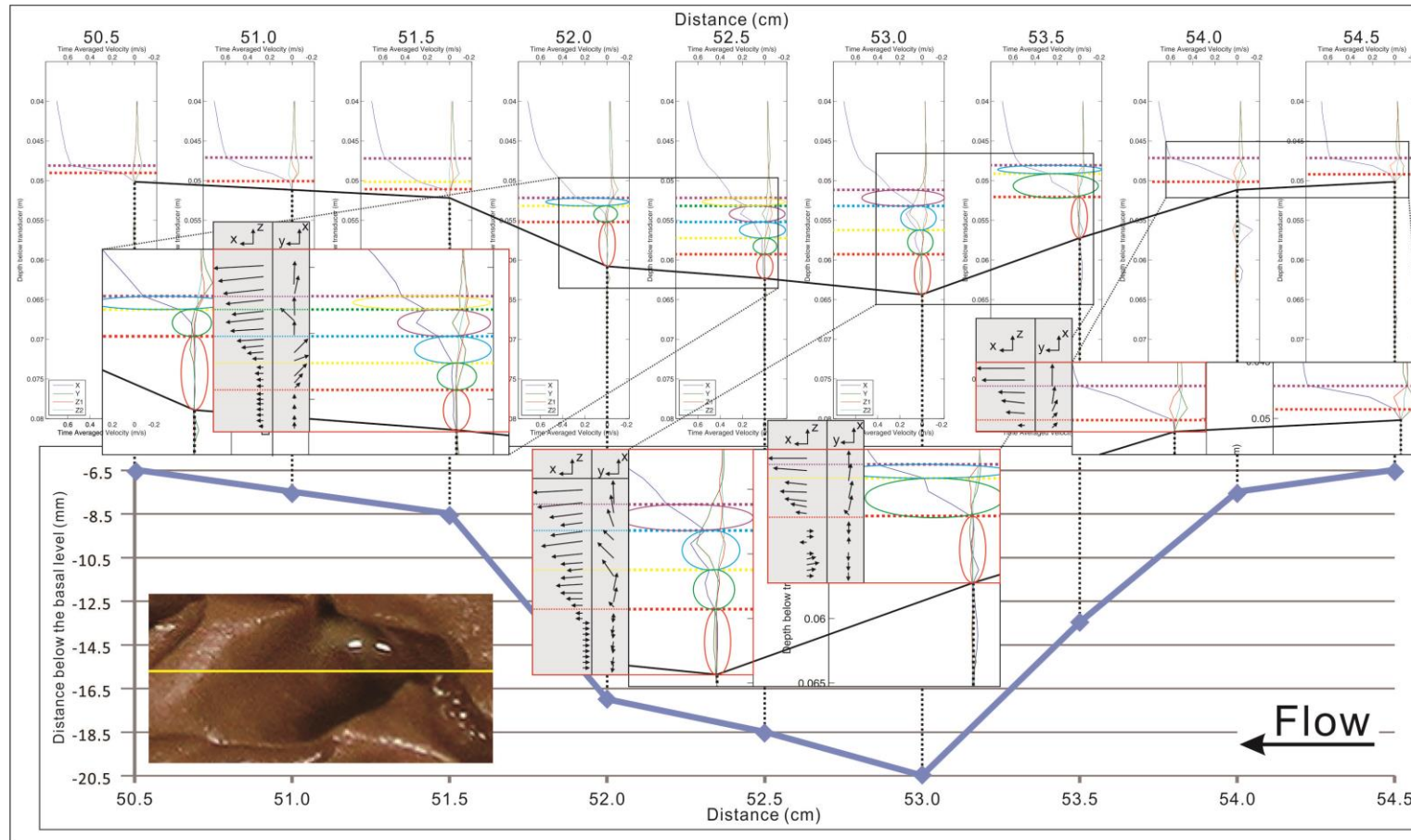


Figure 7.5 Pothole with exit furrow-2. The dashed line divided the water into several layers and the coloured ellipses tag different features of the flow profiles, which will be discussed in detail in the text. The gray boxes with arrows refer to the overhead view (x-y) and the side view (x-z) of the changes of flow direction with increasing height from the bottom. Flow is from right to left. This sampling area is numbered as 6.4-1, which can be found in Figure 7.2.

Pothole with extended exit furrow

The pothole shown by Figure 7.6 was located in the end of a long parallel-sided furrow (see Figure 7.2-12.5). The exit furrow of this pothole was a shallow, narrow, furrow, connecting with the distal rim of the principal pothole. The principal pothole was approximately ellipse in planform shape. The length was 1.5 cm, the width was 1.7 cm, and the depth was nearly 5.0 mm. The exit furrow was 2.5 cm long and 1.0 cm wide and the deepest part of it was 3.0 mm.

The sampling transect here could be divided into two parts: the principal pothole, which is from location 56.5 to location 54.5, and the extended exit furrow, which is from location 54.5 to location 52. The most upstream part (locations 56.5 and 56.0) were located on the surface of the furrow ahead of the pothole. The flow velocity above these two sampling locations was quite similar. In the portions of 1 mm above the bottom surface (Figure 7.6: portions between black bottom line and green dashed lines in the profiles 56.5 and 56.0), the flow direction was 6.3° in horizontal direction and slightly upward by 9.1° . The longitudinal component increased gradually while the transverse decreased to zero, and then increased negatively to -0.3 ms^{-1} with vertical components decreasing to nearly zero. In the outer layer, the flow direction kept towards the downstream direction and a few degrees to right hand side.

When flow enters into the principal depression of the pothole with an extended furrow, the flow structures changed considerably and were much different to the flow structures found in pothole with simpler morphologies. The shape of the curves of the velocities higher than the level of the yellow dashed lines was very similar to those above the location 56.5 and 56.0. This means above the opening of the pothole, the flow structures remain similar. The most notable change happened within the pothole (Figure 7.6: red and green ellipses in the profiles 55.5 and 55.0). In the 2mm thick near-bed sublayer above both locations, the flow moved a few degrees to left hand side above the bottom, although all three velocity components are small and close to zero. This flow structure in the lower shear layer is more complex (Figure 7.6: green ellipses in the profiles 55.5 and 55). The dominant flow direction in the lower portions of the lower shear layer was 66.5° of deviation from the downstream flow and upward by 14.0° . When reaching the lower boundary of the outer layer, the flow direction changed to -2.8° with small up-welling. In the outer layer, the velocities in all three directions increased gently with increasing height. The longitudinal velocity

increased positively, while the transverse and vertical velocities increased slightly negatively. This flow pattern occurred from the location 55.5 to the location 54.5.

After past the location 54.5, flow enters into the exit furrow. Because of the relative flat bottom surface of this exit furrow, the flow field over it changed less than that over the principal pothole. Except for the flow over the distal stoss-side slope of the exit furrow, the longitudinal velocity increased logarithmically. The flow structures in the upstream half of the furrow were that the flow moved mainly towards downstream with small up-welling in the near-bed sublayer, and mainly towards the downstream with a few degrees deviation to right hand side in the outer layer (Figure 7.6: profiles 54.0 and 53.0). Above the downstream half, the longitudinal flow velocity increased with fluctuation as happened above the stoss-side of the potholes (Figure 7.4, Figure 7.5, and Figure 7.6: green ellipses in the profile 52.5). The near transverse velocity presented much greater than that above the upstream half of the furrow (Figure 7.6: green ellipses in the profiles 52.5 and 52.0). The flow direction changed from -29.4° in the lower portions of the shear layer to -7.3° with increasing height (Figure 7.6: the portions between the red and green dashed lines in the profiles 52.5 and 52.0). In the outer layer, the flow direction was mainly towards downstream with flow deviating from a few degrees.

Briefly speaking, the slightly downwards flow above the area ahead of the pothole may contribute to erode the area around the proximal rim of the pothole. The flow structures within and above the principal pothole indicated that the flow in the pothole moves spirally clockwise with small up-welling, which are likely due to upwelling vortices. This upwelling vortex structure, when sediment-laden, probably results in the erosion of the inner wall, widens the opening of pothole and alters the shape of the pothole to ellipse. The flow structure above the extended exit furrow indicates that within the furrow, the flow rotated anti-clockwise with increasing height, which might arouse the erosion of lateral sides of the extended exit furrow of the pothole.

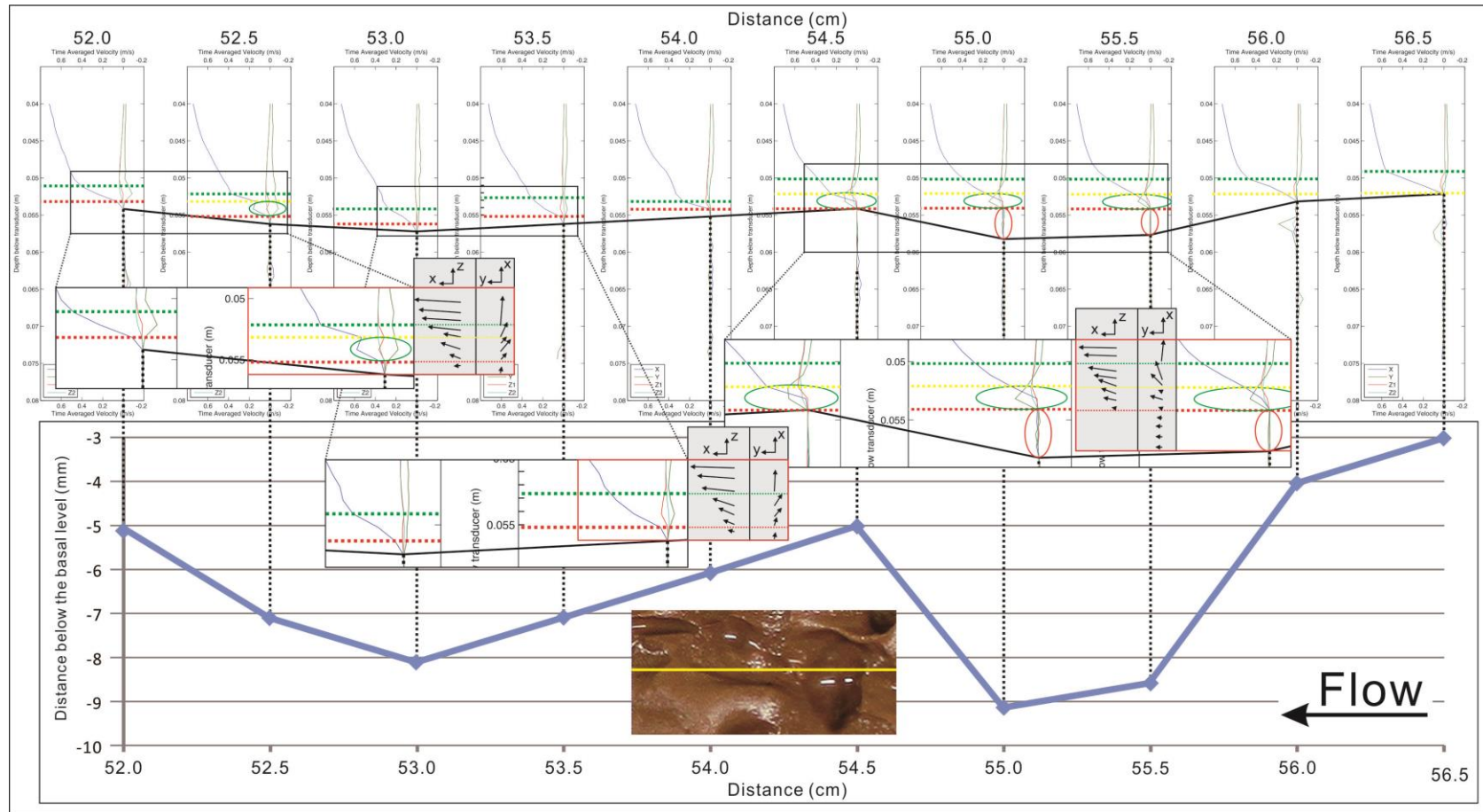


Figure 7.6 Pothole with extended exit furrows. The dashed line divided the water into several layers and the coloured ellipses tag different features of the flow profiles, which are discussed in detail in the text. The gray boxes with arrows refer to the overhead view (x-y) and the side view (x-z) of the changes of flow direction with increasing height from the bottom. Flow is from right to left. The sampling area is numbered as 12.5-2, which can be found in Figure 7.2.

Hierarchical pothole

Hierarchical pothole refers to a larger principal pothole containing at least one secondary pothole within it. The hierarchical pothole in Figure 7.7 contains one shallow secondary pothole (Figure 7.7 a) and one deep secondary pothole (Figure 7.7 b). The shallow pothole also contains a secondary sub-pothole located in the proximal end of the depression (Figure 7.7: tagged by the yellow circle). The total length of this hierarchical pothole was 6.5 cm long. The depth of the shallow pothole was about 7 mm and that of the deeper one was about 10 mm.

Within the flat area ahead of the proximal edge of this experimental hierarchical pothole the flow structure above it was simple (Figure 7.7: profile 23.5 and 23.0). Throughout the flow depth the flow direction mainly towards the downstream end with a few degrees deviation to right hand side.

In the near-bed sublayer above the first sampling location inside the shallow pothole, a small flow separation cell with upstream directed flow can be observed with no transverse and vertical velocity components (Figure 7.7: red ellipse in profile 22.5). In the shear and outer layers of the location 22.5 (Figure 7.7: the portions above the red dashed line in profile 22.5), the flow field presented the same structure as that above the flat bed (Figure 7.7: profiles 23.5 and 23.0).

After the flow moved forward and downward onto the bottom of the shallow secondary pothole, flow velocity components in all 3 directions increased with increasing height above the bottom surface (Figure 7.7: profile 21.5). In the near-bed sublayer of location 21.5, the flow direction was approximately -26.6° with velocity of about 0.05 ms^{-1} (Figure 7.7: the red ellipse in profile 21.5). In the shear layer, the flow direction is -47.2° , with higher velocity of about 0.16 ms^{-1} (Figure 7.7: the green ellipse in profile 21.5). In the outer layer of the flow field, the flow was mainly oriented the downstream end which was accompanied by small up-welling (Figure 7.7: portions above the yellow dashed line in profile 21.5).

In the near bed flow at the location 20.5, there was a small longitudinal separation cell with small recirculation zone with upstream oriented flow (less than -0.05 ms^{-1}). In the shear layer above location 20.5, the flow direction altered from 0° to 22.6° , and then back to -0.5° which was accompanied by small down-welling. Higher in the flow, the flow field was again more uniformly oriented downstream. The flow condition above the location 20.0 was very similar to location 21.5, except that there was no flow

separation cell near the bed and the longitudinal flow component fluctuated like that above the stoss-side slope of the simple pothole.

After flow moving beyond the shallow secondary pothole into the deeper secondary pothole, the flow structure within it exhibit similar pattern as happened in the shallow one. The dominant flow direction changed the direction from directly towards the downstream end in the near-bed sublayer to about 10.5° in the shear layer, and then reversed back to towards downstream in the outer layer in the higher flow field.

From location 19.5 to the downstream location 17.0, only transverse velocity in the shear layer altered the direction from the left hand side to the downstream and then to the right hand side, and then to downstream again. That indicates when the flow past the deepest part of the pothole, reached the stoss-side wall, and then kept moving to the downstream, the flow spiraled in the shear layer above the distal half of the deep secondary pothole.

The overall changes of the flow structure from the upstream to downstream over the Hierarchical pothole are as follows:

(1) Above the proximal part, within the shallow secondary pothole, except for the flow separation cell, the upper flow was oriented downstream with transverse component deviating a few degrees to right hand side. The longitudinal velocity increased exponentially;

(2) Above the first sampling location (location 21.5) within the shallow pothole, the flow in the sublayer and shear layer moved from -26.6° to -47.2° and rotated anti-clockwise back to the downstream directly in the outer layer with small up-welling. The velocity increased with increasing height.

(3) Above the second sampling location (location 20.5) in the shallow pothole, except the upstream-ward flow separation cell, the flow direction rotated anti-clockwise from 0° to 22.6° , and then back to the downstream with small down-welling.

(4) Above the transition location between the shallow and the deep pothole (location 20.0), the flow direction rotated anti-clockwise from 0° to 45° , and then reversed back to directly downstream with the longitudinal velocity increased with fluctuation in the shear layer upward.

(5) Above the whole length of the deep pothole, the main flow direction from the bottom to the outer layer was downstream, except the transverse components changed from a few degrees on the right hand side

to the left hand side from upstream to downstream in the shear layer of the sampling height.

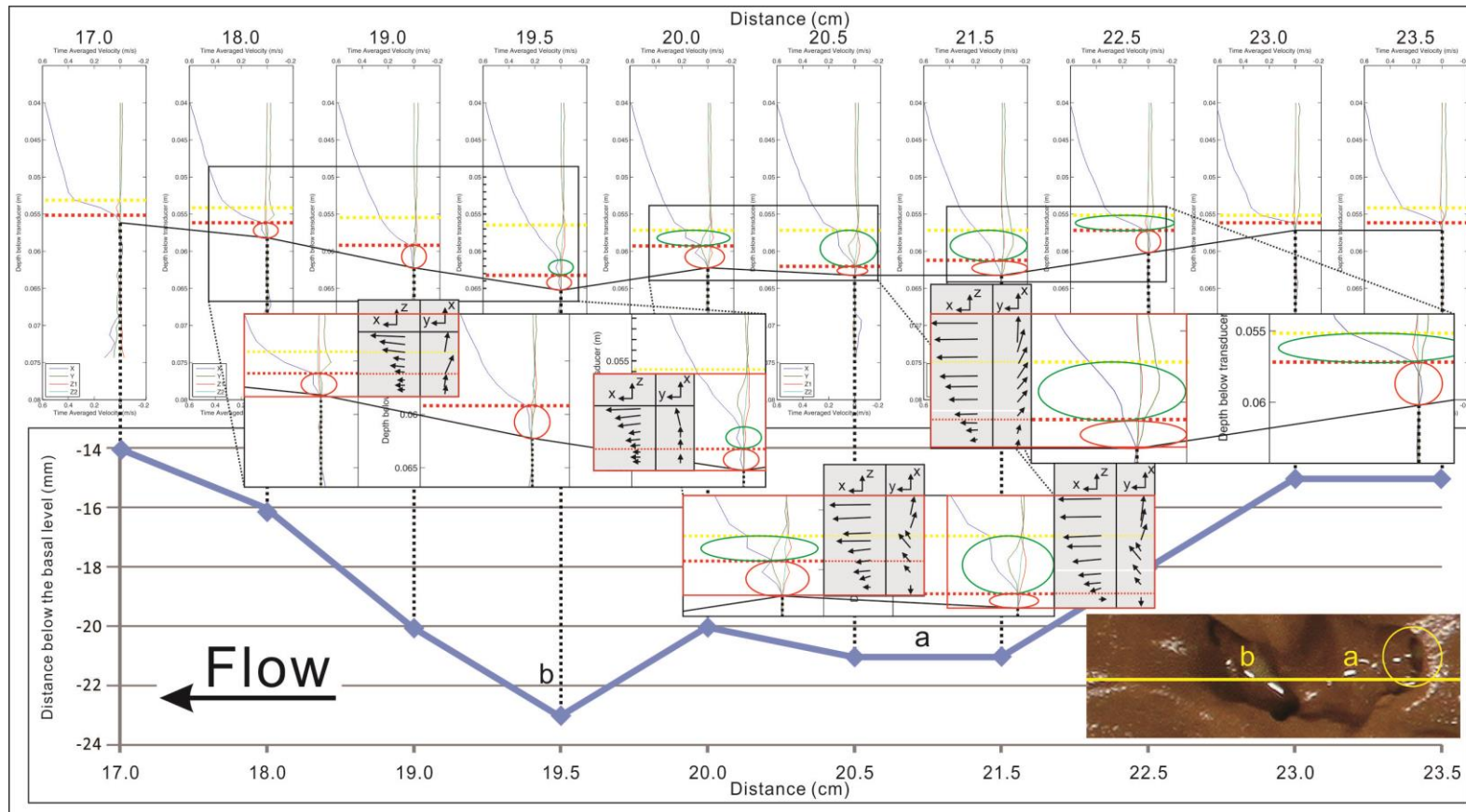


Figure 7.7 Hierarchical pothole. a: the shallow secondary pothole; b: the deep secondary pothole; The yellow circle tagged the sub-pothole in the proximal end of the shallow secondary pothole. The dashed line divided the water into several layers and the coloured ellipses tag different features of the flow profiles, which are discussed in detail in the text. The gray boxes with arrows refer to the overhead view (x-y) and the side view (x-z) of the changes of flow direction with increasing height from the bottom. Flow is from right to left. The sampling area is numbered as 13.1-1, which can be found in Figure 7.2.

7.3.2 Flutes

A range of flutes type forms were found on the bed of Exp. 8. These consisted of simple flutes, flutes with median ridge, and comet-shaped flutes. Compared with the potholes, the depth of all the flute features was relatively shallow, and shapes of them varied. For details, see Chapter 5.

Simple flute

The photo of the flute in Figure 7.8 was one of the simple flutes with an approximately parabolic shape. The length of its main body from the proximal cusped rim to the end of its flank rims was about 1.0 cm. The deepest part of its proximal principal depression was 4.5 mm deep, which was relatively small, compared with the depth of the most potholes described before (see Section 7.3.1 and Chapter 5). The feature also possessed a small median ridge.

Velocity sampling profiles 58.0 and 57.0 were located on the upstream area ahead of the flute, the sampling profiles 56.0 to 55.0 were within the downstream area in the rear of the flute. Above these locations, the flow structure was not complicated. The longitudinal flow increased logarithmically as normal open channel flow with small fluctuation of the transverse component.

The flow velocity mainly changed within the principal depression of the flute (Figure 7.8: profiles 56.5 and 57.0). Location 57.0 is the deepest part of the flute. In the near-bed sublayer, the flow moved towards the direction of -45° of deviation from the downstream flow with small velocity of around 0.07 ms^{-1} (Figure 7.8: red ellipse in the profile 57.0). Higher in the flow velocity increased exponentially with increasing height and flow direction rotated anti-clockwise to mainly downstream with small transverse component to right hand side.

Profile 56.5 was located on the proximal foot of the median ridge. In the lower bottom layer, the flow direction rotated anti-clockwise from 90° to -45° (Figure 7.8: red ellipse in the profile 56.5). In the shear layer, the transverse velocity altered from negative to positive and negative again. In consideration of the positively increasing of the longitudinal flow velocity, the changes of the transverse flow direction induced the direction of the resultant velocity fluctuated from the direction of -45° to almost downstream direction with small up-welling with increasing height in the shear layer. This means the flow moved upward spirally (Figure 7.8: area between red and

green dashed lines in the profile 56.5). In the outer layer, the direction of the resultant flow was mainly towards the downstream.

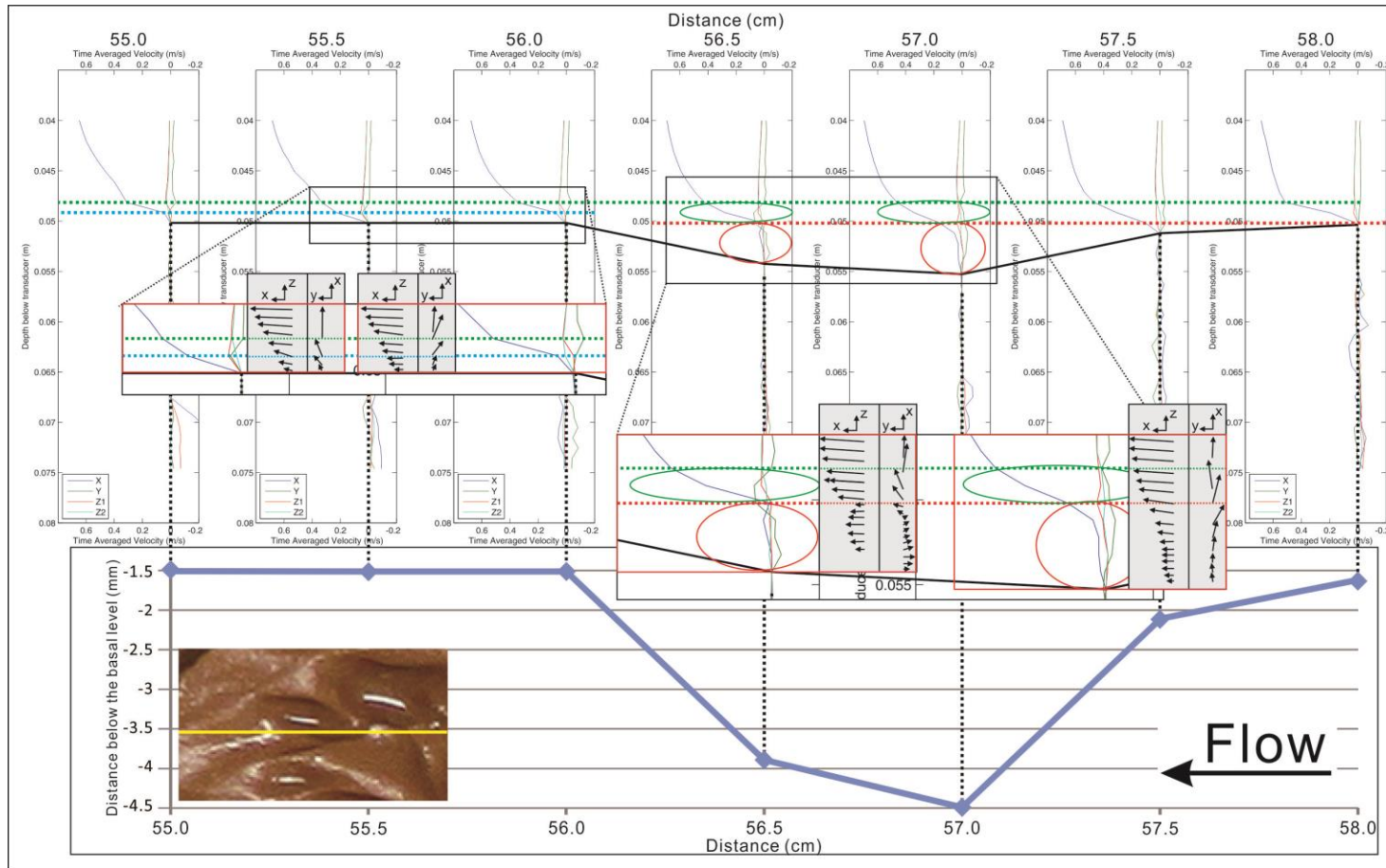


Figure 7.8 Simple flute. The dashed line divided the water into several layers and the coloured ellipses tag different features of the flow profiles, which will be discussed in detail in the text. The gray boxes with arrows refer to the overhead view (x-y) and the side view (x-z) of the changes of flow direction with increasing height from the bottom. Flow is from right to left. This sampling area is numbered as 8.65-3, which can be found in Figure 7.2.

Simple flute without the proximal rim

The photo in Figure 7.9 shows a flute without the proximal rim, which was probably cut through by the downstream part of the adjacent erosional feature ahead of it. The rest of the outline of this flute looks no different from a standard flute. It also contained two external secondary comet-shaped flutes by its flanks (Figure 7.9 a & b). This flute was bigger than the one shown in Figure 7.8. The principal depression was 2.5 to 3.0 cm long, 1.5 cm wide and about 2.0 to 2.5 mm deep. The proximal end of this flute was open with a projection in front of it, the height of which was 2.5 mm higher than the distal end of the flute and about 3.7 mm higher than the deepest part of the flute.

The flow structure over the projection is log-normal above normal open channels. The flow velocity near the bottom was very small. In the outer layer, the longitudinal flow velocity increased logarithmically with increasing height, but with nearly no transverse and vertical flow components (Figure 7.9: profiles 48.5 and 48.0). When flow reached the downstream edge of the projection in location 47.5, the longitudinal flow increased as locations 48.5 and 48.0, but had small transverse component to right hand side and small upward vertical components in the shear layer, which dissipated in the outer layer. This indicates that above location 47.5, the flow rotated anti-clockwise from the bottom to outer layer.

Once flow passed the downstream edge of the projection and moved into the principal depression of the flute, the flow pattern is more complex. The near-bed flow field in profile 47 in Figure 7.9 shows that within the depression, the flow was mainly towards downstream with small velocity ranging from 0.04 to 0.05 ms^{-1} in the 1 mm thick layer above the bottom and then decreased back to zero in the upper 1 mm thick layer above the bottom (Figure 7.9: area between black basal line and red dashed line in the profile 47.0). In the shear layer of this location, the flow rotated clockwise from 0° to -16° with small velocity of 0.07 ms^{-1} , and then reversed back to -6.8° , and then eventually returned back to the downstream direction with the velocity of 0.6 ms^{-1} with increasing height from the shear layer to the outer layer. A similar situation occurred above location 46.5. The flow moved spirally in an anti-clockwise sense, with the velocity increasing firstly gradually and then exponentially. The flow direction deviated from -9.1° in the bottom layer to the downstream direction in the shear layer and outer layer (Figure 7.9: profile 46.5). The flow structure above the next sampling location, location 46.0 changed back to simple condition with the only logarithmically

increasing longitudinal flow. This was probably because the bottom of the flute was relatively flat. The flow structures above the location 45.5, the stoss-side slope of the flute, contained an anti-clockwise rotating upward flow with increasing velocity from the surface of the slope to the outer layer. After the flow passed location 45.5 and moved to the downstream, the flow structures above the rest part of sampling area were only with increasing longitudinal velocity. The anti-clockwise vortices occurred throughout the length of the flute, which probably contributed to the lateral erosion within the flutes to widen the flute.

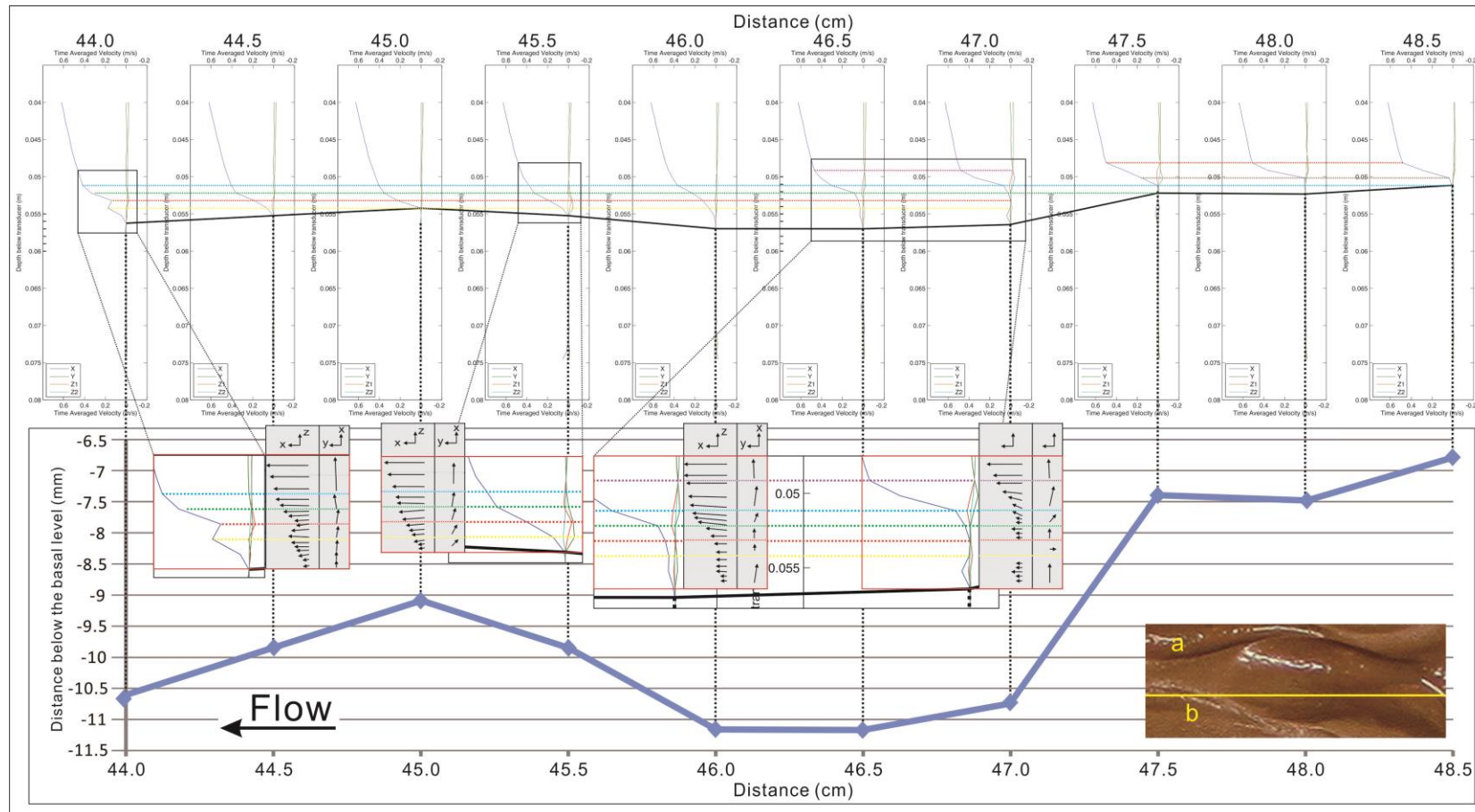


Figure 7.9 Flute without proximal end rim. The dashed line divided the water into several layers and the coloured ellipses tag different features of the flow profiles, which will be discussed in detail in the text. The gray boxes with arrows refer to the overhead view (x-y) and the side view (x-z) of the changes of flow direction with increasing height from the bottom. Flow is from right to left. This sampling area is numbered as 20.7-4, which can be found in Figure 7.2.

Flute with median ridge

The projection shown by the photo in Figure 7.10 is a median ridge remaining on the final bed for Exp. 8, which was not polished by the bedload sediments transporting with flow. All the surrounding features had been polished and removed, including the rim of the flanks of the flute what should be around this median ridge. A median ridge is not a common component of flutes on bedrock substrate, although it is identified as a typical component of flutes on the cohesive substrate (Allen, 1971a; Richardson and Carling, 2005). On current experimental bed, only one to two obvious median ridges could be produced in each series of experiments. This median ridge was the most obvious one remaining on the final bed of Exp. 8. The ridge itself was partially parabolic with round head towards upstream. The principal projection was 2.5 cm long and 2.5 mm high and the widest part of it was 2.5 cm wide.

Because the top surface and the area ahead of it were almost flat, the velocity structure over this sampling area was simple. Only above location 5.5 which was located in the proximal foot of the median ridge, the flow structure delivered relative complicated flow filed. Above this location the transverse flow component remained at zero value. The longitudinal flow increased with fluctuation again which might be caused by the resistance effect of the stoss-side slope of the median ridge, just like flow met the stoss-side wall of a pothole. The vertical component always presented slightly negative throughout the bottom layer and the shear layer, although it slightly fluctuated with increasing height. The direction of the resultant flow of the longitudinal and the vertical components demonstrated that in the near-bed sublayer, the flow was towards directly downstream, in the shear layer to downward by a few degrees, and in the outer layer to the downstream again. All the downward flows could help to polish the surface of the surface of the bed.

Above the locations on the stoss-side slope (Figure 7.10: profile 5.0) and the peak of the median ridge (Figure 7.10: profile 4.5), the longitudinal-section flow structures were very similar with location 5.5. But in the lower layer of these two locations, changeable transverse components were observed. They made the flow rotate slightly clockwise first. Once flow entering the outer layer, the flow direction changed to slightly anti-clockwise and back to towards directly downstream with increasing height. In the rest part of the sampling area, the flow structures were as similar as above the flat beds.

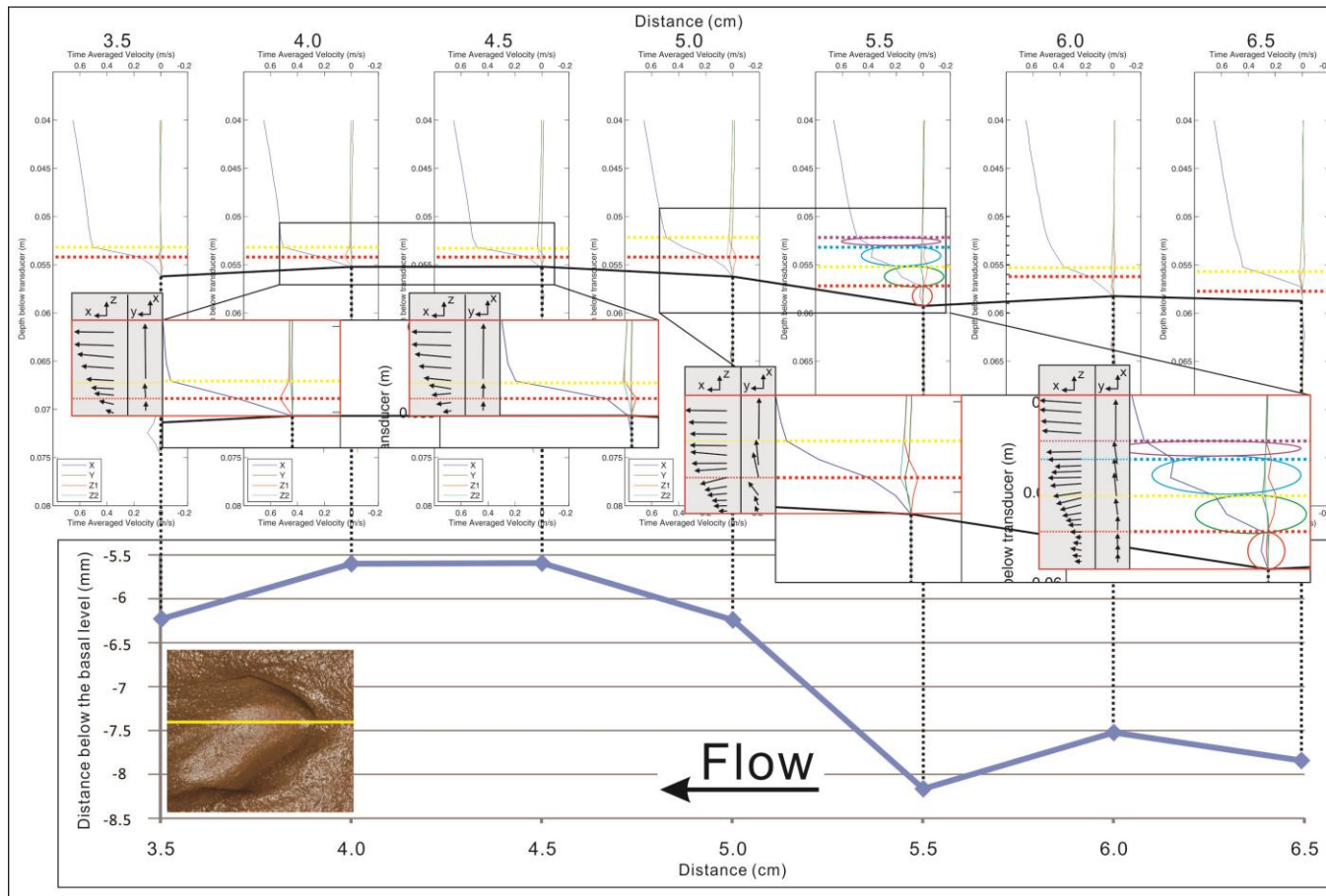


Figure 7.10 Flute with median ridge. The dashed line divided the water into several layers and the coloured ellipses tag different features of the flow profiles, which will be discussed in detail in the text. The gray boxes with arrows refer to the overhead view (x-y) and the side view (x-z) of the changes of flow direction with increasing height from the bottom. Flow is from right to left. This sampling area is numbered as 6.9-3, which can be found in Figure 7.2.

Comet-shaped flutes

Comet-shaped flutes are not one of the typical types in bedrock channels, but are common on cohesive mud bed (Allen, 1971a; Richardson and Carling, 2005). It is still necessary to figure out the flow structure within and above them. A bigger comet-shaped flute was selected from final bed of Exp. 8 (Figure 7.11). The bottom surface of the principal depression of this comet-shaped flute was not uniform. The deeper part of it was selected to measure the flow structure. This comet-shaped flute was 5.5 cm long and the sampling length was 3.5 cm long. The area where flow velocity changed most ranges from location 55.5 to 54.5, the deepest part of this flute was 6.5 mm deep.

Location 55.5 is close to the inner wall of the left flank. The flow in the range from bottom to the rim of flute flank (2 lower layers) of this location was complicated. The lowest layer was about 3 mm above the bottom. Within this height, the longitudinal velocity increased to about 0.05 ms^{-1} first and decreased to close to zero. However, within the same layer, the transverse velocity was -0.1 ms^{-1} and slightly decreased with increasing height until reaching the higher portions of the shear layer, which was in the same level of the left lateral rim of this flutes. Because that there was almost no vertical flow component in the near-bed sublayer and the lower shear layer, the flow direction rotate from -68.2° to -90° , and then reversed anti-clockwise back to the downstream direction at the level of 7 mm above the bottom with transverse velocity decreased back to zero (Figure 7.11: yellow dashed line). In the higher shear layer, the flow direction changed to the directly downstream with small up-welling. In the outer layer, the transverse and vertical components decreased with increasing height and the flow direction was towards the downstream directly. The flow structure above location 55.0 was similar with location 55.5 but contained greater longitudinal velocity in the bottom layer. This made the flow direction in near-bed sublayer rotated anti-clockwise from -45° to 0° from the near-bed sublayer to the upper boundary of the lower shear layer.

The inducement of the transverse velocity towards the right hand side with relative great value might be the effect of the wall reflection of the inner lateral wall of the flute. Owing to the sinuous form of the flank and the inner wall of this comet-shaped flute, when the flow moved along the inner wall and hit the relative project part, the flow would be reflected by the wall towards the opposite direction. The transverse velocity measured might be one of the components of this reflection flow. The near bed longitudinal

velocity above location 55.5 might be balanced by the other components of the reflection.

When the flow reached location 54.5 which was on the stoss-side slope of the flute, the flow structures within the shear layer increased with fluctuation which looked exactly the same of those observed in front of the proximal end of the median ridge. This might be because the gradient of this stoss-side slope, 0.4, was as same as that of the stoss-side of the median ridge mentioned before. The flow direction above this location spiraled several times. In the bottom layer, it moved to the downstream first and then rotated clockwise to right hand side. With increasing height, the flow rotated anti-clockwise to directly downstream again from the lower boundary of shear layer to the outer layer. Within the shear layer, the flow rotated downward with a few degrees. The flow conditions above locations 54.0 and 53.5 were very similar with location 54.5, just missing the fluctuation pattern of the increasing longitudinal flow velocity. Beyond the location 53.5, the flow was going to leave the depression of this comet-shaped flute and the flow structures above the surface of the rest part of the sampling transection returned to normal stable condition.

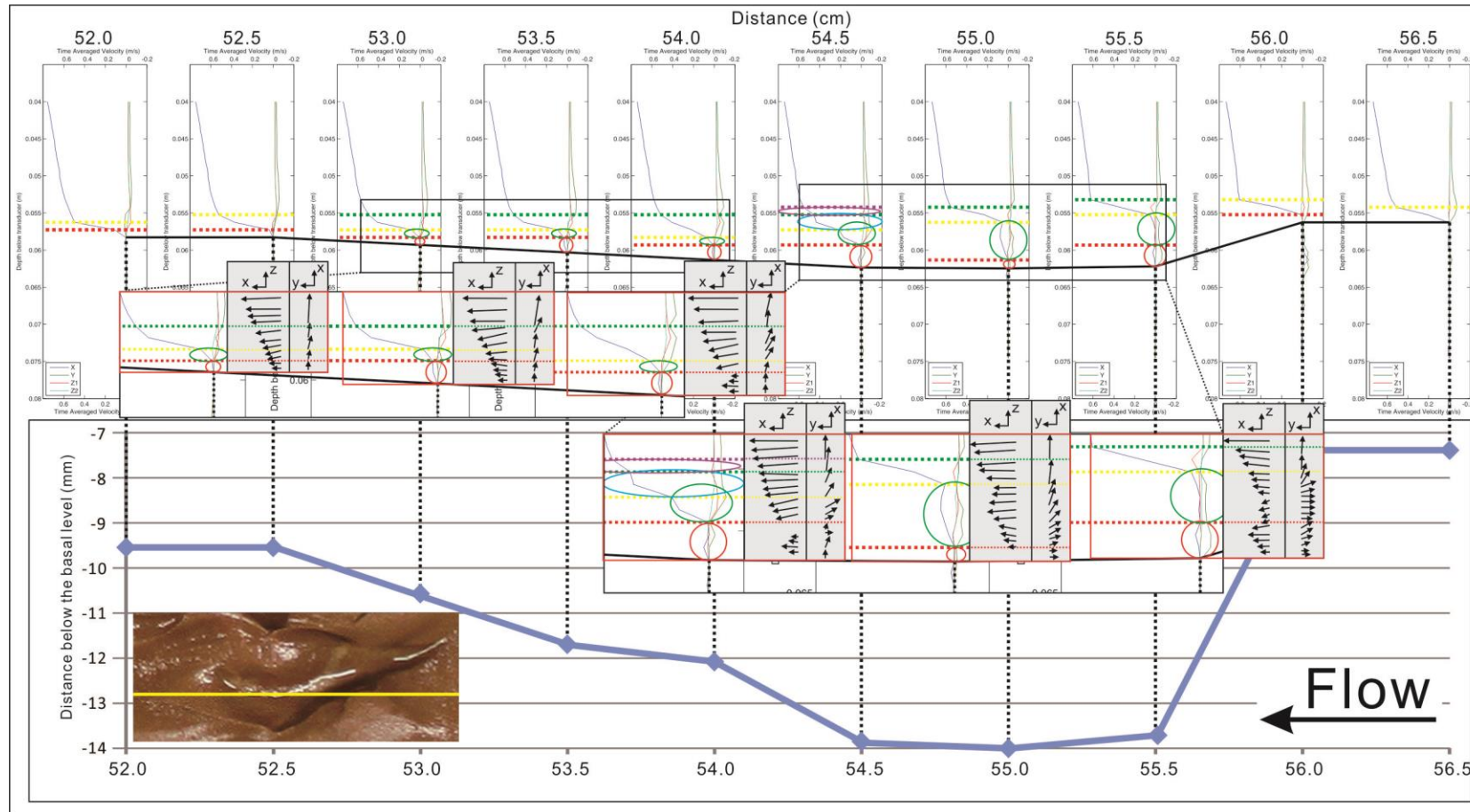


Figure 7.11 Comet-shaped flutes. The dashed line divided the water into several layers and the coloured ellipses tag different features of the flow profiles, which will be discussed in detail in the text. The gray boxes with arrows refer to the overhead view (x-y) and the side view (x-z) of the changes of flow direction with increasing height from the bottom. Flow is from right to left. This sampling area is numbered as 4-3, which can be found in Figure 7.2.

Narrow flute with entry furrow

The last kinds of flute introduced here is a narrow flute with entry furrow. This narrow flute also had a lateral furrow, but which was too narrow and shallow to measure the flow field within it. Therefore, only the principal depression of both the flute and the entry furrow were measured. The section measured was 5.5 cm long, 0.8 cm wide of the widest part. The relative depth of the deepest proximal depression was 5.8 mm. The entry furrow was 0.4 cm wide and relative 2.5 mm deep to the rim of the entry furrow (Figure 7.12). The measured area could be divided into 3 parts: the depression of the entry furrow, the proximal depression of the main flute, and the stoss-side slope of the flute. The variety of the flow field mainly occurred in the first two areas. Above the gentle part of the stoss-side of the flute, the flow structure was relatively simple.

In the main depression of the entry furrow and the flute, the flow field in all layers kept quite stable. In the near-bed sublayer (red ellipses in Figure 7.12), no matter how deep the bottom surface was, the longitudinal flow increased from zero to a certain value and then decrease slightly and entered into next layer. In the lower shear layer (green ellipses in Figure 7.12), the increasing rate of the velocity is higher than that in the lower layer, but the velocity would decreased again from a certain height just as happened in the lower layer. And then, the flow moved into the higher shear layer and increased to a relative stable value of about 0.5 ms^{-1} in the height range of 0.1-0.2 mm. At last, in the outer layer of flow field, the longitudinal velocity increase gently with increasing height.

The shape of the curves of transverse velocity above this sampling transect barely changed. This indicates that the flow structures above all sampling locations in this flute were very similar. The general flow pattern throughout the length of this flute is as follows: Above all sampling locations within the flute, there was almost no vertical flow component. The flow direction rotated slightly anti-clockwise from the downstream direction in the near-bed layer to the direction of approximately -29° in the shear layer, and then rotated clockwise back to the downstream direction in the outer layer again, although the velocity magnitude varies a bit in the different layers above different sampling locations. Compared with the flow above other features, the flow field in this case shows the most regular structures.

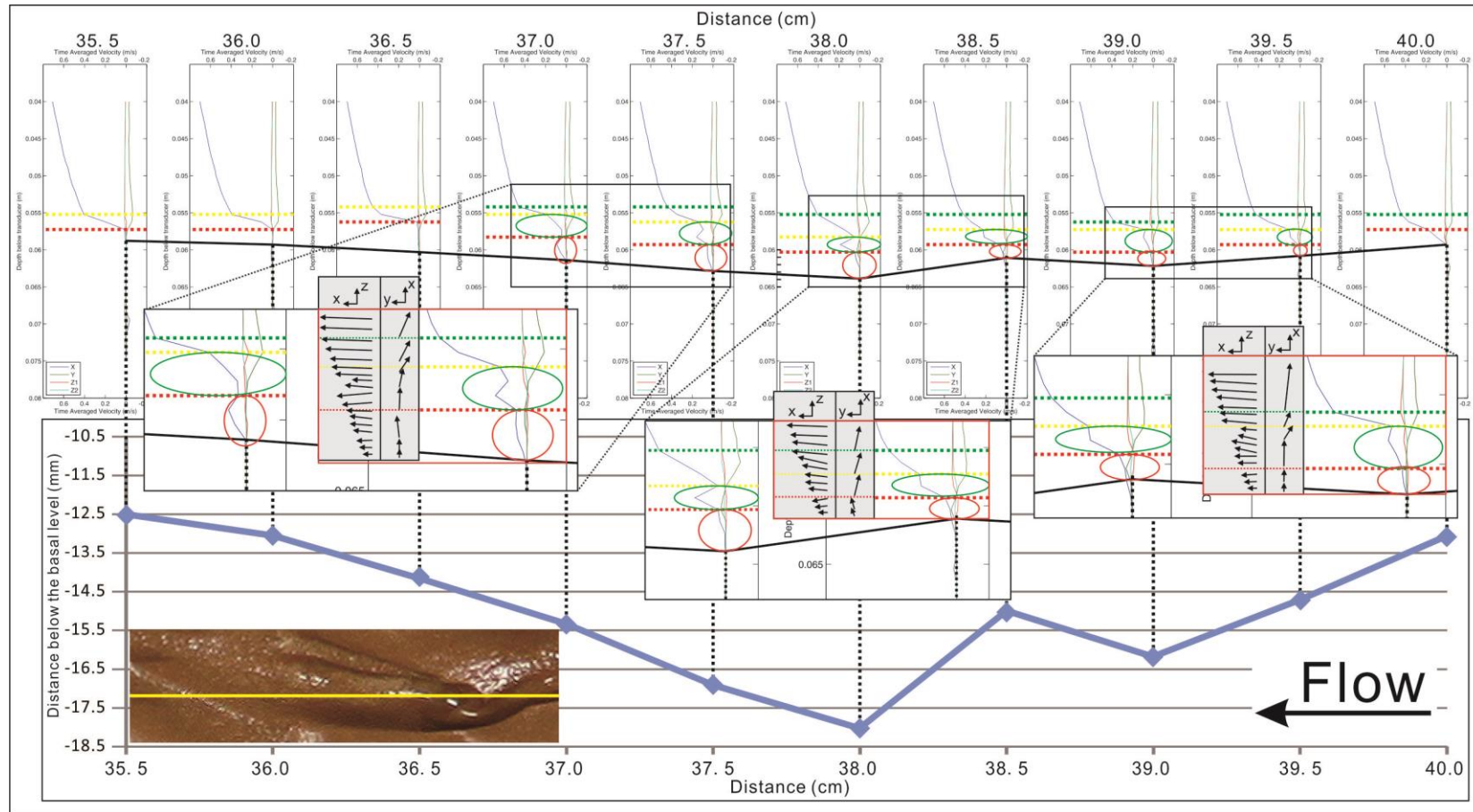


Figure 7.12 Narrow flute with entry furrow. The dashed line divided the water into several layers and the coloured ellipses tag different features of the flow profiles, which will be discussed in detail in the text. The gray boxes with arrows refer to the overhead view (x-y) and the side view (x-z) of the changes of flow direction with increasing height from the bottom. Flow is from right to left. This sampling area is numbered as 4-2, which can be found in Figure 7.2.

7.3.3 Longitudinal furrows

Although many small parallel sided short furrows are distributed in the clay bed of Exp. 8, the dimensions of them were too small to measure the flow structures over them with a Vectrino ADV. However, it was possible to measure flows within larger-scale longitudinal furrows, such as sinuous parallel-sided furrows, regular compound furrows, and expanding furrows.

Sinuous parallel-sided furrows

A surface of longitudinal section throughout a sinuous parallel-sided furrow, covering a part of the main furrow and a part of one side rim of it, was measured. This furrow was about 3.5 cm long, 0.5 cm wide and approximately 0.3 cm deep (Figure 7.13). The current measured longitudinal section contained two lower areas and two higher projections. The two lower parts were separated by one of the projections, which was a part of right bank of the furrow. The other projection was the downstream end rim of this furrow.

Comparison with the examples discussed before, the flow structure over this parallel sided furrow looked as similar as that above a flat surface. The flow pattern kept constant above all the sampling locations. Above the relatively higher and flat areas (Figure 7.13: profile 43.5, 42.0 to 41.0), longitudinal flow component increased exponentially with small transverse and vertical components. Above the relatively lower areas, the flow velocities were nearby zero in the near-bed sublayer. When entering into the shear layer, the flow presented a similar structure as the higher areas. Except for the locations 42.0 to 41.0, flow directions above all sampling areas were mainly towards the downstream directly with logarithmically increasing longitudinal velocity from the bottom to the outer layer. Above the locations 42.0 to downstream, location 41.0, the flow in the lower layer moved a few degrees to the left hand side in the relatively lower layer, but changed back to the downstream in the outer layer.

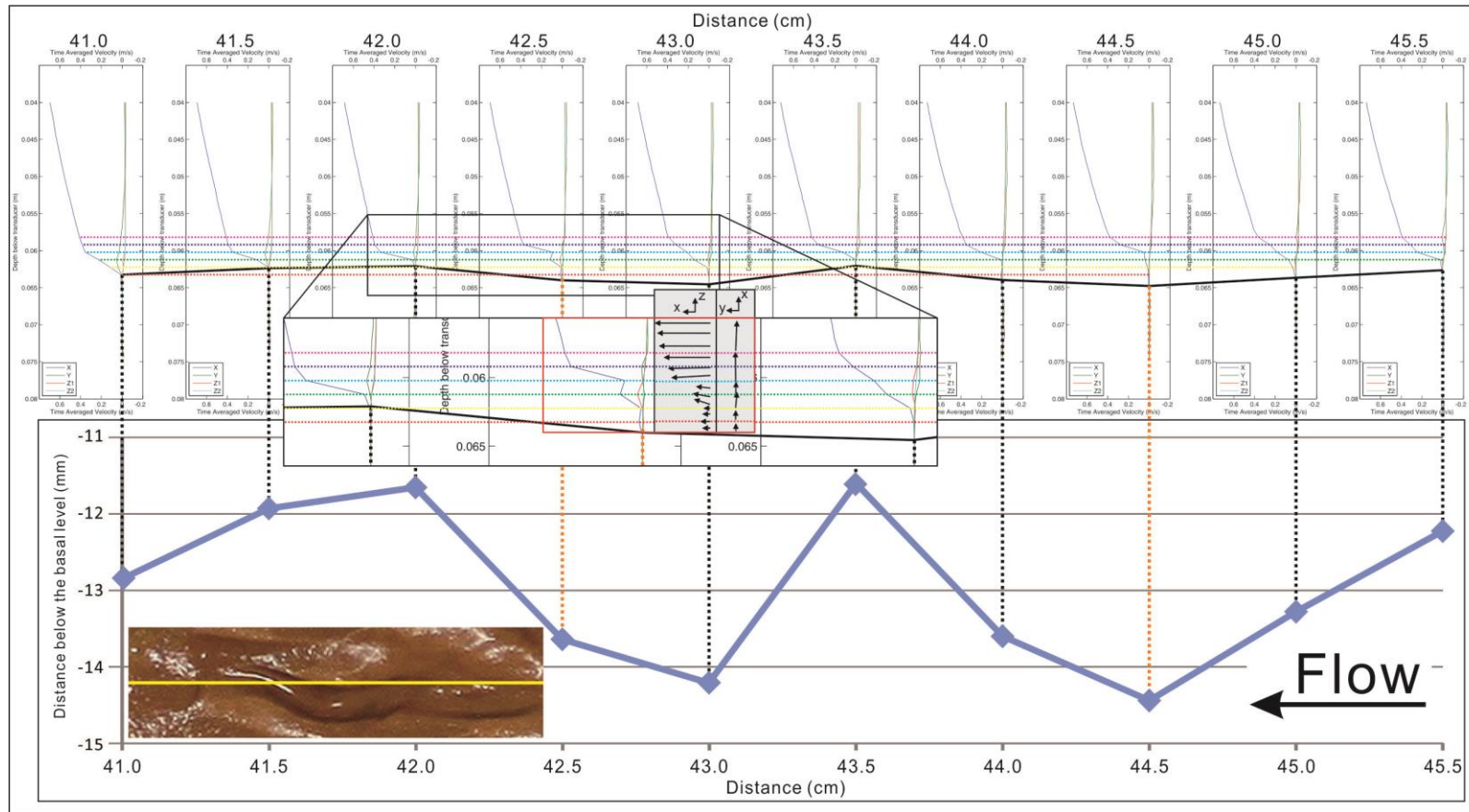


Figure 7.13 Sinuous parallel-sided furrow. The dashed line divided the water into several layers, which will be discussed in detail in the text. The gray boxes with arrows refer to the overhead view (x - y) and the side view (x - z) of the changes of flow direction with increasing height from the bottom. The gray boxes with arrows refer to the overhead view (x - y) and the side view (x - z) of the changes of flow direction with increasing height from the bottom. Flow is from right to left. This sampling area is numbered as 8.1-1, which can be found in Figure 7.2.

Regular compound furrows

A couple of curved short parallel-sided furrows with a similar shape were observed in the clay bed of Exp. 8 and were considered as regular compound furrows (Figure 7.14). They formed in a zigzag pattern instead of the typical linear pattern with abutting end to end. The right one was 2.5 to 3.0 cm long, 1.0 cm wide and 0.8 mm deep and the left one was 2.0 cm long, 0.8 cm wide and 3.8 mm deep. Although the depths of these furrows were not consistent, they were still considered as the regular compound furrows due to the similarity of their shape.

The sampling area of these regular compound furrows can be divided into 3 parts: (1) from the upstream area to the lee-side slope of first furrow: locations 60.5 to 59.0; (2) within the principal depression of the first furrow: locations 59.0 to 57.5; (3) from the shared rim between the first and the second furrows to the downstream end of the secondary furrow: locations 57.5 to 56.0 (Figure 7.14).

Above the first part, from locations 60.5 to 59.5, the flow structures were simple. The flow direction was mainly towards the downstream, except in the shear layer, whilst the longitudinal flow velocity increased approximately exponentially. Small transverse and vertical flow continents were observed in the shear layer, which altered the flow direction to slightly the left hand side. In the shear layer of locations 60.5 and 60.0, the vertical components were slightly positive and that of location 59.5 was slightly negative. This indicates that the leftward longitudinal flow also moved upward by a few degrees in the shear layer of locations 60.5 and 60.0 and lightly downward above location 59.5 (Figure 7.14: yellow circle in profiles 60.5 and 59.5).

In the second part, the principal depression of the first furrow, the flow condition altered. Above the lee-side slope of the first furrow, the flow structure was still in the same flow pattern of location 59.5. Above two locations within the first furrow (Figure 7.14: profiles 58.5 and 58.0), in the near-bed sublayer, there were two flow separation cells (Figure 7.14: red circle in profiles 58.5 and 58.0). The flow separation cell above location 58.5 was towards the direction of about 117° and that above location 58.0 was towards directly the upstream. This indicates that there is a reversed flow occurred above these two locations. In the lower shear layer of location 58.5, flow rotated from 117° to the downstream first and then rotated anti-clockwise to the direction of 26.6° in the middle portions of the shear layer. With increasing height to the outer layer, the flow rotated clockwise from 26.6° back to the downstream direction. The flow structure above location

58.0 was different from location 58.5. The flow changed the direction from towards the upstream in separation zone in the near-bed sublayer to the direction of -30° in the lower shear layer first, and then kept rotating anti-clockwise to the downstream in the outer layer (Figure 7.14: yellow circle in profiles 58.5 and 58.0). After flow passed the location 58.0, it reached the shared rim. The flow structure above the shared rim was uniform. The flow mainly moved towards the downstream with the increasing longitudinal velocity (Figure 7.14: green circle in profile 57.).

Once the flow passed the shared rim, it entered into the third part of the sampling area, the principal depression of the second short furrow (Figure 7.14: profile 57.0). In the bottom layer above the profile 57.0, a flow separation cell directed from toward the direction of -90° to -135° , and then to the upstream could be observed (Figure 7.14: red ellipse in profile 57.0). The flow changed direction to the direction of 61.3° when it reached the lower shear layer. With increasing height, the flow rotated clockwise to approximately the downstream direction with the velocity increasing gradually. When the flow reached the stoss-side slope of the second furrow, the flow rotated clockwise first from downstream to 45° in the near-bed layer, and then to approximately 7° in the shear layer, and then anti-clockwise back to the downstream direction in the outer layer with small up-welling (Figure 7.14: yellow and blue ellipses in profiles 57.0). Above the last sampling location, location 56.0, the near bottom flow and the flow in the higher outer layer were mainly towards the downstream, with flow deviating from a few degrees on the left hand side in the shear layer (Figure 7.14: blue ellipse in profile 56.0).

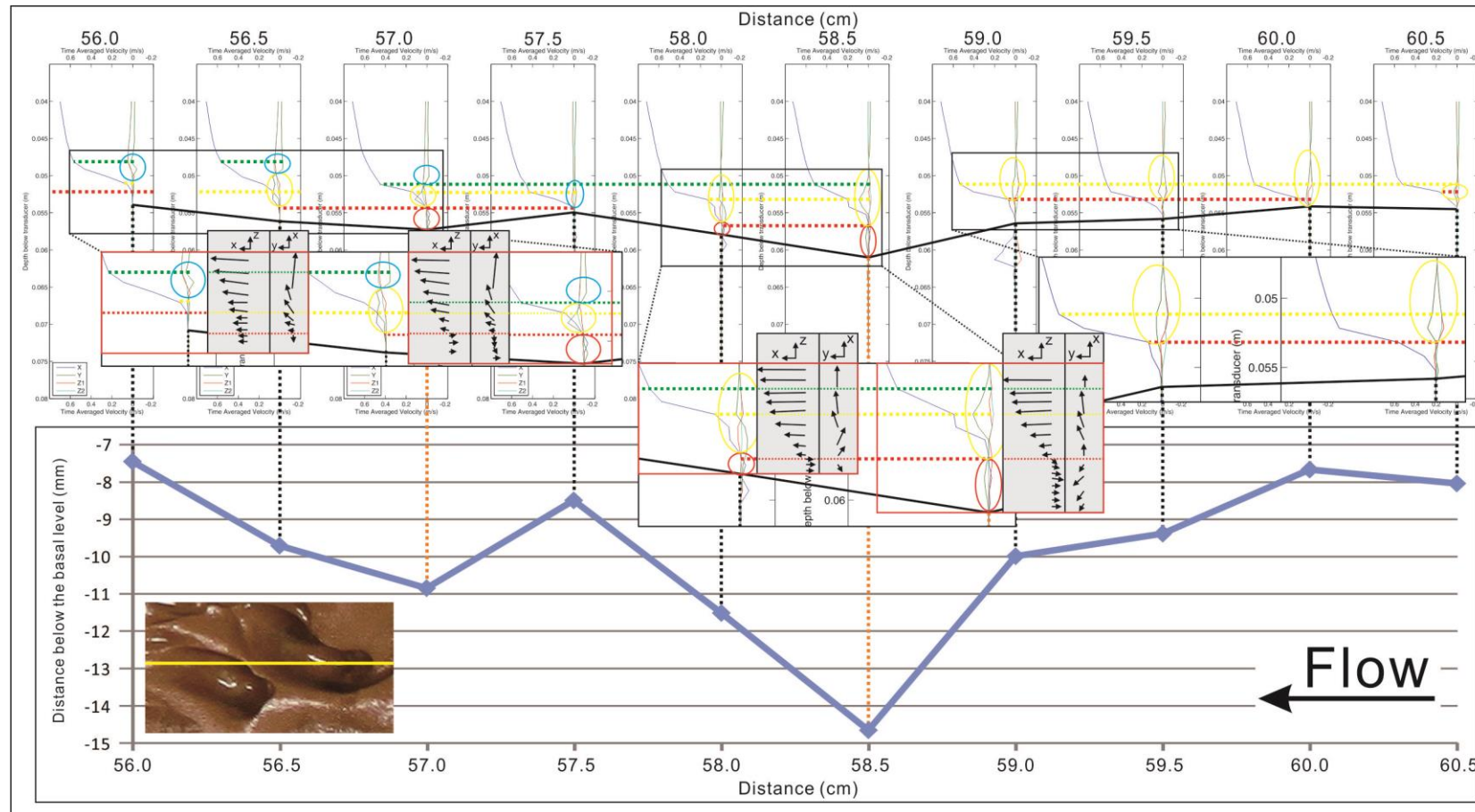


Figure 7.14 Regular compound furrows. The dashed line divided the water into several layers and the coloured ellipses tag different features of the flow profiles, which will be discussed in detail in the text. The gray boxes with arrows refer to the overhead view (x-y) and the side view (x-z) of the changes of flow direction with increasing height from the bottom. Flow is from right to left. This sampling area is numbered as 6.9-2, which can be found in Figure 7.2.

Expanding furrows

Expanding furrows did not distribute widely neither in the natural bedrock channels nor in the experimental substrates. In Exp. 8 bed, only one expanding furrow could be observed (Figure 7.15). The one shown in Figure 7.15 was 4.5 cm long (without the length of small short furrow behind it), and 9.5 mm deep. The width of the curved furrow was 1 cm and the width of the proximal end part of was 2.5 cm. A small short furrow developed behind the expanding furrow and also cut through a part of the downstream rim of the expanding furrow.

The most active area ranged from location 46.0 to 44.5 which cover the principal depression of the expanding furrow. Out of this range, the clay bed tended to become flat that made the flow structures above the bed present normal condition. Within this range, the most complicated flow structures were observed above the junction of the narrow part of the furrow and the expanding part. This junction was also the deepest part of the expanding furrow. Before the flow moved into the furrow, the flow structures were as similar as that above the normally plan bed surface. Significant change of the flow velocity profiles could be observed from when flow entered into the sampling location in the furrow body.

The range of flow field could be divided into 3 layers as usual: the near-bed sublayer (areas between the black bottom line and red dashed lines), shear layer (areas between the red dashed lines and yellow dashed lines), and the outer layer (areas above the yellow dashed lines). The most notable change of the velocities happened in the lowest near-bed sublayer and shear layer. Compared with the nothing special velocity curves of location 46.5, the curves below the red dashed line shown more complicated flow condition within the furrow. In the near-bed sublayer, the main flow direction was to the left hand side with the transverse velocity increasing first and then decreasing back to zero when the height increased to the level of red dashed line (Figure 7.15: red ellipse in profile 46.0). In the shear layer, the flow rotated clockwise from the direction of 45° to approximately -104° towards slightly the upstream, and then anti-clockwise to downstream-ward in the outer layer with increasing of the flow velocity logarithmically (Figure 7.15: green ellipse in profile 46.0).

When the flow moved forward to the location 45.5, the flow field near the bed changed a lot. The flow direction in the lower layer above this location was towards the downstream with the velocity increased firstly and then decreased (Figure 7.15: red ellipse in profile 45.5). The flow direction

changed from towards downstream to the direction of 45° in the lower shear layer and returned back to the downstream direction from the higher shear layer to the outer layer (Figure 7.15: green ellipse in profile 45.5). The flow structures above next two downstream locations, locations 45.0 and 44.5, presented a similar condition of location 45.5 with the flow moving to the downstream in the near-bed layer, changed direction a few degrees leftward in the shear layer and rotated clockwise back to the downstream direction again in the outer layer. The vortices above these four sampling locations probably contributed to the lateral erosion of the principal furrow and widen the left rim of the expanding area. Keep moving forward to locations 44 and 43, the near bottom flow faded to zero and the flow structures in all directions returned to Log-normal condition. The expanding furrow was ended with these near bottom flows gone.

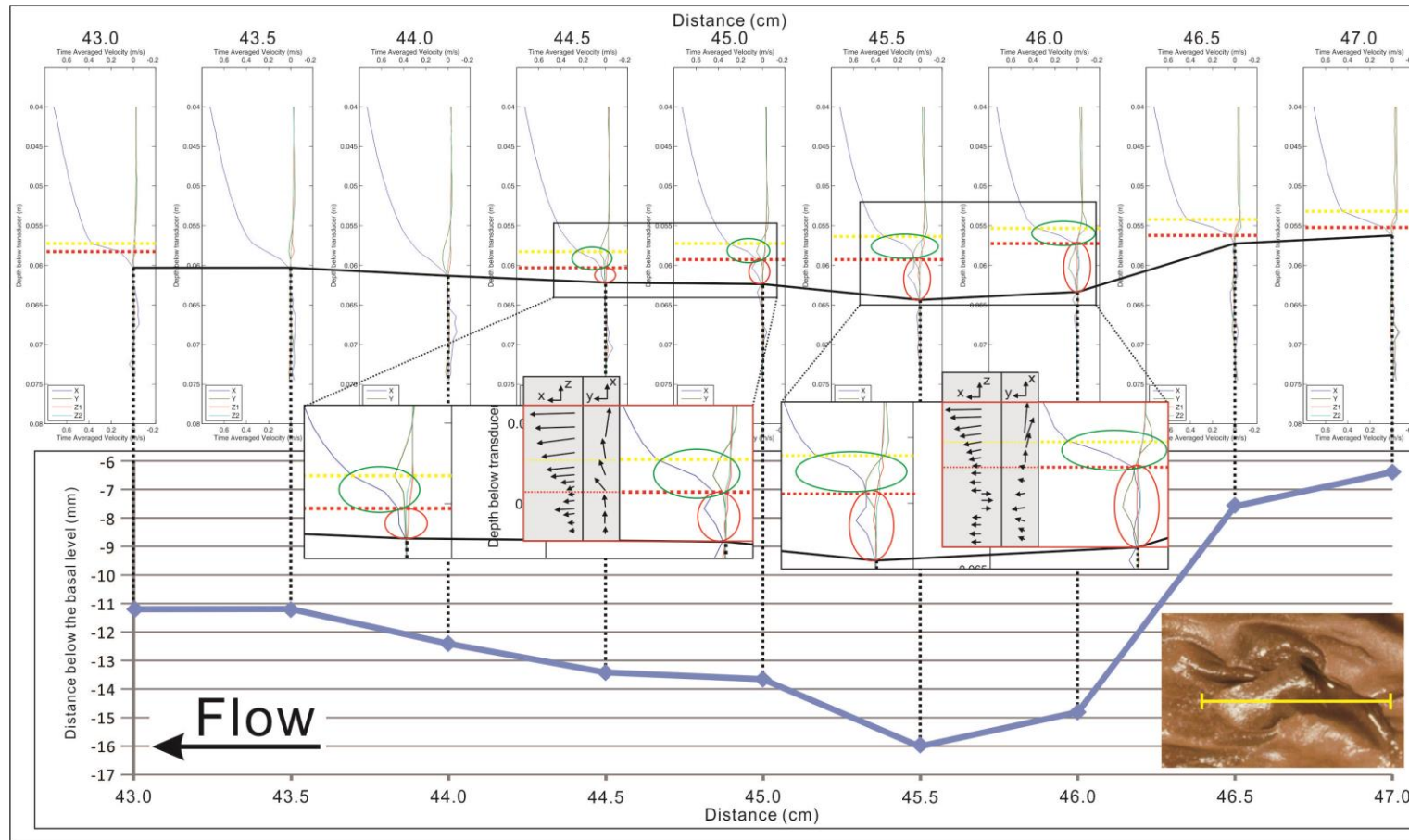


Figure 7.15 Expanding furrow. The dashed line divided the water into several layers and the coloured ellipses tag different features of the flow profiles, which will be discussed in detail in the text. The gray boxes with arrows refer to the overhead view (x-y) and the side view (x-z) of the changes of flow direction with increasing height from the bottom. Flow is from right to left. This sampling area is numbered as 10.1-1, which can be found in Figure 7.2.

7.3.4 Other erosional features

The Erosional features other than the potholes, flutes or longitudinal furrows were not common in Exp. 8. Three kinds of the features including the reversed furrows, the hummocky forms and the obstacle marks, were observed in Exp. 8 and are going to be introduced.

Reversed furrows

Figure 7.16 and Figure 7.17 demonstrate two longitudinal sections above one reversed furrow. The width of the furrow ranged from 1.5 to 2.0 cm and the relative depth of it was about 8.0 to 9.0 mm. Compared with other features in the clay bed, this reversed furrow was relatively deep. The area ahead of the principal furrow was flat, but the area located in the downstream direction was as a projection, and the height of it was slightly higher the upstream end.

Before the flow entered into the principal depression of the reversed furrow, the flow field over the flat bed before the proximal rim of it was similar as those above other flat beds that has been discussed before (Figure 7.16 and Figure 7.17: locations 29.5 to 28.5). After the flow entered into the principal furrow, the longitudinal flow pattern become complicated and the direction of near bed transverse flow velocity altered from positive to negative and would keep negative throughout all the depth of the measurement window (Figure 7.16: profile 27 to 28; Figure 7.17: profile 27.5 and 28). Although the longitudinal flow pattern looked complicated, the resultant flow structures were quite simple above these locations, because the transverse and vertical components presented simple conditions. Above the location 27.5 in Figure 7.16, in the lower shear layer, the flow moved toward downstream directly and slightly upward with velocity increased first and then decreased a bit with increasing height (Figure 7.16: red ellipse in profile 27.5). The main change of the flow direction occurred in in the higher shear layer and the outer layer was because of the genesis of the transverse and vertical components. Flow direction changed from to the downstream with small up-welling, to the direction of -6.8° with small up-welling first and then slightly rotated anti-clockwise back to downstream direction with small down-welling with increasing height (Figure 7.16: green and purple ellipses in profile 27.5).

The flow structure above profile 27.0 was similar with location 27.5, but having a transverse flow component with a few degrees to the right hand side in the near bottom area. From the shear layer to the outer layer, the flow structure was almost the same as location 27.5, with slightly anti-

clockwise increasing flow from lower shear layer to outer layer (Figure 7.16: profile 27.0). The flow structures above locations 28.0 and 27.5 in Figure 7.17 presented also almost the same condition with locations 27.0 in Figure 7.16. These flow structures indicate that the flow within the principle furrow in front of the projection moved to right hand side, which probably contributed to the erosion towards the right hand side which induced the furrow to reverse.

Once the flow passed the deepest part of the furrows and reached the projection at the backward of the furrow, the flow structures above the surface of the projection changed back to log-normal stable condition. However, compared with the positive transverse flow structures before entering into the furrow, the transverse flow velocity changed to negative from the stoss-side slope towards the downstream direction. This might be caused by the resist effect by the projection behind this reversed furrow. In the whole series of the velocity profiles, no anti-streamwise flow separation zone developed above the bed.

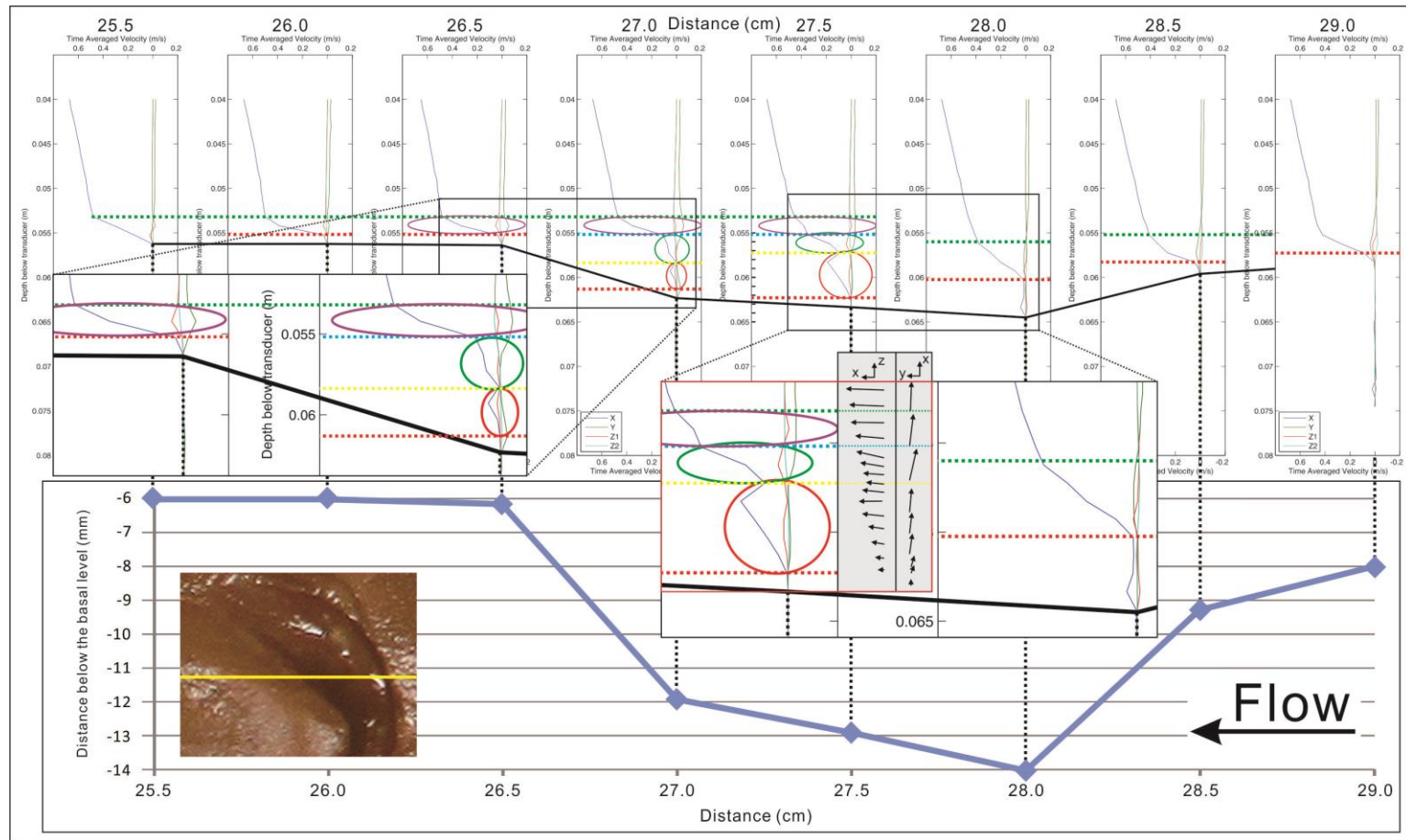


Figure 7.16 Reversed furrow-1 (Flow is from right to left). The dashed line divided the water into several layers and the coloured ellipses tag different features of the flow profiles, which will be discussed in detail in the text. The gray boxes with arrows refer to the overhead view (x-y) and the side view (x-z) of the changes of flow direction with increasing height from the bottom. This sampling area is numbered as 4-1, which can be found in Figure 7.2.

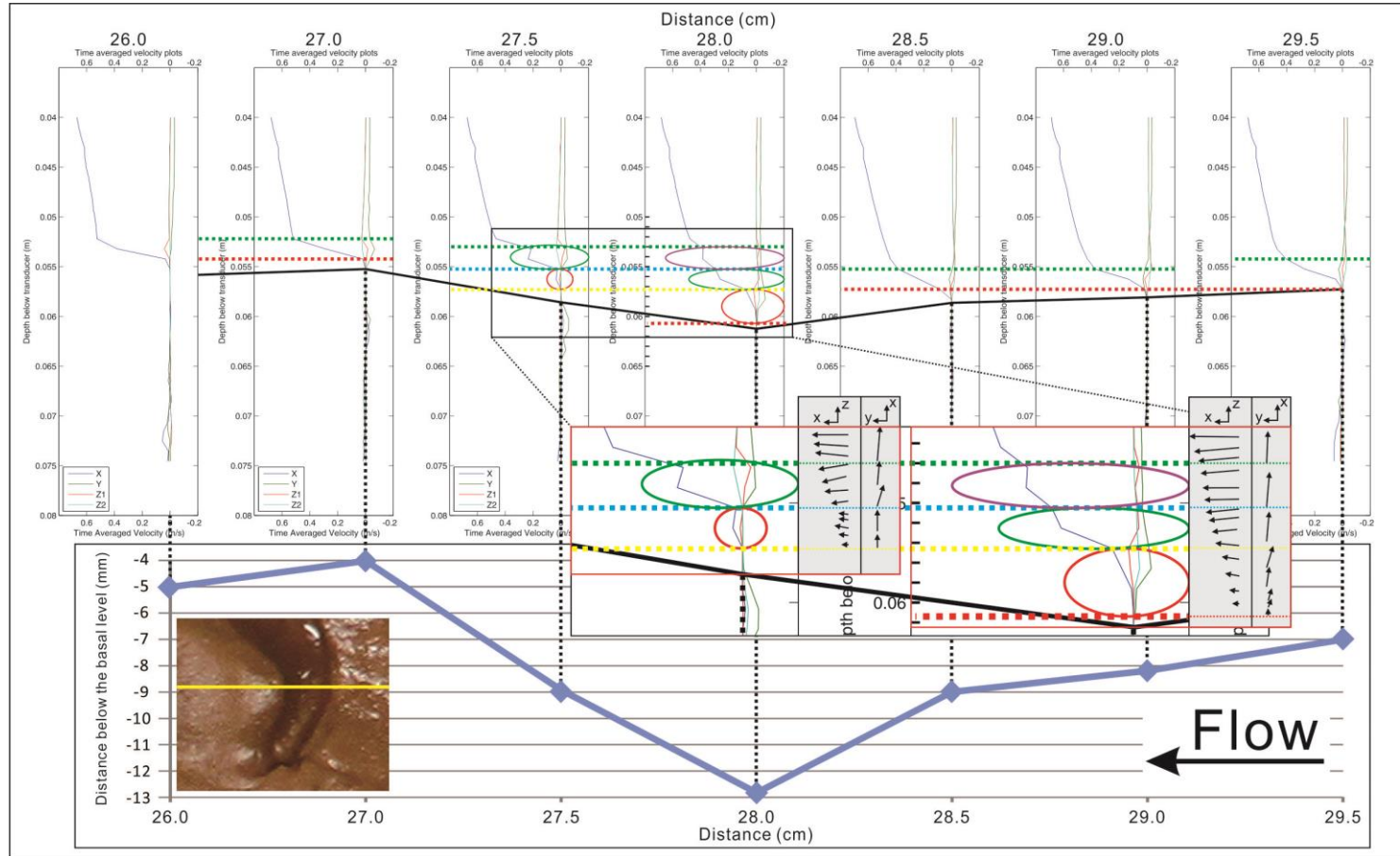


Figure 7.17 Reversed furrow-2. The dashed line divided the water into several layers and the coloured ellipses tag different features of the flow profiles, which will be discussed in detail in the text. The gray boxes with arrows refer to the overhead view (x - y) and the side view (x - z) of the changes of flow direction with increasing height from the bottom. Flow is from right to left. This sampling area is numbered as 3.35-1, which can be found in Figure 7.2.

Hummocky forms

Figure 7.18 illustrates a small part of a hummocky form observed in Exp. 8 bed. This hummocky form was 3.0 cm long, 1.5 cm wide and peak of the relatively higher part was 3 mm higher than the lowest bottom.

Compared with the flow structures above the other kinds of erosional features, the most obvious difference in the flow field above the hummocky forms is that the increasing rate of the flow velocity near the bed is higher than that above the other features. Within the range of distance of 2.5 mm, the longitudinal velocity increased by more than 0.6 ms^{-1} . After the flow velocity reached about 0.62 ms^{-1} and the flow entered into the outer layer, the increasing rate of the velocity decreased dramatically to 0.03 ms^{-1} within the range of height of more than 12.5 mm. On the hummocky forms, the longitudinal velocity increased no longer exponentially with depth. The flow velocity pattern can be divided into 2 linear changing parts, the higher increasing rate part in the bottom layer (Figure 7.18: areas lower than the light blue dashed line of profiles 24, 24.5 and 27; areas lower than the light purple dashed line of profiles 25 to 27) and the lower increasing rate part in outer layer (Figure 7.18: areas higher than light blue dashed line of profile 24, 24.5 and 27; areas higher than light purple dashed line of profile 25 to 27).

The longitudinal flow structures above the higher part increased logarithmically with height increasing. The flow structures above the lower parts were slightly complicated. In the shear layer, the transverse and vertical flow components could be observed (Figure 7.18: profiles 27.5, 27.0, and 25.0-24.0). The transverse components were always positive. The vertical components are negative above the stoss-side of the higher part (Figure 7.18: profiles 27.5 and 27.0) and positive above the lee-side slope of the higher part (Figure 7.18: profiles 25.0 to 24.0). These indicate that above the both stoss-side and lee-side parts, the flow rotated to the left hand side in the shear layer and reversed back to downstream-ward in the outer layer. The leftward flow presented slightly downward above the stoss-side part and upward above the lee-side part (Figure 7.18: profiles 27.5 and 27.0).

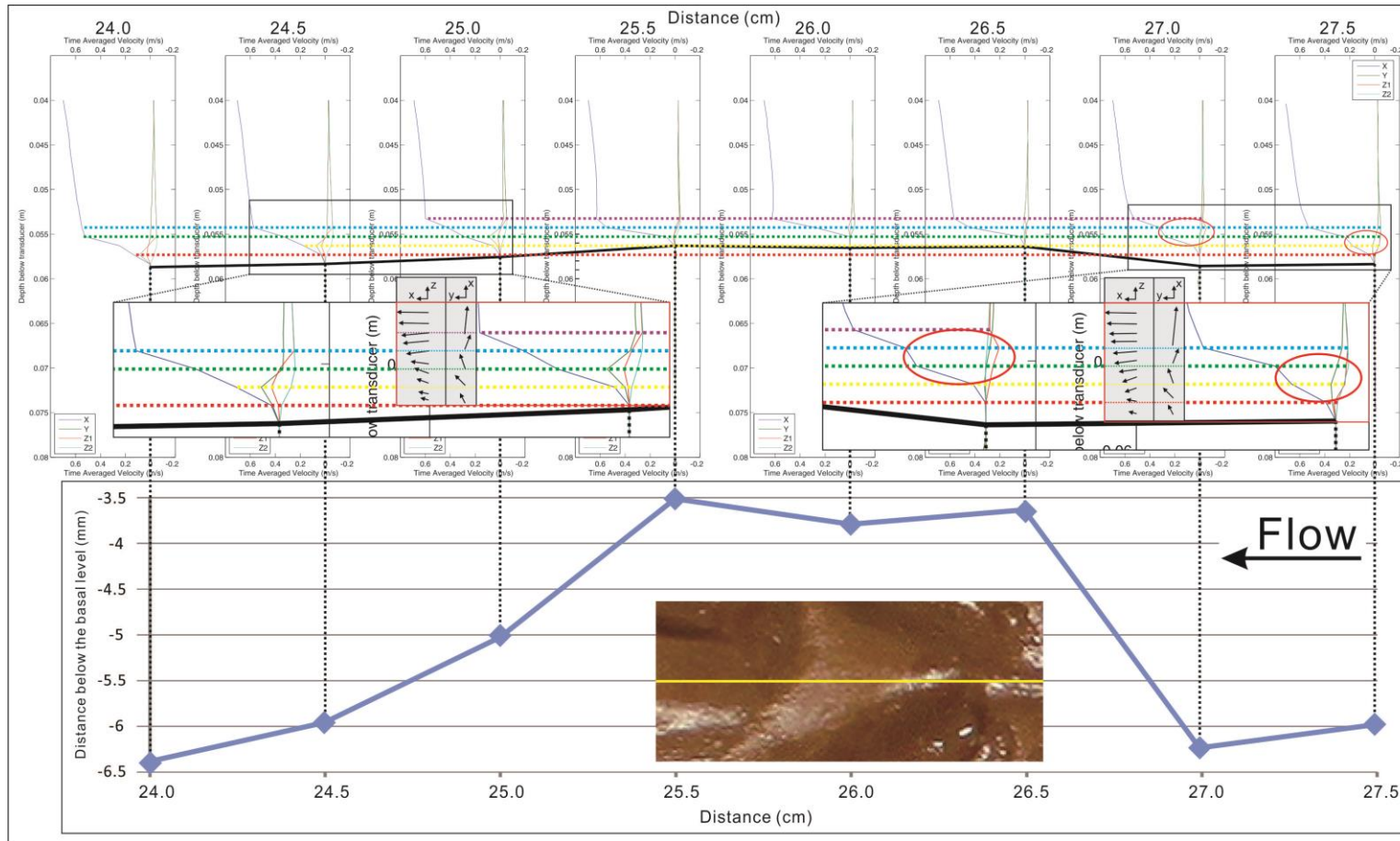


Figure 7.18 Hummocky forms. The dashed line divided the water into several layers and the coloured ellipses tag different features of the flow profiles, which will be discussed in detail in the text. The gray boxes with arrows refer to the overhead view (x - y) and the side view (x - z) of the changes of flow direction with increasing height from the bottom. Flow is from right to left. This sampling area is numbered as 18.3-1, which can be found in Figure 7.2.

Obstacle marks

The obstacle mark on experimental bed looked similar with the reversed forms mentioned before, because both of them have a projection behind the principal furrows of them (Figure 7.19: yellow ellipse; and Figure 7.17). However the curvature of this obstacle mark was much bigger than the reversed furrows shown by Figure 7.17. Compared with the similar forms produced in other experiments, it was distinguished from the reversed furrows. The deepest part was located in the furrow in front of the projection/obstacle and is about 5 mm deep. The second lower part in this longitudinal section was in the rear of the obstacle and within the right end of the principal furrow around the obstacle, if looking downstream.

No matter whether it was within the furrow or above the obstacle, the near bed longitudinal flow velocity demonstrated not complicated structure except that above location 19, which increased with fluctuation. This might be induced by the wall resistant effect of the stoss-side slope of the right end of the furrow (red ellipses in Figure 7.19). The profiles of longitudinal flow velocity barely changed from the upstream to the downstream over this obstacle mark. There was almost no secondary flow zone or flow separation zone observed within and above neither in the furrow nor on the obstacle mark, no matter where it was located on the stoss-side slope or the lee-side slope. This situation is quite different from the flow fields above the other erosional features discussed before. This might be the reason for why the furrow ahead of the obstacle tended to develop towards the cross-section direction instead of along the streamwise.

The most notable change occurred on the transverse flow velocity in the shear layer. Before the flow reached the peak of the obstacle mark, the transverse velocities in the shear layer were near zero. When flow past the peak and reached the lee-side slope of the obstacle mark, the transverse velocity presented negative in the shear layer and the outer layer, with decreasing velocity within increasing height. There was almost no vertical flow component throughout the series of the sampling locations.

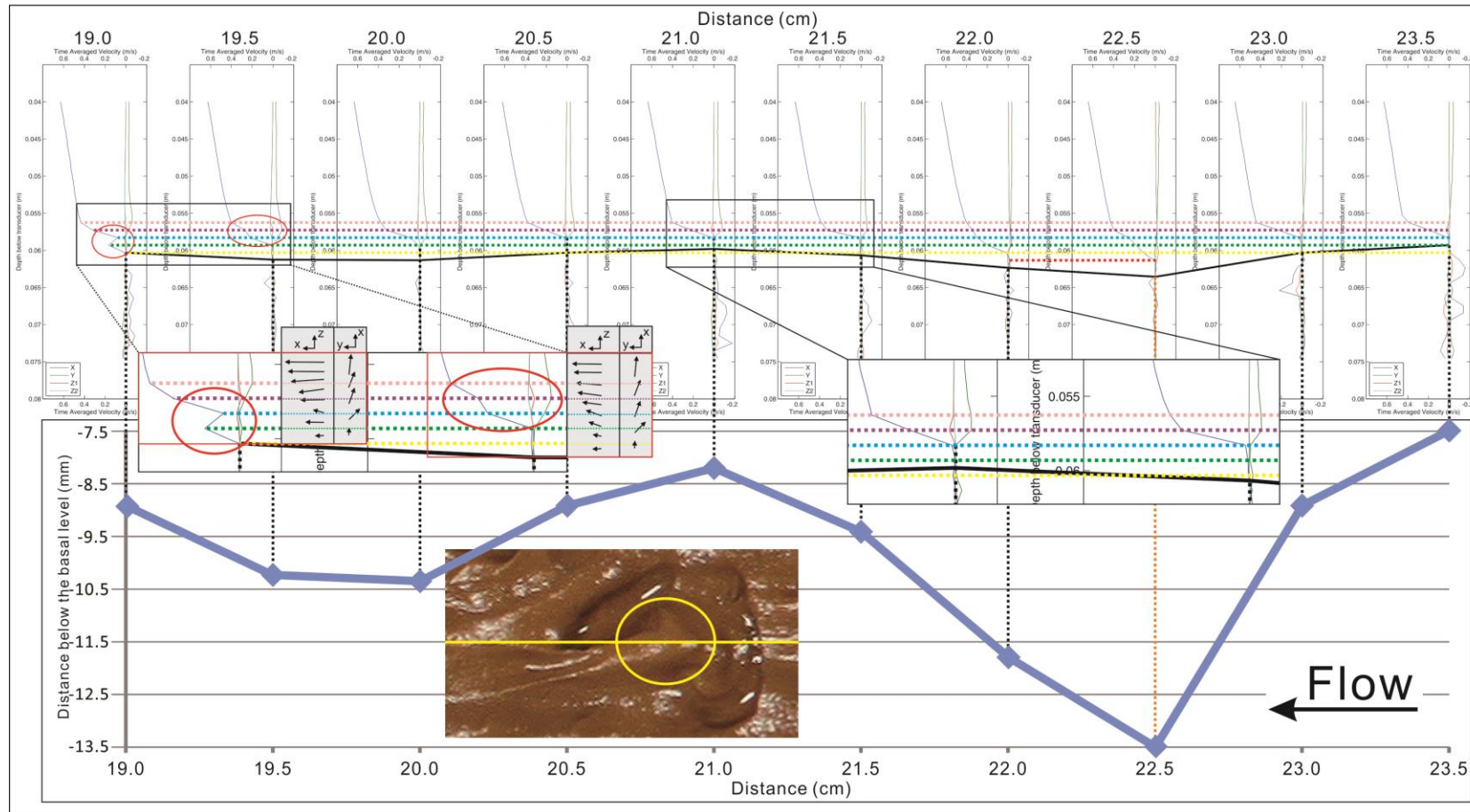


Figure 7.19 Obstacle marks. The dashed line divided the water into several layers and the coloured ellipses tag different features of the flow profiles, which will be discussed in detail in the text. Flow is from right to left. This sampling area is numbered as 8.65-1, which can be found in Figure 7. 2. The gray boxes with arrows refer to the overhead view (x-y) and the side view (x-z) of the changes of flow direction with increasing height from the bottom.

7.4 Discussion

The flow field above major four kinds of erosional bedforms has been described in this chapter. From the experimental results, some commonalities could be observed in the flow structures among the eroded features.

All the sampling areas could be divided into 3 sections along a streamwise axis: the upstream part ahead of the erosional feature, the part of principal depression of the erosional features, and the downstream area in the rear of the erosional features (Figure 7.20). For all features, the zones where the most physical alteration in the flow velocity structure occurred are within the principal depressions. From upstream to the downstream, the principal depression could be further divided into the forepart, the deepest part and the back end (Figure 7.20). Vertically, the flow field could be divided into 3 primary layers with increasing of height from the bottom on the basis of different characteristics of the near-bed flow structures and the changing rate of the longitudinal flow velocity: the inner layer (including the near-bed sublayer, the shear layer) and the outer layer. Among these, the shear layer is the most active layer (Figure 7.21).

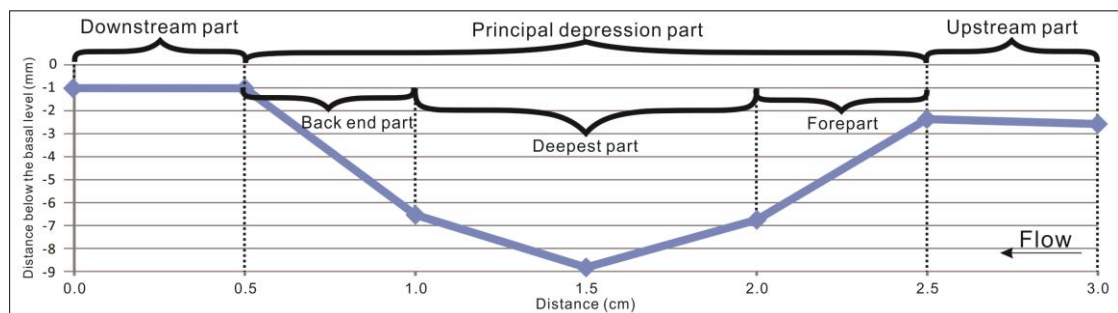


Figure 7.20 Subsection along longitudinal section of erosion features.

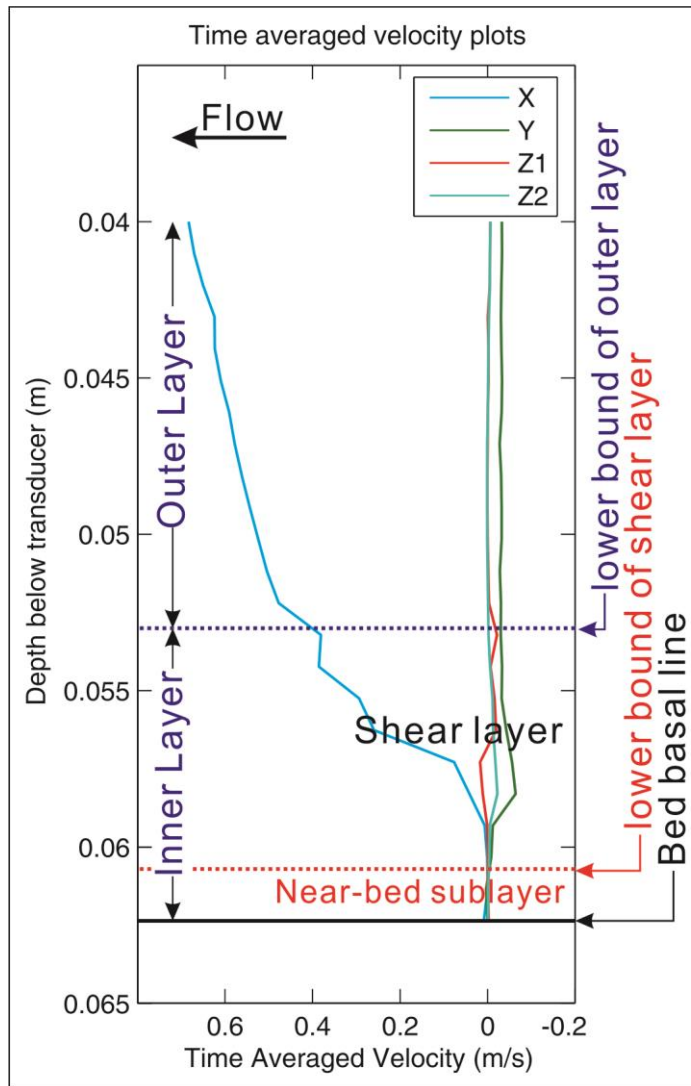


Figure 7.21 Vertical layering of flow field.

7.4.1 General flow pattern above potholes in experiments

The flow over the upstream area of the potholes demonstrated simple condition. If a near-bed sublayer could be distinguished, the flow velocity components towards all directions were close to zero. Once the flow entering into the shear layer, the longitudinal velocity grew positively with increasing of the height and reached a relative higher velocity, normally $0.6 - 0.8 \text{ ms}^{-1}$ in the current experiments, when the height reached the lower boundary of the outer layer. Meanwhile, the increasing rate of the longitudinal flow velocity reached its peak in this layer. In the shear layer, the transverse velocity increased positively first and then decreased back to zero value around the level of the lower bound of outer layer. After the height exceeded the lower bound of outer layer, the transverse velocity would sometimes returned back to zero value or increased negatively by less than

-0.05 ms^{-1} and keep stable upward. The condition of the vertical velocity was opposite of the transverse velocity. It increased and decreased negatively first and then returned back to nearly zero value and kept stable upward (e.g. Figure 7.3: profiles 16.0 & 15.5; Figure 7.4: profile 69.5; Figure 7.7: profile 23.5).

When the flow moved into the principal hollow of potholes, the flow in the lower layer and the outer layer were usually regular and very similar with that above the upstream area. In rare cases, a small flow separation zone with very low negative velocity could be observed in the lower layer just above the bed surface (e.g. Figure 7.5: profile 53.5). The main change occurred in the shear layer. The longitudinal velocity increased with fluctuation in the shear layer. The more the thickness of the shear layer was, the more fluctuated the velocity curve was. This pattern kept consistence throughout the whole depth of the potholes, from the forepart to the back end. It fluctuated more intensely above the back end part of the pothole than the other two parts (e.g. Figure 7.4: profiles 68.0 and 67.5; Figure 7.5: profiles 53.0 to 52.0; Figure 7.7: profile 19.5). The transverse velocity demonstrated a difference above these three parts. When flow just entered into the pothole, the transverse velocity kept slightly negative in both the lower and the shear layer. In the plots of the deepest part, a wave peak of the curve of the transverse velocity could sometimes be observed in the velocity plots. The peak points to the positive direction but the value of it might not be positive, which can be nearly zero decreased from the negative velocity. The layer where this peak observed was the second higher portions in the shear layer. The curves of vertical velocity were slightly positive in the higher shear layer over the forepart of the principal depression, but changed to slightly negative above the deepest part and the back end of principal depression. Although the vertical flow changed the direction, they always remained very small.

7.4.2 General flow pattern above flutes in experiments

The flow structures over the upstream area of the flutes were distinct to those over potholes. The pattern of the longitudinal velocity is similar to those in the pothole cases, but the direction of the transverse and vertical velocity components in the lower layer were at the opposite of those over the potholes. The transverse velocity kept negative throughout the entire flow depth within the hollows of the erosional features and increased logarithmically upward which was positive in the near-bed layer in the pothole cases. The vertical velocity was small and moved upward in the near

layer that was small but moved downward in the pothole cases (e.g. Figure 7.8: profile 58.0).

In the near-bed layer above the forepart of the flutes, there was a small longitudinal flow zone right above the bottom in streamwise direction. The flow increased and then decreased back to zero until the height reaches the lower bound of the shear layer while the transverse velocity fluctuated in the whole depth of near-bed layer. In the shear layer, the velocities in all directions increased approximately linearly and reached the maximum value at the height of the level of the lower bound of the outer layer. In the shear layer, the longitudinal and vertical velocities were positive and the transverse velocity was negative. In this layer, the increasing rate of velocities in all 3 directions was much higher than that in the other layer. Keeping going upward, the longitudinal velocity increased slowly and the other two velocity components decreased gradually and returned back to zero (e.g. Figure 7.9: profile 47.0; Figure 7.11: profile 55.5).

Above the deepest part of the flutes, the longitudinal flow increased from the bottom to the lower bound of the shear layer approximately exponentially, whilst the transverse velocity fluctuated negatively as happened above the forepart of the flutes, and the vertical velocity was slightly negative, and increased and then decreased to zero when the height reached the lower bound of the shear layer. Above the height of the lower bound of the shear layer, the structures of velocity in all 3 directions were almost the same as that in forepart case (e.g. Figure 7.9: profile 46.5; Figure 7.11: profile 55.0).

When the flow reached the back end part within the flutes, which usually was known as the stoss-side slope of the flutes, the longitudinal flow velocity became to increase with fluctuation as same as that above the same part of the potholes. This should be caused by the wall resistant effect of the stoss-side slope again. The transverse velocity profile is very similar with that in the deepest part case with the vertical velocity kept around zero value in all height (e.g. Figure 7.10: profile 5.5; Figure 7.11: profile 54.5; Figure 7.12: profile 37.5).

The velocity structure over the downstream part of the flutes was simply with the longitudinal velocity increasing logarithmically and the directions of transverse and vertical flow components were nearby zero value throughout the whole height above the bottom of the bed.

7.4.3 General flow pattern above longitudinal furrows in experiments

The key part of the longitudinal furrows is the principal depression as well. The forefront of the longitudinal furrow measured in the current experiments was located on the lee-side slope of a part of its lateral inner wall and the back end part referred to the stoss-side of a part of its lateral inner wall. To the relative long longitudinal furrows, the flow structure over the bottom of them is simple, because the bottom of them was flat. If they were not so deep, the transverse and vertical velocities above the bottom kept nearly zero (Figure 7.13).

To the relatively short longitudinal furrows like those observed in Figure 7.14 and Figure 7.15, the flow velocity structures above the foreparts of furrows did not perform regularly due to the different conditions of the sampling locations. Above the first sampling location of the principal depression of the furrows, the velocities demonstrated a bit regular, with the longitudinal and vertical velocities around zero, but the transverse velocity being positive in the near-bed sublayer. The transverse flow component increased from zero then decreased back to zero (e.g. Figure 7.14: profile 58.5; Figure 7.15: profile 46.0). With flow moving forward, the longitudinal flow increased with fluctuation again like happening in the potholes or the flutes cases. However, the difference is that in the inner layer, the transverse velocity increased positively to a high value, about 0.1 ms^{-1} , then decreased obviously. This situation did not happen in the pothole or the flutes cases (e.g. Figure 7.14: profiles 58.5, 57.0 and 56.5; Figure 7.15: profiles 45.5 and 45.0). The vertical velocity kept nearby zero all the time.

7.4.4 General flow pattern above other erosional features in experiments

Except the hummocky forms, the reversed furrows and the obstacle marks looked very similar. Owing to the similar form of them, the flow fields above them shared something in common, especially above the deepest part of the principal depressions. In the shear layer, the longitudinal flow velocity increased with fluctuation again as what happened above the deepest parts and the back end parts of the potholes, flutes, and longitudinal furrows. That was still because the shallow width of the furrow that brought the wall resistance effect to the flow within the furrows. The vertical flow velocity barely changed, but the transverse flow velocity would alter a lot in the higher shear layer and in the lower outer. The transverse flow velocity increased negatively to the peak value at the height of the lower bound of

the outer layer and decreased sharply to stable from the bottom of the outer layer. This transverse flow pattern looked very similar with what observed at the back end of the potholes or over the forepart area of the flutes, though the other two velocity components performed a bit different in that two cases. This indicates that the transverse flow velocity will help to widen the upper opening of the erosional features from the distance slightly below the surface of the surrounding areas to the same level of the surface of the surrounding areas.

7.4.5 The classification of the flow structures above different erosion features in experimental beds

According to the flow profiles plotted using ADV data, the flow conditions over different experimental erosional features share many characteristics in common. The flow structures can be classified into following types according to the different locations on the surface of erosional features (Figure 7.22 and Table 7.1):

1. Flow structures above the relatively flat surface, such as the upstream part, downstream part, and the plane bottom of the longitudinal furrows, were in simple condition. The typical flow structures are shown by Figure 7.22 A-1 and A-2. The features of this flow structures are that: a. The near-bed sublayer, which was usually observed in the principal depression of the erosional features, was missing. b. The longitudinal flow component usually increased logarithmically directly from the bed surface with height above the height. Within the shear layer, the increasing rate of it was high and it could reach 0.6 ms^{-1} before entering into the outer layer. c. The peak value of the transverse velocity presented in the shear layer but the magnitude was usually no greater than 0.1 ms^{-1} . It decreased to nearly zero value in the outer layer. d. The direction of the transverse velocity varies in the shear layer. It was mainly negative in the shear layer of above the upstream part of potholes and flutes (e.g. Figure 7.22 A-1; Figure 7.5: profiles 54.0 ad 54.5; Figure 7.7: profiles 23.0 and 23.5; Figure 7.8: profiles 57.5 and 58.0; Figure 7.9: profiles 47.5 to 48.5). It presented positive above the plane part of reversed furrow and hummocky forms (e.g. Figure 7.22 A-2; Figure 7.16: profiles 28.5 and 29.0; Figure 7.17: profiles 28.5 and 29.5; Figure 7.18: profiles 27.0, 27.5 and 24.0 to 25.0). e. The flow transportation pattern over these plane surfaces shows that the flow slightly deviated from the downstream direction towards right hand side or left hand side by a few degrees in the near-bed sublayer and eventually rotated back to the downstream direction in the outer layer.

2. Above the lee-side slope and the deep part of some potholes, small longitudinal flow separation cells can be observed (e.g. Figure 7.22 B; Figure 7.4: profile 68.0; Figure 7.5: profile 53.5; and Figure 7.6: profile 22.5). This indicates that once the flow entered into the pothole, a small flow separation zone occurred above the proximal end, with the very small velocity which was no bigger than 0.05 ms^{-1} . In the outer layer, the flow conditions were similar with that above the upstream part, with logarithmically increasing longitudinal component, slightly negative transverse component and tiny positive vertical components in the shear layer. The flow pattern was that there was a separation cell in the near-bed sublayer. With increasing height, the flow direction changed a few degrees to right hand side and then rotated anti-clockwise back to the downstream direction.

3. In the deepest part of the depressions of the erosional features, the flow structures were relatively complex (Figure 7.22 C-1 and C-2). In the near-bed sublayer, the velocities were close to zero. The longitudinal flow increased either in logarithmic profiles (e.g. Figure 7.22 C-1; Figure 7.6: profiles 54.5 to 55.5; Figure 7.8: profile 56.5) or with fluctuation (e.g. Figure 7.22 C-2; Figure 7.7: profile 20.0; Figure 7.14: profile 58.5; Figure 7.15: profiles 44.5 to 45.5) with increasing height from the bottom. The feature of this flow pattern is that the peak of the transverse velocity occurred in the higher shear layer or lower outer layer and the direction of it was positive. The vertical component of the velocity was close to zero value in this case. No matter what form the flow profiles look like, the transportation pattern of the flow is that the flow is close to zero in the near-bed sublayer, moved towards the downstream and deviated to left hand side by a few degrees in the shear layer and rotated clockwise to the mainly downstream direction in the outer layer.

4. The flow structures above the stoss-side slope of different erosional features can be divided into two types according to the conditions of the longitudinal and transverse velocities in the near bottom and the shear layers.

The first kind is that the longitudinal component increased with fluctuation with negative transverse velocity in the lower and shear layers (Figure 7.22 D-1; Figure 7.4: profiles 67.5; Figure 7.5: profile 52.5; Figure 7.11: profiles 54.0 to 55.5; Figure 7.14: profile 58.0). The flow direction changed from directly downstream-ward in the near-bed layer to right hand side by a few degrees in the middle portions of the shear layer and returned back to the downstream direction in the higher shear layer with greater velocity. In the

outer layer, the flow moved mainly towards the downstream. In this case, the vertical component slightly increased negatively in the lower outer layer and decreased back to zero with increasing height. This changed the flow direction slightly downward in the lower outer layer.

The second case of flow pattern is that there was only positive longitudinal component in the lower layer. The peak of the transverse velocity appeared in the higher shear layer or lower outer layer (Figure 7.22 D-2; Figure 7.5: profile 52.0; Figure 7.12: profiles 37.0, 37.5, 39.0 and 39.5; Figure 7.16: profiles 27.5; Figure 7.17: profiles 27.5). In this case, in the near-bed layer and the lower shear layer, the flow moved directly towards the downstream. In the higher shear layer or lower outer layer, the flow deviated a few degrees to right hand side accompanied by small down-welling. Once entering into the rest of the outer layer, the flow rotated anti-clockwise back to mainly downstream-ward.

The changes of the flow structures above all the erosional features occurred mainly within the shear layer or sometimes the lower outer layer, the thickness of which was usually about 1 cm thick over the bottom of the experimental erosional features. This thickness covered the depths of the most principal depressions of the erosional features. In this range of height, the flow velocities always contained transverse components, no matter which direction it moved towards. This probably contributed to the lateral erosion of the erosional features. The spiral transportation pattern of the resultant vortices might induce the incision of the principal depressions of the erosional features.

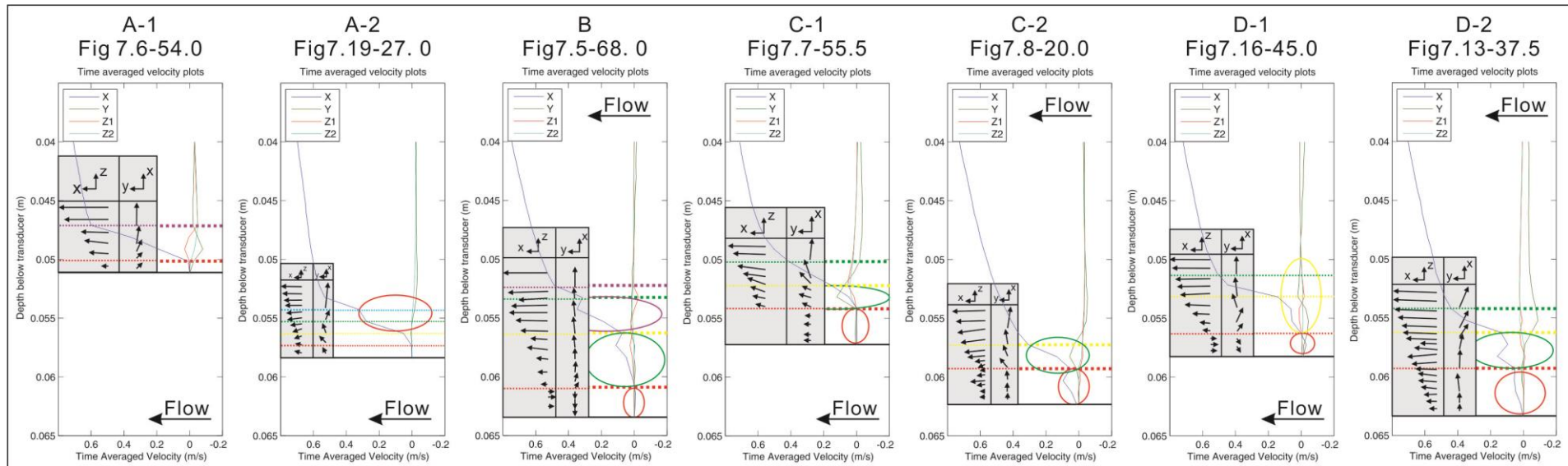


Figure 7.22 The classification of the typical flow velocity structures over the different parts of the erosional features on the experimental beds. A-1: the flow structure above the upstream part of the potholes and flutes; A-2: the flow structure above the plane part of reversed furrow and hummocky forms; B: the flow structure above the lee-side slope and the deepest part of some potholes; C-1 and C-2: the flow structure in the deepest part of the depressions of the erosional features. C-1: longitudinal velocity increases logarithmically, and C-2: longitudinal velocity increases with fluctuation; D-1 and D-2: the flow structures above the stoss-side slope of different erosional features. The ellipses refer to the obvious changes of the velocity profiles. The gray boxes with arrows refer to the overhead view (x-y) and the side view (x-z) of the changes of flow direction with increasing height from the bottom. Flow is from right to left.

Table 7.1 The features of the flow structures within and above the different erosional features in simulated bedrock beds.

| Type | Position | Characteristics of the flow components in each direction | The overall flow pattern | Examples |
|------|--|--|---|--|
| 1 | Above the relatively flat surface: the upstream part, downstream part, and the plane bottom of the longitudinal furrows. | a. The near-bed sublayer was missing. | The flow slightly deviated from the downstream direction towards right hand side or left hand side by a few degrees in the near-bed sublayer and eventually rotated back to the downstream direction in the outer layer. | Figure 7.22 A-1 and A-2. |
| | | b. The longitudinal flow component usually increased logarithmically directly from the bed surface with height. | | i. Figure 7.22 A-1; Figure 7.5: profiles 54.0 and 54.5; Figure 7.7: profiles 23.0 and 23.5; Figure 7.8: profiles 57.5 and 58.0; Figure 7.9: profiles 47.5 to 48.5; |
| | | c. The peak value of the transverse velocity presented in the shear layer (< 0.1 m/s). | | ii. Figure 7.22 A-2; Figure 7.16: profiles 28.5 and 29.0; Figure 7.17: profiles 28.5 and 29.5; Figure 7.18: profiles 27.0, 27.5 and 24.0 to 25.0 |
| | | d. The direction of the transverse velocity varies in the shear layer of above the upstream part of potholes and flutes; | | |
| | | 2. positive above the plane part of reversed furrow and hummocky forms . | | |
| 2 | In the near-bed sublayer above the lee-side slope and the deep part of some potholes. | Small longitudinal flow separation cells can be observed above the proximal end. | There was a separation cell in the near-bed sublayer. With increasing height, the flow direction changed a few degrees to right hand side and then rotated anti-clockwise back to the downstream direction. | Figure 7.22 B; Figure 7.4: profile 68.0; Figure 7.5: profile 53.5; and Figure 7.6: profile 22.5 |
| 3 | In the deepest part of the depressions of the erosional features | a. In the near-bed sublayer, the velocities were close to zero. | Flow is close to zero in the near-bed sublayer, moved towards the downstream and deviated to left hand side by a few degrees in the shear layer and rotated clockwise to the mainly downstream direction in the outer layer. | |
| | | b. The longitudinal flow increased in logarithmic profiles with increasing height from the bottom. | | Figure 7.22 C-1; Figure 7.6: profiles 54.5 to 55.5; Figure 7.8: profile 56.5 |
| | | c. The longitudinal flow increased with fluctuation with increasing height from the bottom. | | Figure 7.22 C-2; Figure 7.7: profile 20.0; Figure 7.14: profile 58.5; Figure 7.15: profiles 44.5 to 45.5 |
| | | d. The peak of the transverse velocity occurred in the higher shear layer or lower outer layer and the direction of it was positive. | | |
| | | e. The vertical component of the velocity was close to zero value. | | |
| 4 | Above the stoss-side slope of different erosional features | a. The longitudinal component increased with fluctuation with negative transverse velocity in the lower and shear layers. | The flow direction changed from directly downstream-ward in the near-bed layer to right hand side by a few degrees in the middle portions of the shear layer and returned back to the downstream direction in the higher shear layer with greater velocity. | Figure 7.22 D-1; Figure 7.4: profiles 67.5; Figure 7.5: profile 52.5; Figure 7.11: profiles 54.0 to 55.5; Figure 7.14: profile 58.0 |
| | | b. There was only positive longitudinal component in the lower layer. | | Figure 7.22 D-2; Figure 7.5: profile 52.0; Figure 7.12: profiles 37.0, 37.5, 39.0 and 39.5; Figure 7.16: profiles 27.5; Figure 7.17: profiles 27.5 |
| | | c. The peak of the transverse velocity appeared in the higher shear layer or lower outer layer. | | |

7.5 Summary

Because of the restriction and the limitation of the previous physical experiments and field observations, flow velocity structures over the erosional bedforms within and above bedrock channels have not been explored in detail. However, the experiments using modeling clay successfully reproduced a huge array of erosional features that have their equivalents in natural bedrock channels. The beds produced in these experiments are ideal reference beds for a study on the flow fields above and within a complex array of erosional features.

By operating the ADV over a latex analogue bedrock bed in the flume, a large amount of multi-dimensional flow velocity data was collected to examine the characteristics of the flow structures over the bedrock substrate. The experimental results illustrated the flow structures over principal kinds of erosion features, including the potholes, flutes, longitudinal furrows and some other erosional features with different types of superimposed features. The experimental results demonstrate relatively typical flow fields over different parts of the bedforms and different layers of the water within and above the principal depressions of the erosional features. These contributed to speculate the transportation pattern of the flow within the erosional features which is useful to interpret the suspended sediments transportation pattern with the flow. Above the specific parts of different kinds of the erosion features, the flow field shared some features in common. These common things would contribute to infer the development tendency of erosional features with time under the effect of the sediment-laden flow. Meanwhile, the interaction between the flow and the bedforms could help to understand how the bed roughness affects the flow field above it.

A range of further work could be performed to further increase the validity and range of applicability of the results. Firstly, as there were limited types of erosional features on the final bed of Exp. 8., further experiments on the substrates with different undrained shear strength need to be undertaken which could produce a wider range of erosional features. This would likely reveal more details of the flow structures over more erosional features. Secondly, in current experiments, only one transection of each erosional feature was selected to sample the flow velocity information. In the further work, the sampling locations should cover the whole area of erosional features to draw an entire picture of flow field within and around different

kinds of the erosional features. Thirdly, the model of each kind of the typical erosional features could be enlarged for running dye-tracer experiments and obtain the details of the moving track of the flow in the different erosional bedforms. This would likely reveal more detailed information of the flow structures in a model of real erosional features than the previous experiments using manmade cylinders (Alexander, 1932). Finally, devices with higher spatial and temporal sampling resolutions, such as the Laser Doppler Anemometry (LDA) or Particle image velocimetry (PIV), could be introduced in order to obtain hi-resolution data of the flow over the sediment bed.

Chapter 8

Summary and conclusion: generation of erosional features on cohesive materials with different characteristics

8.1 Introduction

The main results of the physical modelling experiments on creating erosional features on different cohesive beds are summarized here. Additionally, suggestions for future work are provided for furthering the experimental approach and examining the formative processes of erosional bedforms in more detail.

8.2 Summary of physical modelling experiments with terracotta pottery clay

Cohesive erosional features were successfully produced by flume-scale experiments 0 to 4, with terracotta pottery clay beds of different undrained shear strengths, and uniform sediment-laden flow. The results of these experiments, and those with plain flows indicate that:

1. The genesis of erosional features is dependent on whether the water flow contains sediments or not. Experiments with plain water flow demonstrated that without suspended sediment erosional features cannot form on cohesive substrates, within the range of experimental conditions examined, irrespective of how long the experimental duration is. The experimental substrate shear strengths were typical of modern sea-floor and estuarine muds, whilst basal shear stresses were in the range $1.2\text{-}7.1 \text{ Nm}^{-2}$.
2. The introduction of suspended particles, led to the initiation and development of a diverse array of erosive bedforms.
3. Under controlled boundary conditions, the erosional process and features are repeatable. Experiments 1 and 2 delivered very similar erosional features that developed at the same rate.
4. The undrained shear strength of the substrates is important in determining the erosional rate and the diversity of erosional features in cohesive beds. The lower shear strength clay bed of experiment 3 was eroded more quickly than the harder beds of experiments 1 and 2. In addition, a smaller range of erosional features was created in the lower shear strength substrate of experiment 3.

5. The erosional features produced by these experiments exhibit many similarities with those observed in bedrock rivers, including potholes, furrows and flutes. These flutes do exhibit some similarities with those produced experimentally in plaster-of-Paris and clay substrates (Allen, 1969, 1971a, 1982), but they do not grow to the sizes observed in previous work, nor do they dominate the bed surface as previously observed on cohesive substrates. In addition, the flutes are much simpler features than those observed in plaster-of-Paris without inner lateral furrows and rims on both sides, and rarely exhibiting median ridges. The erosional features observed in the experimental modelling clay beds normally contains some secondary structures by the lateral rims, such as the external furrows, which are missing in the natural bedrock channels, but are visible in the cohesive substrates (Allen, 1971a, 1982; Richardson and Carling, 2005). .

6. The experiments suggest that there is a maximum depth of erosion for individual bedforms, in sharp contrast to the plaster-of-Paris experiments of Allen (1971a) which were not erosion limited since they exhibited a dissolution process. Beds in the present experiments were planed off to a certain depth below the adjacent false floor, where they were covered (experiments 1-3) by sand, or ceased to undergo further erosion (experiment 4). This suggests that there is a limit to the depth to which particles can actively abrade the substrate, though in natural systems gradual deflation of the entire substrate can continue dependent on the flux rate of abrasive particles (e.g., Egholm et al., 2013).

8.3 Summary of physical modelling experiments with modelling clay

Experiments 6 to 8, utilised modelling clay with different undrained shear strengths, and uniform sediment-laden flow. A diverse array of erosional features were produced that were highly analogous to bedrock sculpted forms, and their initiation and evolution were examined. The results of these experiments demonstrate that:

1. Modelling clay is an excellent substrate for simulating analogue bedrock channel erosion in experiments of this scale (flow depths of ~15 cm, and basal shear stresses of 1.0 to 7.0). The experiments succeeded in producing bedforms that were highly analogous to bedrock river bedforms. In total, more than 40 kinds of erosional features were reproduced in the experiments.

2. The diversity of erosional bedforms in the experimental beds documents that most, if not all, bedrock sculpted forms can probably be formed solely as a result of abrasion, since there was no cavitation or plucking occurring in the experiments.

3. The genesis and evolution of natural bedrock bedforms can be inferred from the development process of different erosional features on the experimental modelling clay beds. The evolution processes of more than 40 types of erosional features have been revealed.

4. The optimal development of features analogous to erosive bedrock bedforms is highly sensitive to experimental conditions. An undrained shear strength of the modelling clay of 7 to 8 kPa proved most effective for the flow and concentration conditions applied (mean velocity of 0.9 ms^{-1} ; basal shear stress of $4.5\text{-}7.0 \text{ Nm}^{-2}$, suspended sediment concentration ranging from 0.1% to 0.15%). Presumably, the inter-relationship between substrate strength and basal shear stress, and associated parameters such as the impact velocity of suspended grains, suggests that there is an optimal phase space for analogue modelling of erosional bedforms depending on the scale at which the experiments are run.

5. There appears to be a continuum between mud-bed erosion and bedrock erosion, at least for those features that are formed primarily by abrasion rather than fluid-stressing. The present work with multiple substrates demonstrates that under certain conditions all the bedforms were characteristic of bedrock rivers, whilst some bedform assemblages a little more representative of mud-bed erosion could be formed under other flow and bed parameters.

8.4 Summary of flow velocity measurement over bedrock bedforms using ADV

After obtaining a feasible approach to simulate bedrock erosion the final experimental bed was recreated using a latex rubber model. This enabled flow velocity measurements to be made over bedrock bedform features using a profiling ADV. The interpretation of the velocity data illustrated that:

1. The flow velocity data enabled both the internal and external flow dynamics of these erosive bedforms to be assessed for the first time under controlled conditions.

2. The flow structures shared certain characteristics over specific parts of bedforms, for example the flows over the stoss-side slopes of flutes

and exit furrows of potholes showed similar behaviour. A more detailed study examining the interaction between the flow and bedforms could also enhance understanding of how the bed roughness affects the flow field above it.

8.5 Conclusion

1. Abrasion on experimental beds only occurs under the introduction of particles into the flow as bedload and suspended load. Fluid stressing by clear water cannot initialize the erosive bedforms on cohesive substrates.
2. Different features for the same shear stress and shear strength suggest that shear strength is only one of a number of key bed properties.
3. Shear strength with a given material determines the erosional rate and diversity of erosional features in cohesive beds. However, above a certain threshold, experiments ended up with similar products.
4. Modelling clay with medium shear strength (7 to 8 kPa) is an optimal substrate for simulating bedrock bedform erosion under abrasion of this scale (mean velocity of 0.9 ms^{-1} ; basal shear stress of $4.5\text{-}7.0 \text{ Nm}^{-2}$, suspended sediment concentration ranging from 0.1% to 0.15%) and delivers most diversity of erosional features.
5. The huge array of erosional features generated by the present experiments demonstrate that the bedrock sculpted forms can probably be produced solely as a result of abrasion.
6. A continuum between cohesive erosion and bedrock erosion can be inferred from the current experimental results. Furthermore, the genesis and evolution of bedrock bedforms can also be ascertained from the evolution of the bedforms on cohesive mud beds.
7. The flow velocity data collected over the analogue bedrock substrate enabled the discovery of flow structures within and above the erosional bedforms for the first time, and contribute to the exploration of the interactions between the flow field and erosional bedforms, at least in controlled flume-scale conditions.

8.6 Perspectives on future work

The current study has demonstrated that bedrock bedforms can be successfully simulated under laboratory conditions, using appropriate

cohesive substrates and flow conditions. There is considerable scope to extend and build upon these techniques by:

1. Extending the range of bed substrate yield strengths to assess the role of higher and lower yield strengths on bedform assemblages, and to further assess the nature of the apparent continuum of bedforms between mud-bed and bedrock substrates. Such work would identify whether additional bedform types may emerge that were not captured by the present experimental conditions.

2. Assessing the nature and importance of flow conditions whilst maintaining constant substrate conditions, thus examining the other component of the possible phase space of optimal conditions for erosive bedform development. In particular, velocity, flow depth, and slope could be altered whilst maintaining constant suspended sediment concentration. Such a programme would enable identification of the controlling flow parameter(s), and assess the relative importance of parameters such as mean and maximum flow velocity, shear velocity, and basal shear stress.

3. Examine the role of sediment concentration on bedform development rate, and whether at higher values concentration begins to alter the nature and type of bedforms that develop.

4. Assess whether the size of abrasive particles plays a major role, and whether there is an optimal size relative to the key controlling parameter(s) of the flow.

5. Utilise a wider flume in order to confirm that the observed broad linear erosional gutters are related to wall effects, and if so to study beds for longer, in their central axis, without these features developing. A wider flume and associated changes in flow condition would also be able to assess the scale invariance of these bedforms, and in particular to assess if larger features can be formed.

6. Assess bedform flow dynamics in more detail. The work to date has demonstrated the technique and its applicability, but much remains to be known about how bedforms interact with each other, and what the temporal and spatial velocity flow fields look like. There is an opportunity to assess these aspects in the same way as has long been undertaken for aggradational bedforms. Some of this work can be undertaken at the present small-scale, however, bedform development in larger, wider flumes may enable larger features to be formed (see point above), and thus facilitate other methodologies such as particle image velocimetry that can better

assess spatial and temporal flow variations, albeit only for flows external to the bedforms.

7. Examine the evolution of flow fields within erosive bedforms by measuring the flow field at successive time increments. In order to achieve this a different approach would be required since the method utilised here is only capable of assessing the final form. Utilisation of a technique such as laser scanning would enable detailed bed elevations to be recorded at multiple time periods, although there may be issues related to areas of bedforms that are influenced by overhanging lips. These digital elevation models could then be reproduced using three-dimensional printing, enabling flow measurements to be obtained. Such data would also allow the developing interaction between bedforms and the main flow to be examined as a function of time.

List of References

- Al-Nassar, Y., Al-Jalal, A., Khan, M., and Al-Kaabi, S., 2006, Functional Dependence of Ultrasonic Speed in Water on Salinity and Temperature: *NDT. net*, v. 11, no. 6, p. 1-5.
- Albayrak, I., and Lemmin, U., 2011, Secondary Currents and Corresponding Surface Velocity Patterns in a Turbulent Open-Channel Flow over a Rough Bed: *Journal of Hydraulic Engineering*, v. 137, p. 1318-1334.
- Alexander, H., 1932, Pothole erosion: *The Journal of Geology*, v. 40, p. 305-337.
- Alexander, J., Bridge, J., Cheel, R., and Leclair, S., 2001, Bedforms and associated sedimentary structures formed under supercritical water flows over aggrading sand beds: *Sedimentology*, v. 48, no. 1, p. 133-152.
- Alexander, J., McLelland, S., Gray, T., Vincent, C., Leeder, M., and Ellett, S., 2008, Laboratory sustained turbidity currents form elongate ridges at channel mouths: *Sedimentology*, v. 55, no. 4, p. 845-868.
- Allen, J., 1965, Scour marks in snow: *Journal of Sedimentary Research*, v. 35, no. 2, p. 331-338.
- , 1968, *Current ripples: their relation to patterns of water and sediment motion*, Amsterdam: North-Holland Publishing Company, 433 p.
- , 1969, Erosional current marks of weakly cohesive mud beds: *Journal of Sedimentary Research*, v. 39, no. 2, p. 607-623.
- , 1971a, Transverse erosional marks of mud and rock: their physical basis and geological significance: *Sedimentary Geology*, v. 5, no. 3, p. 167-385.
- , 1971b, Bed forms due to mass transfer in turbulent flows: a kaleidoscope of phenomena: *Journal of Fluid Mechanics*, v. 49, no. 01, p. 49-63.
- , 1973a, Development of flute-mark assemblages, 1. Evolution of pairs of defects: *Sedimentary Geology*, v. 10, no. 3, p. 157-177.
- , 1973b, Phase differences between bed configuration and flow in natural environments, and their geological relevance: *Sedimentology*, v. 20, no. 2, p. 323-329.
- , 1974, *Sedimentology of the Old Red Sandstone (Siluro-Devonian) in the Cleve Hills area, Shropshire, England*: *Sedimentary Geology*, v. 12, no. 2, p. 73-167.
- , 1975, Development of flute-mark assemblages, 2. Evolution of trios of defects: *Sedimentary Geology*, v. 13, no. 1, p. 1-26.
- , 1982, *Sedimentary structures: their character and physical basis*, Elsevier Scientific, v. 30B, 663 p.
- , 1987, Streamwise erosional structures in muddy sediments, Severn Estuary, southwestern UK: *Geografiska Annaler. Series A. Physical Geography*, p. 37-46.
- , 1990, The Severn Estuary in southwest Britain: its retreat under marine transgression, and fine-sediment regime: *Sedimentary Geology*, v. 66, no. 1-2, p. 13-28.
- Ängeby, O., 1951, Pothole erosion in recent waterfalls, Royal University of Lund, Sweden, Department of Geography, 34 p.

- Ashley, G., Renwick, W., and Haag, G., 1988, Channel form and processes in bedrock and alluvial reaches of the Raritan River, New Jersey: *Geology*, v. 16, no. 5, p. 436-439.
- Baas, J., 1994, A flume study on the development and equilibrium morphology of current ripples in very fine sand: *Sedimentology*, v. 41, no. 2, p. 185-209.
- Baas, J., and Best, J., 2002, Turbulence modulation in clay-rich sediment-laden flows and some implications for sediment deposition: *Journal of Sedimentary Research*, v. 72, no. 3, p. 336-340.
- , 2008, The dynamics of turbulent, transitional and laminar clay - laden flow over a fixed current ripple: *Sedimentology*, v. 55, no. 3, p. 635-666.
- Baas, J., Best, J., Peakall, J., and Wang, M., 2009, A phase diagram for turbulent, transitional, and laminar clay suspension flows: *Journal of Sedimentary Research*, v. 79, no. 4, p. 162-183.
- Baas, J., Oost, A., Sztano, O., Boer, P., and Postma, G., 1993, Time as an independent variable for current ripples developing towards linguoid equilibrium morphology: *Terra Nova*, v. 5, no. 1, p. 29-35.
- Baker, V., 1973, Erosional forms and processes for the catastrophic Pleistocene Missoula floods in eastern Washington: *Fluvial Geomorphology*, p. 123-148.
- , 1978, Large-scale erosional and depositional features of the Channeled Scabland: *The Channeled Scabland*, v. 1, p. 81-115.
- Baker, V., and Kale, V., 1998, The role of extreme floods in shaping bedrock channels: *Geophysical Monograph*, American Geophysical Union, v. 107, p. 153-166.
- Baker, V., and Pickup, G., 1987, Flood geomorphology of the Katherine Gorge, Northern Territory, Australia: *Geological Society of America Bulletin*, v. 98, no. 6, p. 635-646.
- Barbhuiya, A., and Talukdar, S., 2010, Scour and three dimensional turbulent flow fields measured by ADV at a 90 degrees horizontal forced bend in a rectangular channel: *Flow measurement and Instrumentation*, v. 21, no. 3, p. 312-321.
- Barton, N., and Choubey, V., 1977, The shear strength of rock joints in theory and practice: *Rock mechanics*, v. 10, no. 1-2, p. 1-54.
- Bennett, R., Freeland, G., Lambert, D., Sawyer, W., and Keller, G., 1980, Geotechnical properties of surficial sediments in a mega-corridor: US Atlantic continental slope, rise, and deep-sea basin: *Marine Geology*, v. 38, no. 1, p. 123-140.
- Bennett, R., and Keller, G., 1973, Physical properties evaluation, *in* van Andel, T. H., Heath, G. R., et al., ed., *Initial Reports of the Deep Sea Drilling Project*, Volume 16, p. 513-520.
- Bennett, S., and Best, J., 1995a, Mean flow and turbulence structure over fixed, two - dimensional dunes: Implications for sediment transport and bedform stability: *Sedimentology*, v. 42, no. 3, p. 491-513.
- , 1995b, Particle size and velocity discrimination in a sediment-laden turbulent flow using phase Doppler anemometry: *Journal of Fluids engineering*, v. 117, no. 3, p. 505-511.
- , 1995c, An experimental study of flow, bedload transport and bed topography under conditions of erosion and deposition and comparison with theoretical models: *Sedimentology*, v. 42, no. 1, p. 117-146.

- Best, J., 1992, On the entrainment of sediment and initiation of bed defects: insights from recent developments within turbulent boundary layer research: *Sedimentology*, v. 39, no. 5, p. 797-811.
- , 1993, On the interactions between turbulent flow structure, sediment transport and bedform development: some considerations from recent experimental research: *Turbulence: Perspectives on Flow and sediment transport*, p. 61-92.
- , 1996, The fluid dynamics of small-scale alluvial bedforms, *in* Carling, P., and Dawson, M., eds., *Advances in fluvial dynamics and stratigraphy*, Chichester, John Wiley and Sons, p. 530.
- Best, J., and Ashworth, P., 1994, A high-resolution ultrasonic bed profiler for use in laboratory flumes: *Journal of Sedimentary Research*, v. 64, no. 3a, p. 674-675.
- Best, J., Bennett, S., Bridge, J., and Leeder, M., 1997, Turbulence modulation and particle velocities over flat sand beds at low transport rates: *Journal of hydraulic engineering*, v. 123, no. 12, p. 1118-1129.
- Best, J., Kirkbride, A., and Peakall, J., 2001, Mean Flow and Turbulence Structure of Sediment - Laden Gravity Currents: New Insights using Ultrasonic Doppler Velocity Profiling: *Particulate gravity currents*, p. 157-172.
- Best, J., and Leeder, M., 1993, Drag reduction in turbulent muddy seawater flows and some sedimentary consequences: *Sedimentology*, v. 40, no. 6, p. 1129-1137.
- Bilaniuk, N., and Wong, G., 1993, Speed of sound in pure water as a function of temperature: *The Journal of the Acoustical Society of America*, v. 93, no. 3, p. 1609-1612.
- Biron, P., Lane, S., Roy, A., Bradbrook, K., and Richards, K., 1998, Sensitivity of bed shear stress estimated from vertical velocity profiles: The problem of sampling resolution: *Earth Surface Processes and Landforms*, v. 23, no. 2, p. 133-139.
- Blank, H., 1958, Pothole grooves in the bed of the James River, Mason County, Texas: *Texas Journal of Science*, v. 10, p. 292-301.
- Blumberg, P., and Curl, R., 1974, Experimental and theoretical studies of dissolution roughness: *Journal of Fluid Mechanics*, v. 65, no. part 4, p. 735-751.
- Bouma, A., and Moore, J., 1975, Physical properties of deep-sea sediments from the Philippine Sea and Sea of Japan: *Initial Reports of the Deep Sea Drilling Project*, v. 31, p. 535-568.
- Boyce, R., 1977, Deep Sea Drilling Project procedures for shear strength measurement of clayey sediment using modified Wykeham Farrance laboratory vane apparatus, *Initial Reports of the Deep Sea Drilling Project*, 1059-1068 p.
- Bretz, J., 1924, The Dalles Type of River Channel: *The Journal of Geology*, v. 32, no. 2, p. 139-149.
- Bridge, J., 2008, *Earth surface processes, landforms and sediment deposits*, Cambridge University Press, 830 p.
- , 2009, *Rivers and floodplains: forms, processes, and sedimentary record*, Wiley, 504 p.
- Bridge, J., and Best, J., 1988, Flow, sediment transport and bedform dynamics over the transition from dunes to upper - stage plane beds:

- implications for the formation of planar laminae: *Sedimentology*, v. 35, no. 5, p. 753-763.
- Bryant, E., 2008, *Tsunami: the underrated hazard*, Praxis Publishing, UK and Cambridge University Press, 330 p.
- Bryant, W., Bennett, R., and Katherman, C., 1981, Shear strength, consolidation, porosity, and permeability of oceanic sediments: *The sea*, v. 7, p. 1555-1616.
- Burland, J., 1990, On the compressibility and shear strength of natural clays: *Geotechnique*, v. 40, no. 3, p. 329-378.
- Cao, Z., and Carling, P., 2005, Further perspectives on the evolution of bed material waves in alluvial rivers: *Earth Surface Processes and Landforms*, v. 30, no. 1, p. 115-120.
- Cao, Z., Carling, P., and Oakey, R., 2003, Flow reversal over a natural pool-riffle sequence: a computational study: *Earth Surface Processes and Landforms*, v. 28, no. 7, p. 689-705.
- Cao, Z., Pender, G., and Carling, P., 2006, Shallow water hydrodynamic models for hyperconcentrated sediment-laden floods over erodible bed: *Advances in Water Resources*, v. 29, no. 4, p. 546-557.
- Carling, P., and Breakspear, R., 2006, Placer formation in gravel-bedded rivers: A review: *Ore Geology Reviews*, v. 28, no. 4, p. 377-401.
- Carling, P., Cao, Z., Holland, M., Ervine, D., and Babaeyan-Koopaei, K., 2002, Turbulent flow across a natural compound channel: *Water Resources Research*, v. 38, no. 12, p. 1270.
- Carling, P., Radecki-Pawlik, A., Williams, J., Rumble, B., Meshkova, L., Bell, P., and Breakspear, R., 2006a, The morphodynamics and internal structure of intertidal fine-gravel dunes: Hills Flats, Severn Estuary, UK: *Sedimentary Geology*, v. 183, no. 3-4, p. 159-179.
- Carling, P., Richardson, K., and Ikeda, H., 2005, A flume experiment on the development of subaqueous fine-gravel dunes from a lower-stage plane bed: *Journal of Geophysical Research: Earth Surface*, v. 110, no. F4, p. 1-15.
- Carling, P., and Shvidchenko, A., 2002, A consideration of the dune: antidune transition in fine gravel: *Sedimentology*, v. 49, no. 6, p. 1269-1282.
- Carling, P., and Tinkler, K., 1998, Conditions for the entrainment of cuboid boulders in bedrock streams: an historical review of literature with respect to recent investigations: *Geophysical Monograph*, American Geophysical Union, v. 107, p. 19-34.
- Carling, P., Whitcombe, L., Benson, I., Hankin, B., and Radecki-Pawlik, A., 2006b, A new method to determine interstitial flow patterns in flume studies of sub-aqueous gravel bedforms such as fish nests: *River Research and Applications*, v. 22, no. 6, p. 691-701.
- Carling, P., Williams, J., Croudace, I., and Amos, C., 2009, Formation of mud ridge and runnels in the intertidal zone of the Severn Estuary, UK: *Continental Shelf Research*, v. 29, no. 16, p. 1913-1926.
- Chassefiere, B., and Monaco, A., 1987, Geotechnical properties and sedimentological processes of the Rhône continental margin: *Marine geology*, v. 74, no. 3, p. 225-235.
- Chien, N., and Wan, Z., 1999, *Mechanics of sediment transport*, American Society of Civil Engineers, 936 p.

- Collinson, J., and Thompson, D., 1982, Sedimentary structures, Allen & Unwin London, 244 p.
- Cossu, R., and Wells, M., 2013, The evolution of submarine channels under the influence of Coriolis forces: experimental observations of flow structures: *Terra Nova*, v. 25, no. 1, p. 65-71.
- Costello, W., and Southard, J., 1981, Flume experiments on lower-flow-regime bed forms in coarse sand: *Journal of Sedimentary Research*, v. 51, no. 3, p. 849-864.
- Craig, R., Loadman, C., Clement, B., Rusello, P., and Siegel, E., Characterization and testing of a new bistatic profiling acoustic doppler velocimeter: The vectrino-ii, *in* Proceedings Current, Waves and Turbulence Measurements (CWTM), 2011 IEEE/OES 10th2011, IEEE, p. 246-252.
- Davie, J., Fenske, C., and Serocki, S., 1978, Geotechnical properties of deep continental margin soils: *Marine Georesources & Geotechnology*, v. 3, no. 1, p. 85-119.
- Debnath, K., Manik, M., and Mazumder, B., 2012, Turbulence statistics of flow over scoured cohesive sediment bed around circular cylinder: *Advances in Water Resources*, v. 41, p. 18-28.
- Demars, K., and Nacci, V., 1978, Significance of Deep Sea Drilling Project sediment physical property data: *Marine Georesources & Geotechnology*, v. 3, no. 2, p. 151-170.
- Diffendal, R., 1982, Gully, scour hole, and pothole development at the base of the Gering Formation (Miocene?), southeastern Banner County, Nebraska: *Rocky Mountain Geology*, v. 21, no. 1, p. 1-6.
- Dingman, S., 1984, Fluvial hydrology, W.H.Freeman & Co Ltd, 384 p.
- DSDP, 1969-1986, Initial Reports of the Deep Sea Drilling Project, v. Vol. 1 - Vol. 96. [EB/OL].
- Dzulynski, S., 1965, New data on experimental production of sedimentary structures: *Journal of Sedimentary Research*, v. 35, no. 1, p. 196-212.
- Dzulynski, S., and Sanders, J., 1962, Current marks on firm mud bottoms: *Transactions of the Connecticut Academy of Arts and Sciences*, v. 42, p. 57-96.
- Dzulynski, S., and Walton, E., 1965, Sedimentary features of flysch and greywackes, Elsevier, 247 p.
- Egholm, D., Knudsen, M., and Sandiford, M., 2013, Lifespan of mountain ranges scaled by feedbacks between landsliding and erosion by rivers: *Nature*, v. 498, no. 7455, p. 475-478.
- Einsele, G., Overbeck, R., Schwarz, H., and Unsold, G., 1974, Mass physical properties, sliding and erodibility of experimentally deposited and differently consolidated clayey muds (approach, equipment, and first results): *Sedimentology*, v. 21, no. 3, p. 339-372.
- Elston, E., 1917, Potholes: their variety, origin and significance: *The Scientific Monthly*, v. 5, p. 554-567.
- , 1918, Potholes: their variety, origin and significance. II: *The Scientific Monthly*, v. 6, p. 37-51.
- Embley, R., Hoose, P., Lonsdale, P., Mayer, L., and Tucholke, B., 1980, Furrowed mud waves on the western Bermuda Rise: *Geological Society of America Bulletin*, v. 91, no. 12, p. 731-740.
- Emiliani, C., 1981, The oceanic lithosphere, Harvard University Press, 1754 p.

- Emiliani, C., and Milliman, J., 1966, Deep-sea sediments and their geological record: *Earth-Science Reviews*, v. 1, no. 2, p. 105-132.
- Emrich, W., 1971, Performance study of soil sampler for deep-penetration marine borings: *Sampling of soil and rock*, p. 30-50.
- Fedele, J., and Garcia, M., 2009, Laboratory experiments on the formation of subaqueous depositional gullies by turbidity currents: *Marine Geology*, v. 258, no. 1-4, p. 48-59.
- Flood, R., 1981, Distribution, morphology, and origin of sedimentary furrows in cohesive sediments, Southampton Water: *Sedimentology*, v. 28, no. 4, p. 511-529.
- , 1983, Classification of sedimentary furrows and a model for furrow initiation and evolution: *Geological Society of America Bulletin*, v. 94, no. 5, p. 630-639.
- Foley, M., 1980, Quaternary diversion and incision, Dearborn River, Montana - Summary: *Geological Society of America Bulletin*, v. 91, no. 10, p. 576-577.
- Ford, D., and Williams, P., 1989, *Karst geomorphology and hydrology*, Unwin Hyman London, 576 p.
- Forster, A., Ellis, R., Henrich, R., Krastel, S., and Kopf, A., 2010, Geotechnical characterization and strain analyses of sediment in the Mauritania Slide Complex, NW-Africa: *Marine and Petroleum Geology*, v. 27, no. 6, p. 1175-1189.
- Francisca, F., Yun, T. S., Ruppel, C., and Santamarina, J. C., 2005, Geophysical and geotechnical properties of near-seafloor sediments in the northern Gulf of Mexico gas hydrate province: *Earth and Planetary Science Letters*, v. 237, no. 3-4, p. 924-939.
- Fredlund, D., Xing, A., Fredlund, M., and Barbour, S., 1996, The relationship of the unsaturated soil shear to the soil-water characteristic curve: *Canadian Geotechnical Journal*, v. 33, no. 3, p. 440-448.
- French, J., and Spencer, T., 1993, Dynamics of sedimentation in a tide-dominated backbarrier salt marsh, Norfolk, UK: *Marine Geology*, v. 110, no. 3-4, p. 315-331.
- Friend, P., 1965, Fluvial sedimentary structures in the Wood Bay series (Devonian) of Spitsbergen: *Sedimentology*, v. 5, no. 1, p. 39-68.
- Gardner, T., 1983, Experimental study of knickpoint and longitudinal profile evolution in cohesive, homogeneous material: *Geological Society of America Bulletin*, v. 94, no. 5, p. 664-672.
- GH, K., DN, L., and RH, B., 1979, Geotechnical properties of continental slope deposits-Cape Hatteras to Hydrographic Canyon: *Geology of Continental slopes*, v. 27, no. SEPM Spec. Publ., p. 131-151.
- Gjessing, J., 1967, Potholes in connection with plastic scouring forms: *Geografiska Annaler. Series A. Physical Geography*, p. 178-187.
- Glasser, N., and Nicholson, F., 1998, Subglacial meltwater erosion at Loch Treig: *Scottish Journal of Geology*, v. 34, no. 1, p. 7-13.
- Goodchild, M., and Ford, D., 1971, Analysis of scallop patterns by simulation under controlled conditions: *The Journal of Geology*, p. 52-62.
- Grant, G., 1997, Critical flow constrains flow hydraulics in mobile - bed streams: A new hypothesis: *Water Resources Research*, v. 33, no. 2, p. 349-358.
- Gupta, A., Kale, V., and Rajaguru, S., 1999, The Narmada River, India, through space and time: *Varieties of Fluvial Form*, p. 114-143.

- Hèuneke, H., and Mulder, T., 2011, Deep-sea sediments, Access Online via Elsevier, 750 p.
- Hancock, G., Anderson, R., and Whipple, K., 1998, Beyond power: Bedrock river incision process and form: Geophysical Monograph, American Geophysical Union, v. 107, p. 35-60.
- Hollister, C., Flood, R., Johnson, D., Lonsdale, P., and Southard, J., 1974, Abyssal furrows and hyperbolic echo traces on the Bahama Outer Ridge: *Geology*, v. 2, no. 8, p. 395-400.
- Hsu, L., Dietrich, W., and Sklar, L., 2008, Experimental study of bedrock erosion by granular flows: *Journal of Geophysical Research-Earth Surface*, v. 113, no. F2, p. 1-21.
- Hutchinson, D., 1996, Runnels, rinnenkarren, and mäanderkarren: form, classification and relationships: *Karren landforms*. Universitat de les Illes Balears, Palma de Mallorca, p. 209-223.
- Hvorslev, M., 1948, Subsurface exploration and sampling of soils for civil engineering purposes, Waterways Experiment Station Vicksburg, MS, 465 p.
- Itakura, M., and Ikeda, H., 1997, On the channel configuration plane-bed bedrock channels on the upper Obitsu River basin: *Bulletin of the Environmental Research Center, University of Tsukuba, Japan*, v. 22, p. 9-21.
- Ives, R., 1948, Plunge pools, potholes, and related features: *Rocks and Minerals*, v. 23, no. 1, p. 3-10.
- Jennings, J., 1983, Swirlholes and related bedrock river channel forms: *The Australian Geographer*, v. 15, no. 6, p. 411-414.
- Johnson, B., Barry, M., Boudreau, B., Jumars, P., and Dorgan, K., 2012, In situ tensile fracture toughness of surficial cohesive marine sediments: *Geo-Marine Letters*, v. 32, no. 1, p. 39-48.
- Johnson, J., and Whipple, K., 2007, Feedbacks between erosion and sediment transport in experimental bedrock channels: *Earth Surface Processes and Landforms*, v. 32, no. 7, p. 1048-1062.
- , 2010, Evaluating the controls of shear stress, sediment supply, alluvial cover, and channel morphology on experimental bedrock incision rate: *Journal of Geophysical Research: Earth Surface (2003–2012)*, v. 115, no. F2, p. 1-21.
- Johnson, J. P., Whipple, K. X., and Sklar, L. S., 2010, Contrasting bedrock incision rates from snowmelt and flash floods in the Henry Mountains, Utah: *Geological Society of America Bulletin*, v. 122, no. 9-10, p. 1600-1615.
- Julien, P., and Klaassen, G., 1995, Sand-dune geometry of large rivers during floods: *Journal of hydraulic engineering*, v. 121, no. 9, p. 657-663.
- Kale, V., Baker, V., and Mishra, S., 1996, Multi-channel patterns of bedrock rivers: An example from the central Narmada basin, India: *Catena*, v. 26, no. 1-2, p. 85-98.
- Kale, V., and Joshi, V., 2004, Evidence of formation of potholes in bedrock on human timescale: Indrayani river, Pune district, Maharashtra: *Current Science*, v. 86, no. 5, p. 723-726.
- Karcz, I., 1968, Fluvial obstacle marks from the wadis of the Negev (southern Israel): *Journal of Sedimentary Research*, v. 38, no. 4.

- , 1973, Reflections on the origin of small scale longitudinal stream-bed scours: *Fluvial Geomorphology*, p. 149-173.
- Keller, G., and Bennett, R., 1970, Variations in the mass physical properties of selected submarine sediments: *Marine Geology*, v. 9, no. 3, p. 215-223.
- , 1973, Sediment mass physical properties—Panama Basin and northeastern equatorial Pacific: *Initial Reports of the Deep Sea Drilling Project*, v. 16, p. 499-512.
- Kikuchi, K., Takeda, Y., Obayashi, H., Tezuka, M., and Sato, H., 2006, Measurement of LBE flow velocity profile by UDVP: *Journal of nuclear materials*, v. 356, no. 1, p. 273-279.
- King, P., 1927, Corrosion and Corrasion on Barton Creek, Austin, Texas: *The Journal of Geology*, p. 631-638.
- Kirby, R., and Parker, W., 1983, Distribution and behavior of fine sediment in the Severn Estuary and Inner Bristol Channel, UK: *Canadian Journal of Fisheries and Aquatic Sciences*, v. 40, p. 83-95.
- Kobor, J., and Roering, J., 2004, Systematic variation of bedrock channel gradients in the central Oregon Coast Range: implications for rock uplift and shallow landsliding: *Geomorphology*, v. 62, no. 3–4, p. 239-256.
- Kor, P., and Cowell, D., 1998, Evidence for catastrophic subglacial meltwater sheetflood events on the Bruce Peninsula, Ontario: *Canadian Journal of Earth Sciences*, v. 35, no. 10, p. 1180-1202.
- Kor, P., Shaw, J., and Sharpe, D., 1991, Erosion of bedrock by subglacial meltwater, Georgian Bay, Ontario: a regional view: *Canadian Journal of Earth Sciences*, v. 28, no. 4, p. 623-642.
- Kostaschuk, R., and Villard, P., Turbulent sand suspension over dunes, *in* *Proceedings of the 6th International Conference on Fluvial Sedimentology*, edited by ND Smith, and J. Rogers 1999, p. 3-14.
- Koyama, T., and Ikeda, H., 1998, Effect of riverbed gradient on bedrock channel configuration: a flume experiment: *Proceedings of the Environmental Research Center*, v. 23, p. 25-34.
- Kuhnle, R., and Southard, J., 1988, Bed load transport fluctuations in a gravel bed laboratory channel: *Water Resources Research*, v. 24, no. 2, p. 247-260.
- Kunert, M., and Coniglio, M., 2002, Origin of vertical shafts in bedrock along the Eramosa River valley near Guelph, southern Ontario: *Canadian Journal of Earth Sciences*, v. 39, no. 1, p. 43-52.
- Lane, S., Biron, P., Bradbrook, K., Butler, J., Chandler, J., Crowell, M., McLelland, S., Richards, K., and Roy, A., 1998, Three - dimensional measurement of river channel flow processes using acoustic Doppler velocimetry: *Earth Surface Processes and Landforms*, v. 23, no. 13, p. 1247-1267.
- Leeder, M., 1982, *Sedimentology: process and product*, Chapman & Hall, 360 p.
- Lhermitte, R., and Lemmin, U., 1994, Open-channel flow and turbulence measurement by high-resolution Doppler sonar: *Journal of Atmospheric and Oceanic Technology*, v. 11, no. 5, p. 1295-1308.
- Lohrmann, A., Cabrera, R., and Kraus, N., Acoustic-Doppler velocimeter (ADV) for laboratory use, *in* *Proceedings Fundamentals and*

- advancements in hydraulic measurements and experimentation 1994, ASCE, p. 351-365.
- Lonsdale, P., Spiess, F., and Mudie, J., 1973, Erosional furrows across the abyssal Pacific floor: EOS (American Geophysical Union Transactions), v. 54, p. 1110 (abstract).
- Lorenc, M., Barco, P., and Saavedra, J., 1994, The evolution of potholes in granite bedrock, W Spain: Catena, v. 22, no. 4, p. 265-274.
- Lugt, H., 1983, Vortex flow in nature and technology, New York, Wiley-Interscience, Translation., 305 p.
- Müller, A., and Gyr, A., 1986, On the vortex formation in the mixing layer behind dunes: Journal of hydraulic research, v. 24, no. 5, p. 359-375.
- Macdonald, H., 2010, Flutes, megaflutes and erosional bedforms: a reappraisal of their dynamics: University of Leeds, 275 p.
- Maxson, J., 1940, Fluting and faceting of rock fragments: The Journal of Geology, p. 717-751.
- Maxson, J., and Campbell, I., 1935, Stream fluting and stream erosion: The Journal of Geology, p. 729-744.
- McBride, E., 1962, Flysch and associated beds of the Martinsburg Formation (Ordovician), central Appalachians: Journal of Sedimentary Research, v. 32, no. 1, p. 39-91.
- McLelland, S., Ashworth, P., Best, J., and Livesey, J., 1999, Turbulence and secondary flow over sediment stripes in weakly bimodal bed material: Journal of hydraulic engineering, v. 125, p. 463-473.
- McManus, M., and Woodson, C., 2012, Plankton distribution and ocean dispersal: The Journal of Experimental Biology, v. 215, no. 6, p. 1008-1016.
- Montgomery, D., and Gran, K., 2001, Downstream variations in the width of bedrock channels: Water Resources Research, v. 37, no. 6, p. 1841-1846.
- Morgan, A., 1970, Late Weichselian potholes near Wolverhampton, England: Journal of Glaciology, v. 9, p. 125-133.
- Nelson, P., and Seminara, G., 2012, A theoretical framework for the morphodynamics of bedrock channels: Geophysical Research Letters, v. 39, no. 6, p. L06408.
- Nemec, W., Lorenc, M., and Saavedra, J., 1982, Potholed granite terrace in the Río Salor valley, western Spain: a study of bedrock erosion by floods: Tecniterrae, v. 50, p. 6-21.
- Neuendorf, K., Mehl Jr, J., and Jackson, J., 2005, Glossary of Geology, 5th edition, Alexandria, American Geological Institute, 779 p.
- Nicholson, D., Geotechnical Parameters for Three Deep Ocean Study Areas, *in* Proceedings Disposal of Radioactive Waste In Seabed Sediments: Proceedings of an international conference 1989.
- Nikora, V., and Goring, D., 1998, ADV measurements of turbulence: Can we improve their interpretation?: Journal of hydraulic engineering, v. 124, no. 6, p. 630-634.
- Ollgaard, J., Slutter, R., and Fisher, J., 1971, Shear strength of stud connectors in lightweight and normal-weight concrete: AISC Engineering Journal, v. 8, no. 2, p. 55-64.
- Packman, A., Brooks, N., and Morgan, J., 2000, Kaolinite exchange between a stream and streambed: Laboratory experiments and validation of a

- colloid transport model: *Water Resources Research*, v. 36, no. 8, p. 2363-2372.
- Packman, A., and MacKay, J., 2003, Interplay of stream-subsurface exchange, clay particle deposition, and streambed evolution: *Water Resources Research*, v. 39, no. 4, p. 1097.
- Peabody, F., 1947, Current crescents in the Triassic Moenkopi formation: *Journal of Sedimentary Research*, v. 17, no. 2, p. 73-76.
- Pollard, A., Wakarani, N., and Shaw, J., 1996, Genesis and morphology of erosional shapes associated with turbulent flow over a forward-facing step: *Coherent Flow Structures in Open Channels*. Wiley, New York, p. 249-265.
- Richards, A., 1961, Investigations of Deep-sea Sediment Cores: Shear strength, bearing capacity, and consolidation.
- , 1988, *Vane Shear Strength Testing in Soils: Field and Laboratory Studies*, Astm International, 365 p.
- Richards, A., McDonald, V., Olson, R., and Keller, G., 1972, In-place measurement of deep sea soil shear strength: Underwater soil sampling, testing and construction control, *ATSM STP*, v. 501, p. 55-68.
- Richards, A., Palmer, H., and Perlow Jr, M., 1975, Review of continental shelf marine geotechnics: distribution of soils, measurement of properties, and environmental hazards: *Marine Georesources & Geotechnology*, v. 1, no. 1, p. 33-67.
- Richards, A., and Parker, H., Surface coring for shear strength measurements, *in Proceedings Proc. ASCE Civil Engineering in Oceans Conf.:(United States)1968*, Illinois Univ.
- Richardson, K., and Carling, P., 2005, A typology of sculpted forms in open bedrock channels, *GSA Bookstore*, v. 392, 108 p.
- , 2006, The hydraulics of a straight bedrock channel: Insights from solute dispersion studies: *Geomorphology*, v. 82, no. 1-2, p. 98-125.
- Rijn, L., 1984, Sediment transport, Part II: Suspended load transport: *Journal of hydraulic engineering*, v. 110, no. 11, p. 1613-1641.
- Rocker, K., 1974, Vane shear strength measurements on Leg 27 sediment, *in PR Robinson, H. B., et al. , ed., Initial Reports of the Deep Sea Drilling Project, Volume 27*, p. 425-432.
- Rolland, T., and Lemmin, U., 1997, A two-component acoustic velocity profiler for use in turbulent open-channel flow: *Journal of hydraulic research*, v. 35, no. 4, p. 545-562.
- Rothwell, R., 2004, Deep ocean pelagic oozes, *in Selley, R., Cocks, R., and Plimer, I., eds., Encyclopedia of Geology*, Elsevier, p. chapter pagination unknown at present. 2750pp. in 2755 volumes.
- Sato, S., Matsuura, H., and Mayazaki, M., 1987, Potholes in Shikoku, Japan: Part I. Potholes and their hydrodynamics in the Kurokawa River, Ehime: *Memoirs of the Faculty of Education of Ehime University, Natural Science*, v. 7, p. 127-190.
- Saunderson, H., and Lockett, F., 1983, Flume experiments on bedforms and structures at the dune-plane bed transition: *Modern and Ancient Fluvial Systems: International Association of Sedimentologists, Special Publication*, v. 6, p. 49-58.
- Sawyer, W., Ransom, B., and Bennett, R., 1997, Geotechnical property variability of continental margin sediments: High - resolution vertical

- and lateral data from the northern California slope: Marine georesources & geotechnology, v. 15, no. 3, p. 283-304.
- Schieber, J., Southard, J., and Schimmelmann, A., 2010, Lenticular shale fabrics resulting from intermittent erosion of water-rich muds—interpreting the rock record in the light of recent flume experiments: *Journal of Sedimentary Research*, v. 80, no. 1, p. 119-128.
- Schieber, J., Southard, J., and Thaisen, K., 2007, Accretion of mudstone beds from migrating floccule ripples: *Science*, v. 318, no. 5857, p. 1760-1763.
- Seidl, M., Weissel, J., and Pratson, L., 1996, The kinematics and pattern of escarpment retreat across the rifted continental margin of SE Australia: *Basin Research*, v. 8, no. 3, p. 301-316.
- Selby, M., 1985, *Earth's changing surface: an introduction to geomorphology*, Clarendon Press, 262 p.
- Shaw, J., 1996, A meltwater model for Laurentide subglacial landscapes, *in* McCann, S., and Ford, D., eds., *Geomorphology Sans Frontieres*, Chichester, UK, John Wiley and Sons, p. 181-236.
- Shaw, J., Faragini, D., Kvill, D., and Rains, R., 2000, The Athabasca fluting field, Alberta, Canada: implications for the formation of large-scale fluting (erosional lineations): *Quaternary Science Reviews*, v. 19, no. 10, p. 959-980.
- Shepherd, R., and Schumm, S., 1974, Experimental study of river incision: *Geological Society of America Bulletin*, v. 85, no. 2, p. 257-268.
- Shrock, R., 1948, *Sequence in Layered Rocks*, McGraw-Hill Book Company, Incorporated, 508 p.
- Sklar, L., and Dietrich, W., 1998, River longitudinal profiles and bedrock incision models: Stream power and the influence of sediment supply, *in* Tinkler, J., and WOHL, E., eds., *Rivers Over Rock: Fluvial Processes in Bedrock Channels*, Volume 107, Geophysical Monograph Series, p. 237-260.
- Sklar, L., and Dietrich, W., 2001, Sediment and rock strength controls on river incision into bedrock: *Geology*, v. 29, no. 12, p. 1087-1090.
- , 2004, A mechanistic model for river incision into bedrock by saltating bed load: *Water Resources Research*, v. 40, no. 6.
- Smith, D., Greenaway, M., Moses, C., and Spate, A. P., 1995, Limestone weathering in Eastern Australia. Part 1: Erosion rates: *Earth Surface Processes and Landforms*, v. 20, no. 5, p. 451-463.
- Soltanpour, M., Haghshenas, S., and Mehta, A., 2009, Fluidized Mud-Wave Interaction under Regular and Irregular Waves: *Journal of Coastal Research*, v. 25, no. 3, p. 616-626.
- Southard, J., 1991, Experimental determination of bed-form stability: *Annual Review of Earth and Planetary Sciences*, v. 19, p. 423.
- Southard, J., and Boguchwal, L., 1973, Flume experiments on the transition from ripples to lower flat bed with increasing sand size: *Journal of Sedimentary Research*, v. 43, no. 4, p. 1114-1121.
- Spaggiari, R., Ward, J., and De Wit, M., 1999, Fluid characteristics of the diamondiferous Droogeveldt Gravels, Vaal Valley, South Africa: *Economic Geology*, v. 94, no. 5, p. 741-747.
- Springer, G., Tooth, S., and Wohl, E., 2005, Dynamics of pothole growth as defined by field data and geometrical description: *Journal of Geophysical Research-Earth Surface*, v. 110, no. F4, p. 1-10.

- , 2006, Theoretical modeling of stream potholes based upon empirical observations from the Orange River, Republic of South Africa: *Geomorphology*, v. 82, no. 1-2, p. 160-176.
- Springer, G., and Wohl, E., 2002, Empirical and theoretical investigations of sculpted forms in Buckeye Creek Cave, West Virginia: *Journal of Geology*, v. 110, no. 4, p. 469-481.
- Takeda, Y., 1991, Development of an ultrasound velocity profile monitor: *Nuclear Engineering and Design*, v. 126, no. 2, p. 277-284.
- Teufel, M., Trimis, D., Lohmüller, A., Takeda, Y., and Durst, F., 1992, Determination of velocity profiles in oscillating pipe-flows by using laser Doppler velocimetry and ultrasonic measuring devices: *Flow measurement and Instrumentation*, v. 3, no. 2, p. 95-101.
- Thibodeaux, L., and Boyle, J., 1987, Bedform-generated convective transport in bottom sediment: *Nature*, v. 325, p. 341 - 343.
- Tinkler, K., 1993, Fluvially sculpted rock bedforms in Twenty Mile Creek, Niagara Peninsula, Ontario: *Canadian Journal of Earth Sciences*, v. 30, no. 5, p. 945-953.
- , 1997a, Rockbed wear at a flow convergence zone in Fifteen Mile Creek, Niagara Peninsula, Ontario: *The Journal of Geology*, v. 105, no. 2, p. 263-274.
- Tinkler, K., and Parish, J., 1998, Recent adjustments to the long profile of Cooksville Creek, an urbanized bedrock channel in Mississauga, Ontario: *Geophysical Monograph, American Geophysical Union*, v. 107, p. 167-188.
- Tinkler, K., and Stenson, R., 1992, Sculpted bedrock forms along the Niagara escarpment, Niagara Peninsula, Ontario: *Géographie physique et Quaternaire*, v. 46, no. 2, p. 195-207.
- Tinkler, K., and Wohl, E., 1998, Rivers over rock: fluvial processes in Bedrock channels, *Amer Geophysical Union*, v. 107, 323 p.
- , 1998a, Rivers over rock: fluvial processes in Bedrock channels, *Amer Geophysical Union*, v. 107, 323 p.
- , 1998b, A primer on bedrock channels: *Geophysical monograph*, v. 107, p. 1-18.
- Tokuhiro, A., and Takeda, Y., 1993, Measurement of flow phenomena using the ultrasonic velocity profile method in a simulated Czochralski crystal puller: *Journal of Crystal Growth*, v. 130, no. 3, p. 421-432.
- Tooth, S., and McCarthy, T., 2004, Anabranching in mixed bedrock-alluvial rivers: the example of the Orange River above Augrabies Falls, Northern Cape Province, South Africa: *Geomorphology*, v. 57, no. 3-4, p. 235-262.
- Tritton, D., 1988, *Physical fluid dynamics*, Oxford, Clarendon Press, 536 p.
- Turowski, J., 2009, Stochastic modeling of the cover effect and bedrock erosion: *Water Resources Research*, v. 45.
- Turowski, J., Hovius, N., Hsieh, M., Lague, D., and Chen, M., 2008, Distribution of erosion across bedrock channels: *Earth Surface Processes and Landforms*, v. 33, no. 3, p. 353-363.
- Vachtman, D., and Laronne, J., 2011, Flow Structure over Bed Irregularities in a Straight Cohesive Open Channel: *Journal of hydraulic engineering*, v. 137, no. 11, p. 1335-1346.

- Vallejo, L., and Mawby, R., 2000, Porosity influence on the shear strength of granular material–clay mixtures: *Engineering Geology*, v. 58, no. 2, p. 125-136.
- Wan, Z., 1985, Bed material movement in hyperconcentrated flow: *Journal of hydraulic engineering*, v. 111, no. 6, p. 987-1002.
- Weissel, J., and Seidl, M., 1997, Influence of rock strength properties on escarpment retreat across passive continental margins: *Geology*, v. 25, no. 7, p. 631-634.
- Wende, R., 1999, Boulder bedforms in jointed-bedrock channels: *Varieties of Fluvial Form*, p. 189-216.
- Whipple, K., 2004, Bedrock rivers and the geomorphology of active orogens: *Annual Review of Earth and Planetary Sciences*, v. 32, p. 151-185.
- Whipple, K., Hancock, G., and Anderson, R., 2000b, River incision into bedrock: Mechanics and relative efficacy of plucking, abrasion, and cavitation: *Geological Society of America Bulletin*, v. 112, no. 3, p. 490-503.
- Whipple, K., Snyder, N., and Dollenmayer, K., 2000a, Rates and processes of bedrock incision by the Upper Ukak River since the 1912 Novarupta ash flow in the Valley of Ten Thousand Smokes, Alaska: *Geology*, v. 28, no. 9, p. 835-838.
- Williams, J., Carling, P., Amos, C., and Thompson, C., 2008, Field investigation of ridge–runnel dynamics on an intertidal mudflat: *Estuarine, Coastal and Shelf Science*, v. 79, no. 2, p. 213-229.
- Wilson, A., Hovius, N., and Turowski, J., 2012, Upstream-facing convex surfaces: Bedrock bedforms produced by fluvial bedload abrasion: *Geomorphology*, v. 180-181, no. 1, p. 187-204.
- Winterwerp, J., de Boer, G., Greeuw, G., and van Maren, D., 2012a, Mud-induced wave damping and wave-induced liquefaction: *Coastal Engineering*, v. 64, p. 102-112.
- Winterwerp, J., and Van Kesteren, W., 2004, Introduction to the physics of cohesive sediment dynamics in the marine environment, Access Online via Elsevier, 576 p.
- Winterwerp, J., van Kesteren, W., van Prooijen, B., and Jacobs, W., 2012b, A conceptual framework for shear flow-induced erosion of soft cohesive sediment beds: *Journal of Geophysical Research-Oceans*, v. 117, p. 1-17.
- Wohl, E., 1992, Bedrock benches and boulder bars: Floods in the Burdekin Gorge of Australia: *Geological Society of America Bulletin*, v. 104, no. 6, p. 770-778.
- , 1993, Bedrock channel incision along Piccaninny Creek, Australia: *The Journal of Geology*, v. 101, no. 6, p. 749-761.
- , 1998a, Bedrock channel morphology in relation to erosional processes: *Geophysical Monograph, American Geophysical Union*, v. 107, p. 133-152.
- , 1998b, Field studies of bedrock channels, *in* Tinkler, J., and WOHL, E., eds., *Rivers Over Rock: Fluvial Processes in Bedrock Channels*, Volume 107, *Geophysical Monograph Series*, p. 261-277.
- , 2000, Substrate influences on step-pool sequences in the Christopher Creek drainage, Arizona: *The Journal of Geology*, v. 108, no. 1, p. 121-129.

- Wohl, E., and Achyuthan, H., 2002, Substrate Influences on Incised - Channel Morphology: *The Journal of Geology*, v. 110, no. 1, p. 115-120.
- Wohl, E., and Ikeda, H., 1997, Experimental simulation of channel incision into a cohesive substrate at varying gradients: *Geology*, v. 25, no. 4, p. 295-298.
- , 1998, Patterns of bedrock channel erosion on the Boso Peninsula, Japan: *The Journal of Geology*, v. 106, no. 3, p. 331-345.
- Wohl, E., and Merritt, D., 2001a, Bedrock channel morphology: *Geological Society of America Bulletin*, v. 113, no. 9, p. 1205-1212.
- Wohl, E. E., and Merritt, D. M., 2001b, Bedrock channel morphology: *Geological Society of America Bulletin*, v. 113, no. 9, p. 1205-1212.
- Yalin, M., and Selim, M., 1992, *River mechanics*, Pergamon Press Oxford, 219 p.
- Zedel, L., and Hay, A., Turbulence measurements in a jet: Comparing the Vectrino and Vectrinoll, *in Proceedings Current, Waves and Turbulence Measurements (CWTM)*, 2011 IEEE/OES 10th2011, IEEE, p. 173-178.
- Zen, E., and Prestegard, K., 1994, Possible hydraulic significance of two kinds of potholes: Examples from the paleo-Potomac River: *Geology*, v. 22, no. 1, p. 47-50.

List of Abbreviations

Abbreviations

ADV Acoustic Doppler velocimetry;

ASPPwEEF Approximate-symmetrical paired pothole with both entry and exit furrows;

BFm Bladed forms;

BFrw Bifurcating furrows;

CFrw Convergent furrows;

CoP Complex potholes;

CpdP Compound potholes;

CPSFrw Cuspate furrows;

CSF Comet-shaped flutes;

CSFrw Curved short furrows;

Exp. X: Experiments X, X=0,1, 2, 3 ... 8, e.g. Exp.8 means Experiments 8;

DSDP Deep Sea Drilling Project;

DSLR Digital single-lens reflex cameras;

EF Expanding furrows;

FwESS Flutes with external secondary structures;

FwISS Flutes with internal secondary structure;

FwMR Flutes with median ridges;

GPSF Groups of parallel-sided furrows;

HF Hummocky forms;

HP Hierarchical potholes;

HSPP Horseshoe-shaped paired potholes;

IRCF Irregular compound furrows;

LDA Laser Doppler anemometry;

NCPSFrw Non-cuspate parallel-sided furrows;

OF Overhanging flutes;

OM Obstacle marks;

OP Open potholes;

PCF Paired convergent flutes;

PF Paired flutes;

PIV Particle image velocimetry;

PwEEF Potholes with extended exit furrows;

PwEF Potholes with exit furrows;

PwEnEF Potholes with both entry and exit furrows;

PwESF Potholes with external secondary furrow;

PwHF Potholes with horizontal furrows;

RCFrw Regular compound furrows;

RF Reversed furrows;

SCHF Sharp-crested hummocky forms;

Seatek Seatek Ultrasonic Ranging System;

SEFDL: the Sorby Environmental Fluid Dynamics Laboratory in the School of Earth and Environment (SEE), University of Leeds;

SF Spindle-shaped flutes;

SFP Spiral furrowed potholes;

SFPwSR Spiral-furrowed pothole with a spiral rib;

SPFrw Straight parallel-sided furrows;

SPSFrw Sinuous parallel-sided furrows;

SRP Standard round potholes;

SSC Suspended sediment concentration;

SSFrw Straight short furrows;

SZFrw Shear zone furrows;

T(x) Time point of x minutes, e.g. T1800 is Time point of 1800 minutes in the experiments;

T(x)-bed The experimental clay at time point of x minutes, e.g. T1800-bed means the clay bed obtained after running the sediment-laden flow for 1800 minutes;

UFSCs Upstream-facing convex surfaces;

UDVP Ultrasonic Doppler velocity profiler probe;

X longitudinally direction;

XRD X-ray diffraction;

Y Transverse direction (across-stream);

Z Vertical direction;

Symbol in calculation

τ shear stress;

c_u Undrained shear strength;

D_{mean} Mean grain size of particle;

D_{10} Grain size at which the particle cumulative volume is 10%;

D_{50} Median grain size of sediment;

D_{90} Grain size at which the particle cumulative volume is 90%;

d Diameter;

Fr Froude number;

$H_{1/2}$ Characteristic height of the flow, defined as the distance from the floor
at which the downstream velocity maximum occurs;

h Height;

PI Plasticity Index, $PI = \text{liquid limit} - \text{plastic limit}$;

R^2 Coefficient of determination;

T Torque;

u Flow velocity;

u^* Shear velocity

$v_{H1/2}$ Flow velocity at $H_{1/2}$ (equivalent to the velocity maximum);

W Water content;